The Phenomenology of Light Flavor-Universal Anomaly-Free Vector Bosons

by

Haidar Esseili

A dissertation accepted and approved in partial fulfillment of the
requirements for the degree of
Doctor of Philosophy
in Physics

Dissertation Committee:
Tien-Tien Yu, Chair
Graham D. Kribs, Advisor
Eric C. Torrence, Core Member
Boris Botvinnik, Institutional Representative

University of Oregon
Spring 2026

© 2026 Haidar Esseili
This work, including text and images of this document but not including supplemental files (for example, not including software code and data), is licensed under a Creative Commons
Attribution 4.0 International License.



DISSERTATION ABSTRACT

Haidar Esseili

Doctor of Philosophy in Physics

Title: The Phenomenology of Light Flavor-Universal Anomaly-Free Vector Bosons

We calculate the terrestrial, astrophysical, and cosmological constraints on a light vector boson X that couples to an arbitrary combination of the electromagnetic and $B-L$ currents of the Standard Model. The dark photon and a vector boson coupling to $B-L$ are special cases of this generalized flavor-universal anomaly-free vector boson, requiring just one additional parameter (the "dark mixing angle" corresponding to the linear combination of the electromagnetic and $B-L$ currents) beyond the overall coupling strength and the vector boson mass. We perform a detailed investigation of a unique combination where the vector boson couplings to electrically charged leptons and protons are highly suppressed: the "chargephobic dark photon". A chargephobic vector boson is very weakly constrained by current terrestrial experiments including beam dumps and collider searches, since they rely on couplings to electrons and protons. Instead, neutrino scattering experiments (such as COHERENT), astrophysical sources (supernova emission), and cosmology ($\Delta N_{\rm eff}$) provide the strongest constraints due to the nonzero couplings of the chargephobic vector boson to neutrinos and neutrons. Indeed, we find that supernova emission and $\Delta N_{\rm eff}$ provide constraints throughout the space of dark mixing angles, demonstrating their importance as model-independent constraints. Given this central role, we carry out the detailed calculation of $\Delta N_{\rm eff}$ for gauged $B-L$ in the mass range $1\,\text{eV}$ to $100\,\text{MeV}$, solving the full system of Boltzmann equations with the temperature and chemical potential of each species and including finite temperature effects. We find

$B - L$ is more strongly constrained by $\Delta N_{\rm eff}$ than previously considered, and identify regions of mass and coupling space that future CMB observatories can access not probed by any other method. For nearly all of the parameter space, a chargephobic vector boson is the most weakly constrained anomaly-free vector boson that couples to flavor-independent or flavor-dependent combinations of standard model currents. Finally, we highlight the importance of future experiments, including SHiP, that *are* able to probe new regions of the chargephobic parameter space due to the significantly improved detector capabilities.

This dissertation contains previously published as well as unpublished coauthored materials.

CURRICULUM VITAE

NAME OF AUTHOR: Haidar Esseili

GRADUATE AND UNDERGRADUATE SCHOOLS ATTENDED:

University of Oregon, Eugene, OR, USA
College of Wooster, Wooster, OH, USA

DEGREES AWARDED:

Doctor of Philosophy, Physics, 2026, University of Oregon
Master of Science, Physics, 2021, University of Oregon
Bachelor of Arts, Physics, 2019, College of Wooster
Bachelor of Arts, Mathematics, 2019, College of Wooster

AREAS OF SPECIAL INTEREST:

Beyond Standard Model phenomenology
Early universe cosmology
Particle astrophysics

PROFESSIONAL EXPERIENCE:

Graduate Research Assistant, University of Oregon, 2019 - 2026
Graduate Teaching Assistant, University of Oregon, 2019 - 2026

GRANTS, AWARDS AND HONORS:

Lokey Dissertation Fellowship, University of Oregon, 2026

PUBLICATIONS:

H. Esseili and G. Kribs. *"Hiding a Light Vector Boson from Terrestrial Experiments: A Chargephobic Dark Photon"*, [arXiv:2512.10916]

H. Esseili and G. Kribs. *"Cosmological Implications of Gauged $U(1)_{B-L}$ on ΔN_{eff} in the CMB and BBN,"*, JCAP 05 (2024) 110. [arXiv:2308.07955]

ACKNOWLEDGEMENTS

Though my name is on this dissertation, none of it is truly mine alone. It belongs to everyone whose thinking, kindness, and patience shaped my own. This list is long and any attempt at naming everyone will fall short, but I will try anyway.

First and foremost, I am deeply grateful to my advisor, Graham Kribs, without whom none of this work would exist. His mentorship was pivotal in shaping the physicist I am, and more importantly, it taught me the correct hierarchy of priorities: mountains, climbing, physics, and though never explicitly said out loud, probably Chipotle. (This dissertation is not sponsored by Chipotle; not for lack of trying.)

I am thankful to the hep Group: Graham Kribs, Tien-Tien Yu, Spencer Chang, Tim Cohen, Dave Soper, Ben Lillard, Pouya Asadi, my fellow graduate students (esp. Tom, Tom, & Thomas) and my collaborators Robert McGehee & Gilly Elor, for creating an environment where it was safe to be confused about Physics and for always being generous with their time whenever I was. I am thankful to Anne McGinley, Claire Staley, and Ellen Macomson for keeping the place from falling apart.

I am thankful to my mentors and teachers: Susan Lehman, my first mentor, for taking a chance on an undergraduate with more enthusiasm than experience at the time. John Lindner & Jennifer Bowen for guiding me through my first independent research project. All the above and Cody Leary, Niklas Manz, Dietrich Belitz, John Toner, Jayson Paulose, Dan Steck, Ben Farr, Stephanie Majewski, Tim Cohen, and Graham Kribs for teaching me the beauty in physics and how to see it.

I am thankful to my friends: Sean for the infinite well of fun facts. Matt for overly convoluted questions. Sangeet for heated late night debates that never once reached consensus. Kevin for always elevating the bit and losing Jeremy. Alyssa for

crab walks and robbing me of a lifetime supply of free pickles. Kylie for blundered queens (on both sides). Jacqui for knuckleheads. Jo for doing everything I do but better. Braeden for never letting me be injured alone. Amber for natural units and tacky Tuesdays. Ben for never taking life too seriously. Cob & Lily for putting up with my game show shenanigans. Uriel, Fran, & Esther for being the kindest humans I know. Avi, Rie, & Shiwani for stellar polka roses. And Taphy for more things than can fit in the page limit of this acknowledgement.

I am thankful to Eugene, and for everyone who turned a place I moved to for a degree into one I will be sad to leave: Jules, Taylor, and Gillian for the showing me all the hidden gems. Phil, Michael, Lincoln, Meg, Briana, and Ross for cultivating an exceptional community. Ethan, Bryce, Matt, David, Shayn, Renzo, Aiden, Jonathan, Turner, Asher, Ben, Tiera, Odi, Kim, Mark, Anna, Nola, Jacob, Eli, Phoebe, Garrett, Kalel, Kade, Champe, Portia, Kai, Jack, and many others for the countless evenings on the wall, the trust that builds when you let people watch you fall, and the closeness that comes from watching them do the same.

I am thankful to those who drifted into my life and, in time, gently out of it, leaving their mark in the space between: JF, AB, MM, IK, AS, KB, PV, AV, TN, BJ, MB, DY, GDG, RA, MM, HH, KJ, SB, JB, AN, MF, YM, AS, HY, FM, IY, SK, RA, AA, NA, JA, JB, MS, MK, VK, RF, EG, SL, TK, TD. There is grace in the ways of water, and in the shore it shapes.

Finally, to my family, who gave me every opportunity I have had and asked for nothing in return. The path that led to this dissertation began long before I did, in the chances they made possible and the foundation they laid without my noticing. Whatever I have made of myself began with them. I would not be here, in any sense, without them. Thank you!

For Elevation,

the kindness in difficult things,

and the people who share them.

TABLE OF CONTENTS

Chapter Page

I. OVERVIEW 14

II. HIDING A LIGHT VECTOR BOSON FROM TERRESTRIAL EXPERIMENTS: A CHARGEPHOBIC DARK PHOTON 21

2.1. Introduction 21

2.2. Model 25

2.2.1. Vector Bosons Coupling to EM and $B - L$ Currents 25

2.3. Overview of Results 28

2.3.1. Dark Photon and $B - L$ Results 28

2.3.2. Chargephobic Dark Photon Results 30

2.3.3. Other Dark Mixing Angles 32

2.4. Production 33

2.4.1. Branching Fraction 37

2.5. Constraints 42

2.5.1. Cosmology: CMB & BBN 43

2.5.2. Astrophysics 49

2.5.2.1. Protoneutron Star Cooling: SN1987A 50

2.5.2.2. High Energy Neutrinos 58

2.5.2.3. Electromagnetic-Based Supernova Signals 59

2.5.3. Neutrino Experiments 61

2.5.3.1. Coherent elastic neutrino-nucleus scattering Experiments 63

2.5.3.2. Neutrino-electron Scattering Experiments 66

2.5.3.3. Invisible Searches 68

Chapter Page

2.5.3.4. Collider Neutrinos 69

2.5.4. Beam Dump & Fixed Target Experiments 70

2.5.5. Collider Experiments 73

2.5.6. Precision Constraints 75

2.6. Discussion 76

III. COSMOLOGICAL IMPLICATIONS OF GAUGED $U(1)_{B-L}$ ON $\Delta N_{\rm EFF}$ IN THE CMB AND BBN 81

3.1. Introduction 81

3.2. Gauged U$(1)_{B-L}$: Majorana and Dirac neutrino cases 83

3.2.1. Neutrino masses: Majorana and Dirac cases 85

3.3. Effective number of relativistic species: $N_{\rm eff}$ 87

3.4. Early universe thermodynamics 89

3.4.1. Approximations 91

3.4.2. Boltzmann equations 93

3.4.3. Collision terms 94

3.4.3.1. Electron-neutrino interactions 96

3.4.3.2. Decays and inverse decays 97

3.4.3.3. Electron-X interactions 98

3.4.3.4. Suppressed interactions 99

3.4.4. Summary of transfer rates 100

3.5. Numerical evolution of the Boltzmann equations and $N_{\rm eff}$ 101

3.5.1. Initial conditions 101

3.5.2. Evolution of Boltzmann equations 102

3.5.3. Numerical results for $N_{\rm eff}$ 108

3.5.4. Other constraints 113

Chapter Page

3.5.5. Constraints from existing CMB observations and prospects for future observatories . . . 114

3.6. Semi-analytic estimates of delta $\Delta N_{\rm eff}$ . . . 117

3.6.1. Majorana case . . . 118

3.6.2. Dirac and generalized cases . . . 119

3.6.2.1. Dirac case . . . 120

3.6.2.2. Large number of massless species . . . 121

3.6.2.3. Massive species . . . 122

3.7. BBN Y_p . . . 122

3.8. Discussion . . . 125

APPENDICES

A. GENERATING THE DARK MIXING ANGLE . . . 131

B. RENORMALIZATION GROUP EQUATIONS . . . 133

C. BREMSSTRAHLUNG IN PROTO-NEUTRON STAR . . . 138

D. RIGHT-HANDED NEUTRINO DECAY IN MAJORANA CASE . . . 140

E. FINITE TEMPERATURE EFFECTS . . . 142

E.1. $m_\gamma(T) \ll m_X$ . . . 144

E.2. $m_\gamma(T) \gg m_X$ . . . 144

E.3. $m_\gamma(T) = m_X$ resonance . . . 145

E.4. Implications of the resonance on our results . . . 146

REFERENCES CITED . . . 148

CHAPTER I

OVERVIEW

The existence of dark matter (DM) is among the most robust conclusions in modern physics [1]. Galactic rotation curves establish that luminous matter alone cannot account for the observed dynamics of spiral galaxies; the observed velocities of stars and gas at large radii require an extended halo of non-luminous (dark) matter with a mass profile that continues to grow beyond the luminous disk [2–7]. Gravitational lensing provides a luminosity-independent probe of total mass distribution and observations across a range of systems, most strikingly the Bullet Cluster [8], consistently find that the inferred mass substantially exceeds that of the luminous matter [9, 10]. On the level of large-scale structure, the observed matter power spectrum cannot be reproduced by baryons alone; a pressureless component is needed to seed the gravitational collapse responsible for the observed patterns of galaxy clustering [11–14]. Finally, the acoustic peaks of the cosmic microwave background (CMB) power spectrum independently determine the baryonic and the total matter densities, and their ratio implies a non-baryonic matter component comprising approximately 26% of the total energy density of the universe [15–17]. Despite this overwhelming evidence, none of these observables reveal the fundamental properties of DM such as its mass, spin, and non-gravitational interactions. Determining these properties has motivated a broad and ongoing theoretical and experimental program spanning terrestrial, astrophysical, and cosmological probes.

A natural organizing principle for this program is to enumerate the possible low dimension operators, dubbed dark sector *portals*, connecting a dark sector to the Standard Model (SM). Four such portals that have attracted sustained theoretical and experimental interest are the Higgs portal, the vector portal, the neutrino portal, and

the pseudoscalar portal [18–20]. Each appears naturally in well motivated extensions of the SM and gives rise to distinct phenomenology with unique experimental signatures. This thesis focuses on the vector portal; specifically, we carry out a complete and exhaustive characterization of the space of anomaly-free flavor universal vector boson.

The vector portal corresponds to a new $U(1)$ gauge boson mixing with the SM. The SM gauge group, $SU(3)_C \times SU(2)_L \times U(1)_Y$, already contains $U(1)$ structure at its core. Here, $U(1)_Y$ is the hypercharge symmetry that, together with $SU(2)_L$, is spontaneously broken at the electroweak scale to the residual $U(1)_{\rm EM}$ of electromagnetism. Beyond hypercharge, the SM contains several additional accidental global $U(1)$ symmetries that emerge purely from the field content and the requirement of renormalizability. These symmetries are baryon number B and the three individual lepton flavor numbers L_e, L_μ, and L_τ. None of these are exact symmetries; baryon number is broken non-perturbatively by electroweak sphalerons and the individual lepton flavor numbers are broken by small neutrino masses. Importantly, however, the combination $B-L$ is preserved by sphaleron processes and is free of all gauge and gravitational anomalies if three right-handed neutrinos are added to the SM particle content. This makes $B-L$ a unique flavor-universal global symmetry of the SM that can be promoted to a local symmetry with minimal new particle content.

The existence of these symmetries is tantalizing; are any of them in fact gauged at low energies by a new light vector boson not yet observed? To address this question systematically, we broadly classify $U(1)$ symmetries into two categories: anomalous and anomaly-free. A gauged $U(1)_X$ is anomaly-free if all triangle diagrams involving the new gauge boson vanish. Concretely, the mixed anomaly

coefficients $[SU(3)_C]^2U(1)_X$, $[SU(2)_L]^2U(1)_X$, $[U(1)_Y]^2U(1)_X$, the cubic $[U(1)_X]^3$, and the gravitational anomaly must vanish.

When this condition fails within the SM field content, the $U(1)_X$ is anomalous and the associated current is not conserved at the quantum level. Gauged baryon number, $U(1)_B$, is the prototypical example where both mixed anomalies coefficients, $[SU(2)_L]^2U(1)_X$ and $[U(1)_Y]^2U(1)_X$, are non-zero [21–24]. Gauged individual and total lepton number are similarly anomalous [25–28], and so are more general constructions with axial coupling to SM fermions and some generation non-universal couplings [29]. The consistency of such theories at high energies requires the introduction of additional heavy chiral fermions, called anomalons, whose electroweak and $U(1)_X$ charges must be chosen to cancel the anomalies. Integrating out these fermions leaves behind Wess-Zumino (WZ) operators coupling X to a pair of SM gauge boson; the WZ coefficients are fixed and are independent of the details of the UV theory [30]. By the usual Goldstone equivalence arguments, amplitudes involving these operators and the longitudinal mode of X will grow with energy as $(E/m_X)^2$. This enhancement drives electroweak decays such as $Z \to X\gamma$ and flavor changing neutral current (FCNC) meson decays such as $B \to KX$ and $X \to \pi X$ placing stringent bounds on X [29, 31]. As a consequence, the parameter space of an anomalous $U(1)$ is substantially reduced before any dedicated search even begins. The longitudinal enhancement is not present in anomaly-free $U(1)$ where the current is conserved.

A complete atlas of anomaly free $U(1)$s, up to $Q_{\max} = 10$, has been catalogued in Ref. [32]. Among those, flavor non-universal combinations generically introduce new phenomenology in the quark and/or lepton sectors that is tightly constrained experimentally. For quarks this occurs through induced FCNC interactions

contributing to meson mixing and decays, and for leptons this occurs through induced non-standard neutrino interactions that modify neutrino propagation in matter; examples include gauged $L_i - L_j$, $B - 3L_i$, $B_3 - 3L_\mu$, and the third family hypercharge model to name a few [33–40]. Again, the parameter space of flavor non-universal anomaly-free $U(1)$s is substantially reduced before any dedicated search even begins.

Finally, we arrive at the subspace of $U(1)$s characterized by being both flavor-universal and anomaly-free which is the theoretical setting of this thesis. This space is far more restrictive; with the inclusion of three right handed neutrinos, there is in fact only two orthogonal $U(1)$s in the SM that fall under this category, namely, hypercharge/electromagnetism and $B - L$. Gauging a copy of hypercharge/electromagnetism is called the dark photon and is the poster child of vector portals in general. The low energy effective theory of a massive dark photon is simply a vector boson with Stückelberg mass and kinetic mixing with electromagnetism $\epsilon F_{A',\mu\nu} F^{\mu\nu}_{\rm em}$. The kinetic mixing can be rotated away resulting in the dark photon coupled to the electromagnetic current, $\epsilon e j^\mu_{\rm em} A'_\mu$ [39, 41–45]. Gauged $B - L$ as a light mediator has also been considered in detail in Refs. [39, 42, 46–51].

The most general flavor-universal anomaly-free vector boson, $U(1)_X$, is characterized by three parameters: its mass m_X, its overall coupling strength to SM field content g_X, and a dark mixing angle φ that specifies the linear combination of the electromagnetic and $B - L$ currents it couples to [52]. The dark mixing angle fixes the $U(1)_X$ charges of the four SM fermions types (charged leptons x_e, neutrinos x_ν, and up [down] type quarks x_u [x_d]) and smoothly transitions between the dark photon and $B - L$ charge assignments. When the boson couples purely to the electromagnetic current, *i.e.* the dark photon limit, it has no coupling to neutrinos and neutrons since neither carry electric charge. When the boson couples purely to the $B - L$ current,

mesons are uncharged but are still accessible through mixing between X and SM vector mesons [23, 42, 53]. These two limits are well established in the literature, however, intermediate angles have been largely neglected and require a dedicated study which is the subject of this thesis. At some intermediate angles, the $U(1)_X$ charges of different fermion types can vanish and subsequently different probes can gain/lose sensitivity to X depending on the available channels. This gives rise to a rich and highly non-trivial phenomenology in these intermediate angles that is absent from the dark photon or $B-L$ limits. Of particular interest to this thesis is the angle corresponding to the *chargephobic dark photon* model where the coupling to charged leptons vanish.

Having established our theoretical framework, the next step is to assess these models' phenomenological viability. This is achieved by constraining a model's parameter space using existing observables from cosmology, astrophysics, neutrino experiments, beam dumps, fixed target experiments, colliders, and precision determination of SM parameters. This thesis presents a systematic and comprehensive study of light flavor-universal anomaly-free $U(1)_X$ gauge bosons across the full range of dark mixing angles. The two chapters that constitute the body of this work correspond to the two papers in Ref. [52, 54]. Each chapter is self-contained, with its own introduction, notation, and conclusions; the two can be read independently, though the cosmological formalism developed in Chapter III underpins the ΔN_{eff} constraint invoked in Chapter II.

Chapter II develops the flavor-universal anomaly-free framework and derives the full suite of constraints that apply to it across the dark mixing angle space and the mass range 1 MeV to 60 GeV. The major constraints are derived independently rather than recast, both to update existing results in the literature and to ensure

that our constraint pipeline applies consistently across the full parameter space. This systematic treatment reveals a structural feature in the experimental layout: beam dumps, fixed target experiments, and collider searches rely critically on production from electron/proton beams and detection through charged particle final states and as such have degraded or vanishing sensitivity to X when its coupling to charged leptons and protons is reduced. The *chargephobic dark photon* model is a unique dark mixing angle where both these couplings vanish at tree level leading to a collapse in terrestrial constraints on X. The constraints that remain are those that rely on the coupling of X to neutrinos and neutrons: coherent neutrino nucleus scattering at experiments such as COHERENT and CONUS+, energy loss via nucleon-nucleon bremsstrahlung and neutrino coalescence in SN1987A, and modifications to ΔN_{eff} in the early universe. Across nearly all the vector boson parameter space, we find that the chargephobic dark photon model is the most weakly constrained at a given $\{m_X, g_X\}$, revealing a systematic gap in the reach of the laboratory program that is closed only by astrophysical and cosmological observations. Future experiments such as SHiP, which combines improved detector capabilities with sensitivity to hadronic final states, can close that gap by accessing regions of the chargephobic parameter space that are unreachable by current terrestrial searches.

The SN1987A cooling and ΔN_{eff} bounds persist across the entirety of the dark mixing angle space, making them the only model independent probes, not just of flavor universal anomaly free vector bosons that are the focus of this thesis, but also of the broader vector bosons landscape outlined in this chapter. Given the central role these probes play, a careful analysis of each is essential. In doing so, we improve the existing supernova bounds on $B - L$ and resolve an order of magnitude discrepancy between the bounds of Ref. [55] and Ref. [56].

Chapter III develops the cosmological formalism necessary to place ΔN_{eff} constraints in the context of gauged $B-L$. The analysis begins with the observation that cancelling the cubic anomaly $[U(1)_{B-L}]^3$ requires the introduction of three right-handed neutrinos and that their mass structure is not uniquely fixed. Neutrino masses may be Dirac, in which case the right-handed neutrinos are light and contribute directly to the radiation density, or Majorana, in which case they are heavy and decouple from the dynamics. Both cases are treated in this chapter, whereas only the Majorana case is considered in Chapter II [1]. The cosmological evolution is tracked by numerically solving the full system of Boltzmann equations including the temperature and chemical potential of each species while also considering finite temperature effects. In doing so, we capture the freeze-in of X, the X population evolving like matter at temperatures $T \sim m_X$, and then the X decay back into the SM bath. In the Majorana case, this back and forth results in the preferential heating of neutrino bath relative to the electron-photon plasma; this in turn increases ΔN_{eff} which is constrained by Planck [15–17]. The resulting bound is significantly stronger than the simple thermalization estimate that was previously made in the literature [57], in some regions by several orders of magnitude. In the Dirac case, X also decays to right-handed neutrinos which directly contribute to N_{eff} drastically strengthening the constraint. Finally, we identify a region of the parameter space that is inaccessible to current probes but will be available to future CMB observatories.

This dissertation contains previously published co-authored materials.

[1] Across the range of dark mixing angles, with the exception of the dark photon, the neutrino charge varies by an $\mathcal{O}(1)$ number. We then expect the ΔN_{eff} constraint placed on $B-L$ for $m_X > 1\,\text{MeV}$ in the Dirac case to roughly translate to other dark mixing angles. Furthermore, this ΔN_{eff} constraint supersedes all other constraints, see Fig. 21, with the exception of portions of the electromagnetic-based supernova constraints which vanish in the chargephobic limit.

CHAPTER II

HIDING A LIGHT VECTOR BOSON FROM TERRESTRIAL EXPERIMENTS: A CHARGEPHOBIC DARK PHOTON

This work will appear in Physical Review D shortly and was carried out in collaboration with Graham Kribs. It was modified to fit into the format of a chapter for this dissertation.

2.1 Introduction

Light vector bosons are ubiquitous in dark sectors, with their utility to connect the SM with the dark sector. An essential ingredient to achieve a relic abundance of light dark matter consistent with cosmology requires a light mediator, and a light vector boson has long been considered a prime candidate for this interaction. The diversity of uses and implications of light vector boson mediators have motivated a vast range of experimental searches. Extensive reviews (see, e.g., [39, 42–45]) have surveyed the terrestrial, astrophysical, and cosmological constraints on light vector boson couplings and masses.

The simplest model of a light vector boson mediator is the dark photon A'. The low energy effective theory of a massive dark photon is simply a vector boson with Stückelberg mass and kinetic mixing with electromagnetism[1], $\epsilon F_{A',\mu\nu} F^{\mu\nu}_{\rm em}$. The kinetic mixing can be rotated away resulting in the dark photon coupled to the electromagnetic current, $\epsilon e j^{\mu}_{\rm em} A'_{\mu}$. Electromagnetic current conservation ensures the longitudinal mode of the massive vector boson does not couple to the SM (at zero temperature). Other anomaly-free currents in the SM include $B - L$, the only other flavor-universal conserved current, when three right-handed neutrinos are added to the

[1]Above the electroweak scale, kinetic mixing with $U(1)_Y$.

model (early discussions include [46–49,58–62] and a review of massive Z's [63]), while a light vector boson coupled to $B-L$ has been considered in detail in [39, 42, 50, 51]). Other anomaly-free flavor-dependent combinations of B, L_e, L_μ, L_τ have also been considered (there is a vast literature, including [64–76] and more recently [40, 77–84]).

In this paper we consider a single, massive vector boson X^μ, that couples to a *linear combination* of the electromagnetic current and the $B-L$ current of the SM. The notion that a new vector boson could couple to an arbitrary linear combination of these currents is not new, and was emphasized long ago [59–62], in the context of Z's detectable at LHC [85], as well as for light vector bosons in [51]. Indeed, Refs. [51, 85] emphasized that it is expected that a vector boson coupling purely to $B-L$ at a high scale will automatically develop couplings to the hypercharge current (becoming a rescaled electromagnetic current below electroweak symmetry breaking) through renormalization group evolution. The size of these induced couplings depends critically on the field content and the extent of running. We will be agnostic towards the UV theory, and instead focus on the phenomenology within the low energy effective theory with no UV priors on the coupling strength, mixing angle, and vector boson mass.

A vector boson with a Stückelberg mass is a vector boson without gauge invariance [86]. Consequently, the vector boson can be directly coupled to an arbitrary vector current, i.e., $j_\mu X^\mu$, within or beyond the SM. That said, not all vector currents are the same, and in particular, nonconserved currents (such as baryon number) have significant additional constraints that arise from new processes enabled by anomalous couplings [29, 31] (see also [86]). For this reason, in this paper we focus on coupling to anomaly-free conserved currents, and choose to restrict to (linear combinations of) flavor-independent currents of the SM.

Readers who are already familiar with the constraints on a dark photon and a $B-L$ vector boson will recognize that there is a *large* overlap of the terrestrial, astrophysical, and cosmological constraints on these two distinct "pure" vector mediators. The overlap arises because just as a dark photon couples to charged leptons and protons, a $B-L$ vector boson also couples to leptons and hadrons. The main distinction is that there are additional constraints that arise on $B-L$ due to its couplings to neutrinos (as well as couplings to neutrons). Yet, much of the constraints that rely on couplings to electrons and/or protons broadly carry over from the case of a dark photon to the case of a $B-L$ vector boson.

In this paper, we show that there is an anomaly-free light vector boson with *qualitatively* different flavor-independent couplings: a "chargephobic" vector boson. A chargephobic vector boson couples to a specific linear combination of the electromagnetic current and the $B-L$ current, $-j^{\mu}_{\rm em}+j^{\mu}_{B-L}$, where the couplings to charged leptons and singly positively charged baryons vanish.[2] In this case, the vast majority of constraints from terrestrial experiments *disappear*. This is because most terrestrial experiments rely on the coupling of the vector boson to electrons or muons and/or the coupling to protons. At first glance, this has the potential to wipe clean the constraints in the coupling versus mass parameter space for a light vector boson mediator. However, as we will see, several constraints remain: terrestrial experiments that measure neutrino scattering off nuclei restrict much of the parameter space at larger couplings, while constraints on supernova cooling and constraints on

[2]Note that a vector boson with "chargephobic" couplings is *neither* "leptophobic" (since there are couplings to neutrinos) nor "protophobic" [42] (since protophobic vector bosons typically assumes there are couplings to charged leptons, while chargephobic does not couple to charged leptons). Yet another flavor-dependent current that is distinct from what we consider is $B-2L_{\mu}-L_{\tau}+r_{\mu\tau}(L_{\mu}-L_{\tau})$, where $r_{\mu\tau}$ is arbitrary. This has been called "electrophobic" [80], since the vector boson does not couple to electrons, but does couple to muons and/or taus.

modifications to early universe cosmology from $\Delta N_{\rm eff}$ restrict smaller couplings for smaller vector boson masses.[3]

The particular linear combination of currents that leads to chargephobic couplings is a tuned choice of parameters in the low energy effective theory. There is no technical obstacle to achieving this tuning from a UV theory. Indeed, for larger couplings, Ref. [85] suggested that $g_Y \sim -g_{B-L}$ could be an attractor of the renormalization group evolution that is close (but not identical) to achieving chargephobic couplings. Our interest will generally be much smaller couplings, and so we do not anticipate RG fixed points with SM couplings. We briefly discuss how linear combinations of electromagnetism and $B-L$ could arise by renormalization group evolution from a high scale in Appendix A.

What is more relevant for phenomenology is that there is renormalization group evolution of the dark mixing angle, and hence the couplings to SM fields. As we show, this effect is smaller than one might think, leaving a substantial range of energies where chargephobic couplings are present; see Appendix B. Nevertheless, we take into account this coupling evolution in our analysis, and show the constraints from experiments that operate at larger energies (such as LHCb and CMS searches for vector boson resonances to e^+e^- or $\mu^+\mu^-$), where the small regenerated coupling to charged leptons and protons is relevant.

Finally, in the course of calculating the constraints on a vector boson with chargephobic couplings, we also revisit the constraints on dark photons, $B-L$, and other linear combinations (that are not chargephobic). While we have employed recasting for a handful of constraints such as collider searches, we have also performed independent calculations of the major constraints that apply to a chargephobic gauge

[3]Ref. [51] presaged several of these constraints, but did not carry out a detailed investigation.

boson and other mixing angles φ. This includes a full out-of-equilibrium evolution of early universe dynamics of X including finite temperature effects to determine the cosmological implications. For supernova, we have carefully considered the production processes that arise as a function of φ, and used the Garching simulations [87] to model the detailed proto-neutron star properties that are essential to determine the cooling constraint. This has not only allowed us to determine the constraint on the chargephobic case, but it has also allowed us to obtain an accurate cooling constraint on a $B-L$ vector boson (clearing up some tension in past literature). Finally, we have performed a thorough analysis of the constraints from neutrino scattering off nucleons, using the data releases from the experiments, to determine the constraints that arise for $\varphi \neq 0$. These constraints are the most powerful when couplings to electrons and protons are suppressed.

2.2 Model

2.2.1 Vector Bosons Coupling to EM and $B-L$ Currents. We now provide an overview of the extension to the SM that we consider in the paper, specifying the parameters and couplings relevant to our analysis. Consider a vector boson X^μ with Proca Lagrangian

$$\mathcal{L}_X \;=\; -\frac{1}{4}F_{X,\mu\nu}F_X^{\mu\nu} + \frac{1}{2}m_X^2 X_\mu X^\mu\,, \tag{2.1}$$

where we are interested broadly in the mass range 1 MeV $\lesssim m_X \lesssim$ 60 GeV. For the purposes of this paper, the vector boson mass could arise from a spontaneously broken theory with suitable Higgs sector, where we assume the Higgs states are heavy enough to be neglected in our analysis, or it could simply be a Stückelberg mass. We will adopt the latter point of view, i.e., the vector field has a Stückelberg mass, and hence X^μ has no gauge invariance [86]. This immediately implies that we are free to

write interactions of X^μ to arbitrary currents of the SM. In this paper we further restrict the interactions of X^μ:

- Couplings to the SM are flavor-independent;
- Couplings only to conserved currents[4] of the SM; and,
- Dark sector interactions, if present, do not affect the couplings to the SM nor the decay width of X^μ.

While there are rather stealthy anomaly-free combinations of baryon number and one or more specific flavors of lepton number (for example, $B - 3L_\tau$), these interactions have strong constraints from non-standard neutrino interactions (NSI), for example [40, 79, 80, 82, 83]. Couplings to non-conserved currents have also been considered in [29–31, 86, 88, 89], where non-trivial phenomenology arises because longitudinal mode of X^μ also can couple to the SM. This can result in amplitudes involving X^μ that diverge at large $\sqrt{s}/m_X$, leading to a host of other strong experimental constraints. Finally, interactions between a light vector boson and the dark sector have been considered in a variety of contexts. For our purposes, if X^μ couples to other dark sector fields, we assume these interactions do not affect the couplings to the SM, nor do they change the decay width of X^μ.

The interactions of X^μ to the SM that we consider are thus

$$\mathcal{L}_{\rm int} \;=\; \left(\varepsilon e j_\mu^{\rm EM} + g_{B-L} j_\mu^{B-L}\right) X^\mu \,, \tag{2.2}$$

[4]More precisely, only linear interactions of X^μ with SM conserved currents. We do not include a Higgs portal interaction $H^\dagger H X^\mu X_\mu$.

where

$$j_\mu^{\rm EM} = \sum_f Q_f \bar{f}\gamma_\mu f \tag{2.3}$$

$$j_\mu^{B-L} = \sum_f q_f \bar{f}\gamma_\mu f \tag{2.4}$$

and $Q_f = (-1, 0, 2/3, -1/3)$ are the usual electric charges of the SM fermions (e, ν, u, d) while

$$q_f = (B-L)_f = \begin{cases} +1/3 & u,\ d \\ -1 & e,\ \nu_L,\ \nu_R\,, \end{cases} \tag{2.5}$$

are also the usual $B - L$ charges of the SM fermions. We have normalized the relative strength of X^μ couplings to the $B-L$ current with g_{B-L} and the EM current with εe which is familiar from dark photon literature. We have included right-handed neutrinos to ensure $B-L$ is anomaly-free, however we take the right-handed neutrinos to be heavy, above at least the weak scale, so that they do not directly affect the phenomenology of X^μ. A detailed discussion of the role of right-handed neutrinos, and the effects of taking them heavy can be found in our previous work [54].

We can rewrite the interactions of X^μ as

$$\mathcal{L}_X = g_X j_\mu^X X^\mu \tag{2.6}$$

$$j_\mu^X = \cos\varphi\, j_\mu^{\rm EM} + \sin\varphi\, j_\mu^{B-L} = \sum_f x_f\, \bar{f}\gamma_\mu f\,, \tag{2.7}$$

where we define the overall coupling strength and dark mixing angle as

$$g_X \equiv \sqrt{(\varepsilon e)^2 + g_{B-L}^2} \tag{2.8}$$

$$\varphi \equiv \tan^{-1}\frac{g_{B-L}}{\varepsilon e}\,, \tag{2.9}$$

such that the "charges" (or couplings) for an arbitrary fermion to the j_μ^X current are

$$x_f = Q_f \cos\varphi + q_f \sin\varphi \tag{2.10}$$

and for the SM fermions,

$$x_e = -\cos\varphi - \sin\varphi, \quad x_\nu = -\sin\varphi, \quad x_u = \frac{2\,\cos\varphi}{3} + \frac{\sin\varphi}{3}, \quad x_d = -\frac{\cos\varphi}{3} + \frac{\sin\varphi}{3}\,, \tag{2.11}$$

that we illustrate in Fig. 1. Note that under $X^\mu \to -X^\mu$, $\varphi \to \varphi + \pi$, and so without loss of generality we can restrict $0 \le \varphi < \pi$.

Mesons obviously do not carry $B-L$ number, and so their couplings to X^μ are determined just by their couplings to the electromagnetic current. For example, the pions

$$x_{\pi^\pm} = \pm\cos\varphi \tag{2.12}$$

$$x_{\pi^0} = 0\,. \tag{2.13}$$

Similarly, neutral baryons obviously do not carry electric charge, with their coupling to X^μ being the same as their coupling to a $B-L$ vector boson. Positive electrically charged baryons have a φ-dependent coupling to X^μ, which is easy to see is identical to the coupling of an electrically charged anti-lepton. For example, for the proton, $x_p = -x_e$ (and $x_{\bar{p}} = x_e$). Similarly, the neutron and neutrino have equal and opposite couplings, $x_n = -x_\nu$ (and $x_{\bar{n}} = x_\nu$). The couplings to baryons with different electrical charges differ from one another, for example for the Δ multiplet:

$$x_{\Delta^{++}} = 2\cos\varphi + \sin\varphi \tag{2.14}$$

$$x_{\Delta^+} = x_p = \cos\varphi + \sin\varphi \tag{2.15}$$

$$x_{\Delta^0} = x_n = \sin\varphi \tag{2.16}$$

$$x_{\Delta^-} = -\cos\varphi + \sin\varphi\,. \tag{2.17}$$

2.3 Overview of Results

2.3.1 Dark Photon and $B-L$ Results. In general, small deviations in φ result in small modifications to observables, and thus unsurprisingly small

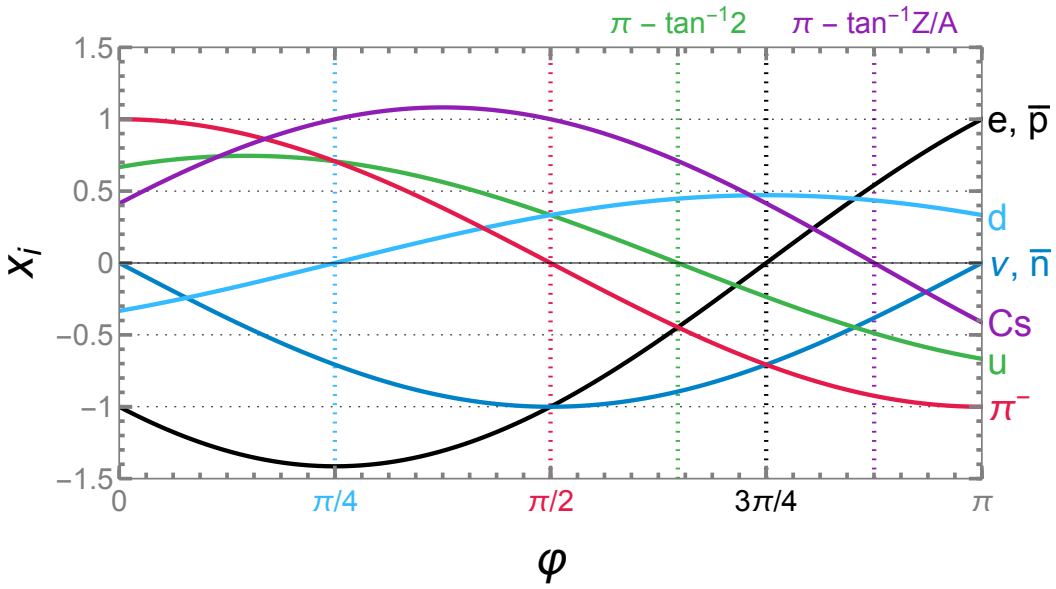


Figure 1. Charges x_i defined in Eq. (2.11). The proton, neutron, and π^+ charges are equal and opposite to the electron, neutrino, and π^- respectively. We also show the scaled Cesium charge $x_{\rm Cs}/A_{\rm Cs}$ which is relevant for CEνNS experiments. The vertical dotted lines correspond to specific combinations of the electromagnetic and $B-L$ currents that are of interest, as shown in Fig. 2.

modifications to the constraints for a given φ. This general result does *not* hold when the charge of a particle or set of particles is close to or exactly zero, i.e., $x_i = 0$. In these special cases, unique and nontrivial phenomenology arises. The best known example is the dark photon, corresponding to $\varphi = 0$, and thus $x_\nu = 0$: the dark photon has no coupling to neutrinos. The next best known example is the $B-L$ vector boson, corresponding to $\varphi = \pi/2$. In this case, the couplings to mesons vanish, while the proton and neutron couplings are identical.

Anticipating the many various constraints arising from terrestrial experiments, astrophysics, and cosmology, we first show the bounds we obtain on the well-known cases of the dark photon and $B-L$ in Fig. 3. Besides some minor differences in constraint shapes, the main difference between the dark photon and the $B-L$ vector boson cases is the additional set of constraints from neutrino-dependent observables

that arise with $B-L$. Our results are broadly consistent with prior equivalent results that can be found in [39, 42, 45]. The primary purpose of showing our calculated constraints is to demonstrate that our analysis pipeline for general φ broadly reproduces existing results in the specific $\varphi = 0$ (dark photon) and $\varphi = \pi/2$ ($B-L$ vector boson) limits. In later sections, we highlight a few specific distinctions between our results and those in past literature.

In order to orient the reader to which results correspond to which mixing angle, we provide a mixing angle "compass" defined in Fig. 2. This shows the cases of interest in the paper (dark photon, $B-L$, chargephobic) as well as several additional angles with their own unique properties.

2.3.2 Chargephobic Dark Photon Results. Our main purpose is to explore the chargephobic case, $\varphi = 3\pi/4$. The tree-level couplings to quarks, leptons, the proton, neutron, and charged pions are:

$$\left.\begin{array}{rcl} x_u &=& -\frac{1}{3\sqrt{2}} \\ x_d &=& \frac{\sqrt{2}}{3} \end{array}\right\} \longrightarrow \left\{\begin{array}{rcl} x_p &=& 0 \\ x_n &=& \frac{1}{\sqrt{2}} \\ x_{\pi^\pm} &=& \mp\frac{1}{\sqrt{2}} \end{array}\right. \qquad (2.18)$$
$$x_e = 0$$
$$x_\nu = -\frac{1}{\sqrt{2}}$$

A chargephobic X^μ couples to quarks, and therefore baryons, in a very specific way: X^μ is "phobic" only to singly positively charged baryons (and singly negatively charged anti-baryons). Moreover, while X^μ couples to charged mesons, there is no coupling to neutral mesons. The couplings to neutrons and neutrinos implies important astrophysical and cosmological consequences. For astrophysics, the constraint from excessive cooling of SN1987A by X^μ emission remains strongly constrained in a way broadly comparable to the dark photon and $B-L$. This occurs

dominantly because of X^μ bremsstrahlung and other emission processes from neutrons in the supernova. Differences are present, however, since once X^μ is emitted from a supernova, it decays nearly 100% of the time into neutrinos, whereas both a dark photon and $B-L$ vector boson have a large branching fraction to charged leptons. Similarly, for cosmology, X^μ can be produced from its interactions with neutrinos, modifying $\Delta N_{\rm eff}$, again broadly comparable to $B-L$ (where production of X can occur from all leptons) or the dark photon (production of X restricted to just charged leptons).

Our results for the chargephobic case are shown in Fig. 4. The majority of constraints from beam dump experiments, fixed target experiments, colliders, precision constraints, neutrino-electron scattering experiments, and searches to invisible decays are either *absent* or *suppressed*. What remains are constraints from coherent neutrino nuclear scattering experiments, a small region related to hadron beam fixed target experiments that are specifically sensitive to neutrinos (DONuT and FASERν), early universe modification to $\Delta N_{\rm eff}$, and excessive cooling of protoneutron star after supernova (SN1987A), and all of which are resilient to a vanishing charged lepton coupling.

The astute reader will observe that Fig. 4 still contains weakened "stalactite" bounds in green from collider experiments, despite the fact that these constraints rely on couplings to muons. The re-appearance of these bounds arises because the mixing angle φ has a loop-induced energy dependence due to the renormalization group evolution of the underlying couplings. In Fig. 4, we made the particular choice $\varphi(\mu = m_e) = 3\pi/4$, and evolved the angle using the renormalization of the couplings detailed in App. B. While the electromagnetic coupling evolves with renormalization scale above $\mu = m_e$ as usual, the dark mixing angle φ does not actually start to

deviate from its low energy value until $\mu \gtrsim m_\pi$; see Appendix B. This explains why the collider experiment bounds appear only above about 200 MeV, and get slightly stronger with increasing mass up to $m_X = 60$ GeV at the upper right-edge of the plot.

Fig. 4 is the main result of our paper, with the subsequent sections of the paper detailing how the individual terrestrial, astrophysical, and cosmological constraints are obtained. What should be clear from Fig. 4 is that current terrestrial experiments are highly insensitive to a chargephobic vector boson.

2.3.3 Other Dark Mixing Angles. There are several other dark mixing angles (beyond $\varphi = 0, \pi/2$) that have their own interesting properties. In particular, consider $\varphi = \pi - \tan^{-1}(Z_\mathcal{N}/A_\mathcal{N})$, where the coupling to an entire nucleus with charge number $Z_\mathcal{N}$ and mass number $A_\mathcal{N}$ can vanish. (The vanishing of the coupling assumes that X^μ couples *coherently* to the nucleus, i.e., the momentum transfer is small compared with inverse size of the nucleus.) We will call this angle *nucleophobic*, and consider the implications in the context of the CEνNS analysis. (A related idea, "xenophobic", tunes the proton and neutron couplings so that the coherent response of xenon nuclei is strongly suppressed for the purposes of suppressing dark matter direct detection signals in [90].) Of particular interest to our analysis are the nuclei of cesium, iodine, and germanium. For example, $\varphi = \pi - \tan^{-1}(55/133)$ results in a model with vanishing tree level coupling to Cesium; here $x_p/x_n \approx -1.42$ which leads to $x_p Z_{\rm Cs} + x_n N_{\rm Cs} = 0$. The angle has the added consequence of suppressing the coupling to other intermediate mass stable nuclei which share a similar number ratio of proton to neutrons; for example, $N_{\rm Cs}/Z_{\rm Cs} \approx N_{\rm I}/Z_{\rm I} \approx 1.4$. This is evident in the valley of stability relation as derived from the semi-empirical mass formula $A/2Z \approx 1{+}0.007A^{2/3}$. The suppression is still in effect but less severe for lighter nuclei

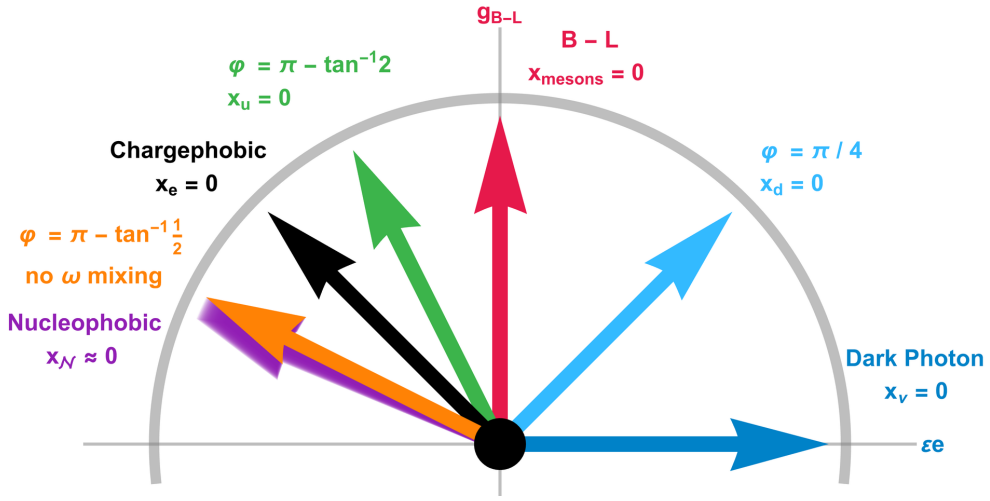


Figure 2. The dark mixing angle "compass". Each arrow corresponds to a dark mixing angle φ that has a vanishing tree-level coupling to at least one SM state. The compass is used in subsequent plots to easily illustrate which dark mixing angles are being considered.

such as germanium and argon where $N/Z \approx 1.2$. Explicitly, the nuclear coupling to X are $\{x_{\rm Cs},\ x_{\rm I},\ x_{\rm Ge},\ x_{\rm Ar}\}_{B-L} = \{133,\ 127,\ 72,\ 40\}$ for $B-L$ and are suppressed to $\{x_{\rm Cs},\ x_{\rm I},\ x_{\rm Ge},\ x_{\rm Ar}\}_{\not{Cs}} = \{0,\ -0.4,\ -2,\ -1.3\}$ in the nucleophobic case with vanishing Cesium coupling.[5]

2.4 Production

In constraining our parameter space, we encounter a variety of production mechanisms that depend nontrivially on $\{m_X, g_X, \varphi\}$. These production mechanisms are well cataloged in the literature for some vector bosons, such as the dark photon, denoted by A'. In this section, we generalize these production mechanisms to include dependence on the dark mixing angle, φ, and compare the rates to their respective counterparts in dark photon case. Doing so will reveal the regions in the parameter

[5]Note that $\varphi = \pi - \tan^{-1} Z/A$ is quite close to $\varphi = \pi - \tan^{-1} 1/2$, which is the angle where ω mixing vanishes in Fig. 2. In the former case, $x_p = -x_n(A-Z)/Z$ and the coupling to the nucleus vanishes. As for the latter case $x_p = -x_n$ and X effectively couples to the difference $A - 2Z$ rather than the full nucleus A as it would occur for $B-L$. The two angles converge for light nuclei with $A = 2Z$.

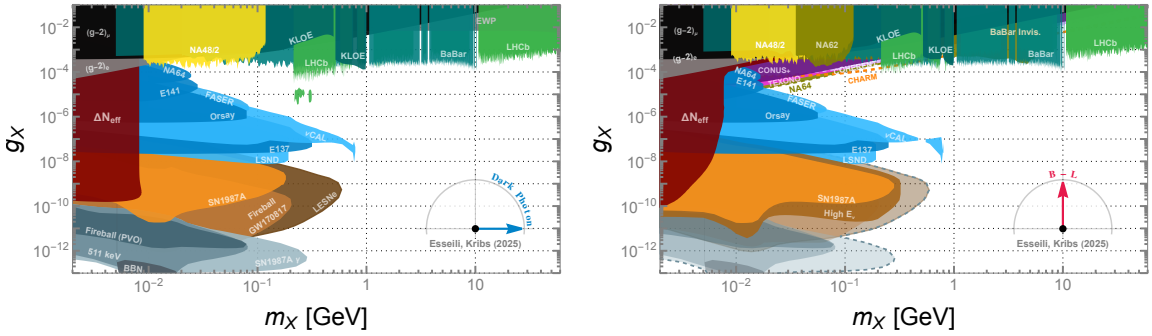


Figure 3. Terrestrial experiment constraints, astrophysical constraints, and cosmological constraints on the dark photon ($\varphi = 0$) and $B - L$ case ($\varphi = \pi/2$), see text for full details. For $B - L$, there are additional constraints that arise due to non-zero couplings to neutrinos, in particular those labeled CHARM, COHERENT, CONUS, NA64, and TEXONO. For the dark photon case, the constraints labeled BBN, LESNe, SN1987A γ, 511 keV line, Fireball PVO/GW170817 were taken directly from Ref. [45]. Since the branching fraction to charged leptons in the $B - L$ case is comparable to the dark photon case, we anticipate the same processes that led to the bounds [45] to also apply to $B - L$. We have taken the liberty to overlay these dark photon bounds from [45] as unlabeled light-shaded regions with dashed-lines in the $B - L$ case. This is illustrative of where one might expect these constraints to appear, however, a detailed calculation for $B - L$ is beyond the scope of the paper.

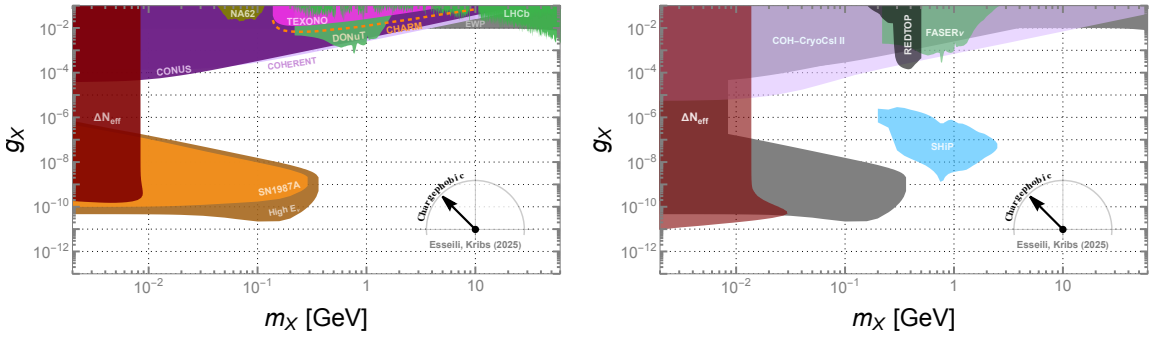


Figure 4. The central results of our paper: the current constraints (left) and anticipated future sensitivity (right) on a chargephobic dark photon ($\varphi = 3\pi/4$). The absence of the vast majority of terrestrial experiments (compare with Fig. 3) arises due to the specific couplings that vanish for chargephobic dark photon: charged leptons and protons. See text for full details.

space where we expect significant deviations from the dark photon constraints, to be distinguished from other regions where the change is expected to be modest.

The experiments/probes that will be used to set constraints on the generalized vector boson X (with arbitrary φ) can be broadly classified into five production mechanism categories:

i) X bremsstrahlung – emission in nucleon-nucleon scattering, $NN \to NNX$, in the dense nuclear medium of a proto–neutron star, as well as in the production processes $eZ \to eZX$ and $pZ \to pZX$ in electron and proton beam dumps, with Z the nucleus of the target material.

ii) Drell-Yan processes $f\bar{f} \to X$ with f being a charged fermion – an important production mode in the early universe evolution of X, and a key production mechanism in collider experiments.

iii) Meson decay – for example: $\pi^0 \to X\gamma$ and $\eta \to X\gamma$ in FASER [91, 92] and $\phi \to X\eta$ in the KLOE [93].

iv) QCD vector meson $V = \omega, \rho, \phi$ mixing $V \to X$ using the vector meson dominance framework (VMD) [23, 42, 53].

v) Enhancement of electron-neutrino scattering $\nu e \longrightarrow \nu e$, such as TEXONO [94, 95], or coherent elastic neutrino-nucleus scattering (CEνNS) $\nu N \longrightarrow \nu N$ such as COHERENT [96], both occurring through X-exchange.

In order to most easily see the changes resulting from varying φ, we consider the production ratio $\mathbb{P}_X$, defined by the cross section ratio $\sigma_X/\sigma_{A'}$, and the decay width ratio $\Gamma_X/\Gamma_{A'}$ for a given process. This ratio is summarized for various production mechanisms in Table 5 and Fig. 5. Importantly, the production ratio vanishes for

Process	$\mathbb{P}_X \equiv \sigma_X/\sigma_{A'}$
$\omega \longrightarrow X$	$(\cos\varphi + 2\sin\varphi)^2$
$eZ \longrightarrow eZX$ $pZ \longrightarrow pZX$	$(\cos\varphi + \sin\varphi)^2$
$u\bar{u} \longrightarrow X$	$\frac{1}{4}(2\cos\varphi + \sin\varphi)^2$
$\rho \longrightarrow X$	$\cos^2\varphi$
$d\bar{d} \longrightarrow X$ $\phi \longrightarrow X$	$(\cos\varphi - \sin\varphi)^2$

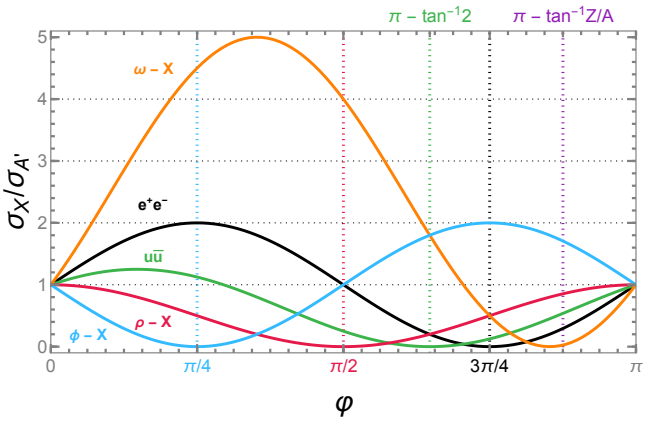


Figure 5. Tree level cross section ratio of X to A' production rate. All values in the table are multiplied by a factor of $g_X^2/(\varepsilon e)^2$; we set this extra term to one in the plot. The ratio also sets energies in both models equal when necessary.

special values of φ as detailed in the previous section. Thus, when an experiment relies on one such production mechanism, it can lose sensitivity to X for some values of φ.

Next we discuss four relevant decay width ratios processes by adapting the VMD framework developed in [23, 42] to our case. These decay ratios are

$$\mathbb{P}_{\omega\to\pi^0 X} = \cos^2\varphi \tag{2.19}$$

$$\mathbb{P}_{\phi\to X\eta} = (\cos\varphi - \sin\varphi)^2 \tag{2.20}$$

$$\mathbb{P}_{\pi^0\to X\gamma} = \frac{|\,\mathrm{BW}_\rho\cos\varphi + \mathrm{BW}_\omega\,(\cos\varphi + 2\sin\varphi)\,|^2}{|\,\mathrm{BW}_\rho + \mathrm{BW}_\omega\,|^2} \tag{2.21}$$

$$\mathbb{P}_{\eta\to X\gamma} = \frac{|\,9\,\mathrm{BW}_\rho\cos\varphi - 2\,\mathrm{BW}_\phi\,(\cos\varphi - \sin\varphi) + \mathrm{BW}_\omega\,(\cos\varphi + 2\sin\varphi)\,|^2}{|\,9\,\mathrm{BW}_\rho - 2\,\mathrm{BW}_\phi + \mathrm{BW}_\omega\,|^2} \tag{2.22}$$

$$\mathbb{P}_{\eta'\to X\gamma} = \frac{|\,9\,\mathrm{BW}_\rho\cos\varphi + 4\,\mathrm{BW}_\phi\,(\cos\varphi - \sin\varphi) + \mathrm{BW}_\omega\,(\cos\varphi + 2\sin\varphi)\,|^2}{|\,9\,\mathrm{BW}_\rho + 4\,\mathrm{BW}_\phi + \mathrm{BW}_\omega\,|^2} \tag{2.23}$$

Here,

$$\mathrm{BW}_V(m_X) = \frac{m_V^2}{m_V^2 + m_X^2 - i m_X \Gamma_V(m_X)}\,, \tag{2.24}$$

is the Breit-Wigner expression for vector meson V and $\Gamma_V(m_X)$ is the total decay width. The π^0 and η decays ratios are shown in Fig. 6 for some critical values of φ.

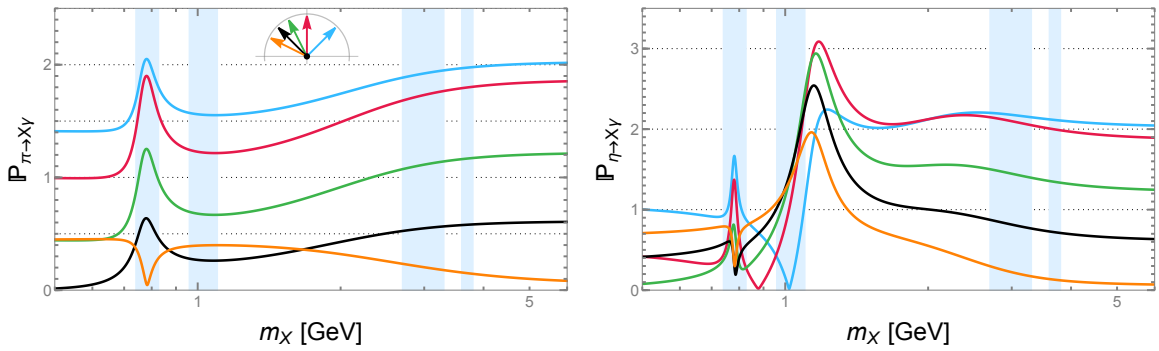


Figure 6. Decay widths for $\pi^0 \to X\gamma$ (left) and $\eta \to X\gamma$ (right), each normalized to the corresponding dark photon widths $\pi^0 \to A'\gamma$ and $\eta \to A'\gamma$ as given in Eqs. (2.21) and (2.22). The mixing angles are represented with colors indicated by the inset compass: $\varphi = \pi/4$ (blue), $B-L$ (red), $\varphi = \pi - \tan^{-1} 2$ (green), chargephobic (black), and $\varphi = \pi - \tan^{-1}(1/2)$ (orange).

In Eqs. (2.21 –2.23), the ρ, ϕ, and ω contributions to the decay width vanishes for $\varphi = \pi/2, \pi/4$, and $\pi - \tan^{-1}(1/2)$ respectively.[6] Furthermore, $m_\rho \approx m_\omega$ leads to a partial cancellation between the two Breit-Wigner terms in the chargephobic limit at $\varphi = 3\pi/4$. These limits correspond to dips in Fig. 6 near the resonance of the relevant meson.

The production mechanisms discussed in this section have important implications to collider, fixed target, and beam dump experiments and their associated constraints. Production in the early universe, proto-neutron star cooling, and neutrino scattering experiments require a more careful analysis and will be the subject of later sections.

2.4.1 Branching Fraction. We assume X decays entirely to SM final states, and so the partial decay widths and branching ratios of X are completely determined by $\{g_X, m_X, \varphi\}$. For fermions, the decay width is

$$\Gamma_{X\longrightarrow f\bar{f}} = \frac{\mathcal{C}_f\, g_X^2 x_f^2}{12\pi} m_X \left(1 + 2\frac{m_f^2}{m_X^2}\right)\sqrt{1 - 4\frac{m_f^2}{m_X^2}} \tag{2.25}$$

[6]For $\varphi = \pi - \tan^{-1}(1/2)$, the charges are given by $x_e = x_d = x_n = -x_\nu = -x_u = -x_p = 1/\sqrt{5}$ and pion charges $m_{\pi^\pm} = \mp 2/\sqrt{5}$.

where x_f are the couplings in Eq. (2.11) and $\mathcal{C}_f$ is 1 for charged leptons, 3 for quarks, and 1/2 for neutrinos. Decay into hadrons is considered separately in two regimes on either side of $m_X = 2$ GeV. The simpler of the two is $m_X > 2$ GeV where the decay is given by

$$\Gamma_{X\to\text{hadrons}} = \frac{\sum_q \Gamma_{X\longrightarrow q\bar{q}}}{\sum_q \Gamma_{\gamma^*\longrightarrow q\bar{q}}} \Gamma_{\gamma^*\longrightarrow\mu^+\mu^-}\mathcal{R}(m_X), \tag{2.26}$$

with the sum ranging over all kinematically accessible quarks, and $\mathcal{R}(m_X)$ is the experimentally determined cross section ratio given by $\mathcal{R}(m_X) = \sigma_{e^+e^-\longrightarrow\text{hadrons}}/\sigma_{e^+e^-\longrightarrow\mu^+\mu^-}$ [97, 98]. For $m_X \lesssim 2$ GeV, QCD becomes non-perturbative and the decay into hadrons can no longer be estimated by summing the contribution of $q\bar{q}$ decays. In this range, we are also interested in decays into specific hadronic final states, i.e., $\pi^+\pi^-$, rather than the total sum of all hadronic decays. Accordingly, we employ the data driven analysis in [42] based in the vector meson dominance (VMD) framework [23]. In this approach, the data from the most important hadronic contributions $\mathcal{F}$ [99–106] at low mass are fit to

$$\mathcal{R}^{\mathcal{F}}_{\mu}(m) \;=\; \frac{\sigma_{e^+e^-\longrightarrow\mathcal{F}}}{\sigma_{e^+e^-\longrightarrow\mu^+\mu^-}} \;=\; \frac{9}{\alpha^2_{\text{EM}}}|\mathcal{A}_{\mathcal{F}}|^2, \tag{2.27}$$

where $\mathcal{A}_{\mathcal{F}}$ is the sum of a real function and functions of a Breit-Wigner form accounting for the contributions of the three vector mesons ρ, ω, ϕ. The fits are then used to decompose the decay into hadrons to ρ-like $\mathcal{R}^{\rho}_{\mu}$, ω-like $\mathcal{R}^{\omega}_{\mu}$, and ϕ-like $\mathcal{R}^{\phi}_{\mu}$ contributions giving

$$\Gamma_{X\longrightarrow\text{hadrons}} \;=\; \frac{g^2_X m_X}{12\pi}\left(\sum_V \mathcal{R}^V_X + \mathcal{R}^{\omega-\phi}_X\right) \tag{2.28}$$

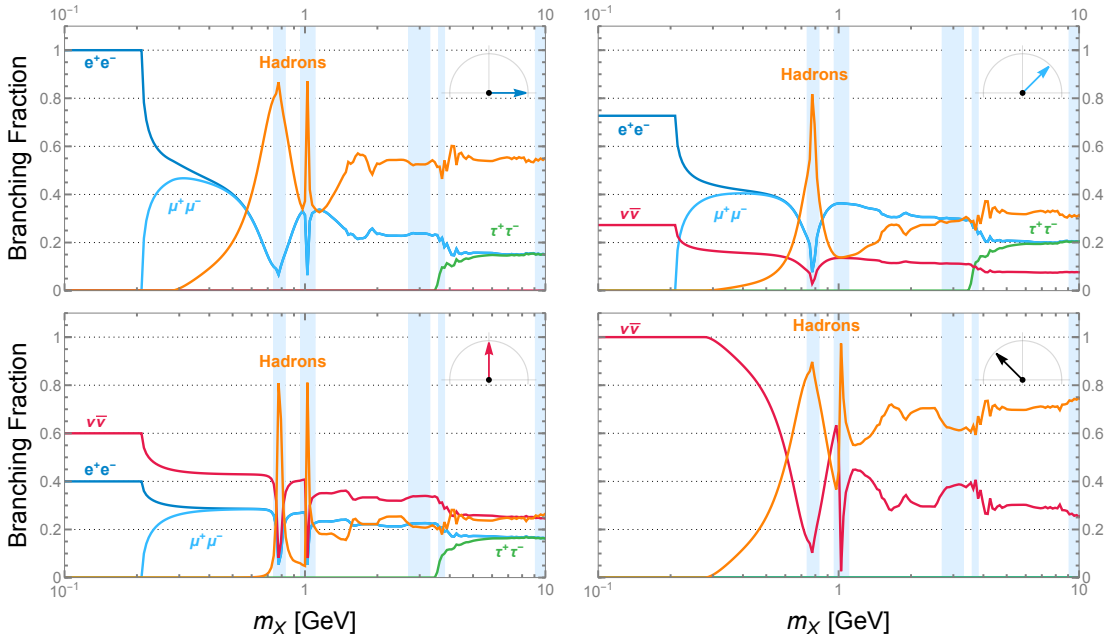


Figure 7. Branching fraction of X with $\varphi = \{0, \frac{\pi}{4}, \frac{\pi}{2}, \frac{3\pi}{4}\}$ as indicated by the inset compass. The blue shaded regions correspond to meson resonances.

with

$$\begin{aligned}
\mathcal{R}_X^{\rho}(m) &= \cos^2\varphi\, \mathcal{R}_\mu^{\rho}(m) \\
\mathcal{R}_X^{\omega}(m) &= (\cos\varphi + 2\sin\varphi)^2\, \mathcal{R}_\mu^{\omega}(m) \\
\mathcal{R}_X^{\phi}(m) &= (\cos\varphi - \sin\varphi)^2\, \mathcal{R}_\mu^{\phi}(m) \\
\mathcal{R}_X^{\omega-\phi}(m) &= [1 - 3\cos 2\varphi - 2\sin 2\varphi]\ \mathcal{R}_\mu^{\omega-\phi}(m)
\end{aligned} \tag{2.29}$$

and $\mathcal{R}_X^{\omega-\phi}$ is the only non-negligible interference term between ω-like and ϕ-like to the $\pi^+\pi^-\pi^0$ final hadronic decay state.

The branching ratios for four mixing angles $\varphi = \{0, \frac{\pi}{4}, \frac{\pi}{2}, \frac{3\pi}{4}\}$ are shown in Fig. 7; of those, the branching ratio to individual hadronic modes for $\sqrt{s} < 2$ GeV are shown in Fig. 8. The $\varphi = 0$ and $\varphi = \pi/2$ correspond to the dark photon and $B - L$ cases respectively and have been discussed thoroughly in the literature. The $\varphi = \pi/4$ figure shows the transition between the two aforementioned models with a nonzero

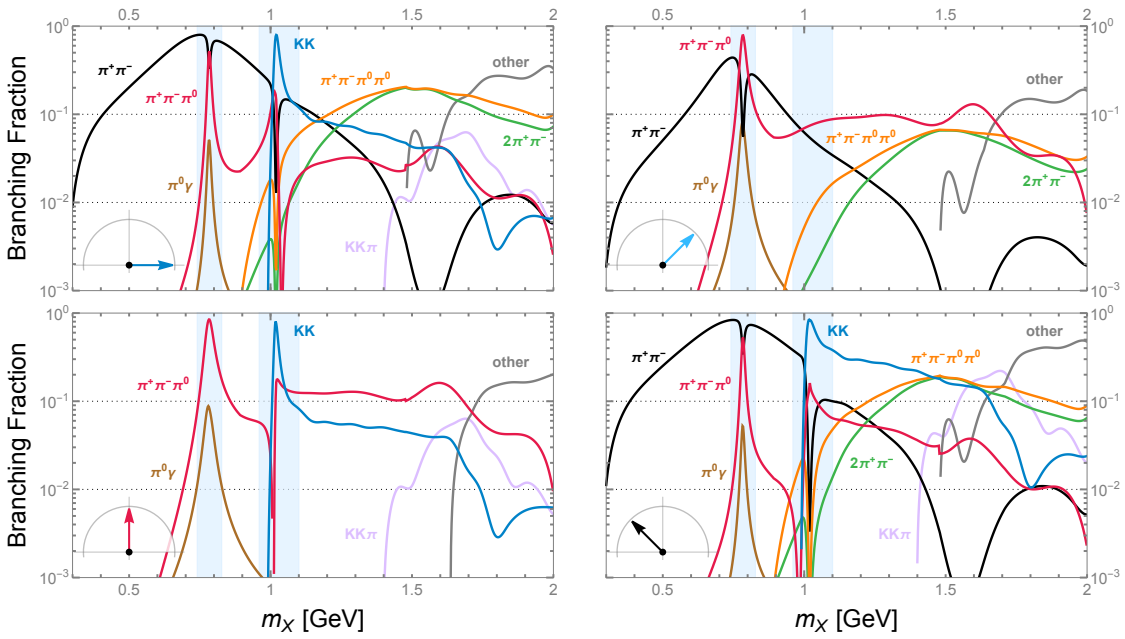


Figure 8. Branching fraction of X to individual hadronic that compose the results in Fig. 7 for $\varphi = \{0, \frac{\pi}{4}, \frac{\pi}{2}, \frac{3\pi}{4}\}$ as indicated by the inset compass.

neutrino branching fraction, where the absence of $\phi - X$ mixing, as in Eq. (2.29), leads to the disappearance of the ϕ resonance and the subsequent KK and $KK\pi$ decay modes. The case $\varphi = \pi/2$ $(B - L)$ does not have $\rho - X$ mixing, leading to the disappearance of $\pi^+\pi^-$, $\pi^+\pi^-\pi^0\pi^0$, and $\pi^+\pi^-\pi^+\pi^-$ decay modes. This distinction means that X decay to hadronic modes for $B - L$ (and related flavor-dependent currents such as $B - 3L_\tau$) remain suppressed up to $m_X \simeq 700$ MeV, whereas for all of the mixing angles, including the chargephobic case, there are hadronic decay channels (X mixing ρ decaying to $\pi^+\pi^-$) that start appearing once $m_X \gtrsim 300$ MeV.[7] Fig. 7 demonstrates that the chargephobic case $\varphi = 3\pi/4$ has the most striking differences in branching fraction with the other angles given the absence of a tree-level coupling

[7]For the case $\varphi = \pi - \tan^{-1} 1/2$ (not shown), the absence of $\omega - X$ mixing leads to the disappearance of $\pi^+\pi^-\pi^0$ and $\pi^0\gamma$.

to charged leptons. The plots include the RGE evolution of x_e as discussed in App. B, although the branching ratio to charged leptons is at most $\mathcal{O}(10^{-4})$.

The blue shaded regions in Fig. 7 correspond to the following meson resonances in mass ranges [MeV]: ρ and ω at $(741, 827)$, ϕ at $(960, 1100)$, J/ψ at $(2700, 3300)$, $\psi(2S)$ & $\psi(3770)$ at $(3600, 3800)$, and $\Upsilon(1S) - \Upsilon(4S)$ at $(9100, 10600)$. These bands are obtained from [107] where prompt-like A' searches are vetoed due to the large resonance contribution, and are meant only to illustrate an example of experimental veto window rather than a theoretical limitation. In our analysis, we have not explicitly included the $J/\psi, \psi(2S), \psi(3770)$, and $\Upsilon(1S) - \Upsilon(4S)$ resonances in hadronic decays, but their effects are consistently considered in the constraints.

Experiments search for the decay products of X, or lack thereof, as a signal to set constraints on the $\{m_X, g_X\}$ parameter space. The branching fraction is a guide for experiments as to which SM particles can be suitably employed as a signal for a given mass m_X. The ratio of branching fraction of X to A' provides a quantitative guide to how the sensitivity of a given search to X differs from the corresponding dark photon case. For some experiments, a constraint on A' can be recast to a constraint on X via $\sigma_X \mathrm{Br}_{X \longrightarrow \mathcal{F}} \mathrm{Eff}(\tau_X) = \sigma_{A'} \mathrm{Br}_{A' \longrightarrow \mathcal{F}} \mathrm{Eff}(\tau_{A'})$, where Br is the branching ratio and $\mathrm{Eff}(\tau_X)$ is the experimental efficiency with explicit dependence on X lifetime. Equivalently, when applicable, constraints can be recast using

$$\mathbb{P}_X \, \mathbb{B}_{X \longrightarrow \mathcal{F}} \, \mathbb{E}(\tau_X) = 1, \tag{2.30}$$

where $\mathbb{P}_X$ is shown in Fig. 5 and Fig. 6, $\mathbb{B}_{X \longrightarrow \mathcal{F}}$ is the ratio of branching fractions and $\mathbb{E}(\tau_X)$ is the efficiency ratio. The ratio of branching fractions $\mathbb{B}_{X \to \mathbb{F}}$ for charged leptons and hadrons for $\varphi = \{\frac{\pi}{4}, \frac{\pi}{2}, \pi - \tan^{-1} 2, \frac{3\pi}{4}, \pi - \tan^{-1}(1/2)\}$ are shown in Fig. 9.

The recasting equation, Eq. (2.30), is powerful and can be applied to a variety of constraints set by fixed target experiments, colliders, beam dumps, and searches

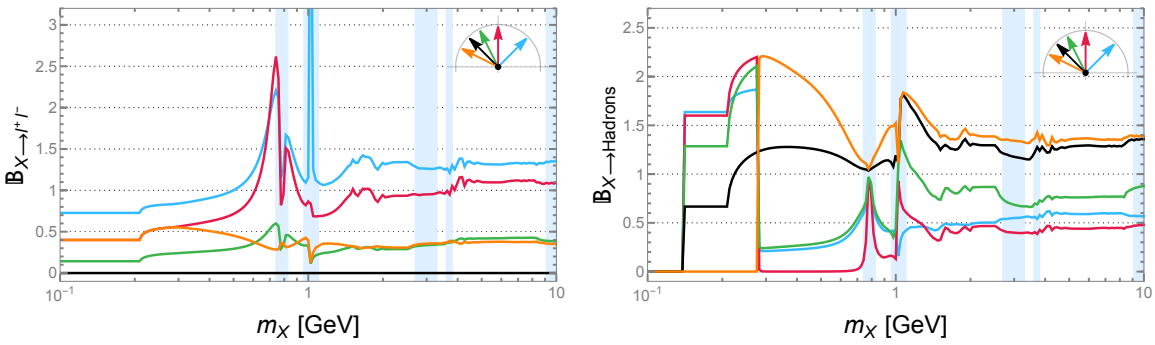


Figure 9. Ratio of the branching fractions of X to those of the dark photon A' into charged leptons (left) and hadrons (right). The mixing angles are represented with colors indicated by the inset compass: $\varphi = \pi/4$ (blue), $B - L$ (red), $\varphi = \pi - \tan^{-1} 2$ (green), chargephobic (black), and $\varphi = \pi - \tan^{-1}(1/2)$ (orange).

to invisible final states. For these experiment categories, we use the methodology developed in [42][8] to recast the constraints. Otherwise, we rederive the constraints set on beam dump experiments[9], neutrino experiments, SNe cooling, early universe ΔN_{eff} modification and some precision experiments. In the following sections, we summarize the derivation of all aforementioned constraints.

2.5 Constraints

We now detail the derivation of the constraints in Figs. 3,4 that span a rich set of cosmological, astrophysical and terrestrial experiment observables. As we have seen, cosmology and astrophysics provide constraints throughout the range of dark mixing angles φ. Consequently, we present these constraints first, since we have carried out independent calculations of the contribution of X production and decay to ΔN_{eff} during the early universe as well as our own X emission from SN1987A. Next, we derive constraints on neutrino experiments, since they provide some of the strongest

[8]The reference [42] also provides a publicly available code `Darkcast https://gitlab.com/philten/darkcast` which we have recreated in `Mathematica` and used to recast constraints from some experiments as discussed in the text.

[9]We rederive constraints from electron beam dump experiments and the bremsstrahlung process in proton beam dump experiments even though those can be recast. Constraints set from meson decay in proton beam dumps are recast from dark photon constraints.

constraints on the chargephobic case. We then consider beam dump experiments and colliders, and detail the effects of X production and decay with the critically important φ dependence. Finally, we consider constraints from precision tests of the Standard Model, which provide leading bounds on the large m_X in the chargephobic model.

2.5.1 Cosmology: CMB & BBN. The precision determination of the effective number of relativistic species in the early universe, $N_{\rm eff}$, from CMB power spectra [15–17] and primordial element abundances [108–111] is in good agreement with the SM prediction [112–126]. Hence, BSM physics that alters $N_{\rm eff}$ before recombination is strongly constrained [81, 84, 127–150]. In our case, a well known effect is that an X boson can "freeze in" [151], become nonrelativistic, redshift as matter, and then decay back into SM states, modifying $\Delta N_{\rm eff}$. This constraint was derived for a dark photon [143], $U(1)_{\mu-\tau}$ [81], and $U(1)_{B-L}$ [54, 152][10].

In this paper, we utilize the formalism and approximations outlined in [54, 81, 141, 144] to derive constraints on X. Specifically, our previous work in [54] can be fully adapted to this case by modifying the couplings appropriately. For each given

[10]The constraint in our previous work [54] is stronger than that in Ref. [152] as the latter neglected including the coupling to charged leptons (electrons) and finite temperature effects in their $B-L$ constraint calculation. These effects play a crucial role in determining the constraint in a large portion of the parameter space.

$\{m_X, g_X, \varphi\}$, we solve the five Boltzmann equations

$$\begin{aligned}
\frac{dT_X}{dt} &= \mathbb{D}(T_X,\mu_X)\left[-3H\left((\rho_X+P_X)\frac{\partial n_X}{\partial \mu_X}-n_X\frac{\partial \rho_X}{\partial \mu_X}\right)+\frac{\partial n_X}{\partial \mu_X}\frac{\delta \rho_X}{\delta t}-\frac{\partial \rho_X}{\partial \mu_X}\frac{\delta n_X}{\delta t}\right],\\
\frac{dT_\nu}{dt} &= \mathbb{D}(T_\nu,\mu_\nu)\left[-3H\left((\rho_\nu+P_\nu)\frac{\partial n_\nu}{\partial \mu_\nu}-n_\nu\frac{\partial \rho_\nu}{\partial \mu_\nu}\right)+\frac{\partial n_\nu}{\partial \mu_\nu}\frac{\delta \rho_\nu}{\delta t}-\frac{\partial \rho_\nu}{\partial \mu_\nu}\frac{\delta n_\nu}{\delta t}\right],\\
\frac{dT_\gamma}{dt} &= \left(\frac{\partial \rho_\gamma}{\partial T_\gamma}+\frac{\partial \rho_e}{\partial T_\gamma}\right)^{-1}\left[4H\rho_\gamma+3H(\rho_e+P_e)+\frac{\delta \rho_e}{\delta t}\right], \qquad (2.31)\\
\frac{d\mu_X}{dt} &= -\mathbb{D}(T_X,\mu_X)\left[-3H\left((\rho_X+P_X)\frac{\partial n_X}{\partial T_X}-n_X\frac{\partial \rho_X}{\partial T_X}\right)+\frac{\partial n_X}{\partial T_X}\frac{\delta \rho_X}{\delta t}-\frac{\partial \rho_X}{\partial T_X}\frac{\delta n_X}{\delta t}\right],\\
\frac{d\mu_\nu}{dt} &= -\mathbb{D}(T_\nu,\mu_\nu)\left[-3H\left((\rho_\nu+P_\nu)\frac{\partial n_\nu}{\partial T_\nu}-n_\nu\frac{\partial \rho_\nu}{\partial T_\nu}\right)+\frac{\partial n_\nu}{\partial T_\nu}\frac{\delta \rho_\nu}{\delta t}-\frac{\partial \rho_\nu}{\partial T_\nu}\frac{\delta n_\nu}{\delta t}\right]\\
\mathbb{D}(T,\mu) &= \left(\frac{\partial n}{\partial \mu}\frac{\partial \rho}{\partial T}-\frac{\partial n}{\partial T}\frac{\partial \rho}{\partial \mu}\right)^{-1},
\end{aligned}$$

numerically from $T \sim \mathcal{O}(100)$ MeV all the way down to recombination at $T \simeq 0.3$ eV.

In writing these equations, we made the implicit assumption that fermions and bosons follow Fermi-Dirac (FD, positive) and Bose-Einstein (BE, negative), $f(E) = [e^{(E-\mu)/T} \pm 1]^{-1}$ distributions respectively. Here n, ρ, P are the number, energy, and pressure densities for a particle i with d_i degrees of freedom obtained by integrating the particle distribution f over $d_i\, d^3p/(2\pi)^3$, $d_i\, E\, d^3p/(2\pi)^3$, and $d_i\, \frac{p^2}{3E}\, d^3p/(2\pi)^3$ respectively. $\delta n/\delta t$ and $\delta \rho/\delta t$ are the number and energy transfer rates between particle species obtained by integrating collision terms over the same measures. Finally, $H = \sqrt{\rho_{\rm tot}/(3M_{\rm Pl}^2)}$ is the Hubble expansion rate and $M_{\rm Pl} = 2.4 \times 10^{18}$ GeV. The formulae for these thermodynamic quantities and their derivatives can be found in Appendix A.6 of [144].

The $\delta n/\delta t$ and $\delta \rho/\delta t$ terms account for all relevant interactions driving the dynamics. At the temperature range of interest, $e^+e^- \leftrightarrow \bar{\nu}_\alpha \nu_\alpha$, $e^\pm \nu_\alpha \leftrightarrow e^\pm \nu_\alpha$, and $e^\pm \bar{\nu}_\alpha \leftrightarrow e^\pm \bar{\nu}_\alpha$ are the only SM interactions needed. These interactions, mediated by W and Z exchange, drive the neutrino and electron population to equilibrium for temperatures above neutrino decoupling $T \sim 2$ MeV. If X couples to neutrinos

and electrons, these interactions can also be mediated by X. We also include the interactions $X \leftrightarrow \nu\bar{\nu}$, $X \leftrightarrow e^+e^-$, $\gamma X \leftrightarrow e^+e^-$, and $e^\pm X \leftrightarrow e^\pm\gamma$ when applicable. Interactions such as $e^+e^- \leftrightarrow \gamma X$, $\nu\bar{\nu} \leftrightarrow XX$, $Xe^\pm \leftrightarrow Xe^\pm$, and $X\nu \leftrightarrow X\nu$ are subdominant to the aforementioned interactions and can be neglected. The rates, along with a detailed discussion of the dynamics, can be found in [54]. These rates are trivially adapted to our case with the appropriate coupling substitutions.

Following the discussion in [54,110] and based on the datasets in [15,16,153–166], constraints in Fig. 4 are set on modifications to $N_{\rm eff}$ of $|\Delta N_{\rm eff}| \geq 0.4$ and/or helium mass fraction Y_p of $\Delta Y_p > 0.008$; we also show future projected sensitivity at $|\Delta N_{\rm eff}| \geq 0.05$. The first constraint is set from X modifying the effective number of relativistic species in the early universe defined as

$$N_{\rm eff} \;=\; \frac{8}{7}\left(\frac{11}{4}\right)^{4/3}\left(\frac{\rho_{\rm rad}-\rho_\gamma}{\rho_\gamma}\right), \tag{2.32}$$

which is the ratio of non-photon to photon radiation density. The state-of-the-art calculation in the SM gives $N_{\rm eff}^{\rm SM} = 3.045$-$3.046$, that takes into higher order corrections, non-thermal neutrino distribution functions, neutrino oscillations, etc. [112, 113]. Using the method outlined above without X, we obtain the photon-to-neutrino temperature ratio, the neutrino chemical potential, and $N_{\rm eff}$ in the SM

$$T_\gamma/T_\nu = 1.3945\,, \qquad \mu_\nu/T_\nu = -4.82\times10^{-3}\,, \qquad N_{\rm eff}^{\rm SM} = 3.042\,. \tag{2.33}$$

This demonstrates that our calculation is able to reproduce the non-instantaneous decoupling of neutrinos in the SM to an accuracy of order $\Delta N_{\rm eff} \sim 0.01$. The value of $N_{\rm eff}$ in Eq. (3.10) will be modified when solving the Boltzmann equations in Eq. (2.31) including X and a constraint is set if $\Delta N_{\rm eff} \geq 0.4$. The constraint from ΔY_p can also be derived as in [54]; however, this constraint is weaker than that derived from $\Delta N_{\rm eff}$ everywhere in our parameter space.

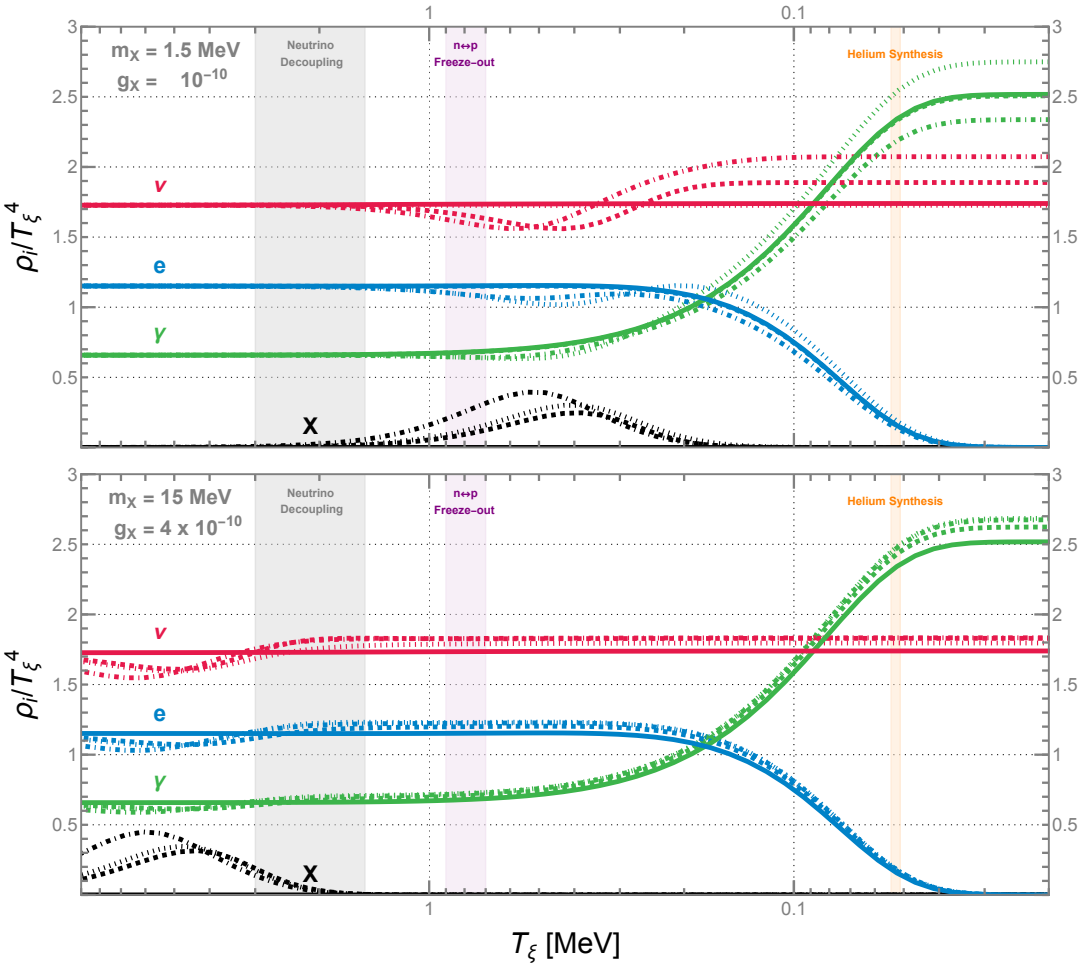


Figure 10. The normalized energy density evolution ρ/T_ξ^4 of the neutrino (red), electron (blue), photon (green), and X (black) around the BBN era as a function of a reference temperature T_ξ explained in the text. (Top) $m_X = 1.5$ MeV with $g_X = 10^{-10}$ and (bottom) $m_X = 15$ MeV with $g_X = 4 \times 10^{-10}$. In both plots, (solid) lines are SM evolution with no X included, (dotted) dark photon ($\varphi = 0$), (dot-dashed) $B - L$ ($\varphi = \pi/2$) and (dashed) chargephobic case ($\varphi = 3\pi/4$).

The normalized density evolution for two representative points in the parameter space is shown in Fig. 10. Here, T_ξ is a reference temperature as in [54] that can be thought of as the evolution of a fictitious massless particle with a temperature that is initially set to the SM temperature but is actually decoupled from all other particles. Using T_ξ makes it simple to compare different values of φ where X couples differentially to neutrinos and electron photon bath.

When the mass of X is of order a few MeV, the majority of the production and decay dynamics occur after neutrino decoupling as can be seen in the representative example $m_X = 1.5$ MeV in Fig. 10. For this mass and in the chargephobic limit (dashed), X is slowly populated at the expense of the ν population through $\nu\bar{\nu} \to X$. The rates are maximal around $T_\xi \sim m_X/3$ where the X population becomes non-relativistic and starts decaying back into neutrinos. Importantly, the X distribution evolves as matter $\rho_X \propto a^{-3}$ before dumping its entropy back into neutrinos, that themselves have been evolving as radiation $\rho_\nu \propto a^{-4}$. Hence, this back and forth exchange in energy heats up the neutrino plasma. The result is a neutrino energy density that is larger than it would have been in the SM as compared to the photon energy density. This effect *increases* the value of $N_{\rm eff}$ in Eq. (3.9) and gives $\Delta N_{\rm eff} = 0.27$ for $m_X = 1.5$ MeV and $g_X = 10^{-10}$. The small shift in the electron and photon densities here is due to the dynamics commencing slightly before neutrinos are fully decoupled.

The dark photon limit (dotted) for $m_X = 1.5$ MeV proceeds similarly with the dynamics now occurring between X and the electron-photon bath instead of neutrinos. The result is a photon energy density that is larger than it would have been in the SM as compared to neutrino density and a *decrease* in $N_{\rm eff}$; in this case $\Delta N_{\rm eff} = -0.27$. In the $B - L$ case (dot-dashed), X couples to e and ν and has access to a larger

energy density bath. This leads to a larger X population produced at a slightly earlier time as compared to the previous two cases. The X population then decays back into both e and ν. However, this decay occurs around the time that electrons also become non-relativistic and the dynamics become highly nontrivial as discussed in [54]. The upshot is a preferential heating of the neutrinos and an increase in N_{eff} giving $\Delta N_{\text{eff}} = 0.86$ for $m_X = 1.5$ MeV and $g_X = 10^{-10}$.

For $m_X = 15$ MeV and $g_X = 4 \times 10^{-10}$, the majority of X production occurs before the neutrinos are fully decoupled. This means that regardless of the charge assignment, X has access to the entire SM thermal bath. For example, in the chargephobic limit, X is produced via $\nu\bar{\nu} \to X$ which effectively cools the neutrino population. However, in this case, processes such as $e^+e^- \leftrightarrow \bar{\nu}_\alpha\nu_\alpha$, which have previously kept neutrinos and the electron-photon bath in equilibrium, are still active. These processes transfer energy from the electron-photon bath to neutrinos driving the system to a new equilibrium at a lower temperature. These two effects occur simultaneously and proceed until the neutrinos decouple from SM. After X decays and heats up the neutrino plasma, some of this energy is transferred into the electron-photon bath through $e^+e^- \leftrightarrow \bar{\nu}_\alpha\nu_\alpha$ interactions which are still partially active. This leads to an attenuated increase in N_{eff} giving $\Delta N_{\text{eff}} = 0.03$ for $m_X = 15$ MeV and $g_X = 4 \times 10^{-10}$. A similar effect is seen in dark photon case where $\Delta N_{\text{eff}} = -0.1$. Lastly, in the $B - L$ case, X decays and heats up both neutrinos and electron-photon bath with comparable amounts leading to a weaker increase in N_{eff}; in this case $\Delta N_{\text{eff}} = -0.02$. For larger values of m_X, the production and decay of X terminates completely before neutrino decoupling. This gives the SM enough time to return to thermal equilibrium leading to no change in N_{eff}.

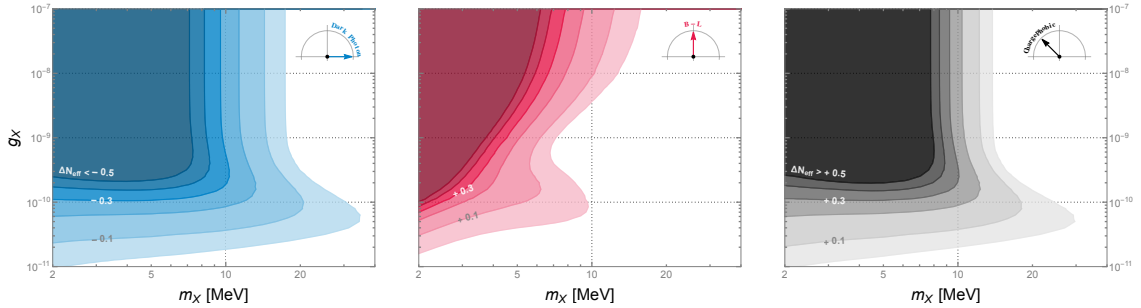


Figure 11. $\Delta N_{\rm eff}$ contours for the dark photon, $B-L$, and chargephobic cases as indicated by compass inset plot. The color shading from lighter to darker corresponds to $|\Delta N_{\rm eff}| = \{0.05,\ 0.1,\ 0.2,\ 0.3,\ 0.4,\ 0.5\}$ and contours greater than 0.5 are not shown. Note that the dark photon case drags $N_{\rm eff}$ below its SM value (negative $\Delta N_{\rm eff}$) as opposed to $B-L$ and chargephobic cases with positive $\Delta N_{\rm eff}$ values. For the three models, the constraint is set on $|\Delta N_{\rm eff} = 0.4|$, and the future CMB experimental sensitivity is taken to be $|\Delta N_{\rm eff}| = 0.05$.

Fig. 11 contains a summary of the $\Delta N_{\rm eff}$ constraints on a dark photon, a $B-L$ vector boson, and on a chargephobic vector boson. Given the discussion above, we find that $\Delta N_{\rm eff}$ receives positive contributions in the $B-L$ and chargephobic cases, and negative contributions in the dark photon case. This last result is potentially interesting in the context of some CMB results that find a best fit to $\Delta N_{\rm eff} < 0$ [17].

2.5.2 Astrophysics. The explosion of the blue supergiant Sanduleak $-69\,202$ in the Large Magellanic Cloud and its subsequent detection is known as supernova 1987A (SN1987A). The supernova is estimated to have released $\approx 3\times10^{53}$ erg in the form of neutrinos. The Kamiokande II [167] and IMB collaboration [168] detection of $\sim$ 20 neutrino events within $\sim$ 10 seconds of the explosion agrees with the predictions of the Standard Model for total energy, average neutrino energy, and burst duration based on simulation of neutrino emission from stellar core collapse for SN1987A [169–171]. For reviews of supernova core collapse theory see [172–175]. This agreement allows constraints to be established on BSM models that provide an additional cooling mechanism to the proto-neutron star (PNS) after collapse [173], as

discussed in Sec. 2.5.2.1. In addition, there are constraints on the nonobservation of high energy neutrino events during the same time window that low energy neutrinos were observed, that is relevant to models where such emission is possible [176–182], as discussed in Sec. 2.5.2.2. Finally, there are also several supernova based constraints arising from the production and decay to visible modes (especially e^+e^-) [183–190]; these bounds were most recently derived on a dark photon in [45] and will be the discussed in Sec. 2.5.2.3.

2.5.2.1 Protoneutron Star Cooling: SN1987A. For dark photons, the PNS cooling constraint was determined by Refs. [45, 191–193], which improved on previous constraints [194–197] by including finite temperature and density effects. For a $B-L$ vector boson, calculations were carried out in Refs. [55,56], however the resulting constraint differs between the two references in certain regions of parameter space by up to an order of magnitude in the values of g_{B-L}. As discussed below, we rederive the constraints from PNS cooling in our parameter space. In the dark photon case, our results are in good agreement with the previous results [45,191,192]. In the $B-L$ case, our results resolve the discrepancy between the constraints in [55] and [56], by including effects neglected in both analyses. Finally, we derive PNS cooling constraints in the chargephobic case; this is an important result since PNS cooling is one of the few ways the chargephobic vector boson couplings can be constrained.

The PNS cooling constraint is traditionally set by demanding the instantaneous luminosity of the new particles $L_X(m_X, g_X)$ not exceed the "Raffelt Criterion", $L_\nu = 3 \times 10^{52}$erg/s [173] . Specifically, this limit is applied around $t = 1\,\mathrm{s}$ post-bounce where the PNS core reaches peak density. The duration of SN1987A neutrino burst is reduced by half if the luminosity exceeds this limit which is inconsistent with observations. In order to obtain the constraints on X emission, we have utilized

Refs. [182, 198, 199], calculating the instantaneous luminosity

$$L_X(m_X, g_X, R_\nu) = \int_0^{R_\nu} dr 4\pi r^2 N(r)^2 \int_{m_X/N(r)}^{\infty} d\omega \frac{\omega^3 v}{2\pi^2} \Gamma_{\rm prod}(r,\omega)\, O(r,\omega), \qquad (2.34)$$

with the direction-averaged optical depth,

$$O(r,\omega) = \frac{1}{2}\int_{-1}^{+1} d\cos\theta \exp\left[-\int_0^{s_{\rm max}} ds \frac{\Gamma_{\rm abs}(\sqrt{r^2+s^2+2rs\cos\theta},\omega)}{v}\right]. \qquad (2.35)$$

The luminosity accounts for X production inside the neutrinosphere, $r < R_\nu$, that escapes the PNS, therefore constituting energy loss or cooling. The optical depth ensures that X decay/absorption that occurs inside the PNS does not contribute to the luminosity (see also Refs. [200,201]). This is done by taking the direction-averaged absorption of X along its propagation path parameterized by (s, θ), the chord distance between the production and escape radii and emission angle respectively. In this context, the chord distance from r to $R_{\rm max}$ is

$$s_{\rm max} = -r\cos\theta + \sqrt{R_{\rm max}^2 - r^2 + r^2\cos^2\theta}. \qquad (2.36)$$

In this work, we take $R_{\rm max} = R_\nu \sim 25\,{\rm km}$ as advocated for in Ref. [202]. Finally, general relativistic effects of the PNS gravitational well are encoded in gravitational lapse factor, $N(r)$ [182, 187]. The $N(r)^2$ term accounts for the time dilation of the production rate and the redshifting of emitted X, whereas the $m_X/N(r)$ term accounts for necessary escape velocity.

To ensure our bounds are robust with respect to SN modeling, we use four representative models to derive the constraints. The models are SFHo-18.6, SFHo-18.8, SFHo-20.0, and LS220-20.0, where SFHo [203] and LS220 [204] are the equations of states used at supernuclear densities, and 18.6 [205], 18.8 [206], and 20.0 [207] are the progenitor masses. More information of these models can be found in [208]. The temperature profiles and normalized number densities of particles in the PNS at 1 s

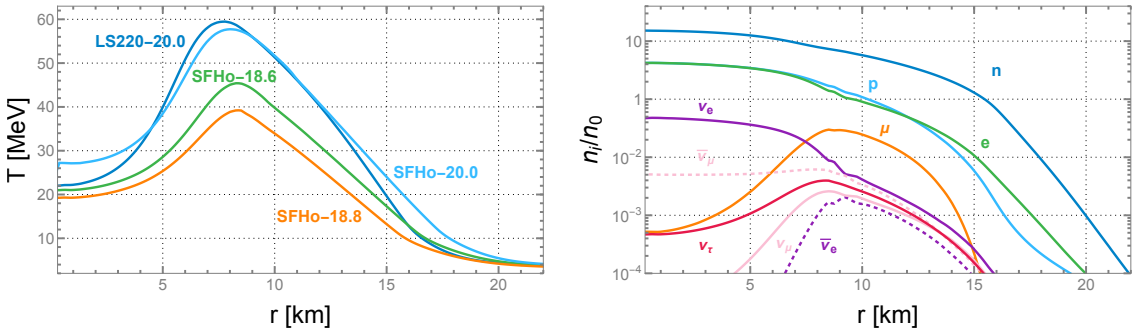


Figure 12. (Left) temperature profile of the 4 models used, and (right) particle number density profile in the SFHo-18.8 model normalized to $n_0 = 0.181$ fm^{-3} corresponding to nuclear density of 3×10^{14} g cm^{-3}.

after core collapse are shown in Fig. 12.[11] For all φ, we find that the SFHo-18.8 model leads to the most conservative bounds, and so we adopt this model when presenting our results.

In medium, the SM photon acquires nonzero effective plasma mass [209, 210] which is characterized by the real part of the photon polarization tensor

$$\mathrm{Re}\,\Pi_{\mathbf{L}} = \frac{3\omega_p^2}{v^2}(1-v^2)\left[\frac{1}{2v}\ln\left(\frac{1+v}{1-v}\right)-1\right] \qquad \mathrm{Re}\,\Pi_{\mathbf{T}} = \frac{2\omega_p^2}{2v^2}\left[1-\frac{1-v^2}{2v}\ln\left(\frac{1+v}{1-v}\right)\right]. \tag{2.37}$$

Here $\omega_p^2 = 4\pi\alpha_{\rm EM} n_e/\sqrt{m_e^2+(3\pi^2 n_e)^{2/3}}$ is the plasma frequency, v is the photon velocity, and $\mathbf{T}$, $\mathbf{L}$ are the transverse and longitudinal polarizations of the photon each with a different in-medium dispersion relation. The polarization tensor also dynamically changes the coupling of X with the SM particles charged under $U(1)_{\rm EM}$. Explicitly,

$$g_X \longrightarrow g_{X,m} = \frac{m_X^2}{m_X^2-\Pi} g_X \equiv \xi_m g_X \qquad (e,q,p) \tag{2.38}$$

$$g_X \longrightarrow g_X \qquad (\nu,n), \tag{2.39}$$

[11] The full profile data can be found at the Garching Core Collapse Supernova Archive [87].

where

$$\xi_m^2 \;=\; \frac{1}{\left(1-\mathrm{Re}\,\Pi/m_X^2\right)^2+\left(\mathrm{Im}\,\Pi/m_X^2\right)^2}\,. \tag{2.40}$$

The imaginary part of the polarization tensor is $\mathrm{Im}\,\Pi_{\mathbf{L},\mathbf{T}} = -\omega(\Gamma_{\mathrm{abs}|\mathbf{L},\mathbf{T}} - \Gamma_{\mathrm{prod}|\mathbf{L},\mathbf{T}})$, where Γ_{abs} and Γ_{prod} are the absorption width and production rate of SM photon at energy ω [211]. In local thermal equilibrium at temperature T, these rates are related through detailed balance $\Gamma_{\mathrm{prod}} = e^{-\omega/T}\Gamma_{\mathrm{abs}}$. The absorption rates of interest in a proto-neutron star are inverse bremsstrahlung, semi-Compton scattering, and X decays into e^+e^- and $\nu\bar{\nu}$.

The bremsstrahlung rate is composed of pn, pp, and nn collisions and is derived in App. C using the soft radiation approximation,

$$\Gamma^{ij}_{\mathrm{ibr}|\mathbf{L},\mathbf{T}} = \frac{8n_in_j}{15\pi^2\omega^3 S_{\mathbf{L},\mathbf{T}}}\left(\frac{\pi T}{m_N}\right)^{3/2}\begin{cases}\left[10q_-^2\langle\sigma_{ij}^{(2)}\rangle + 9q_+^2\frac{Tv^2}{m_N}\langle\sigma_{ij}^{(4)}\rangle\right] & (\mathbf{T})\\ \left[5q_-^2\langle\sigma_{ij}^{(2)}\rangle + 6q_+^2\frac{Tv^2}{m_N}\langle\sigma_{ij}^{(4)}\rangle\right](1-v^2) & (\mathbf{L})\,.\end{cases} \tag{2.41}$$

Here $q_\pm = q_1 \pm q_2$ with q_1, q_2 the charges of the two nucleons, $\langle\sigma_{ij}^{(2)}(T)\rangle = \frac{1}{2}\int_0^\infty dx e^{-x}x^2\sigma_{ij}^{(2)}(xT)$ and $\langle\sigma_{ij}^{(4)}(T)\rangle = \frac{1}{6}\int_0^\infty dx e^{-x}x^3\sigma_{ij}^{(4)}(xT)$ are the energy and angle-averaged nucleon-nucleon scattering cross section found in [197]. The production rate is identical with the restriction that the energy of X must not exceed the energy of the collision. This takes $\int_0^\infty \to \int_{\omega/T}^\infty$; for example $\langle\sigma_{ij}^{(2)}(T)\rangle \to \langle\sigma_{ij}^{(2)}(T,\omega)\rangle = \frac{1}{2}\int_{\omega/T}^\infty dx e^{-x}x^2\sigma_{ij}^{(2)}(xT)$.

When calculating the imaginary part of the polarization tensor of the SM photon $\mathrm{Im}\,\Pi_{\mathbf{L},\mathbf{T}}$, the charges in question are $q_p = e$ for the proton and $q_n = 0$ for the neutron. When calculating the absorption rate for X, the proton charge is $q_{p,\mathrm{med}} = \xi_m q_p = \xi_m g_X(\cos\varphi + \sin\varphi)$ and the neutron charge $q_{n,\mathrm{med}} = q_n = g_X\sin\varphi$. In a general

model, the pn, pp and nn charges in Eq. (2.41) become

$$(q_p \pm q_n)^2_{\rm med} = q_n^2 + \xi_m^2 \left[(q_p^2 \pm 2 q_p q_n) \mp 2 \frac{{\rm Re}\,\Pi}{m_X^2} q_p q_n \right] \tag{2.42}$$

$$(q_p + q_p)^2_{\rm med} = 4 \xi_m^2 q_p^2 \tag{2.43}$$

$$(q_n + q_n)^2_{\rm med} = 4 q_n^2 \,. \tag{2.44}$$

When the couplings of the proton and neutron to X are the same [$q_-^2 = 0$ in Eq. (2.41)], the bremsstrahlung rate arises only at the quadrupole order and is suppressed. When the couplings are different, the pn bremsstrahlung rate dominates. In the dark photon case, there is no coupling to neutrons and we are left with two diagrams for pn and four for pp. For pp bremsstrahlung rate, $q_- = q_p - q_p = 0$ and first contribution is suppressed by T/m_N as compared to the pn bremsstrahlung rate. Hence only the pn bremsstrahlung rate is important in the dark photon limit. In the $B-L$ case with ${\rm Re}\,\Pi \ll m_X^2$, the couplings of X to the proton and neutron are the same, and so the leading contribution to bremsstrahlung is of order $\mathcal{O}(T/m_N)$ requiring all of pn, pp, and nn bremsstrahlung rates to be included [the $q_+^2 \langle \sigma_{ij}^{(4)} \rangle$ terms]. However, when ${\rm Re}\,\Pi \gg m_X^2$, only the pn bremsstrahlung rate (off of neutrons) is important since the in-medium proton charge is suppressed and is thus non-degenerate with the neutron charge. Similarly, in the chargephobic limit, only the pn bremsstrahlung rate is important, though in this case, the bremsstrahlung is X off neutrons (and not protons). Hence, the pp and nn bremsstrahlung are only important in the $B-L$ case when $m_X \gtrsim 10\,{\rm MeV}$.

The decay rates $X \to e^+ e^-$ and $X \to \nu_i \bar{\nu}_i$ provide an important contribution to the optical depth. The widths are

$$\Gamma_{f\bar{f}|\mathbf{L},\mathbf{T}} = \mathcal{C}_f \frac{1}{4\pi} \frac{(q_f)_m^2 m_X^2}{\sqrt{\omega^2 - m_X^2}} \int_{x_-}^{x_+} \frac{\mathbf{m}_f (\omega x)^2_{\mathbf{L},\mathbf{T}}\, dx}{\left[\exp\left(\frac{\mu_f - \omega x}{T} \right) + 1 \right] \left[\exp\left(-\frac{\mu_f + \omega(1-x)}{T} \right) + 1 \right]}, \tag{2.45}$$

where μ_f is the chemical potential, and $x_\pm = \frac{1}{2}\left[1 \pm \sqrt{(1-4(m_f^{\rm eff})^2/m_X^2)(1-m_X^2/\omega^2)}\right]$ are the limits of integration, and $\mathcal{C}_f = 1$ (1/2) for e^+e^- ($\nu_i\bar{\nu}_i$). We also have the dimensionless squared matrix elements $\mathbf{m}_f(E_1)^2_{\mathbf{T}} = (m_f^{\rm eff})^2/m_X^2 + z(E_1)$ and $\mathbf{m}(E_1)^2_{\mathbf{L}} = 1 - 2z(E_1)$ where

$$z(E_1) = \frac{E_1 E_2}{m_X^2} - \frac{(E_1\omega - m_X^2/2)(E_2\omega - m_X^2/2)}{\omega^2 - m_X^2}, \tag{2.46}$$

and $E_2 = \omega - E_1$ [191]. The two factors in the denominator of Eq. (2.45) are due to Pauli blocking of f and $\bar{f}$ respectively. In particular, $\mu_e/T \gg 1$ and so the second term reduces to unity, since the positron abundance is negligible in the PNS. On the other hand, $\mu_{\nu_\tau} = 0$, and so both terms contribute to blocking. In medium, the electrons also acquire an effective mass [212]

$$m_e^{\rm eff} = \frac{m_{e,0}}{2} + \sqrt{\frac{m_{e,0}^2}{4} + \frac{\alpha}{2\pi}(\pi^2 T^2 + \mu_e^2)}. \tag{2.47}$$

This electron effective mass ranges between $0.6-11.3$ MeV within R_ν and the electron-positron decay channel is accessible only when $m_X \geq 2m_e^{\rm eff}$. As a consequence, this channel can never be resonant since $m_X < 2m_e^{\rm eff}$ is always true when $m_X^2 = \mathrm{Re}\,\Pi_{\mathbf{L},\mathbf{T}}$. It is unclear if previous results in the literature have considered this effect. Furthermore, electron-positron coalescence can be safely ignored everywhere since positrons are so rare in the PNS. On the other hand, neutrino-antineutrino coalescence is only important in the high mass region of the $B-L$ case where the bremsstrahlung rate is suppressed. The PNS cooling constraints on the dark photon, $B-L$, and chargephobic cases are shown in Fig. 13. In the $B-L$ and chargephobic case, Fig. 13 also shows constraints from the non-observation of high energy neutrinos which will be discussed in Sec. 2.5.2.2.

In the dark photon case, we find excellent agreement with previous cooling bounds in Refs. [45, 191]. The small discrepancy between the three bounds can be

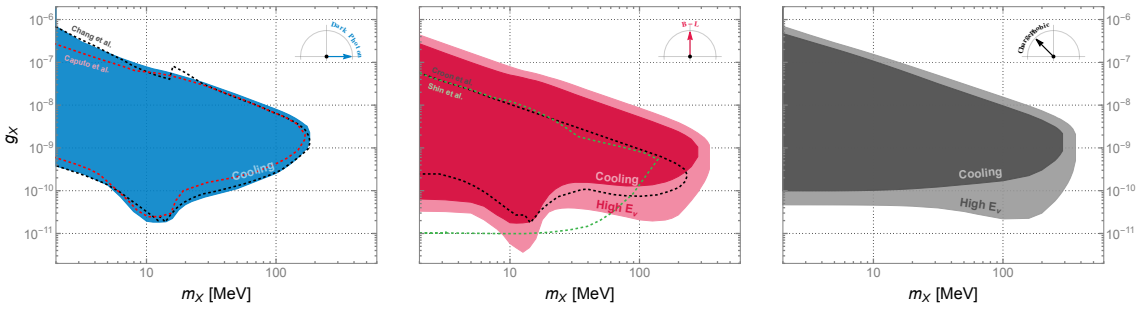


Figure 13. SN1987a constraints on the dark photon case $\varphi = 0$ (left, blue), the $B-L$ case $\varphi = \pi/2$ (middle, red), and the chargephobic case $\varphi = 3\pi/4$ (right, gray). The colors are chosen to match the compass inset, with the darker and lighter shades corresponding to PNS cooling and non-observation of high energy neutrinos bounds respectively. In the dark photon case, the black and red dashed lines are cooling bounds taken from Refs. [191] and [45] with $R_{\rm max} = R_\nu$. In the $B-L$ case, the black and green dashed lines are the cooling bounds taken from Ref. [55] ($R_{\rm max} = 100\,{\rm km}$, and using a similar analysis to Ref. [191]) and Ref. [56] ($R_{\rm max} = 1000\,{\rm km}$); our cooling constraint resolves the tension between these two previous bounds as discussed in the text.

attributed to differences in the adopted CCSN model, and a small variation in the treatment of bremsstrahlung production rate.

In the $B-L$ case, there are several qualitative differences between our bound and the two previous bounds in Refs. [55, 56] (where these two prior results also disagreed with each other in parts of the parameter space). First, the upper bound is set by the choice of $R_{\rm max}$, the maximum radius where X can be reabsorbed or decay without contributing to the cooling luminosity. Our choice of $R_{\rm max} = R_\nu \sim 25\,{\rm km}$, as advocated for in Ref. [202], predictably results in a stronger upper bound when compared to the choice of $R_{\rm max} \sim 1000\,{\rm km}$ in Ref. [56] due to the reduced trapping. We have explicitly checked that we reproduce the upper bound in Refs. [55, 56] for $R_{\rm max} \sim 1000\,{\rm km}$.

Next we explain the features observed for the lower bounds of $B-L$ case. For $m_X \gtrsim 20$ MeV, in-medium effects are negligible and the proton/neutron charges are degenerate resulting in quadrupole suppressed bremsstrahlung production and

absorption rates. In this regime, neutrino coalescence is an important production mode. For $m_X \lesssim 10$ MeV, finite temperature effects alter the proton effective charge but not for the neutron. This alleviates the quadrupole suppression in pn bremsstrahlung and the resulting production is two fold: pn bremsstrahlung off of neutrons which is m_X independent, and resonant production off of protons when $m_X^2 = \mathrm{Re}\,\Pi_{\mathbf{L},\mathbf{T}}$. The resonance around $m_X \sim 10$ MeV in the lower bound of the $B - L$ case is the same as that in the dark photon case; this is to be expected since the resonant production can be understood as a thermal bath of photons slowly transitioning to X independent of the details of the production process [210].

The lower bound in Ref. [56] (dashed green) is an order of magnitude stronger than ours. This discrepancy can be attributed to the way the bremsstrahlung rates are implemented. Ref. [56] used one-pion exchange, which is known to overestimate this rate as compared to nucleon-nucleon bremsstrahlung data. This overestimate was first shown in [197] and more recently in [213]. Following the argument in Appendix D of [213], we have used soft radiation approximation in deriving our bremsstrahlung rates Eq. (2.41). The lower bound in Ref. [55] (dashed black) for $m_X \lesssim 10$ MeV was obtained by recasting the constraint on a vector boson coupling to just baryon number. However, in this process they did not take into account finite temperature effects lifting the bremsstrahlung quadrupole suppression, and hence arrived at a bound that is weaker than ours.

In the chargephobic case, the dominant production mode is pn bremsstrahlung off of neutrons which is both m_X independent and oblivious to finite temperature corrections. This rate sets the lower bound. The upper bound is set by inverse bremsstrahlung and decays into neutrinos inside the PNS. Furthermore, with the absence of the $X \to e^+e^-$ decay channel, there are no efficient processes to facilitate

the absorption of X outside the neutrinosphere. Consequently, the constraint is insensitive $R_{\rm far}$. In terms of complexity, the chargephobic SN cooling constraint is the simplest to derive among the three cases that we considered. Nevertheless, this limit demonstrates the resilience of the SN cooling bound even when X has no couplings to electrons and protons.

2.5.2.2 High Energy Neutrinos. The observed neutrino signal from SN1987A shows no evidence of neutrinos with $E_\nu \gtrsim 75$ MeV [167, 168]; again, in accordance with CCSN numerical simulations [169–171]. However, the luminosity of X contributing to cooling in Sec. 2.5.2.1, can also contribute an additional flux of high energy neutrinos that could have been observed in the same terrestrial detectors. This can arise through the direct decay $X \to \nu_i \bar{\nu}_i$ or through $X \to \mu^+\mu^-$ ($\pi^+\pi^-$) and subsequent neutrinos from muon/pion decay. The non-observation of high-energy neutrinos has been used to set constraints on various models [176–182]. In this work, we adapt the analysis employed to Ref. [182] to our model as follows. The differential ν_e flux at the detector is

$$\frac{d\Phi_{\nu_e}}{dE_\nu} = \frac{1}{3}\frac{\mathrm{BR}(\nu)}{4\pi R_{1987A}^2}\int_0^\infty d\omega \frac{1}{\omega}\frac{\Theta(E_\nu - E_\nu^{\rm min})\times\Theta(E_\nu^{\rm max}-E_\nu)}{E_\nu^{\rm max}-E_\nu^{\rm min}}\frac{dL_X}{d\omega}, \tag{2.48}$$

where $\mathrm{BR}(\nu)$ is the branching fraction of X to neutrinos, $R_{1987A} = 51.4\,\mathrm{kpc}$ is the distance between Earth and SN1987A, $dL_X/d\omega$ is the differential luminosity in Eq. (2.34), and the Heaviside theta term is the probability a neutrino with energy E_ν is obtained from X with energy ω. At the detector level, two detection channels are at play: inverse beta decay $\bar{\nu}_e + p \to n + e^+$, and scattering off oxygen $\bar{\nu}_e/\nu_e + {}^{16}\mathrm{O} \to e^\pm + Y$; these cross sections can be found in Refs. [176, 214–217]. For the IMB detector [218], the expected number of high energy events is

$$N_{\rm ev} = \epsilon_{\rm det}\sum_i \int_0^{10\,\mathrm{s}} dt \int_{90\,\mathrm{MeV}}^{215\,\mathrm{MeV}} dE_\nu \frac{d\Phi_{\nu_e}}{dE_\nu}\sigma^i_{\rm det}(E_\nu)N_i, \tag{2.49}$$

with $\epsilon_{\rm det}$ the energy-independent detection efficiency. Here, we consider an exposure time of 10 s and a fiducial mass of 6.8 kton corresponding to $N_{^{16}\rm O} = 2.3 \times 10^{32}$ and $N_{^1\rm H} = 4.5 \times 10^{32}$. The time integral is performed by evaluating the differential luminosity/flux at the set of time snapshots provided by the Garching Archive [87]. Finally, assuming Poissonian statistics, we set 95 % confidence level bounds on parameter space that yields $N_{\rm ev} \geq 3$. These constraints are shown in Fig. 13 for the $B - L$ and chargephobic limits.

2.5.2.3 Electromagnetic-Based Supernova Signals. When $X \to e^+e^-$ is accessible, such as in the dark photon case, core collapse supernovae are capable of constraining X emission not only through cooling but also through several electromagnetic signatures labeled in Fig. 3 as LESNe, SN1987A γ, 511 keV line, and the fireball bounds PVO/GW170817 that were taken directly from Ref. [45].

The LESNe constraint arises by requiring that the energy deposited in the mantle, due to dark photon decays into e^+e^-, does not over-energize a sample of very low-energy Type II supernovae whose light curves imply explosion energies $\lesssim 0.1$ Bethe [183,185–187,189]. Instead of decaying in the mantle, if the dark photons escape the progenitor and subsequently decays into e^+e^- pairs and photons outside the star, this would yield a detectable prompt MeV γ-ray burst signal; the absence of such signal in the Gamma-Ray Spectrometer (GRS) in SN1987A [219] sets the constraint labeled SN1987A γ. A similar constraint can be placed from stacking Type Ic SNe events as was done for ALPs [190]; translating this constraint to vector mediators is left for future studies. When the decays of escaped X are frequent enough that the produced e^+e^- and photons become optically thick and thermalize, they form a fireball [220]. The Pioneer Venus Orbiter, which was sensitive to photons in the $0.2 - 2$ MeV range consistent with the expected thermalized fireball spectrum,

saw no significant γ-ray excess from SN1987A [221,222], thereby setting the constraint fireball (PVO). Similarly, for the compact binary merger GW170817 [223, 224], X-ray observations from CALET/CGBM, Konus-Wind, and Insight-HXMT/HE place an upper limit on any GRB-like fireball emission [188], setting the constraint fireball (GW170817). The injection of positrons into the Milky Way through these decays can substantially enhance the diffuse γ-ray emission from the Galactic Center, which is tightly constrained by the INTEGRAL/SPI measurement of the 511 keV line [184, 222].

We emphasize that we did not derive or recast these constraints, but rather simply adopted them directly from [45] for the dark photon case in Fig. 3. In the $B-L$ case, we expect these constraints to remain but with some slight changes compared to the dark photon case. The difference can be characterized as follows: the $X \to e^+e^-$ branching fraction in $B-L$ is 40 % smaller than in the DP case which reduces the signal from these constraints. Furthermore, important differences arise for the dominant production modes for X inside the PNS between the dark photon and $B-L$ cases as discussed in Sec. 2.5.2.1. For example, an estimate of the lower bound of the LESNe constraint can be obtained by simply rescaling the lower bound of the cooling bound [45]. Hence, we expect the qualitative shape of the LESNe bound in the $B-L$ to mimic that of the $B-L$ cooling bound in Fig. 13. Recasting these constraints to $B-L$, and more general angles φ, requires a dedicated analysis that is beyond the scope of our work. We have taken the liberty to overlay these dark photon bounds from [45] as unlabeled light-shaded regions with dashed-lines in the $B-L$ case shown in Fig. 3. This is merely illustrative of where one might expect these constraints to appear.

In the chargephobic vector boson case, virtually all of aforementioned constraints vanish due to the absence of X decays to charged leptons. The one potential exception to this is the LESNe constraint, since this extends up to a dark photon mass of about 500 MeV. For chargephobic masses $m_X \gtrsim 200$ MeV, a very small branching fraction to charged leptons ($\sim 10^{-6}$) develops from the renormalization-group evolution of the couplings. However, we suspect this is much too small to lead to a constraint on its own. Instead, for $m_X > 2m_\pi$, a chargephobic vector boson has an increasing branching fraction to $\pi^+\pi^-$ (few to 20%), that may or may not affect the low energy supernova dynamics. While we have not shown a constraint in Fig. 4, we caution the reader that a small region of LESNe parameter space may be constrained, if the convolution of X decay and π decay leads to enough energy deposition. This is an interesting question, but beyond the scope of our work.

2.5.3 Neutrino Experiments. Neutrino experiments can be classified into four categories: neutrino-electron scattering (NES) experiments, coherent elastic neutrino-nucleus scattering (CEνNS) experiments, experiments sensitive to collider neutrinos, and searches for invisible final states. The last of these relies on the assumption that the invisible final states can be treated as X decaying to neutrinos. NES and CEνNS rates are mediated by the neutral and charged electroweak current interactions in the SM and obtain a new contribution through X exchange. The resulting enhancement in these rates can be detected in experiments sensitive to the NES and CEνNS process, or conversely, the lack of signal can be interpreted as constraints on the $\{m_X, g_X\}$ parameter space. In this section, we describe how X modifies each of these four classes of neutrino observables and outline the procedure used to translate them into constraints on the parameter space of a given φ.

In the SM, the electron-neutrino scattering amplitude consists of contributions from the charged and neutral currents. The SM differential cross section is

$$\left[\frac{d\sigma}{dE_r}(\nu e^- \to \nu e^-)\right]_{\rm SM} = \frac{2G_F^2 m_e}{\pi E_\nu^2}\left(a_1^2 E_\nu^2 + a_2^2(E_\nu - E_r)^2 - a_1 a_2 m_e E_r\right), \quad (2.50)$$

where G_F is Fermi coupling constant, E_r is the recoil energy of the electron, E_ν is the energy of incoming neutrino, and $\{a_1, a_2\} = \sin^2\theta_W\{1,1\} + \frac{1}{2}A$ with $A = \{1,0\}$ for $\nu_e e$, $\{0,1\}$ for $\bar{\nu}_e e$, $\{-1,0\}$ for $\nu_\alpha e$, and $\{0,-1\}$ for $\bar{\nu}_\alpha e$. The incoming neutrino must have a minimum energy of $E_\nu^{\rm min} = \frac{1}{2}\left(E_r + \sqrt{E_r^2 + 2E_r m_e}\right)$ for a given recoil energy. The X contributions to NES and the interference between X exchange and the SM Z exchange are given by

$$\left[\frac{d\sigma}{dE_r}\right]_{\rm X} = \frac{g_X^4 m_e \sin^2\varphi\,(\cos\varphi + \sin\varphi)^2}{4\pi E_\nu^2(m_X^2 + 2m_e E_r)^2}\left(2E_\nu^2 + E_r^2 - 2E_\nu E_r - m_e E_r\right), \quad (2.51)$$

$$\left[\frac{d\sigma}{dE_r}\right]_{\rm Int} = \frac{g_X^2 G_F m_e \sin\varphi(\cos\varphi + \sin\varphi)}{2\sqrt{2}\pi E_\nu^2(m_X^2 + 2m_e E_r)^2}\left(b_1(2E_\nu^2 - m_e E_r) + b_2(2E_r^2 - 4E_\nu E_r) + \beta\right), \quad (2.52)$$

where $\beta = \sin^2\theta_W(8E_\nu^2 - 8E_\nu E_r - 4m_e E_r + 4E_r^2)$, and $\{b_1, b_2\}$ are $\{1,0\}$ for $\nu_e e$, $\{1,1\}$ for $\bar{\nu}_e e$, $\{-1,0\}$ for $\nu_\alpha e$, and $\{-1,-1\}$ for $\bar{\nu}_\alpha e$ [94].

CEνNS occurs when the momentum transfer between the neutrino and the nucleus is comparable to inverse of the nuclear radius. The differential cross section is

$$\left[\frac{d\sigma}{dE_r}\right]_{\rm CE\nu NS} = \frac{G_F^2 Q^2}{2\pi} M F^2(2ME_r)\left(2 - M\frac{E_r}{E_\nu^2} - 2\frac{E_r}{E_\nu} + \frac{E_r^2}{E_\nu^2}\right) \quad (2.53)$$

where M is the mass of the target nucleus and $F(Q^2)$ is the nuclear form factor. In the SM, the effective charge is $Q_{\rm SM} = Z(\frac{1}{2} - 2\sin^2\theta_W) - \frac{1}{2}N$ for a nucleus with Z protons and N neutrons. This charge is approximately $Q_{\rm SM} \sim -\frac{1}{2}N$ since the proton weak charge is quite small. When we include the contribution from X, the effective

charge [225] becomes

$$Q^2_{\mathrm{SM}+X} \;=\; \left(Q_{\mathrm{SM}} - [Z(\cos\varphi + \sin\varphi) + N\sin\varphi]\sin\varphi \frac{g_X^2}{2\sqrt{2}G_F(2ME_r + m_X^2)}\right)^2 . \tag{2.54}$$

The CEνNS related constraints are of particular interest in this paper as they are some of the few terrestrial experiment constraints that do not vanish in the chargephobic case.

2.5.3.1 Coherent elastic neutrino-nucleus scattering Experiments.

The first observation of CEνNS in 2017 by the COHERENT collaboration [226] spurred an extensive experimental program aimed at precision measurements of this process [227]. The CEνNS rate is sensitive to modifications by BSM mediators coupled to neutrinos and nucleons and can be leveraged to set constraints on light vector mediators [225, 228–242]. In our mass range of interest, the current leading CEνNS constraints on light vector mediators are placed by COHERENT [226,243,244] and CONUS+ [245]. These two constraints will be the focus of this section and will be treated as representative of the current CEνNS constraint landscape for vector mediators of masses $m_X > 1$ MeV.

The COHERENT collaboration has measured the CEνNS process using two detectors, in a sodium doped CsI scintillator [226, 243] and in a liquid argon detector [244] with future plans expanding to more detector materials [246]. These detectors are exposed to the neutrino emissions from the Spallation Neutron Source (SNS) at Oak Ridge National Laboratory. In the CsI detector [243], the SM best fit prediction models the observed data with a $\chi^2/\mathrm{dof} = 82.6/98$ and the observed data rejects the no-CEνNS hypothesis at 11.6 σ. The X exchange contribution to the CEνNS rate, Eq. (2.53), can spoil this agreement and lead to a constraint on the couplings of X. In this work, we focus on constraints obtained from the CsI data release only;

the inclusion of argon data provides only slight improvements. We set constraints following the analysis in [96] using a Poissonian least-squares function over event counts in 9 energy and 11 timing bins.

Three neutrino flavors are produced in the SNS; prompt mono-energetic 30 MeV ν_μ produced via the decay of stopped π^+, and delayed $\bar{\nu}_\mu$ and ν_e produced from the decay of μ^+ which was in turn produced from pion decay. Neutrino fluxes $d\Phi_\nu/dE_\nu$ and timing spectra $f_T^\nu(t)$ can be found in [247]. For a given nucleus $\mathcal{N}$, the expected number of events per energy i and time j bin is

$$N_{i,j}^{\mathrm{CE}\nu\mathrm{NS},\,\mathcal{N}} = \sum_{\nu=\nu_e,\nu_\mu,\bar{\nu}_\mu} N_{\mathrm{target}} \int_{t^j}^{t^{j+1}} dt f_T^\nu(t,\alpha_6)\epsilon_T(t) \int_{E_{\mathrm{nr}}^j}^{E_{\mathrm{nr}}^{j+1}} dE_{\mathrm{nr}}\epsilon_E(E_{\mathrm{nr}},\alpha_7)\times$$
$$\int_0^{E_{\mathrm{nr}}^{\prime\,\mathrm{max}}} dE'_{\mathrm{nr}} P(E_{\mathrm{nr}},E'_{\mathrm{nr}}) \int_{E_\nu^{\mathrm{min}}(E'_{\mathrm{nr}})}^{E_\nu^{\mathrm{max}}} dE_\nu \frac{d\Phi_\nu}{dE_\nu}(E_\nu)\frac{d\sigma_{\nu\mathcal{N}}}{dE_r}(E_\nu,E'_{\mathrm{nr}},\alpha_4), \quad (2.55)$$

where N_{target} is the number of target atoms in the detector, $\epsilon_T(\epsilon_E)$ are the time (energy)-dependent detector efficiencies, and E_{nr} and E'_{nr} are the reconstructed and true nuclear recoil energy respectively related via the energy resolution function $P(E_{\mathrm{nr}},E'_{\mathrm{nr}})$. The first two integrals are bounded by bin edges, the third integral by $E_{\mathrm{nr}}^{\prime\,\mathrm{max}} = 2(E_\nu^{\mathrm{max}})^2/m_N$, and the fourth by $E_\nu^{\mathrm{min}} \simeq \sqrt{m_N E'_{\mathrm{nr}}/2}$ and $E_\nu^{\mathrm{max}} = m_\mu/2$. The total binned number of events is given by $N_{i,j}^{\mathrm{CE}\nu\mathrm{NS}} = N_{i,j}^{\mathrm{CE}\nu\mathrm{NS},\,\mathrm{Cs}} + N_{i,j}^{\mathrm{CE}\nu\mathrm{NS},\,\mathrm{I}}$.

The analysis is then performed using a Poissonian least-squares function

$$\chi^2_{\mathrm{CsI}} \;=\; 2\sum_{i=1}^{9}\sum_{j=1}^{11}\left[N_{\mathrm{th}}^{\mathrm{CsI}} - N_{ij}^{\mathrm{exp}} + N_{ij}^{\mathrm{exp}}\ln\left(\frac{N_{ij}^{\mathrm{exp}}}{N_{\mathrm{th}}^{\mathrm{CsI}}}\right)\right] + \sum_{k=0}^{4}\left(\frac{\alpha_k}{\sigma_k}\right)^2, \quad (2.56)$$

$$N_{\mathrm{th}}^{\mathrm{CsI,CE}\nu\mathrm{NS}} = (1{+}\alpha_0)N_{i,j}^{\mathrm{CE}\nu\mathrm{NS}}(\alpha_4,\alpha_6,\alpha_7){+}(1{+}\alpha_1)N_{i,j}^{\mathrm{BRN}}(\alpha_6){+}(1{+}\alpha_2)N_{i,j}^{\mathrm{NIN}}(\alpha_6){+}(1{+}\alpha_3)N_{i,j}^{\mathrm{SSB}}. \quad (2.57)$$

We use the CsI unbinned data events provided by the COHERENT collaboration [243] to extract the measured binned event number N_{ij}^{exp} and to estimate the number of events $N_{i,j}^{\mathrm{SSB}}$ from the beam-uncorrelated steady-state background (SSB). We also

include the prompt beam-related neutron (BRN) and neutrino-induced neutron (NIN) events. The nuisance parameters are as follows: α_0 encodes the efficiency and flux uncertainties, α_1 (α_1) [α_3] correspond to the BRN (NIN) [SSB] uncertainties, α_4 modifies the nuclear form factor $R_A = 1.23A^{1/3}(1 + \alpha_4)$, α_6 accommodates the uncertainty in beam timing ($\pm 250\,\text{ns}$), and α_7 allows for deviations in the energy-dependent detector efficiency ($\epsilon_E[x + \alpha_7]$ with α_7 allowed to vary in the range $[-1, 1] \times$ PE) [12]. Finally, the uncertainties σ_i associated with nuisance parameter α_i are given by $\{\alpha_0, \ldots, \alpha_4\} = \{11,\ 25,\ 35,\ 2.1,\ 5,\ 3.8\}\,\%$.

The CONUS+ collaboration recently achieved the first clear observation of reactor neutrino CEνNS [245], with earlier evidence from Dresden-II [248] and prior CONUS runs [236]. Furthermore, many reactor-based experiments aim to lower detection thresholds and in doing so enhance sensitivity to light mediators; such as TEXONO [249], NUCLEUS [250], RICOCHET [251], and CONNIE [252]. Reactor-based CEνNS experiments probe neutrino energies of a few MeV, providing leading CEνNS sensitivity to light vector mediators below roughly $m_X \lesssim 10$ MeV. This mass range is dominated by ΔN_{eff} constraints discussed in Section 2.5.1, however, the CONUS+ constraint still rules out a novel region of parameter space. Similar to the COHERENT analysis, we follow the procedure laid out in [240, 241] to place constraints from the CONUS+ data release [245]. Note, the combined analysis of CONUS+, TEXONO, and COHERENT data [253] result in a slightly stronger bound; this is beyond the scope of our analysis and we do not attempt to replicate these results.

[12] The nuisance parameter α_5 is associated with the quenching factor. This parameter can be neglected in the region of the parameter space ($m_X > 1\,\text{MeV}$) where electron scattering does not play an important role. We drop this parameter but keep the numbering convention to match [243].

An example of the excess count calculation for $B-L$, chargephobic, and nucleophobic cases in COHERENT and CONUS+ detectors is shown in Fig. 14. The nucleophobic case is chosen such that the effective charge of a cesium nucleus vanishes. This specific choice is arbitrary, but captures the typical extent to which CEνNS experiment sensitivity to X is suppressed. The nucleus charge scales as A in $B-L$, $\sim N$ in the SM and the chargephobic case, and $(N-(N_{\rm Cs}/Z_{\rm Cs})Z)$ in the nucleophobic case. This explains the extent to which each model contributes to the excess count as is evident in the BSM excess (BSM $-$ SM) in both experiments. The excess count does not vanish in the nucleophobic case since there are couplings to Ge and I nuclei. These couplings are, however, suppressed: $\{x_{\rm Cs},\ x_{\rm I},\ x_{\rm Ge}\}_{\not{Cs}} = \{0,\ -0.4,\ -2\}$ when compared to $\{x_{\rm Cs},\ x_{\rm I},\ x_{\rm Ge},\ x_{\rm Ar}\}_{B-L} = \{133,\ 127,\ 72,\ 40\}$ for $B-L$. Furthermore, the negative nucleus charge in the nucleophobic case interferes destructively with the SM nucleus charge in Eq. (2.54). This can lead to excess counts lower than those in the SM as shown in Fig. 14. Finally, the COHERENT and CONUS+ constraints are shown in Fig. 15 where we emphasize constraints from the neutrino experiments discussed in Sec. 2.5.3. The aforementioned interference effect can also be seen through the unconstrained band in the COHERENT and CONUS+ nucleophobic bounds.

Finally, to illustrate the potential of next-generation CEνNS experiments, we show the recasted projected COH-CryoCsI II sensitivity [254] in Fig. 4 for the chargephobic limit. Here, the combination of a larger cryogenic CsI target, a lower nuclear recoil threshold, and an increased SNS beam power allows this setup to substantially improve upon current CEνNS bounds.

2.5.3.2 Neutrino-electron Scattering Experiments. Experiments in this category are sensitive to deviations from the SM NES rate via the X mediated

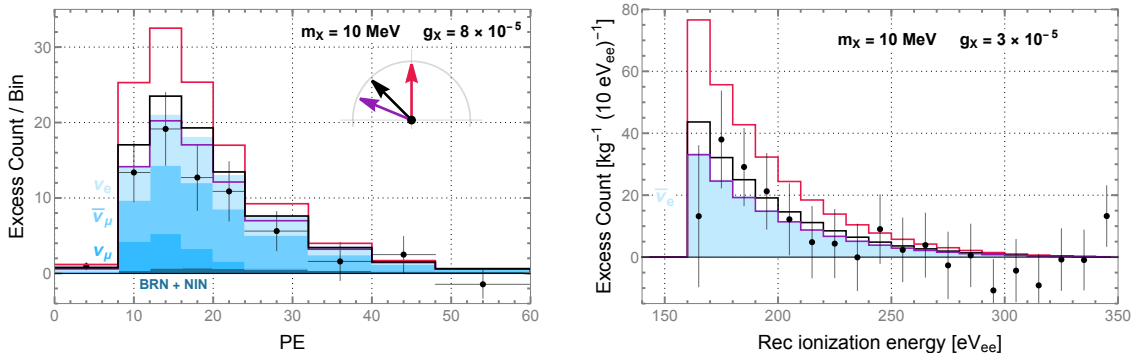


Figure 14. (Left) COHERENT CsI detector data residual over SSB background [243]. (Right) CONUS+ excess counts from three HPGe detectors (C2, C3, C5) [245]. The axes are chosen to match those in the original plots in the data release. The shaded steps represent the ν_i SM CEνNS prediction and the BRN and NIN backgrounds. The lines with no filling correspond to total excess count (SM + BSM) when X with charge assignment of $B-L$, $\varphi = 3\pi/4$, and $\varphi = \pi - \tan^{-1}(55/133)$ are considered. In all BSM cases, we have $m_X = 10\,\text{MeV}$ with (right) $g_X = 8\times10^{-5}$ and (left) $g_X = 3\times10^{-5}$.

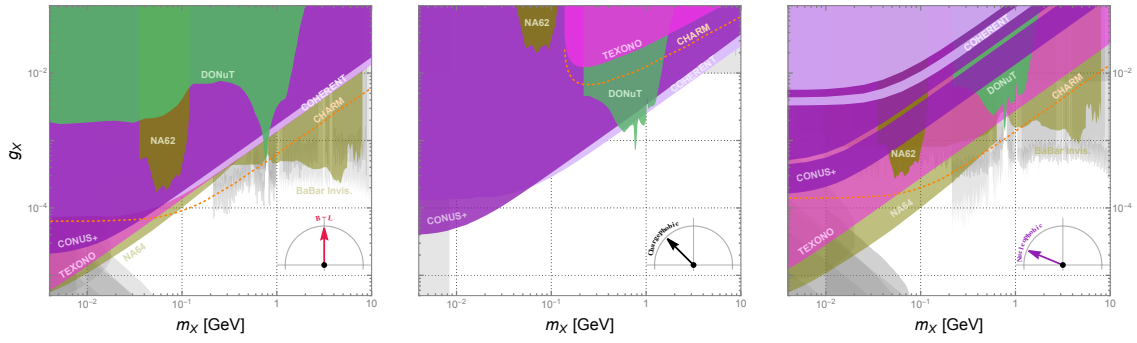


Figure 15. Constraints on (left) $B-L$ ($\varphi = \pi/2$), (middle) chargephobic ($\varphi = 3\pi/4$), and (right) nucleophobic [$\varphi = \pi - \tan^{-1}(55/133)$] limits with a focus on the neutrino constraints discussed in Sec. 2.5.3. Other constraints in Fig. 3 are displayed in gray.

NES channel. In our parameter space, the leading NES experimental constraints are set by Borexino Phase-II [255–260], TEXONO [261], and CHARM-II [262, 263]. TEXONO is a CsI(Tl) scintillating crystal array measuring $\bar{\nu}_e e^-$ elastic scattering with the $\bar{\nu}_e$ produced at the Kuo-Sheng Nuclear power station. The detector is exposed to an average $\bar{\nu}_e$ flux of 6.4×10^{12} cm^{-2} s^{-1} with standard reactor $\bar{\nu}_e$ spectrum [264]. We derive the constraint from TEXONO following the analysis in [94, 95]. Borexino presents a comprehensive measurement of the solar neutrino spectrum from the pp chain in the energy range of $(0.19 - 16)$ MeV. This data set in conjunction with standard solar model were used in [50, 94, 265] to set a constraint on the $B - L$ case. We adopt this constraint, without reproducing it, for the $B - L$ case and recast it using the appropriate charge scaling. For $m_X \gtrsim 3$ MeV, TEXONO is the leading NES constraint whereas Borexino leads in the region below where the $\Delta N_{\rm eff}$ constraint dominates. Hence, we focus on TEXONO constraints when presenting our analysis in Fig. 15. As for CHARM-II, it was pointed out in [39] that the exact neutrino fluxes seem to be unknown in the experimental publication. This casts some doubt on the validity of neutrino rate calculation in [94, 95]. Following [39], we show the CHARM bound as a dashed line to remind the reader of this subtlety and we assume that the correct neutrino flux was used for the bound calculation.

2.5.3.3 Invisible Searches. Invisible searches assume that the dark photon decays predominantly into a dark sector state χ via $X \to \chi\bar{\chi}$, which occurs when $m_X > 2m_\chi$ and the coupling g_X is sufficiently small that visible decays are subdominant [266–273]. The experimental signature is a visible SM particle accompanied by large missing energy and momentum. The same signature arises

if X instead decays mainly to neutrinos, $X \to \nu\bar{\nu}$. As a result, existing invisible searches can be recast using the neutrino branching fraction for a given φ.[13]

In our analysis, we consider three invisible searches to provide constraints on X. The BaBar invisible search uses 53 fb^{-1} of e^+e^- collision data to search for a single high-energy photon and a large missing momentum and energy via the process $e^+e^- \longrightarrow \gamma X$ followed by X invisible decay [268]. The invisible search in NA64 uses an electron beam dump setup to look for single electron events with large missing energy from $eZ \to eZX$ production followed by invisible X decay [273]. The NA62 invisible search uses the process $K^+ \longrightarrow \pi^+\pi^0,\ \pi^0 \longrightarrow \gamma X$ followed by an invisible decay of X [270]. BaBar and NA64 set leading constraints on $B-L$ and nucleophobic cases as shown in Fig. 15. NA62 is one of the few constraints that remain in the chargephobic case as it does not rely on a charged lepton coupling for either production or detection. The constraint is nonetheless significantly weakened due to the $\pi^0 \longrightarrow \gamma X$ suppression in the chargephobic case as seen in Fig. 6.

2.5.3.4 Collider Neutrinos. Collider neutrino experiments [274–277] are sensitive to new physics that produces an additional forward flux of tau neutrinos on top of the SM ν_τ component from D_s and other heavy meson decays. In our model, X is produced via bremsstrahlung or meson decays and can subsequently decay as $X \to \nu_\tau\bar{\nu}_\tau$, thereby enhancing the flux incident on these detectors. To illustrate this, we use two representative experiments: the fixed target DONuT experiment at Fermilab as a current constraint and the forward LHC detector FASERν for future projected sensitivity. In the $B-L$ case, we simply adopt these constraint from [278]. We recast this constraint using Eq. (2.30) and the LHCb production fractions in Figure

[13] At the $J/\psi, \psi(2S)$, $\psi(3770)$, and $\Upsilon(1S) - \Upsilon(4S)$ resonances, the $X \to \nu\bar{\nu}$ branching ratio can be non-trivially altered from the one reported in Fig. 7. In these narrow regions, the invisible search constraints can lose sensitivity or even vanish. We have not included this effect and report the invisible search constraints as they are traditionally displayed in the literature [39, 42].

11 from [42] for masses $m_X > 0.2$ GeV. We do not recast or show the constraints for $m_X < 0.2$ GeV in the chargephobic and nucleophobic cases in Fig. 15; this region of parameter space is already well covered by NES and CEνNS experiments.

There are several qualitative differences in the shape of the DONuT constraint between the $B-L$, chargephobic, and nucleophobic cases. For $B-L$, the resonance near $m_X \sim 0.8$ GeV is driven by ω–X mixing, while the ρ–X production mode is absent. In the chargephobic case, the ρ–X channel is active, leading to a broader resonance, while the ω–X mixing is reduced by a factor of 8, as shown in Fig. 5. In the nucleophobic case, $\omega - X$ mixing is highly suppressed and so the resonance reach is reduced. The branching fraction to tau neutrinos is also affected by the width of the hadronic resonance; see the $B-L$ and chargephobic cases in Fig. 7. The combination of these effects accounts for the shape of the DONuT constraint near the resonance. In our analysis, we used the LHCb production fractions [42] to determine the relative rates, however, they are not provided near the ω resonance. We have used interpolations in the mass ranges where no results were shown in [42], and so our recasted DONuT resonant behavior in this mass range should be taken as approximate. A robust bound near the ω resonance requires a dedicated reanalysis of Ref. [278] taking into account the production modes in Ref. [279], but this is beyond the scope of this work.

2.5.4 Beam Dump & Fixed Target Experiments. Electron and proton beam dump (BD) experiments direct high intensity beams onto thick targets, which can produce X via bremsstrahlung (in eBD & pBD) or meson decay/mixing (in pBD). A long-lived X vector boson that is produced in this collision and survives the shielding can decay in a downstream decay volume, with its decay products registered in a detector located anywhere from meters to hundreds of meters away. Decay modes

of X that lead to visible signals are typically $X \to \ell^+\ell^-$ and in particular $X \to e^+e^-$, which appears as an electromagnetic shower. Accordingly, constraints set by these beam dump experiments vanish in the chargephobic case. A notable exception is the projected sensitivity of SHiP [280–282], whose ability to fully reconstruct displaced X decay vertices extends the signal reach to the broad range of hadronic decays in Fig. 8. This makes SHiP uniquely positioned to probe the chargephobic parameter space in the future.

In electron beam dumps, the production cross section of X can be approximated using the Weizsäcker Williams approximation where the target nuclei $\mathcal{N}$ are replaced by an effective flux of photons [283]. The bremsstrahlung process is simplified to semi-Compton scattering, $e\,\gamma \longrightarrow e\,X$, and is given to a good approximation by

$$\frac{d\sigma_X}{dr_e} \simeq \frac{\alpha^2}{\pi} g_X^2 (1+\sin 2\varphi)\, \xi \sqrt{1-\frac{m_X^2}{E_e^2}} \frac{1-r_e+\frac{r_e^2}{3}}{m_X^2 \frac{1-r_e}{xre} + m_X^2 r_e}, \tag{2.58}$$

where $r_e \equiv E_X/E_e$ is the fraction of electron beam's energy carried by X and $\xi(E_e, m_X, Z, A)$ is the effective photon flux [194]. The electron beam can interact with the shielding material which diminishes its energy from initial beam energy E_0 to E_e. The energy distribution of the electron beam as function of penetration depth t [284] is

$$I_e(E_0, E_e, t) = \frac{1}{E_0} \frac{\ln\left(\frac{E_0}{E_e}\right)^{\frac{4}{3}t-1}}{\Gamma(\frac{4}{3}t)}. \tag{2.59}$$

The expected number of e^+e^- events in the detector for an electron beam of N_e electrons and energy E_0 is

$$N \simeq N_e \frac{N_0 X_0}{A} \int_{m_X}^{E_0-m_e} dE_X \int_{E_X+m_e}^{E_0} dE_e \int_0^{T_{\rm sh}} dt_{\rm sh} \left[I_e(E_0, E_e, t_{\rm sh}) \frac{1}{E_e} \frac{d\sigma_X}{dr_e} e^{-L_{\rm sh}/l_X} \left(1 - e^{-L_{\rm dec}/l_X}\right) \right] {\rm Br}_{e^+e^-}. \tag{2.60}$$

Here N_0 is Avogadro's number, X_0 and $\rho_{\rm sh}$ are the unit radiation length and density of target material, A is mass number of target, $T_{\rm sh} = L_{\rm sh}\rho_{\rm sh}/X_0$, and $l_X = \beta\gamma\tau$ is the X decay length in the lab frame. The exponential terms ensure that X must decay after the shielding but before or within the detector where $L_{\rm dec}$ is the length of the decay region. This term is obtained by integrating the differential decay probability $dP(l)/dl = e^{-l/l_X}/l_X$ from $L_{\rm sh}$ and $L_{\rm tot} = L_{\rm sh} + L_{\rm dec}$. A detailed explanation of computing this integral is provided in the appendix of [285]. Constraints are placed by excluding regions of the $\{m_X, g_X\}$ parameter space that result in excess events over the 95% C.L. upper limit of the number of observed events in each experiment. Using this framework, we derive constraints from Orsay [286], KEK [287], NA64 [288, 289], E137 [283], E141 [290], and E774 [291].

In proton beam dumps, X can be produced either via bremsstrahlung or through the decays of mesons (π^0, η, η') produced in the target. The bremsstrahlung process is analogous to the electron beam dump case, with the effective cross section for proton collision determined experimentally [292]. Constraints on a dark photon have been derived in [293–295] on U70 [296], NOMAD [297], PS191 [298], CHARM [299], LSND [39], νCal [299], and FASER [91, 92]. In our analysis, we recast these dark photon constraints to our model using Eq. (2.30) and the methodology developed in [42]. The same procedure is applied to fixed target experiments: APEX [300], A1/MAMI [301, 302], HPS [303, 304], and NA48/2 [305]. These experiments probe $m_X < 1$ GeV and rely on $X \to e^+e^-$ decay as their signal channel. In this mass range, the RGE induced electron charge in the chargephobic limit is at most $x_e \sim \mathcal{O}(10^{-3})$, so both the bremsstrahlung production channel and e^+e^- decay are suppressed by

x_e^2. As a result, the expected event yields in the chargephobic case are negligible and so the constraints vanish.

For the projected SHiP sensitivity, we recast the dark photon reach from Ref. [281] using the LHCb production fractions [42]. In the chargephobic case, the charged lepton decays are negligible and the SHiP sensitivity is effectively determined by the hadronic modes. Therefore, we find that SHiP gains sensitivity starting at $m_X \simeq 2m_\pi$, where the $X \to \pi^+\pi^-$ channel becomes kinematically accessible. For larger masses, multi-pion and kaon final states also contribute to detection signal, see Fig. 8. Above the pion threshold, a dominant fraction of the production and detection channels remains unsuppressed, so SHiP retains substantial reach in the chargephobic limit. Thus, SHiP is a uniquely powerful probe of the chargephobic case, complementing the CEνNS constraints and providing outstanding opportunities for future discovery.

As a final remark, recent studies of neutron initiated production at FASER/FASER2 show that a "neutron beam dump" can enhance sensitivity to the protophobic model [279, 306]. These results still rely on $X \to \ell^+\ell^-$ decays for detection and as such do not set constraints on the chargephobic model.

2.5.5 Collider Experiments. In this section, we summarize the constraints obtained from collider searches at LHCb [307], CMS [107], KLOE [93,308–310], BESIII [311], and BaBar [312]. We recast these bounds to our general φ model using Eq. (2.30), following the production, decay, and experimental efficiency rescaling procedures outlined in [42]. Note that there are projections Refs. [313, 314] (and other possible constraints [315]) for the improvements in the sensitivity to the dark photon by the LHCb experiment. However, we do not anticipate the large improvements in the dark photon parameter space $m_{A'} \lesssim 500$ MeV to extend to the

chargephobic vector boson case given the very small branching fraction to charged leptons.

The LHCb dark photon search [307] considers both prompt and displaced $X \longrightarrow \mu^+\mu^-$ decays in pp collisions at 13 TeV using 1.6 fb^{-1} of data. Because the analysis relies on the dimuon final state, the constraint weakens considerably on the chargephobic case. The constraint does not vanish, however, due to the loop induced charged lepton coupling $x_e \sim \mathcal{O}(10^{-2})$ at larger masses $m_X \gtrsim 1$ GeV that is generated by the RGE running as described in App. B. The relevant production modes include meson decays ($\eta \to X\gamma$, $\omega \to X\pi^0$), vector meson mixing ($\omega \to X$, $\rho \to X$, $\phi \to X$), and Drell–Yan ($q\bar{q} \to X$). The dominant production modes vary across the m_X mass range. Consequently, each φ value can suppress/remove some but not all production mechanisms. For $m_X \lesssim 0.4$ GeV and $m_X \gtrsim 1$ GeV, the leading channels are $\eta \to X\gamma$ ($\sim 65\%$) and $u\bar{u} \to X$ ($\sim 70\%$) which are suppressed/vanish at $\varphi = \pi - \tan^{-1} 2$. In the intermediate region $0.4 - 0.9$ GeV, the leading channels are $\omega \to X\pi^0$ ($\sim 45\%$) and $\rho \to X$ mixing ($\sim 65\%$) both of which vanish for the $B - L$ case. A similar analysis is applied to the CMS constraint [107].

The KLOE experiment conducted several searches for dark photon using data taken at DAΦNE with $\sqrt{s} \simeq 1020\,\text{MeV}$ [93, 308–310]. These analyses considered the process $e^+e^- \longrightarrow \gamma X$ with $X \longrightarrow e^+e^-$, $X \longrightarrow \mu^+\mu^-$, and $X \longrightarrow \pi^+\pi^-$, as well as the decay chain $\phi \longrightarrow X\eta$ with $X \longrightarrow e^+e^-$. In both cases, constraints on the chargephobic parameter space are highly suppressed due to the x_e^2 suppression on the production and/or the decay.

Finally, the BaBar dark photon search [312] considered the process $e^+e^- \longrightarrow \gamma X$ with $X \longrightarrow e^+e^-$ and $X \longrightarrow \mu^+\mu^-$ primarily at the $\Upsilon(4S)$ but also at $\Upsilon(3S)$ & $\Upsilon(2S)$ resonances. The reported constraint spans 0.02 GeV $< m_X <$ 10.2 GeV and has a

sensitivity scaling as x_e^4 since both the production and decay proceed through electron coupling. Consequently, the bound vanishes for the chargephobic case even after including small RGE induced couplings. A similar suppression applies to BESIII [311].

2.5.6 Precision Constraints. Precision measurements of SM observables provide powerful probes of new light vectors, since even weak couplings can shift well measured quantities away from their SM predictions. In this section, we discuss the constraints set from the electron/muon anomalous magnetic moments and electroweak precision tests. We also comment on the sensitivity of the proposed REDTOP experiment [316].

We first consider the one-loop contribution of X to the anomalous magnetic moments $(g-2)_\ell$ of the electron and muon, a_ℓ^X, computed following Ref. [317]. The $(g-2)_e$ constraint is set such that the effective shift of the fine structure constant, $\Delta\alpha = 2\pi a_e^X$, does not exceed 1 ppb in line with the current $\mathcal{O}(1\,\text{ppb})$ spread among the most precise determinations of α [318–320]; previous constraints were set at 15 ppb [317] based on older α determinations including Ref. [321]. For the $(g-2)_\mu$, we use the updated SM prediction and final world average measurement of a_μ [322] and require $a_\mu^X < (a_\mu^{\text{exp}} - a_\mu^{\text{SM}} + 2\sigma)$ where σ is the quoted uncertainty on this difference. These constraints are relevant in the dark photon case where they cover the region of parameter space where collider constraints are not sensitive due to masking out meson resonances. For other φ, these constraints become subdominant to NES and CEνNS constraints. In particular, in chargephobic case, the absence of couplings to charged leptons when $m_X \lesssim 200$ MeV combined with the very small renormalization

group induced couplings above this scale imply that both $(g-2)_{e,\mu}$ are negligible throughout the parameter space.

At low energies, X couples to the electromagnetic current, while at electroweak scales, this becomes a coupling to the hypercharge current. This causes a mass mixing between X and the Z boson. This mixing shifts the physical Z mass and its couplings to fermions, leading to constraints from electroweak precision observables. For a dark photon, constraints were derived in Refs. [323–325] by performing global fits to LEP, SLC, Tevatron, and LHC electroweak precision data. In our analysis, we adopt the 95% C.L. exclusion curve based on the PDG world average value of m_W (solid blue curve in Fig. 1 of Ref. [325]) in the dark photon limit and recast this constraint for arbitrary φ using the relation $\epsilon e = g_X \cos\varphi$. We show this constraint, labeled EWP, in Figs. 3-4.

Finally, REDTOP is a proposed high-intensity η/η' factory that aims to collect a data sample of order 10^{14} η and 10^{12} η' mesons to study very rare decays and to search for BSM physics in the MeV-GeV range [316, 326]. In our case, X can be produced at REDTOP via $\eta, \eta' \to \gamma X$ and the detector is sensitive to the following subsequent decays $X \to e^+e^-$, $X \to \mu^+\mu^-$, and $X \to \pi^+\pi^-$. In particular, the hadronic channel $X \to \pi^+\pi^-$ remains open in the chargephobic limit. In Fig. 4, we show the recasted projected REDTOP sensitivity with 10^{18} protons on target (solid black in Fig. 39 of Ref. [327]).

2.6 Discussion

There is a huge effort exploring the space of possibilities for light vector boson mediators. In this paper, we have demonstrated that when a vector boson X^μ couples to a specific "chargephobic" linear combination of the electromagnetic and $B-L$ currents, there are dramatic changes to the constraints within the $\{m_X, g_X\}$

parameter space. The changes arise because a chargephobic vector boson does not have (tree-level) couplings to electrons and protons. The resulting sensitivity of most beam dump and collider based experiments is negligible or highly suppressed because they rely on production from proton or electron beams and/or they rely on the decays to leptons that produce an easily visible signal. Two classes of constraints on X^μ remain largely unaffected when the couplings to charged leptons and singly-charged baryons are absent: supernova cooling constraints and the constraints on the contributions to $\Delta N_{\rm eff}$ in the early universe, due to the nonzero couplings to neutrinos and neutrons.

It is interesting to compare the constraints on the chargephobic case to those on other combinations of currents that are also more weakly constrained. Two specific examples are: $B-3L_\tau$ and baryon number by itself. A vector boson coupled to $B-3L_\tau$ also has highly suppressed constraints (e.g. [40,80]) from beam dump experiments and collider experiments due to the absence of interactions with the first two generations of charged leptons. Moreover, because $B-3L_\tau$ does not couple to electron or muon neutrinos, it is also unconstrained by COHERENT experiment results on neutrino-nucleus scattering. However, as emphasized in Refs. [80, 83] $B-3L_\tau$ is strongly constrained by the neutrino flavor-dependent non-standard interactions (NSI) that affect neutrino oscillations. These turn out to be stronger than the constraints from COHERENT neutrino-nucleus scattering, and so for much of the parameter space we find that the chargephobic limit is *more weakly constrained* than $B-3L_\tau$.

A vector boson coupled to just baryon number is problematic, because baryon number is a non-conserved (anomalous) current in the SM. Refs. [29,31] examined this case in detail, finding that rare meson decay mediated by the anomalous interaction set several constraints on the parameter space that lead to constraints that are

more restrictive than those on the chargephobic case for $m_X \lesssim 200$ MeV and 600 MeV $\lesssim m_X \lesssim 4$ GeV. In other ranges the two cases are similar, and for larger m_X, chargephobic is more constrained due to LHCb searches that are (re-)activated due to the small renormalization group-generated couplings to the charged leptons (see App. B) as well as from electroweak precision constraints.

Several open questions remain: one is the prospects for gaining *improved* sensitivity to the chargephobic case. In Fig. 4 we present a rough guide to the increased sensitivities for a handful of experiments, but there are no doubt more possibilities that are worth exploring. One of our primary goals in the paper is to point out that relying on a charged lepton decay of a light gauge boson can be disastrous for an experiment's sensitivity. SHiP [275, 277, 281] will be able to probe new regions of the chargephobic parameter space due to the significantly improved detector capabilities that enable it to be sensitive to the hadronic decays of X when $m_X \gtrsim 300$ MeV. Also, the proposed REDTOP experiment [316] can gain sensitivity to chargephobic couplings due to rare decays of η, η' mesons to vector bosons.

There are also detailed questions one can ask regarding whether there are additional production or decay modes that experiments could be sensitive to. The production of vector bosons in beam dump experiments occurs through bremsstrahlung "coherently" off the proton beam. However, one might expect there is also a rate for incoherent contribution (emission from the quarks)[14], that is either form-factor suppressed or suppressed by the degree of inelastic scattering. We also have seen that there are improved constraints on both the chargephobic case and $B - L$ by considering the absence of high energy neutrino events from SN1987A, as was found for the case of $L_\mu - L_\tau$ [182].

[14]We thank Ryan Plestid for pointing this out to us.

It is also worth commenting on the very interesting ensemble of bounds on a dark photon arising from its production in supernovae and decay into e^+e^-, leading to significant observable signals [45]. Most of these constraints do not apply to the chargephobic vector boson because of the dominance of the decay $X \to \nu\bar{\nu}$ throughout the mass range that these constraints apply. One needs to be a bit more careful with the low energy supernova constraint (LESNe), since for the dark photon case this extends to $m_{A'} \sim$ 500 MeV. A chargephobic vector boson with mass $m_X > 2m_\pi$ has an increasing branching fraction to $\pi^+\pi^-$ (few to 20%), that may or may not affect the low energy supernova dynamics. It would be interesting to determine if a small region of chargephobic parameter space could be constrained, though it requires the convolution of X decay and π decay to lead to enough energy deposition to disrupt the supernova explosions. This is an interesting question, but beyond the scope of our work.

Finally, while we have focused much of the paper on the specific case of chargephobic, $\varphi = 3\pi/4$, our analysis pipeline allows us to consider any angle. As we have pointed out in the paper, some angles have suppressed rates for specific processes where mixing with a particular QCD vector resonance does not occur. We have also pointed out the "nucleophobic" (a related idea to "xenophobic" in Ref. [90]) case where $\varphi = \pi - \tan^{-1}(Z_\mathcal{N}/A_\mathcal{N})$, and the coherent interaction of the vector boson with the nucleus vanishes for a specific isotope. Our interest in this particular case was to explore how much weaker the constraints from COHERENT and other neutrino-nucleus scattering experiments can be. Of course when we consider mixing angle away from the chargephobic limit, constraints from neutrino-electron scattering reappear, as well the ensemble of beam dump and collider experiments, as we show in Fig. 15 (right). Nevertheless, there could be a host of interesting phenomenology when a

nucleophobic gauge boson is fused with a model of dark matter – there could be an interesting parameter space where dark matter - electron scattering experiments could have sensitivity in regions of parameter space what would otherwise have been considered ruled out by nuclear recoil (or Migdal) scattering.

Acknowledgments

We thank Hans-Thomas Janka and Daniel Kresse for providing access to the Garching supernova model data used in this analysis. We thank Andrea Caputo, Ryan Plestid, and Yotam Soreq for helpful discussions and are grateful to Andrea Caputo, Pierre Fayet, Damiano Fiorillo and Edoardo Vitagliano for insightful comments on an earlier version of the paper. This work is supported in part by the U.S. Department of Energy under grant number DE-SC0011640.

CHAPTER III

COSMOLOGICAL IMPLICATIONS OF GAUGED $U(1)_{B-L}$ ON $\Delta N_{\rm EFF}$ IN THE CMB AND BBN

This work was published in the Journal of Cosmology and Astroparticle Physics at JCAP 05 (2024) 110 and was carried out in collaboration with Graham Kribs. It was modified to fit into the format of a chapter for this dissertation.

3.1 Introduction

Light mediators – new massive, unstable particles that couple to the SM – have seen tremendous interest over the past decade (for reviews, see [19, 20]). They are essential to models of light dark matter [317, 328, 329], providing mechanisms that lead to the correct abundance as well as providing detectable signals in the myriad landscape of light dark matter detection experiments. A panoply of experiments have been considered to gain sensitivity to these mediators.

Specializing to light $U(1)$ vector boson mediators, several varieties have been considered: the dark photon (for a recent review, see [43]); $U(1)_{B-L}$ (early discussions include [46–49] and a review of massive Z's [63]), while gauged $U(1)_{B-L}$ as a light mediator has been considered in detail in [39, 42, 50, 51]; $U(1)_B$ [21, 26, 330]; and flavor-dependent $U(1)$s such as $U(1)_{\mu-\tau}$ [64, 65, 331] (some recent work [81, 89]). A huge variety of constraints restrict the parameter space of these light vector bosons [39,42,50,51,332] including colliders, fixed target experiments, energy loss from stars; energy loss from supernovae, changes to big-bang nucleosynthesis; etc.

Our focus in this paper is to calculate the contributions to the effective number of relativistic species, $N_{\rm eff}$, from a light $U(1)_{B-L}$ gauge boson mediator X, determining both the existing constraints and prospects for future CMB observatories. Precision

determination of $N_{\rm eff}$, from CMB power spectra [15, 16] and primordial element abundances [108–111] is in strong agreement with SM prediction [112–126]. This makes $N_{\rm eff}$ a powerful tool in testing BSM physics that affects early universe cosmology before recombination [81, 127–150]. We carry out the full Boltzmann evolution, allowing the X boson to "freeze in" [151], become nonrelativistic, redshift as matter, and then decay back into SM states, modifying $\Delta N_{\rm eff}$. Earlier calculations have considered the contributions to $\Delta N_{\rm eff}$ from the freeze in of a dark photon [143] and $U(1)_{\mu-\tau}$ [81]. The cosmological constraints from $\Delta N_{\rm eff}$ on the dark photon are relatively strong when the dark photon mass is near the temperature of BBN, $\sim$ 1 MeV, when the dark photon can interact with the electron plasma and thus (indirectly) affect the neutrino energy density, but weaker below this since the dark photon does not interact with neutrinos. By contrast, mediators that freeze in from their interactions with neutrinos have substantially stronger constraints, e.g., $U(1)_{\mu-\tau}$ [81]. In this paper, we utilize the formalism and approximations outlined in [81, 141, 144], extended and applied to the case of a $U(1)_{B-L}$ gauge boson.

The central observation is that an out-of-equilibrium abundance of new particles that interact with the SM can be well approximated by using *equilibrium* distributions with nonzero chemical potentials. We will discuss the formalism and approximations in detail, as applied to $U(1)_{B-L}$. The result is that since $U(1)_{B-L}$ has a nonzero coupling to neutrinos, there are strong bounds from $\Delta N_{\rm eff}$ from the CMB that get *stronger* with *decreasing* mass of X, down to of order $m_X \sim 1$ eV. In the regime $m_X < 2m_e$, our results are qualitatively consistent with a similar analysis done for $U(1)_{\mu-\tau}$ [81]. At even smaller masses, $m_X \lesssim 1$ eV, fifth force constraints [333–336] become very strong and dominate the bounds [50]. For gauge boson masses near

(and below) 1 eV, a more sophisticated treatment of the CMB is necessary to fully elucidate cosmological bounds. We will comment on this in the Discussion.

To our knowledge, the first paper that considered constraints on the mass and coupling of a light $U(1)_{B-L}$ gauge boson from its effects on $\Delta N_{\rm eff}$ is [57]. They considered a light $U(1)_{B-L}$ gauge boson with just left-handed neutrinos among the fermionic relativistic degrees of freedom. The critical difference between our study and [57] is that the latter only considered the constraints from $\Delta N_{\rm eff}$ from BBN, using simple thermalization scaling arguments. Ref. [57] found that for $m_X \gtrsim 10$ MeV, requiring the scattering process $e^- \nu \to e^- \nu$ through off-shell X exchange is not larger than the weak interaction sets a constraint. We verify this constraint also applies to $\Delta N_{\rm eff}$ measured by the CMB, using our Boltzmann equation evolution. Ref. [57] also considered $m_X < 10$ MeV. In this region, [57] required only that $X \leftrightarrow \nu\bar{\nu}$ did not reach thermal equilibrium at $T \sim 1$ MeV, so that X does not contribute excessively to $\Delta N_{\rm eff}$ during BBN. As we will see, we find much stronger constraints in the region $m_X < 10$ MeV from detailed numerical calculations of $\Delta N_{\rm eff}$ at the CMB era as well as strong constraints on the helium mass fraction Y_p, at the BBN era.

There are also constraints on *very* weakly coupled mediators that are completely out-of-equilibrium, but decay on timescales that can disrupt BBN [337–339] or to cause spectral distortion in the CMB [135, 145, 340]. We show these constraints on the parameter space of $U(1)_{B-L}$, obtained from [145], that are complementary to our results.

3.2 Gauged U(1)$_{B-L}$: Majorana and Dirac neutrino cases

$U(1)_{B-L}$ is among the most interesting possible new forces since it is the only flavor-universal global symmetry of the SM that is gaugeable. All mixed $U(1)_{B-L} \times \mathrm{SM}^2$ anomalies automatically vanish within the SM. The $[U(1)_{B-L}]^3$

anomaly remains, requiring additional chiral fermions that transform under just $U(1)_{B-L}$. The simplest solution is to add one chiral fermion per generation with lepton number equal and opposite to ν_L, namely, one right-handed neutrino per generation.

To establish notation, gauged $U(1)_{B-L}$ is mediated by a vector boson X^μ that interacts with the SM quarks and leptons with charge

$$q_f = (B-L)_f = \begin{cases} +1/3 & Q_L,\ u_R,\ d_R \\ -1 & L,\ e_R,\ \nu_R \end{cases} , \tag{3.1}$$

where we have written the fermions in four-component notation consistent with [341]. We assume $U(1)_{B-L}$ is broken, and so X acquires a mass m_X. The spontaneous breaking of $U(1)_{B-L}$ can be accomplished by introducing a complex scalar, ϕ_X, transforming under $B-L$ with charge q_X, and gauge coupling g_X, with a potential engineered to spontaneously break the symmetry. The scalar Lagrangian is

$$\mathcal{L} \ = \ (D_\mu \phi_X)^\dagger D^\mu \phi_X - V(\phi_X) \tag{3.2}$$

where $D^\mu \equiv \partial^\mu - i g_X q_X X^\mu$, with

$$V(\phi_X) \ = \ \lambda_X \left(\phi_X^\dagger \phi_X - \frac{v_X^2}{2} \right)^2 \tag{3.3}$$

and the minimum of the scalar potential occurs at $\langle \phi_X \rangle = v_X/\sqrt{2}$. Expanding around the minimum, with $\phi_X = (h_X + v_X)/\sqrt{2}$, where h_X is the $B-L$ Higgs boson, the physical states in the theory have masses

$$X^\mu : \qquad m_X \ = \ g_X q_X v_X \tag{3.4}$$

$$h_X : \qquad m_{h_X}^2 \ = \ 2\lambda_X v_X^2 \ . \tag{3.5}$$

Throughout the paper, we work in the limit $g_X q_X \ll \lambda_X$, and so, $m_X \ll m_{h_X}$. Consequently, we will not need to consider the h_X participating in the degrees of freedom in the thermal bath for $\Delta N_{\rm eff}$ calculations. The ability to adjust the $B-L$ charge of ϕ_X implies m_X can be made arbitrarily small relative to $g_X v_X$. That is,

from the perspective of the gauge and Higgs sector, one can independently adjust m_X and g_X (as well as m_{h_X}, through λ_X).

3.2.1 Neutrino masses: Majorana and Dirac cases. We do need to address neutrino masses. Given that $U(1)_{B-L}$ is gauged, the usual dimension-5 Weinberg operator for Majorana neutrino masses, $(LH)^2/\Lambda$, is forbidden. Instead, Yukawa couplings of left-handed and right-handed neutrinos are permitted,

$$y_D^{ij} \bar{L}_i H^\dagger \nu_{R,j} + h.c.\,, \tag{3.6}$$

giving neutrinos Dirac masses that preserve $U(1)_{B-L}$. This "**Dirac case**" is one of the two cases we will consider in this paper. In the Dirac case, since neutrinos acquire their mass from Yukawa couplings to the SM Higgs field, there is (still) no restriction on the ability to adjust m_X and g_X independently.

The alternative, "**Majorana case**", is one where the right-handed neutrinos that are required to cancel the $[U(1)_{B-L}]^3$ anomaly acquire Majorana masses after $U(1)_{B-L}$ is spontaneously broken. When combined with the Dirac mass terms, equation (3.6), after electroweak symmetry is broken, this leads to the usual see-saw formula that results in left-handed neutrinos acquiring small Majorana masses. Right-handed neutrinos can acquire mass with just one Higgs field transforming under $U(1)_{B-L}$ if the $B-L$ charge is fixed to be $q_X = \pm 2$, such that Yukawa-like interactions are permitted,

$$\frac{y_M^{ij}}{2} \nu_{R,i}^c \nu_{R,j}^c \phi_X^{(\dagger)} + h.c.\,, \tag{3.7}$$

where $\nu_{R,i}^c$ are the right-handed neutrinos written with 2-component left-handed fermion notation (in order to avoid Majorana notation). In this scenario, the vev of ϕ_X not only gives mass to the gauge boson, but it also gives Majorana masses to the right-handed neutrinos, $M_R \sim y_M v_X$.

For us, the key distinction is that in the Majorana case, the right-handed neutrinos can be much heavier, and thus not contribute in any way to $\Delta N_{\rm eff}$. This is in contrast to the Dirac scenario, where if the right-handed neutrinos were ever in equilibrium (through, for example, X^μ exchange), they necessarily contribute to $\Delta N_{\rm eff}$ [142, 146, 342]. The size of the contribution to $\Delta N_{\rm eff}$ is controlled just by the dilution of the number of relativistic degrees of freedom after heavier SM fields annihilate (or decay) and dump their entropy into the photon bath.

It is interesting to consider the bounds on the Majorana masses for right-handed neutrinos from cosmology. Obviously if the right-handed neutrinos were in thermal equilibrium with the SM, they would excessively contribute to $\Delta N_{\rm eff}$ during BBN and CMB if their mass were less than approximately 10 MeV. Thermal equilibrium is naturally achieved through X^μ exchange, so long as g_X is not excessively small. (We'll quantify this in detail later in the paper.) Once the right-handed neutrinos are heavier than about 10 MeV, their abundance would be at least somewhat suppressed as they become nonrelativistic once the temperature of the Universe drops well below their mass.

Even if right-handed neutrinos decoupled early in the Universe, they can and will decay to left-handed neutrinos and a (possibly off-shell) Higgs boson, with a significant suppression in the rate due to the smallness of the (Dirac) Yukawa coupling of the right-handed neutrinos to the left-handed neutrinos. In appendix D, we estimate the rate, and find that for $M_R \gtrsim 20$ GeV, the right-handed neutrinos decay before the onset of BBN.

Finally, it is also instructive to consider the case where $U(1)_{B-L}$ is explicitly broken without any scalar sector, i.e., a Stückelberg mass for the X vector field (for a recent detailed discussion of the Stückelberg mechanism, see [86]). In the

Dirac scenario, we can stop there, since Dirac masses respect $U(1)_{B-L}$ (see also [51]). (This is equivalent, in the spontaneously broken theory, to holding $m_X = q_X g_X v_X$ fixed, λ_X fixed, but then taking $q_X \ll 1$ while v_X is taken large. This limit permits any (perturbative) value for g_X.) In the Majorana case, we must also explicitly break $U(1)_{B-L}$ by 2 units when writing explicit Majorana masses $(M_R)_{ij}\nu_i^c\nu_j^c + h.c.$. The explicit breaking implies the $[U(1)_{B-L}]^3$ anomaly will appear below the scale M_R. Thus, the right-handed neutrinos induce a 3-loop anomalous contribution to the mass of the (Stückelberg) X^μ vector field. The size of this contribution is easily estimated [343, 344]

$$\Delta m_X \simeq \frac{g_X^3 M_R}{64\pi^3} \tag{3.8}$$

which implies a lower bound on the mass of X^μ that decreases rapidly as g_X is lowered. This bound is always weaker than equation (D.4), so that if we require right-handed neutrinos decay before BBN, there is no further constraint. Only if M_R were large, such as a traditional see-saw mechanism with $y_D \sim 1$, with $M_R \sim 10^{14-15}$ GeV, would there be any constraint at all on g_X, though even then this constraint is quite mild.

3.3 Effective number of relativistic species: $N_{\mathbf{eff}}$

In standard cosmology at temperature $T \sim 10$ MeV [345], electrons, photons, and neutrinos were in thermal equilibrium. As the universe cooled, the weak interaction rate dropped below the Hubble expansion rate and neutrinos decoupled from the electromagnetic plasma around $T \sim 2$ MeV. As the universe continued to cool, the temperature dropped below the electron mass, e^+e^- annihilation depleted the vast majority of charged leptons. In the limit of instantaneous neutrino decoupling, the electron-positron entropy was transferred solely to photons resulting in a temperature ratio of $T_\gamma/T_\nu = (11/4)^{1/3} \approx 1.401$ after annihilation completed. However, the weak interaction remained slightly active during e^+e^- annihilation, resulting in a small but

appreciable heating of neutrinos. This gives rise to a small increase to the energy density of neutrinos, conventionally defined by the *effective number of relativistic species*,

$$N_{\rm eff} \;=\; \frac{8}{7}\left(\frac{11}{4}\right)^{4/3}\left(\frac{\rho_{\rm rad}-\rho_\gamma}{\rho_\gamma}\right), \tag{3.9}$$

which is the ratio of non-photon to photon radiation density. Any new BSM radiation density present well before recombination can be treated as an additional contribution to $N_{\rm eff}$. The normalization in equation (3.9) is chosen such that $N_{\rm eff} = N_\nu = 3$ in the instantaneous neutrino decoupling limit.

The state-of-the-art calculation in the SM gives $N_{\rm eff}^{\rm SM} = 3.045$-$3.046$, that takes into higher order corrections, non-thermal neutrino distribution functions, neutrino oscillations, etc. [112, 113]. In this paper, we have followed Refs. [141, 144] that have provided an efficient calculation of $N_{\rm eff}$ which employs certain approximations that nevertheless result in excellent accuracy, which we will discuss in detail in section 3.4.1. For instance, using this method, we obtain the photon-to-neutrino temperature ratio, the neutrino chemical potential, and $N_{\rm eff}$ in the SM

$$T_\gamma/T_\nu = 1.3945\,, \qquad \mu_\nu/T_\nu = -4.82\times10^{-3}\,, \qquad N_{\rm eff}^{\rm SM} = 3.042\,. \tag{3.10}$$

The point of re-doing the SM calculation here is to demonstrate that we can achieve reasonable accuracy of $N_{\rm eff}$ even with the approximations that have been employed. The very small $\sim 0.1\%$ discrepancy between our calculation and the precise determination is slightly accidental – some of the effects we have neglected, that contribute at a level of $\sim 0.3\%$, happen to very nearly cancel out when summed together (see [144] for details). In any case, our calculation is able to reproduce the non-instantaneous decoupling of neutrinos in the SM to an accuracy of order $\Delta N_{\rm eff} \sim 0.01$.

After e^+e^- annihilation is complete, the number of relativistic degrees of freedom remains the same in the SM down to the CMB era.[1] In the presence of physics beyond the SM, there can be new degrees of freedom that appear (or disappear) before or after BBN. This can be characterized by the number of relativistic degrees of freedom at CMB, $N_{\rm eff}^{\rm CMB}$, to be distinguished from the number of relativistic degrees of freedom at BBN, $N_{\rm eff}^{\rm BBN}$. In this paper, $N_{\rm eff}$ refers exclusively to $N_{\rm eff}^{\rm CMB}$, and hereafter $N_{\rm eff}$ and $\Delta N_{\rm eff}$ refer to the quantities at the CMB era. We do, however, calculate the shift to the helium mass fraction Y_p at BBN, separately from $\Delta N_{\rm eff}$. We will present our calculations of $N_{\rm eff}$ in section 3.5 and Y_p in section 3.7, and compare to the observational determinations at the end of each of those sections.

3.4 Early universe thermodynamics

Our method to calculate thermodynamic quantities in the early universe utilizes several approximations in order to solve the Boltzmann equations that were described in detail in [141,144].[2] The key insight from [141,144] is that we can approximate the effects of out-of-equilibrium ("freeze-in") X bosons using *equilibrium* distributions with nonzero chemical potentials. How this works requires some explanation. At temperatures near BBN, the dominant contributions to the energy density are from electrons (and positions), photons, and neutrinos. In the SM, the annihilation and scattering rates between electrons, positions, and photons is very efficient ensuring $T_\gamma = T_e$. Since photon number is not conserved, the processes $e^+e^- \leftrightarrow \gamma$, $e^+e^- \leftrightarrow \gamma\gamma$, and $e^+e^- \leftrightarrow \gamma\gamma\gamma$ imply that the chemical potential for photons, electrons and positions vanishes, $\mu_\gamma = \mu_e = 0$ (to a very good approximation [346]). When neutrino-

[1] We do not need to consider SM neutrino masses, since they are bounded to be smaller than the temperatures we consider in the paper [16].

[2] We have benefited from viewing the code NUDEC_BSM as a reference to setup our calculations. However, all of our calculations are based on our own code.

electron scattering is active for temperatures $T \gtrsim 2$ MeV, the processes $e^+e^- \leftrightarrow \bar{\nu}_\alpha \nu_\alpha$, $e^\pm \nu_\alpha \leftrightarrow e^\pm \nu_\alpha$, and $e^\pm \bar{\nu}_\alpha \leftrightarrow e^\pm \bar{\nu}_\alpha$ ensure that $\mu_\nu \simeq 0$. Hence, in the SM, chemical potentials do not play a critical role in determining the thermodynamic evolution near and below the BBN era.

When we introduce a light $U(1)_{B-L}$ gauge boson X, there are three possible regimes of interest: heavy ($m_X \gg 1$ MeV), intermediate ($m_X \sim 1$ MeV), and light ($m_X \ll 1$ MeV). In all regimes, we assume $\mu_\gamma = \mu_e = 0$ throughout the Boltzmann evolution, given that the electromagnetic interactions will always be much faster than interactions among X bosons. Nevertheless, we allow for chemical potentials for X and neutrinos to develop and evolve with temperature, as X freezes-in through its very weak interactions with the SM. As we will see, the thermodynamic evolution of the SM particles plus X will be quite different in these different regimes.

In the heavy regime, $m_X \gg 1$ MeV, as the temperature drops below m_X, the X bosons become nonrelativistic while the weak interactions that keep electrons and neutrinos in thermal and chemical equilibrium remain active. At these high temperatures, there is competition between $1 \leftrightarrow 2$ processes involving $X \leftrightarrow \nu\bar{\nu}$, that will cause μ_X and μ_ν to develop, and the electroweak-mediated $2 \leftrightarrow 2$ processes, that drive $\mu_\nu \to 0$. Initially, X is out-of-equilibrium, and so a chemical potential for X and neutrinos can (and will) develop. As the temperatures decrease, X becomes nonrelativistic, the $2 \leftrightarrow 2$ processes dominate, driving μ_ν (and μ_X) to small values. At still larger masses, for temperatures 10 MeV $\lesssim T \ll m_X$, the $1 \leftrightarrow 2$ processes are irrelevant, and instead off-shell X-exchange can contribute to $2 \leftrightarrow 2$ processes qualitatively similar to electroweak gauge boson exchange. Here, there is a constraint on the strength of the X boson interactions with the SM that arises from delaying

neutrino freeze-out, but this is much weaker than the constraints from lighter masses, as we will see below.

In the light regime, when $m_X \ll 1$ MeV, electron-position annihilation is fully complete, leaving only photons, neutrinos, and X as the relativistic degrees of freedom. In this regime, neutrinos are out of thermal and chemical equilibrium with the SM, and thus as X freezes-in, the evolution of Boltzmann equations result in a chemical potential for X and neutrinos through the process is $X \leftrightarrow \nu\bar{\nu}$. If this is efficient enough to reach chemical equilibrium, $\mu_X = 2\mu_\nu$. Note that since $U(1)_{\mathrm{B-L}}$ is flavor-conserving, we necessarily have $\mu_\nu = \mu_{\bar{\nu}}$.

Finally, the intermediate regime, $m_X \sim 1$ MeV, is the trickiest one to model. When $T \sim 1$ MeV, the weak interactions have recently decoupled, and so the $2 \leftrightarrow 2$ electroweak processes that enforce $\mu_\nu \simeq 0$ have just recently shut off. This means that as a chemical potential for μ_X develops from its out-of-equilibrium production, the resulting μ_ν that also develops, can remain. However, electron-photon interactions are in thermal and chemical equilibrium, and so $\mu_e = 0$. If X were to be in thermal equilibrium with both electrons and neutrinos, the electron interactions $X \leftrightarrow e^+e^-$ would bias $\mu_X \simeq 0$. Instead, when X is out-of-equilibrium, a chemical potential for X can develop as X freezes-in from both $e^+e^- \to X$ and $\nu\bar{\nu} \to X$ interactions. As the universe cools, more X is produced, but then e^+e^- annihilation into photons rapidly depletes the electron-positron bath. This means X could reach thermal equilibrium with neutrinos, with a nonzero chemical potential, since the remaining electrons and positions have dropped out of chemical equilibrium.

3.4.1 Approximations. We assume that all fermions and bosons follow Fermi-Dirac (FD, positive) and Bose-Einstein (BE, negative), $f(E) = [e^{(E-\mu)/T} \pm 1]^{-1}$ distribution functions respectively. This assumption is well-established when the

energy and momentum exchange between particles is efficient. If interactions are not fully efficient, i.e. out-of-equilibrium evolution, distributions may obtain spectral distortion corrections. An example of this is shown in figures 9, 10 of [81] for the case of $U(1)_{L_\mu - L_\tau}$. These corrections are expected to be small.

We assume, to an excellent approximation, that the electron/positron plasma is highly thermalized with the photon plasma such that $T_\gamma = T_e$ and $\mu_\gamma = \mu_e = 0$. Here, we leverage the strong annihilation and scattering rate between electrons, positrons, and photons and that the number of photons is not conserved in the early universe. As for neutrinos, we describe a neutrino fluid with a single distribution characterized by $T_\nu \equiv T_{\nu_e} = T_{\nu_\mu} = T_{\nu_\tau}$ and μ_ν. Here, we ignored neutrino oscillations which become active for temperatures $T =$ 3-5 MeV, [347, 348], and model this effect by setting the temperature of the different neutrino species equal. The correction due to neutrino oscillations in SM is $\Delta N_{\rm eff} = 0.0007$ [112]. The correction due to evolving distinct neutrino species temperature rather than a single T_ν was found to be $\Delta N_{\rm eff} = 0.001$ using the approximations [141, 144] we employ in this paper.

For the collision terms we have implemented the correct particle distributions for the $1 \leftrightarrow 2$ collision terms, and approximate particle distributions for $2 \leftrightarrow 2$ collision terms. For the $1 \leftrightarrow 2$ processes, this means we use a Fermi-Dirac distribution for fermions, a Bose-Einstein distribution for bosons, and include Pauli blocking and Bose enhancement. For the $2 \leftrightarrow 2$ processes, we use Maxwell-Boltzmann distributions for all particles, which reduces the number of integrations needed for the collision terms and significantly decreases the numerical computation time. Our implementation of using the correct statistics for the $1 \leftrightarrow 2$ collision processes is motivated by the relative importance of these processes in determining an accurate calculation of $N_{\rm eff}$. While the qualitative features of our results remain unaffected even if Maxwell-Boltzmann

distributions were used for $1 \leftrightarrow 2$ processes, quantitatively we find that the contours of $\Delta N_{\rm eff}$ shift to slightly overestimate the impact of the X boson within the (m_X, g_X) parameter space.

Finally, we have also taken into account finite temperature effects that result from shifts in the masses and self-energies from their vacuum values. In the SM, these finite temperature effects [120, 141, 349] result in an $\mathcal{O}(0.01)$ correction to $N_{\rm eff}$. We have outlined the relevant finite temperature effects in appendix E, where we show that for the case $m_X > 2m_e$, these corrections yield at most $1-2\%$ shift relative to the vacuum evolution, and so we neglect them in this regime. This result is consistent with [350] where finite temperature corrections to the dark photon in early universe were found to be negligible in this mass range. However, for $m_X < 2m_e$, finite temperature corrections become important when the e^+e^- interactions contribute significantly to the X abundance, as discussed in section 3.4.3.3.

3.4.2 Boltzmann equations. The distribution for a particle species f evolves in accordance with the Liouville equation

$$\frac{\partial f}{\partial t} - Hp\frac{\partial f}{\partial p} = \mathcal{C}[f], \tag{3.11}$$

for particle momentum p, Hubble expansion rate $H = \sqrt{8\pi\rho_{\rm tot}/(3M_{\rm Pl}^2)}$, and distribution dependent collision term $\mathcal{C}[f]$. The collision terms account for interactions affecting particle distributions, i.e., decays, annihilations, scattering, and their inverse processes.

With the approximations discussed in section 3.4.1, the Liouville equation in equation (3.11) can be reformulated in terms of the distribution's temperature and

chemical potential,

$$\frac{dT_i}{dt} = \mathbb{D}(T_i,\mu_i)\left[-3H\left((\rho_i+P_i)\frac{\partial n_i}{\partial \mu_i} - n_i\frac{\partial \rho_i}{\partial \mu_i}\right) + \frac{\partial n_i}{\partial \mu_i}\frac{\delta \rho_i}{\delta t} - \frac{\partial \rho_i}{\partial \mu_i}\frac{\delta n_i}{\delta t}\right], \quad (3.12a)$$

$$\frac{d\mu_i}{dt} = -\mathbb{D}(T_i,\mu_i)\left[-3H\left((\rho_i+P_i)\frac{\partial n_i}{\partial T_i} - n_i\frac{\partial \rho_i}{\partial T_i}\right) + \frac{\partial n_i}{\partial T_i}\frac{\delta \rho_i}{\delta t} - \frac{\partial \rho_i}{\partial T_i}\frac{\delta n_i}{\delta t}\right], \quad (3.12b)$$

$$\mathbb{D}(T,\mu) = \left(\frac{\partial n}{\partial \mu}\frac{\partial \rho}{\partial T} - \frac{\partial n}{\partial T}\frac{\partial \rho}{\partial \mu}\right)^{-1}. \quad (3.12c)$$

Here n, ρ, P are the number, energy, and pressure densities for a particle i with d_i degrees of freedom obtained by integrating f over $d_i\, d^3p/(2\pi)^3$, $d_i\, E\, d^3p/(2\pi)^3$, and $d_i\, \frac{p^2}{3E}\, d^3p/(2\pi)^3$ respectively. $\delta n/\delta t$ and $\delta \rho/\delta t$ are the number and energy transfer rates between particle species obtained by integrating $\mathcal{C}[f]$ over the same measures. The formulae for these thermodynamic quantities and their derivatives can be found in appendix A.6 of [144]. Explicitly, the seven Boltzmann equations parameterizing our system are given by

$$\begin{aligned}
\frac{dT_X}{dt} &= \mathbb{D}(T_X,\mu_X)\left[-3H\left((\rho_X+P_X)\frac{\partial n_X}{\partial \mu_X} - n_X\frac{\partial \rho_X}{\partial \mu_X}\right) + \frac{\partial n_X}{\partial \mu_X}\frac{\delta \rho_X}{\delta t} - \frac{\partial \rho_X}{\partial \mu_X}\frac{\delta n_X}{\delta t}\right],\\
\frac{dT_{\nu_R}}{dt} &= \mathbb{D}(T_{\nu_R},\mu_{\nu_R})\left[-3H\left((\rho_{\nu_R}+P_{\nu_R})\frac{\partial n_{\nu_R}}{\partial \mu_{\nu_R}} - n_{\nu_R}\frac{\partial \rho_{\nu_R}}{\partial \mu_{\nu_R}}\right) + \frac{\partial n_{\nu_R}}{\partial \mu_{\nu_R}}\frac{\delta \rho_{\nu_R}}{\delta t} - \frac{\partial \rho_{\nu_R}}{\partial \mu_{\nu_R}}\frac{\delta n_{\nu_R}}{\delta t}\right],\\
\frac{dT_{\nu_L}}{dt} &= \mathbb{D}(T_{\nu_L},\mu_{\nu_L})\left[-3H\left((\rho_{\nu_L}+P_{\nu_L})\frac{\partial n_{\nu_L}}{\partial \mu_{\nu_L}} - n_{\nu_L}\frac{\partial \rho_{\nu_L}}{\partial \mu_{\nu_L}}\right) + \frac{\partial n_{\nu_L}}{\partial \mu_{\nu_L}}\frac{\delta \rho_{\nu_L}}{\delta t} - \frac{\partial \rho_{\nu_L}}{\partial \mu_{\nu_L}}\frac{\delta n_{\nu_L}}{\delta t}\right],\\
\frac{dT_\gamma}{dt} &= \left(\frac{\partial \rho_\gamma}{\partial T_\gamma} + \frac{\partial \rho_e}{\partial T_\gamma}\right)^{-1}\left[4H\rho_\gamma + 3H(\rho_e+P_e) + \frac{\delta \rho_e}{\delta t}\right],\\
\frac{d\mu_X}{dt} &= -\mathbb{D}(T_X,\mu_X)\left[-3H\left((\rho_X+P_X)\frac{\partial n_X}{\partial T_X} - n_X\frac{\partial \rho_X}{\partial T_X}\right) + \frac{\partial n_X}{\partial T_X}\frac{\delta \rho_X}{\delta t} - \frac{\partial \rho_X}{\partial T_X}\frac{\delta n_X}{\delta t}\right],\\
\frac{d\mu_{\nu_R}}{dt} &= -\mathbb{D}(T_{\nu_R},\mu_{\nu_R})\left[-3H\left((\rho_{\nu_R}+P_{\nu_R})\frac{\partial n_{\nu_R}}{\partial T_{\nu_R}} - n_{\nu_R}\frac{\partial \rho_{\nu_R}}{\partial T_{\nu_R}}\right) + \frac{\partial n_{\nu_R}}{\partial T_{\nu_R}}\frac{\delta \rho_{\nu_R}}{\delta t} - \frac{\partial \rho_{\nu_R}}{\partial T_{\nu_R}}\frac{\delta n_{\nu_R}}{\delta t}\right],\\
\frac{d\mu_{\nu_L}}{dt} &= -\mathbb{D}(T_{\nu_L},\mu_{\nu_L})\left[-3H\left((\rho_{\nu_L}+P_{\nu_L})\frac{\partial n_{\nu_L}}{\partial T_{\nu_L}} - n_{\nu_L}\frac{\partial \rho_{\nu_L}}{\partial T_{\nu_L}}\right) + \frac{\partial n_{\nu_L}}{\partial T_{\nu_L}}\frac{\delta \rho_{\nu_L}}{\delta t} - \frac{\partial \rho_{\nu_L}}{\partial T_{\nu_L}}\frac{\delta n_{\nu_L}}{\delta t}\right].
\end{aligned} \quad (3.13)$$

The ν_R equations are included only in the Dirac case. The transfer rates $\delta n_i/\delta t$ and $\delta \rho_i/\delta t$ will be discussed in the next section.

3.4.3 Collision terms.

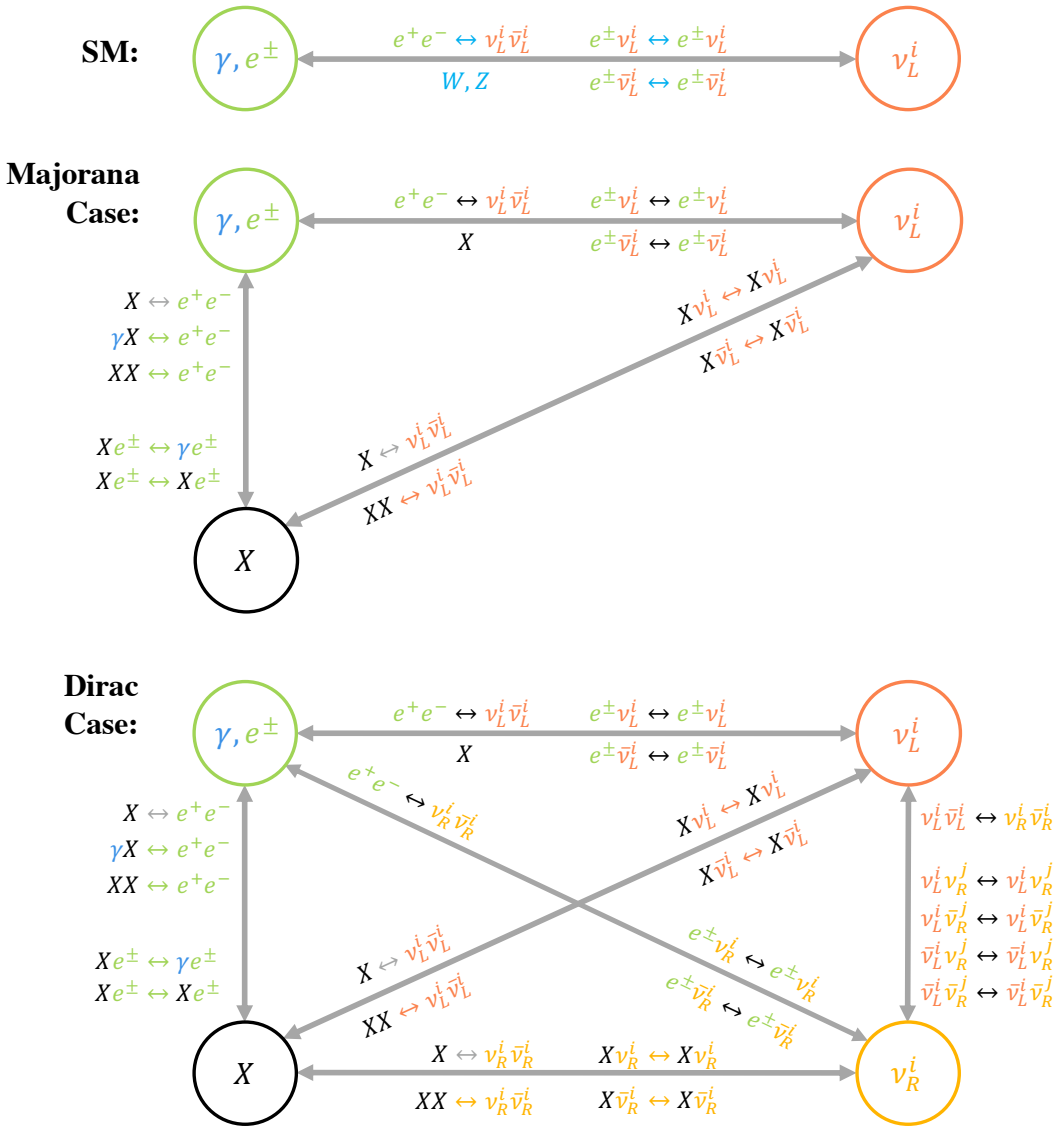


Figure 16. Summary of the processes considered in deriving the collision terms that relate different thermodynamic sectors in our model. All of the $1 \leftrightarrow 2$ processes are renormalizable contact interactions, while the $2 \leftrightarrow 2$ processes include all s,t, and u-channel exchange diagrams that preserve lepton number, electric charge, and flavor. Arrow color implies the mediator (or absence thereof): X (black); W, Z (light blue); ν_L^i (red); ν_R^i (yellow); and $1 \leftrightarrow 2$ contact interaction (grey).

3.4.3.1 Electron-neutrino interactions. In the SM, the relevant interactions between electrons and left-handed neutrinos are the weak interactions $e^+e^- \leftrightarrow \bar{\nu}_\alpha\nu_\alpha$, $e^\pm\nu_\alpha \leftrightarrow e^\pm\nu_\alpha$, and $e^\pm\bar{\nu}_\alpha \leftrightarrow e^\pm\bar{\nu}_\alpha$. The transfer rates for these processes are given by [144]

$$\frac{\delta\rho^{\rm SM}_{e-\nu}}{\delta t} = 2\frac{G_F^2}{3\pi^5}\left[C_V^2 + C_A^2 + 2\left(\tilde{C}_V^2 + \tilde{C}_A^2\right)\right] F_\rho(T_\gamma, T_\nu, \mu_\nu) \tag{3.14a}$$

$$\frac{\delta n^{\rm SM}_{e-\nu}}{\delta t} = 16\frac{G_F^2}{3\pi^5}\left[C_V^2 + C_A^2 + 2\left(\tilde{C}_V^2 + \tilde{C}_A^2\right)\right] F_n(T_\gamma, T_\nu, \mu_\nu)\,. \tag{3.14b}$$

Here we defined

$$F_\rho(T_\gamma, T_\nu, \mu_\nu) = 32\,(T_\gamma^9 - T_\nu^9 e^{\frac{2\mu_\nu}{T_\nu}}) + 56\,T_\gamma^4 T_\nu^4 e^{\frac{\mu_\nu}{T_\nu}}\,(T_\gamma - T_\nu)\,, \tag{3.15a}$$

$$F_n(T_\gamma, T_\nu, \mu_\nu) = T_\gamma^8 - T_\nu^8 e^{\frac{2\mu_\nu}{T_\nu}}\,. \tag{3.15b}$$

with $C_V = g_L^{\nu_e} + g_R^{\nu_e} = \frac{1}{2} + 2s_W^2$, $C_A = g_L^{\nu_e} - g_R^{\nu_e} = \frac{1}{2}$, $\tilde{C}_V = g_L^{\nu_{\mu,\tau}} + g_R^{\nu_{\mu,\tau}} = -\frac{1}{2} + 2s_W^2$, and $\tilde{C}_A = g_L^{\nu_{\mu,\tau}} - g_R^{\nu_{\mu,\tau}} = -\frac{1}{2}$ being the weak vector and axial couplings, $s_W^2 \simeq 0.223$ is the weak mixing angle, and $G_F \simeq 1.16 \times 10^{-11}\,\text{MeV}^{-2}$ is the Fermi constant.

These interactions mediated by weak boson exchange can also be mediated by X-exchange. Since the weak interactions drop out-of-equilibrium near $T \sim 1$ MeV, we are interested in the strength of X-exchange interactions when X can also be integrated out. For $m_X \gtrsim 10$ MeV, we can write the effective interaction Lagrangian

$$\mathcal{L}_{\rm int} \;=\; -\frac{g_X^2}{m_X^2}\left[(\bar{\nu}_L\gamma^\alpha\nu_L + \bar{\nu}_R\gamma^\alpha\nu_R)\right](\bar{e}\gamma_\alpha e)\,. \tag{3.16}$$

The transfer rates now have the same form as equation (3.14) that only differs by the overall coefficient. Given that $\tilde{C}_V$ and $\tilde{C}_A$ correspond to the coefficients for just Z-exchange in the SM, we can obtain the transfer rate for X-exchange by setting $C_V = C_A = 0$ and $2(\tilde{C}_V^2 + \tilde{C}_A^2) \to 3q_X^2$, where X-exchange proceeds through a purely vector interaction with charge $q_X^2 = 1$ for each lepton flavor, and $G_F \to \frac{g_X^2}{2\sqrt{2}m_X^2}$. The

full $e-\nu$ transfer rates are

$$\frac{\delta\rho_{e-\nu}}{\delta t} = \frac{1}{3\pi^5}\left[G_F^2\left(3 - 4\,s_W^2 + 24\,s_W^4\right) + \frac{3}{4}\frac{g_X^4}{m_X^4}\right] F_\rho(T_\gamma, T_\nu, \mu_\nu) \tag{3.17a}$$

$$\frac{\delta n_{e-\nu}}{\delta t} = \frac{8}{3\pi^5}\left[G_F^2\left(3 - 4\,s_W^2 + 24\,s_W^4\right) + \frac{3}{4}\frac{g_X^4}{m_X^4}\right] F_n(T_\gamma, T_\nu, \mu_\nu)\,. \tag{3.17b}$$

The X-exchange interaction can overpower the SM weak process when $g_X^2/m_X^2 \sim \mathcal{O}(G_F) \sim 10^{-11}\,\mathrm{MeV}^{-2}$. In this case, electron-neutrino (proton-neutron) decoupling is delayed to temperatures lower than that predicted in standard cosmology. As an extreme example, if the neutrino decoupling temperature was pushed below the electron-positron annihilation regime, then $T_\nu = T_\gamma$ today [as opposed to $T_\nu \sim (4/11)^{1/3}\,T_\gamma$], which would result in $N_{\rm eff} \simeq 3(11/4)^{4/3} \simeq 11.6$

3.4.3.2 Decays and inverse decays. When kinematically accessible, the dominant BSM processes are $X \leftrightarrow e^+e^-$, $X \leftrightarrow \nu_L\bar{\nu}_L$, and $X \leftrightarrow \nu_R\bar{\nu}_R$. The partial decay widths of X to electron-positron or neutrino pair (left- or right-handed, one generation) is given by

$$\Gamma_{X\to e^+e^-} = \frac{g_X^2}{12\pi} m_X \left(1 + 2\frac{m_e^2}{m_X^2}\right)\sqrt{1 - 4\frac{m_e^2}{m_X^2}} \qquad \Gamma_{X\to\nu_i\bar{\nu}_i} = \frac{g_X^2}{24\pi} m_X. \tag{3.18}$$

In Eq. 3.18, we use the vacuum value for the electron mass since we have verified that the finite temperature corrections shift our results only by a very small (at most 1-2%) amount (see Sec. 3.4.1 for details on our approximations). The collision term for the decay and inverse decay $X \leftrightarrow a\bar{a}$ is

$$\mathcal{C}_{X\to a\bar{a}}(p_X) = -\Gamma_{X\to a\bar{a}}\frac{m_X}{m_*}\frac{m_X}{E_X p_X}\int_{E_-}^{E_+} dE_a\,[f_X(1-f_a)(1-f_a) - f_a f_a(1+f_X)] \tag{3.19}$$

with $E_X^2 = p_X^2 + m_X^2$, $m_*^2 = m_X^2 - 4m_a^2$ and the bounds $E_\pm = \frac{1}{2}[E_X \pm (p_X m_*)/m_X]$. For example in $X \leftrightarrow \nu\bar{\nu}$, the first term in equation (3.19) is explicitly

$$f_X(1-f_a)(1-f_a) \longrightarrow f_X(E_X, T_X, \mu_X)\,[1 - f_\nu(E_\nu, T_\nu, \mu_\nu)]\,[1 - f_\nu(E_X - E_\nu, T_\nu, \mu_\nu)]\,. \tag{3.20}$$

The integral in equation (3.19), can be solved analytically taking a Bose-Einstein distribution for X and a Fermi-Dirac distribution for neutrinos and electrons, giving

$$\mathcal{C}_{X\to a\bar{a}} = -\Gamma_X \frac{m_X}{m_*}\frac{m_X T_a}{E_X p_X}\frac{e^{\frac{E_X}{T_a}+\frac{\mu_X}{T_X}} - e^{\frac{E_X}{T_X}+\frac{2\mu_a}{T_a}}}{\left(e^{\frac{E_X}{T_a}} - e^{\frac{2\mu_a}{T_a}}\right)\left(e^{\frac{E_X}{T_X}} - e^{\frac{\mu_X}{T_X}}\right)} \log\left[\frac{\left(e^{\frac{E_X}{T_a}} + e^{\frac{E_-+\mu_a}{T_a}}\right)\left(e^{\frac{E_+}{T_a}} + e^{\frac{\mu_a}{T_a}}\right)}{\left(e^{\frac{E_X}{T_a}} + e^{\frac{E_++\mu_a}{T_a}}\right)\left(e^{\frac{E_-}{T_a}} + e^{\frac{\mu_a}{T_a}}\right)}\right]. \tag{3.21}$$

Finally, the decay and inverse decay transfer terms are

$$\frac{\delta\rho_{X\leftrightarrow a\bar{a}}}{\delta t} = \frac{d_X}{(2\pi)^3}\int d^3p_X E_X \mathcal{C}_{X\to a\bar{a}}(p_X) \tag{3.22a}$$

$$\frac{\delta n_{X\leftrightarrow a\bar{a}}}{\delta t} = \frac{d_X}{(2\pi)^3}\int d^3p_X\, \mathcal{C}_{X\to a\bar{a}}(p_X) \tag{3.22b}$$

where $d_X = 3$ is the number of spin degrees of freedom of X.

3.4.3.3 Electron-X interactions. When $m_X < 2m_e$, the $X \leftrightarrow e^+e^-$ process is kinematically forbidden, and so the available e-X interactions are $\gamma X \leftrightarrow e^+e^-$ and $e^\pm X \leftrightarrow e^\pm\gamma$. These transfer rates can be derived following appendix A.7 of [144] giving,

$$\frac{\delta\rho_{2\leftrightarrow 2}}{\delta t} = -\frac{d_1 d_2}{64\pi^4}\int_{s_{\min}}^{\infty} ds\; s\,\sigma_{2\leftrightarrow 2}(s)\left[s\,T_\gamma\,K_2\left(\frac{\sqrt{s}}{T_\gamma}\right) - \mathcal{A}(s,T_\gamma,T_X,\mu_X)\right], \tag{3.23a}$$

$$\frac{\delta n_{2\leftrightarrow 2}}{\delta t} = -\frac{d_1 d_2}{64\pi^4}\int_{s_{\min}}^{\infty} ds\; s\,\sigma_{2\leftrightarrow 2}(s)\left[2\sqrt{s}\,T_\gamma\,K_1\left(\frac{\sqrt{s}}{T_\gamma}\right) - \mathcal{B}(s,T_\gamma,T_X,\mu_X)\right], \tag{3.23b}$$

where d_1, d_2 are the number of spin degrees of freedom of incoming particles 1 and 2, and $\sigma_{2\leftrightarrow 2}$ is the cross section of the aforementioned interactions given in appendix C of [350], and

$$\mathcal{A}(s) = e^{\frac{\mu_X}{T_X}}\int dE_+ dE_- \frac{E_+ + E_-}{2}\exp\left[-\frac{E_+ - E_-}{2T_\gamma}\right]\exp\left[-\frac{E_+ + E_-}{2T_X}\right] \tag{3.24a}$$

$$\mathcal{B}(s) = e^{\frac{\mu_X}{T_X}}\int dE_+ dE_- \exp\left[-\frac{E_+ - E_-}{2T_\gamma}\right]\exp\left[-\frac{E_+ + E_-}{2T_X}\right] \tag{3.24b}$$

with $|E_- - E_+(m_2^2 - m_1^2)/s| \le 2p_{12}\sqrt{(E_+^2 - s)/s}$, $p_{12} = [s - (m_1+m_2)^2]^{1/2}[s - (m_1-m_2)^2]^{1/2}/(2\sqrt{s})$, and $E_+ \ge \sqrt{s}$. Part of Eqs. (3.23),(3.24) can be evaluated analytically, while the remainder must be done numerically. To further simply our

evaluation of the phase space integrals in equation (3.24), we have taken $m_X = 0$, thereby slightly overestimating the integration region. In practice, this overestimate is only possibly relevant when $m_X \sim 2m_e$, and in this region, the $2 \to 2$ processes do not set the strongest bounds.

Finite temperature effects make significant corrections to these interactions, as we have explained in detail using analytic arguments presented in appendix E. In our Boltzmann evolution, we include these effects by replacing the vacuum coupling g_X in $\sigma_{2\leftrightarrow 2}$ by the in-medium coupling

$$g_X^2 \longrightarrow g_{X,m}^2 = \frac{g_X^2 m_X^4}{[m_X^2 - m_\gamma(T)^2]^2 + [\mathrm{Im}\,\Pi(T)]^2}, \tag{3.25}$$

where m_γ is the in-medium effective photon mass and $\mathrm{Im}\,\Pi$ is the imaginary part of the photon polarization tensor. This demonstrates that there will be a *resonant enhancement* that occurs when $m_X = m_\gamma(T)$ at a specific temperature T_r for a given m_X. The in medium photon mass $m_\gamma(T)$ is calculated using the formalism in [209] for the real part of the photon polarization tensor. It should be noted that $m_\gamma(T)$ is also dependent on the photon energy, however, this weak dependence does not alter any dynamics and can be neglected. Our numerical evaluation of $m_\gamma(T)$ matches Eq. E.1 in the limits shown, $T \gg m_e$ and $T \ll m_e$. Next, we take $\mathrm{Im}\,\Pi(T) = -\omega\Gamma$ as in Eq. E.7 [211]. We consider only Compton scattering and so $\Gamma = 8\pi\alpha^2/(3m_e^2)n_e$ (for $T \ll m_e$), $\Gamma \sim \alpha^2 T^2/(\pi\omega)\log(4T\omega/m_e^2)$ (for $T \gg m_e$) [350], and then take a linear interpolation between these two limiting expressions. Note that the kink in the $\Delta N_{\mathrm{eff}} = 0.4, 0.5$ contours in figure 20 and $\Delta N_{\mathrm{eff}} = 0.2$ and larger contours in figure 21 around $m_X \sim 50$ keV are a result of this linear interpolation. The contours on either side of the kink are accurate.

3.4.3.4 Suppressed interactions. In Table 16, we have shown several other interactions between X and the SM as well as interactions mediated by (virtual)

X-exchange. We now briefly summarize the suppressions that these interactions have, and why we can neglect them in our evaluation of the Boltzmann evolution.

The interaction $e^+e^- \leftrightarrow XX$ is suppressed by a factor of g_X^2/e^2 compared to $e^+e^- \leftrightarrow \gamma X$. For the neutrino-mediated processes $\nu_L\bar{\nu}_L \leftrightarrow XX$ and $\nu_R\bar{\nu}_R \leftrightarrow XX$, the interaction rate $n_\nu\langle\sigma v\rangle_{\nu_i\bar{\nu}_i\leftrightarrow XX}$ is suppressed by an additional power of g_X^2 as compared to equivalent decay channels $X \leftrightarrow \nu_i\bar{\nu}_i$. Similarly, $Xe^\pm \leftrightarrow Xe^\pm$, $X\nu_L \leftrightarrow X\nu_L$, $X\nu_R \leftrightarrow X\nu_R$ are also suppressed by g_X^2 compared to the (inverse) decay processes, but in addition, also do not contribute to the change in number density of individual particle species. These interactions can be safely neglected.

In the Dirac neutrino case, there are additional processes involving right-handed neutrinos that arise, similar to the ones discussed in section 3.4.3.1. These include $e^+e^- \leftrightarrow \bar{\nu}_R\nu_R$, $e^\pm\nu_R \leftrightarrow e^\pm\nu_R$, $e^\pm\bar{\nu}_R \leftrightarrow e^\pm\bar{\nu}_R$ in the e-ν_R system and $\nu_L\bar{\nu}_L \leftrightarrow \nu_R\bar{\nu}_R$, $\nu_L\bar{\nu}_R \leftrightarrow \nu_L\bar{\nu}_R$, and $\nu_L\nu_R \leftrightarrow \nu_L\nu_R$ in the ν_L-ν_R system. We did not include X-exchange to right-handed neutrinos for the same reasons as above, namely, they are further suppressed by an additional power of g_X^2.

3.4.4 Summary of transfer rates. Following the discussion of the collision terms, section 3.4.3, we now explicitly provide the transfer rates $\delta\rho_i/\delta t$ that we use in equation (3.13):

$$\frac{\delta\rho_X}{\delta t} = \frac{\delta\rho_{X\leftrightarrow e^+e^-}}{\delta t} + \frac{\delta\rho_{2\leftrightarrow 2}}{\delta t} + N_\nu\left[\frac{\delta\rho_{X\leftrightarrow\nu_L\bar{\nu}_L}}{\delta t} + \left\{\frac{\delta\rho_{X\leftrightarrow\nu_R\bar{\nu}_R}}{\delta t}\right\}\right], \tag{3.26a}$$

$$\frac{\delta\rho_{\nu_R}}{\delta t} = \left\{-\frac{1}{2}\frac{\delta\rho_{X\leftrightarrow\nu_R\bar{\nu}_R}}{\delta t}\right\}, \tag{3.26b}$$

$$\frac{\delta\rho_{\nu_L}}{\delta t} = \frac{1}{2}\left[\frac{\delta\rho_{e-\nu}}{\delta t} - \frac{\delta\rho_{X\leftrightarrow\nu_L\bar{\nu}_L}}{\delta t}\right], \tag{3.26c}$$

$$\frac{\delta\rho_\gamma}{\delta t} = -N_\nu\frac{\delta\rho_{e-\nu}}{\delta t} - \frac{\delta\rho_{X\leftrightarrow e^+e^-}}{\delta t} - \frac{\delta\rho_{2\leftrightarrow 2}}{\delta t}. \tag{3.26d}$$

Note that the neutrino Boltzmann equations in equation (3.13) evolve a single neutrino species (rather neutrino and anti-neutrino) which accounts for the factor

of 1/2 in Eqs. (3.26b)-(3.26c). The $\delta n_i/\delta t$ rates can be straightforwardly deduced from Eqs. (3.26).

3.5 Numerical evolution of the Boltzmann equations and $N_{\rm eff}$

We now discuss the details of solving the Boltzmann equations in equation (3.13) in order to determine the thermodynamic evolution of the universe with X interactions. The final result from this section, calculating the contours of $\Delta N_{\rm eff}$ in the (m_X, g_X) parameter space, is the central result of this paper.

3.5.1 Initial conditions. We start with the initial condition $T_0 \equiv T_\gamma = T_{\nu_L} = \text{Max}[10\text{ MeV},\ 10\, m_X]$. and $\mu_{\nu_L} = -10^{-5}\, T_0$. This ensures that all the dynamics before neutrino decoupling are captured. Furthermore, we start $T_X = T_{\nu_R} = 10^{-2}\, T_0$ and $\mu_X = \mu_{\nu_R} = -10^{-5}\, T_0$, so that both X and ν_R begin with a negligible abundance compared to the SM bath, $\rho_X/\rho_\nu \sim 10^{-8}$. The specific (small) initial values of T_X, μ_X and their relation to T_{ν_R}, μ_{ν_R} do not impact the evolution, since the Boltzmann equations quickly evolve these quantities to their correct values.

The evolution of particle distributions is often shown as ρ_i/T_γ^4, using T_γ to show dimensionless ratios of energy densities of difference species. This is useful because in evolving over several orders of magnitude in temperature, a relativistic species energy density spans *many* orders of magnitude. Moreover, in cases where new physics does not affect photons, e.g. [81, 144], the evolution of T_γ can be used to provide a convenient measure of time that is independent of the new physics dynamics.

In our case, X interactions affect the evolution of photons, electrons, and neutrinos distributions. This means that in trying to compare the energy densities and number densities of different species with different choices of parameters (m_X, g_X), there can be differential effects on the evolution of T_γ, and thus both the numerator ρ_i and the denominator T_γ^4. We therefore introduce a "reference" temperature, T_ξ,

obtained by solving the Boltzmann equation $dT_\xi/dt = -HT_\xi$ with $T_\xi(t_0) = T_0$.[3] In the following, we show energy and number densities scaled by T_ξ^4 or T_ξ^3 respectively, and this allows us to much more easily compare different choices of (m_X, g_X) with each other.

3.5.2 Evolution of Boltzmann equations. In this section, we discuss the solution to the Boltzmann equations in equation (3.13) at representative points in the parameter space. To do so, we examine the evolution of density and effective interaction rate for the particles in our system. The effective interaction rate[4] is defined as

$$\frac{\langle \Gamma_i \rangle}{H} \equiv \frac{1}{HT_\xi^3} \frac{\delta n_i}{\delta t} \tag{3.27}$$

where $\delta n_i/\delta t$ is the sum of all number density transfer rates (section 3.4.4) for interactions between two species $i = X \leftrightarrow e$ or $X \leftrightarrow \nu$. This is the rate to which the forward or backward interaction dominate the other as compared to Hubble expansion rate. For example, a positive $\langle \Gamma_{X \leftrightarrow \nu} \rangle / H$ means the $\nu_i \bar{\nu}_i \to X$ dominates the backward rate and the neutrinos number density is decreasing in favor of X. Similarly, zero means forward/backward rates are equal and a zero plateau implies that X and neutrinos are thermalized while X is relativistic.

We first consider an example of an X boson that is light, $m_X = 10$ keV, that is representative of the light regime $m_X \ll 2m_e$. This is among the simpler cases since

[3] One way to think about this is to imagine ξ is a (fictitious) massless particle with a temperature that is initially set to the temperature of the SM but is actually decoupled from all other particles. Taking ξ to be massless with an infinitesimal small number of degrees of freedom means ξ always evolves as radiation and does not affect Hubble expansion rate ($\rho_\xi \sim 0$).

[4] In [144], this quantity is instead defined as $(\delta n_{X \to \nu_i \bar{\nu}_i} \delta t)/(H n_\nu)$ for the one-way interaction. This is done to estimate the interaction strength at which X thermalizes with neutrinos, $\langle \Gamma_i \rangle \sim H$, without solving the Boltzmann equations. We replace n_ν by T_ξ^3 as we are also interested in electron interactions and $n_e \to 0$ after electron-positron annihilation. Secondly, we consider the forward and backward interaction in the transfer rates instead of just the forward rate [first term in square bracket of equation (3.22b)].

the $X \leftrightarrow e^+e^-$ process is kinematically forbidden and for sufficiently low coupling the only relevant interaction is $X \leftrightarrow \nu_L\bar{\nu}_L$. In figure 17, we show the scaled density and effective interaction rates for several values of $g_X = 10^{-10}$ to 10^{-12}. At the smaller end of the couplings, $g_X = 10^{-11}$ and $g_X = 10^{-12}$, neutrinos populate X without fully thermalizing (at $g_X = 10^{-11}$, $X \leftrightarrow \nu_L\bar{\nu}_L$ is almost thermalized). X then proceeds to evolve as matter $\rho_X \propto a^{-3}$ before dumping its entropy back into neutrinos. The nonrelativistic X's decay into neutrinos that are now more energetic than the primordial neutrino plasma that evolves as radiation $\rho_\nu \propto a^{-4}$. Therefore, the resulting neutrino energy density is larger than it would have been in the SM. This implies a positive N_{eff} is generated, as shown in the figure caption.

Also, in figure 17, for $g_X = 10^{-10}$, the most obvious feature is the resonance near $T_\xi \sim 0.15$ MeV resulting from the finite temperature corrections to $\gamma X \leftrightarrow e^+e^-$ and $e^\pm X \leftrightarrow e^\pm\gamma$. In fact, the resonance is also present at the same temperature for the smaller values $g_X = 10^{-11}, 10^{-12}$, but it is only barely visible in the plot given the smaller coupling. This results in a finite contribution to X shown by the step-up its energy density, and then $\nu_L^i\bar{\nu}_L^i \to X$ also becomes efficient at a later time, resulting in the bump in production of X near $T_\xi \sim 0.1$ MeV. Note that the $X \leftrightarrow e$ effective interaction rate is always positive since $m_e > m_X$ and electron-positron annihilation occurs before X decay. This means that the forward reactions ($\gamma X \to e^+e^-$ and $e^\pm X \to e^\pm\gamma$) never dominates over the backward reactions. So while electrons transfer their energy to X, the energy is never returned (unlike the case with neutrinos). This affects the evolution two-fold: (i) electron-positron annihilation dumps less entropy into photon plasma, decreasing ρ_γ; (ii) entropy stolen from electrons/positrons is later dumped into neutrinos, further increasing ρ_ν. Both effects result in a larger value of N_{eff}.

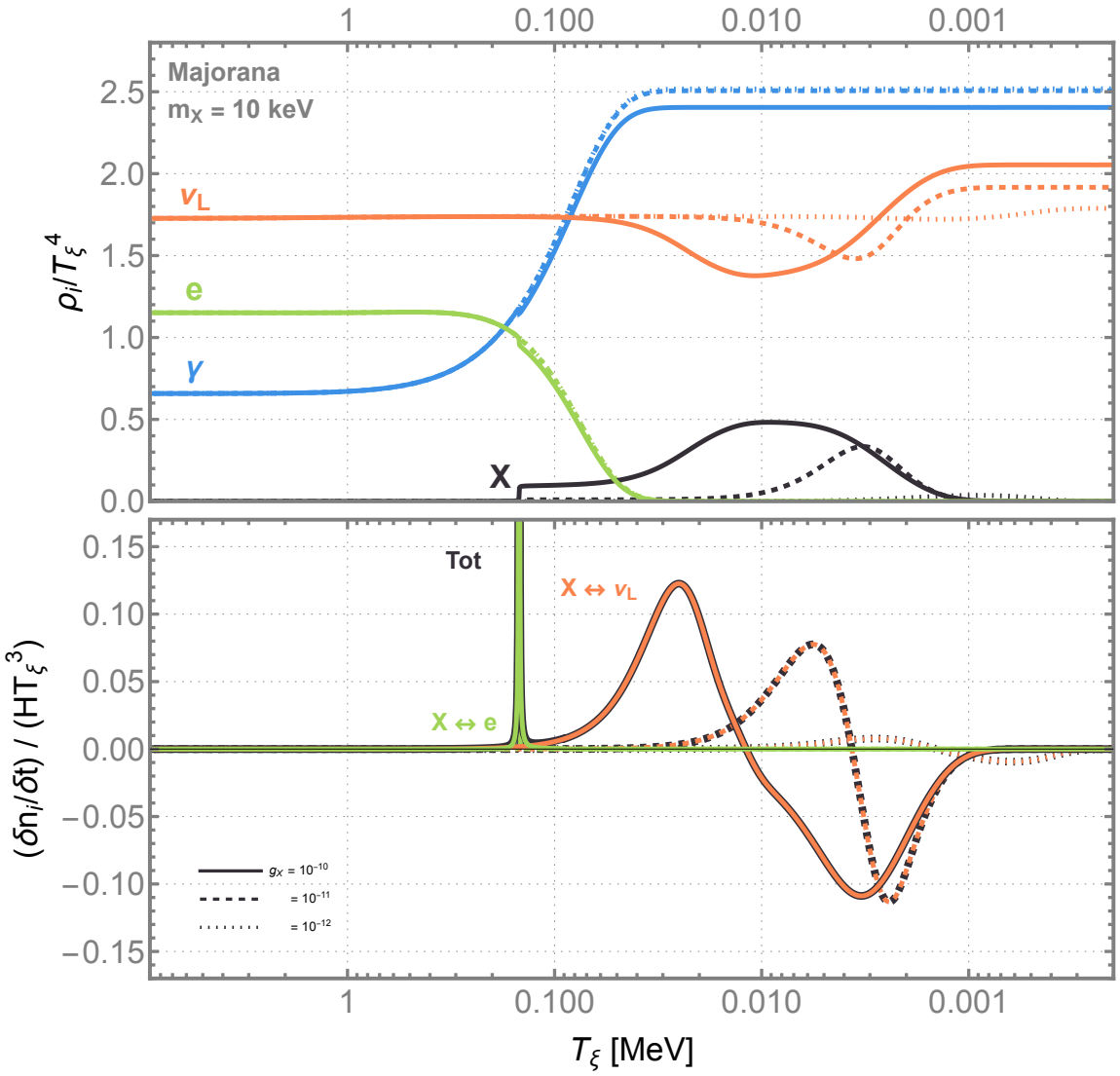


Figure 17. Top: The scaled density and *bottom:* and effective interaction rate for $m_X = 10\,\text{keV}$ for couplings $g_X = 10^{-10}$ (solid, $\Delta N_{\text{eff}} = 0.72$), $g_X = 10^{-11}$ (dashed, $\Delta N_{\text{eff}} = 0.33$), and $g_X = 10^{-12}$ (dotted, $\Delta N_{\text{eff}} = 0.08$).

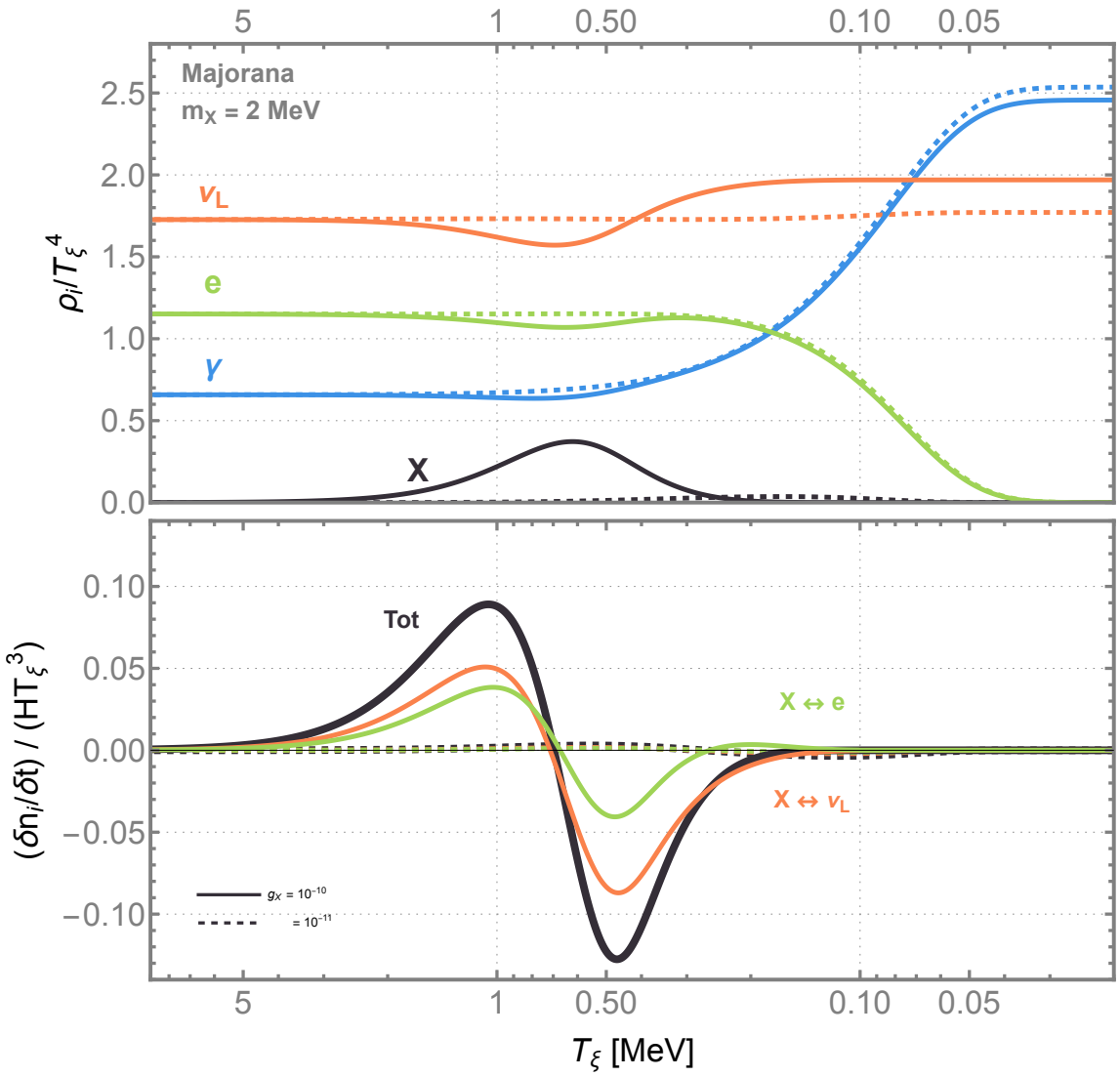


Figure 18. Top: The scaled density and *bottom:* and effective interaction rate for $m_X = 2\,\mathrm{MeV}$ for couplings $g_X = 10^{-10}$ (solid, $\Delta N_{\mathrm{eff}} = 0.49$) and $g_X = 10^{-11}$ (dashed, $\Delta N_{\mathrm{eff}} = 0.03$).

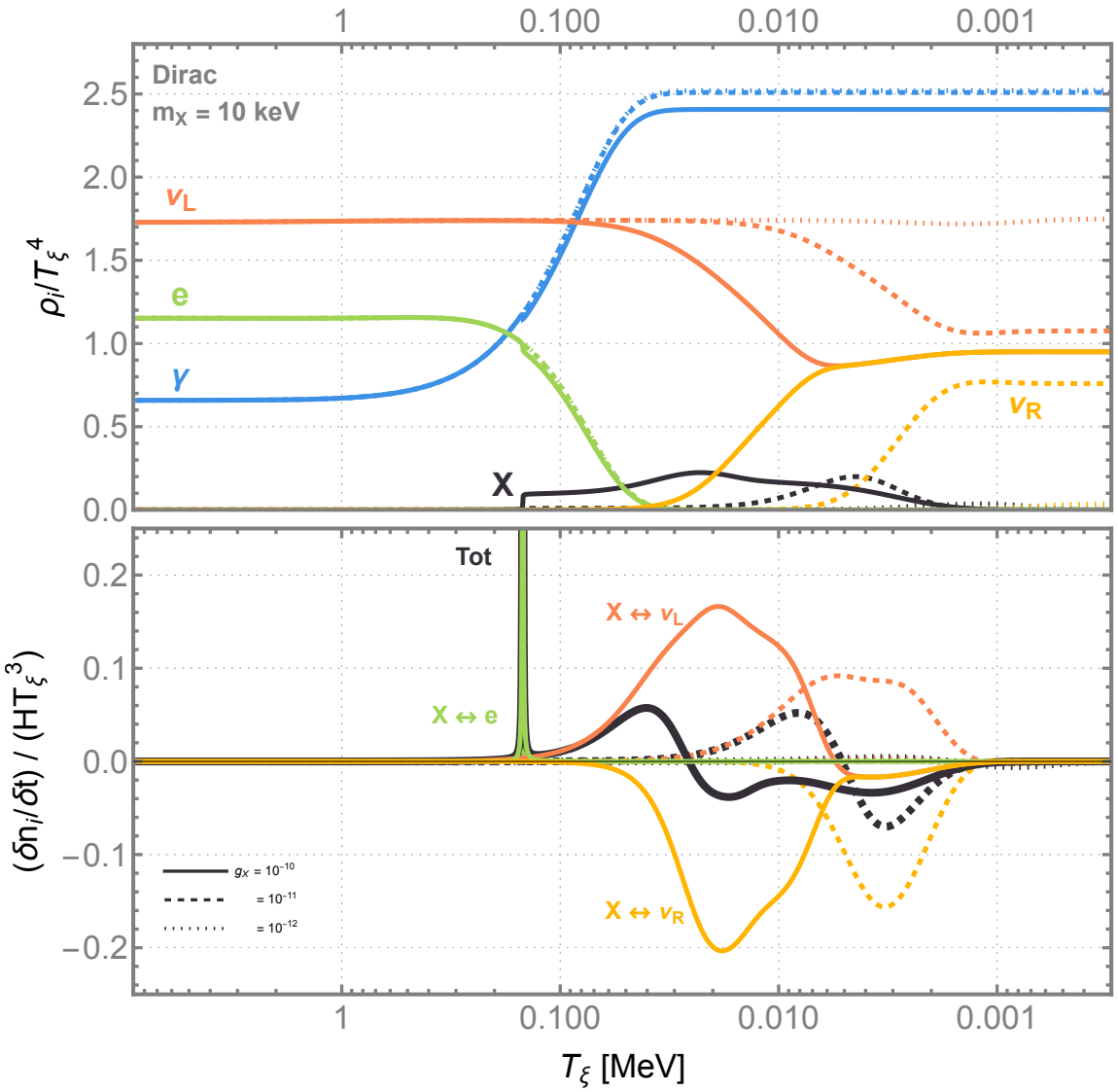


Figure 19. Top: The scaled density and *bottom:* and effective interaction rate for $m_X = 10\,\mathrm{keV}$ with Dirac neutrinos for couplings $g_X = 10^{-10}$ (solid, $\Delta N_{\mathrm{eff}} = 0.43$), $g_X = 10^{-11}$ (dashed, $\Delta N_{\mathrm{eff}} = 0.18$), and in the upper figure only, $g_X = 10^{-12}$ (dotted, $\Delta N_{\mathrm{eff}} = 0.07$).

In figure 18, we show the same plot for $m_X = 2$ MeV. In this case, the $X \leftrightarrow e^+e^-$ process is active and the population of X particles is depleted (the decays of Xs) before electron-positron annihilation has completed. For $g_X = 10^{-10}$, electrons and neutrinos populate a distribution of X until $T_\xi \simeq 0.7$ MeV, then X decay takes over and dumps its entropy back into both electrons and neutrinos. However, for this mass, both $e^\pm$ and X become non-relativistic and evolve as matter around roughly the same time. This means that the back and forth exchange in energy does not comparatively increase the energy density of electrons as it does for neutrinos. Another effect shown in figure 18 (lower) is the evolution of the effective $X \leftrightarrow e$ interaction rate from positive to negative, and then back to positive. The first positive bump is the forward reaction $e^+e^- \to X$, followed by X going nonrelativistic, with X decaying into e^+e^- and $\nu_L\bar{\nu}_L$, and then finally $e^+e^- \to X$ occurs on the Boltzmann tail of the electron distribution, and this small regenerated population of X decays mostly back into neutrinos.

In figure 19, we show the evolution for $m_X = 10$ keV with Dirac neutrinos. For low couplings, $\nu_L^i\bar{\nu}_L^i \to X$ populates X and $X \to \nu_R^i\bar{\nu}_R^i$ populates right-handed neutrinos driving $X - \nu_L - \nu_R$ system into thermal equilibrium. The energy density of primordial left-handed neutrinos is now distributed among X, ν_L, and ν_R. Hence, the maximum energy density that X can achieve is smaller than in the Majorana neutrino case. Increasing the coupling from $g_X = 10^{-12}$ to $g_X = 10^{-10}$ shows the trend towards thermalization of ν_L with ν_R as the interaction rate becomes efficient. For $g_X = 10^{-10}$, the resonance in the $X \leftrightarrow e$ system is, again, the most prominent feature in the plot. The dynamics of resonance are identical to those in figure 17. Furthermore, for $g_X = 10^{-10}$, the initial distribution of left-handed neutrinos has been converted to an equal distribution of left- and right-handed neutrinos. If this

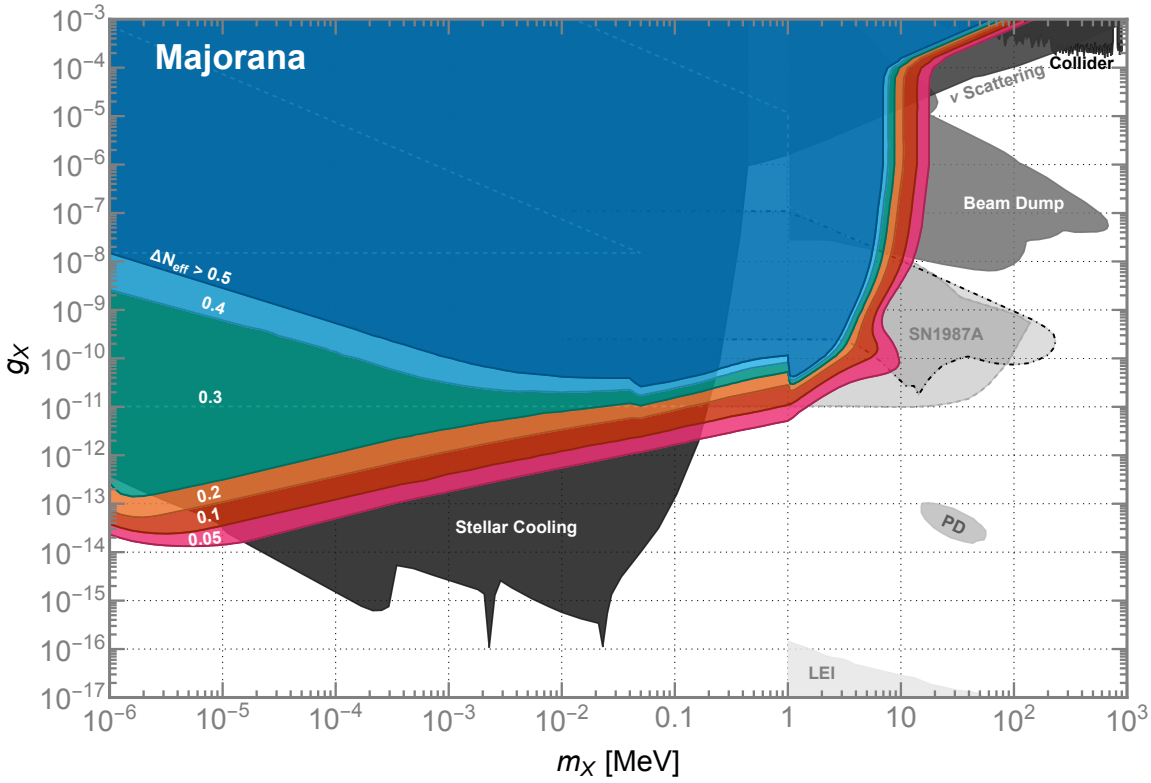


Figure 20. Calculations of $\Delta N_{\rm eff}$ for the "Majorana" neutrino case. The regions correspond to $\Delta N_{\rm eff} > 0.05$ (pink), 0.1 (red), 0.2 (orange), 0.3 (green), 0.4 (light blue), and 0.5 (dark blue). The dashed gray and dot-dashed black lines show the constraints from SN1987A from [56] and [55] respectively. See section 3.5.4 for a discussion of SN1987A and other background constraints. Current constraints from Planck data exclude $\Delta N_{\rm eff} \gtrsim 0.3$-0.4 (depending on the choice of dataset) [16], while future CMB observatories, such as CMB-S4, are expected to reach $\Delta N_{\rm eff} \sim 0.06$ [342]. See section 3.5.5 for further discussion of current and future constraints.

were to happen instantaneously, there would be no effect on $N_{\rm eff} \propto (\rho_{\nu_L} + \rho_{\nu_R})/\rho_\gamma$. However, since this thermalization process generates an abundance of X, which then becomes nonrelativistic, evolves as matter, and then decays, there is an increase in $N_{\rm eff}$ just as occurred in the Majorana case in figure 17.

3.5.3 Numerical results for $N_{\rm eff}$. We now show the full results of our evaluation of $N_{\rm eff}$ in the (m_X, g_X) plane in figure 20 (Majorana neutrino case) and figure 21 (Dirac neutrino case).

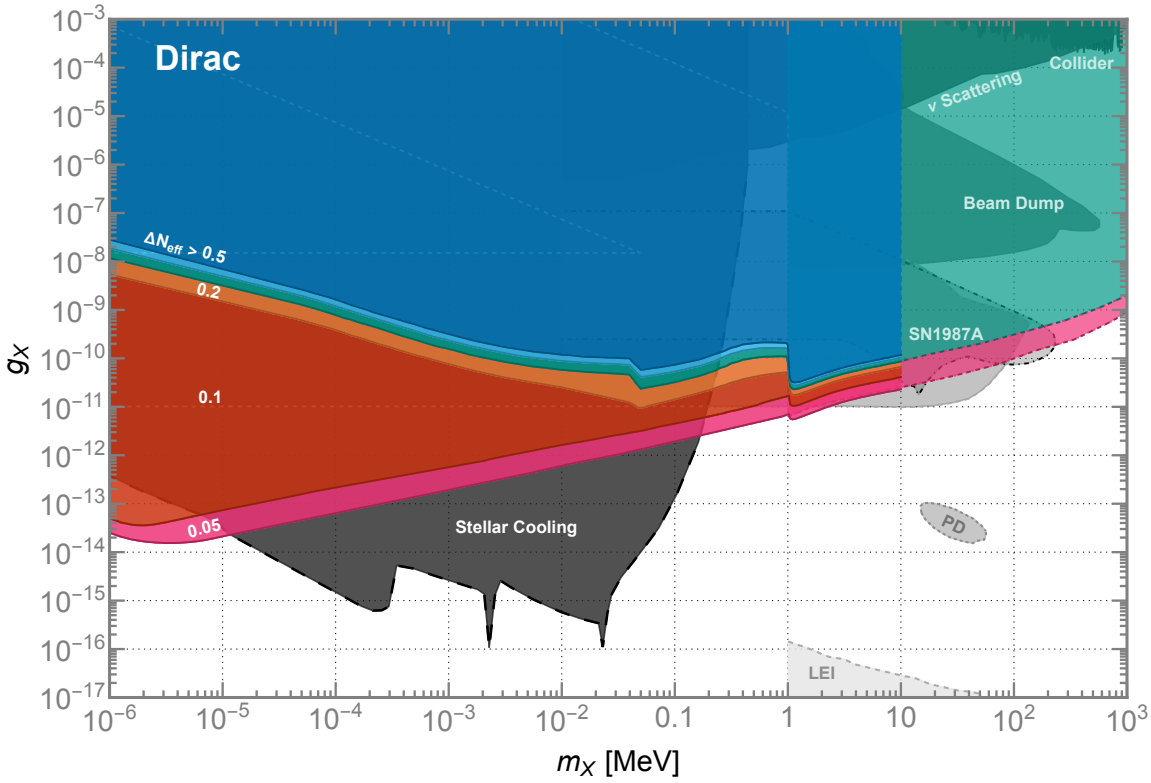


Figure 21. Same as figure 20, but for the "Dirac" neutrino case. As before, the regions correspond to $\Delta N_{\rm eff} > 0.05$ (pink), 0.1 (red), 0.2 (orange), 0.3 (green), 0.4 (light blue), and 0.5 (dark blue). The dashed pink and green contours correspond to $\Delta N_{\rm eff} = 0.06\,\{0.3\}$ in [148] respectively. The dashed gray and dot-dashed black lines show the constraints from SN1987A from [56] and [55] respectively. See section 3.5.4 for a discussion of SN1987A and other background constraints.

Let's first discuss the Majorana neutrino case, figure 20. This is a contour plot in $\Delta N_{\rm eff}$, where colored regions provide our result for $\Delta N_{\rm eff}$ as shown in the plot. In each colored region, $\Delta N_{\rm eff}$ is greater than the value as shown, and less than its nearest neighboring region. For the dark blue region, $\Delta N_{\rm eff} > 0.5$, and we did not delineate any larger values, for reasons that we will discuss shortly.

There are three regimes of m_X that reveal the qualitatively different processes that are occurring to determine the contribution to $\Delta N_{\rm eff}$. In the low mass region, $m_X < 2m_e$, with $\Delta N_{\rm eff} \sim 0.05$ to 0.2, the process $X \leftrightarrow \nu_L \bar{\nu}_L$ is approaching thermal

equilibrium. The shape of the contour in (m_X, g_X) space, $g_X \sim \sqrt{(24\pi m_X)/M_{\rm Pl}}$, can be obtained from $\Gamma_{X\leftrightarrow\nu_L\bar{\nu}_L}/H \sim 1$ and $T = m_X$. The precise value of $N_{\rm eff}$ requires the numerical modeling of the Boltzmann evolution. (However, as we will see in section 3.6, we can also estimate the value of $\Delta N_{\rm eff}$ using semi-analytic arguments.) We see that in this region, the bounds on g_X strengthen with *decreasing* m_X. Holding m_X fixed, as g_X is further increased, X and left-handed neutrinos reach thermal equilibrium, saturating the contribution to $\Delta N_{\rm eff} \sim 0.3$. Once the process $X \leftrightarrow \nu_L\bar{\nu}_L$ is in thermal equilibrium, there is no further increase in $\Delta N_{\rm eff}$ for larger values of g_X, as evident by the green plateau region in figure 20. The $\Delta N_{\rm eff} = 0.4$,0.5 contours, that have a different shape, arise because there are additional scattering processes that are contributing to $\Delta N_{\rm eff}$: the $2 \leftrightarrow 2$ processes $e^+e^- \to X\gamma$ and $e\gamma \to eX$. These processes become efficient when $n_e\langle\sigma v\rangle_{2\leftrightarrow 2}/H \sim 1$ at $T \sim m_e$; this corresponds to couplings of order $g_X \gtrsim 10^{-10}$ if we naively treat the rates in vacuum. However, unlike $X \leftrightarrow \nu\bar{\nu}$, these processes have important finite temperature corrections[5] that require the use of the in-medium coupling $g_{X,m}$ that is suppressed in the small m_X limit as explained in appendix E. The small kink in these contours near $m_X \sim 0.05$ MeV is the result of a linear interpolation as discussed in section 3.4.3.3.

In the intermediate mass region, 1 MeV $\lesssim m_X \lesssim$ 20 MeV, the contours in $\Delta N_{\rm eff}$ rise rapidly in g_X as m_X increases. The major contributor to the rapid rise of $\Delta N_{\rm eff}$ contours in g_X as m_X increases is that as X becomes more massive, it becomes nonrelativistic earlier in the universe, and most of its decays back into SM matter occurs before neutrino decoupling. The SM processes rapidly equilibrate the relativistic species, erasing the effect of X production and decay. There is detailed

[5]Had finite temperature effects been neglected, the vacuum $e^+e^- \to X\gamma$ and $e\gamma \to eX$ rates are m_X independent (for $m_X \ll m_e$), and so the 0.4,0.5 contours would have become horizontal.

structure, such as the shape of the contours near $\Delta N_{\text{eff}} \sim 0.05$ and masses $m_X \sim$ 10 MeV, that is a more complicated interplay between X, electrons, and neutrinos.

Finally, in high mass region, $m_X > 20$ MeV, the Boltzmann evolution is calculated only involving photons, electrons, and neutrinos, with virtual X-exchange in the $2 \leftrightarrow 2$ processes $e^+e^- \leftrightarrow \bar{\nu}_\alpha \nu_\alpha$, $e^\pm \nu_\alpha \leftrightarrow e^\pm \nu_\alpha$, and $e^\pm \bar{\nu}_\alpha \leftrightarrow e^\pm \bar{\nu}_\alpha$. The ΔN_{eff} contours in this region have a shape that can be determined by requiring X-exchange is no larger than W, Z exchange. This occurs when $g_X \sim m_X \sqrt{G_F}$, providing an excellent characterization of the shape. The physics of this process is that if X exchange exceeds the weak interaction rate, this delays neutrino decoupling in the evolution of the universe, which has the effect of increasing ΔN_{eff}. Our contour shape agrees with that shown in [57].

Now, let's discuss the contours in the Dirac neutrino case, figure 21, comparing and contrasting with the Majorana neutrino case. In the low mass region, $m_X < 2m_e$, the shape of the ΔN_{eff} contours is the same as the Majorana case, with the only difference being that the contour values of ΔN_{eff} are somewhat lower. As we discussed in section 3.5.2, what is happening is that the the energy density of primordial left-handed neutrinos is now distributed among X, ν_L, and ν_R. Hence, the maximum energy density that X can achieve is smaller than in the Majorana case, and so the entropy dump of X into neutrinos is smaller. Later in section 3.6 we will verify this with a semi-analytic analysis. To be explicit, the $\Delta N_{\text{eff}} = 0.05$ contour corresponds to the $X \leftrightarrow \nu_L \bar{\nu}_L$ and $X \leftrightarrow \nu_R \bar{\nu}_R$ processes approaching equilibrium. Thermal equilibrium of these processes occurs around $\Delta N_{\text{eff}} \sim 0.1$ at which point the contribution to ΔN_{eff} from left and right handed neutrinos is saturated. We also see that at larger couplings the constraint from $e^+e^- \to X\gamma$ and $e\gamma \to eX$ processes

remains, but now extends to the 0.2-0.5 contours analogous to the 0.4,0.5 contours described in the Majorana case.

At intermediate masses, $m_X \gtrsim 1$ MeV, as X is populated, then becomes nonrelativistic, it decays into both left-handed *and* right-handed neutrinos. Hence, it contributes significantly to $\Delta N_{\rm eff}$ because X is providing a mechanism to siphon off energy density from left-handed neutrinos into a "new" species, right-handed neutrinos, that are completely decoupled from the SM. This is unlike the Majorana case, where again for $m_X \gtrsim$ few MeV, X decays back entirely into SM states that equilibrate with the SM through electromagnetic or weak interactions. This effect of populating right-handed neutrinos implies the contours in $\Delta N_{\rm eff}$ are at much smaller values of g_X when $m_X \gg 1$ MeV. We have calculated the result to $m_X = 10$ MeV, and then we show the contours obtained by [148] for larger masses. In particular, the dashed pink and green contours, that correspond to $\Delta N_{\rm eff} = 0.06\,\{0.3\}$, match well onto our calculations for $m_X < 10$ MeV.

There is one last issue to discuss. At the very smallest masses that we consider, the lifetime of X becomes comparable to the time of recombination

$$\tau = \frac{c}{\Gamma} \simeq 330\ \text{kyr} \times \left(\frac{1\ \text{eV}}{m_X}\right)\left(\frac{4\times 10^{-14}}{g_X}\right)^2 , \tag{3.28}$$

for the Majorana neutrino case (for the Dirac case the lifetime is 1/2 of this). This means not all of the X bosons that freeze-in have decayed back to relativistic neutrino degrees of freedom. We have taken this effect into account by evaluating $N_{\rm eff}$ after all of the X bosons have decayed or at the temperature of recombination, $T \simeq 0.3$ eV, whichever occurs first. This can be seen in both Figs. 20,21, where the contours of $\Delta N_{\rm eff}$ change slope from positive to negative as m_X drops below $\sim$ few eV, leading to slightly weaker bounds on g_X for the smallest masses of X that we consider. A very similar effect was also found in [150] for the $U(1)_{\mu-\tau}$ model.

3.5.4 Other constraints. In Figs. 20,21, we have also shown several other constraints on the mass and coupling of a $U(1)_{B-L}$ gauge boson. An overview of previously obtained constraints can be found from [39, 42, 50, 51, 145].

Supernova 1987A (SN1987A) provides well-known constraints on the emission of light mediators [351]. The presence of a light vector mediator provides an additional cooling mechanism in the proto-neutron star that competes with electroweak interactions and alters its neutrino luminosity. Constraints on a variety of gauged $U(1)$ bosons have been derived in [55, 56, 191, 192]. The constraints for $U(1)_{B-L}$ in [55] and [56] are derived using slightly different methods and arrive at slightly different constraints. For completeness, we show both of these in the figures, and we will return to this issue in future work.

Similarly, constraints can be set if the energy loss rate due to light gauge boson emission from the sun, red giants (RG), and horizontal branch (HB) stars exceeds a maximally allowed limit [192, 352, 353]. Note both constraints from stellar cooling and SN1987A are derived explicitly for the case where right-handed neutrinos are heavy and do no contribute to the dynamics ("Majorana case"). To the best of our knowledge, a similar derivation has not been done in the literature for the Dirac case, though we do not suspect major differences in the results. So, we have included these constraints in figure 21, though denoted as dashed to remind the reader of this subtlety.

We also show the constraints from photodissociation (PD) of light elements, and separately, late energy injection (LEI) at the CMB era, that were obtained for $U(1)_{B-L}$ in [145]. These constraints are at much smaller coupling, where X was very far from reaching thermal equilibrium, and for masses $m_X > 2m_e$ so that the decay $X \to e^+e^-$ is kinematically available. In Figs. 20,21 we show only the upper part of

the LEI contour; we refer readers to [145] for the full region that extends to couplings values $g_X < 10^{-17}$.

Neutrino experiments that probe electron-neutrino or coherent elastic neutrino-nucleus scattering (CEνNS) are sensitive to the contribution of X to their amplitudes [94, 95, 243, 244, 258, 261, 265, 354]. Experiments searching decays into invisible final states can also be used to set constraints with the assumption that invisible states can be treated as decays to neutrino final states [104, 266, 267, 269, 270]. In beam dump experiments [283, 286, 287, 290, 291, 293–295, 297, 298, 355], X is produced via the bremsstrahlung process where a beam of electron/protons is dumped on some target material; X then travels through shielding material before decaying into SM particles that can be observed in the detector. Constraints are derived by comparing the number of expected and observed events in the detector. Finally, colliders set constraints on promptly decaying X [42, 307, 312]. These beam dump and collider constraints apply to both the Majorana and Dirac case. However in the Dirac case, collider and beam dump and neutrino scattering constraints have been recast to account for the additional branching fraction of $X \to \nu_R \bar{\nu}_R$ [51].

3.5.5 Constraints from existing CMB observations and prospects for future observatories. We have presented our results in Figs. 20,21 with our calculated contours of $\Delta N_{\rm eff}$ as would be measured by the CMB within the (m_X, g_X) model parameter space. Determining the current and future constraints on $\Delta N_{\rm eff}$ requires significant care with regard to two critical issues. First, the *era* at which new physics modifies $N_{\rm eff}$, and what other cosmological parameters are also modified, particularly between BBN and CMB. Second, the *datasets* used to constrain the cosmological parameters, and the potential correlations among observables. In this section, our focus is on the CMB determination of $N_{\rm eff}$.

Nevertheless, we can consider two proxies for BBN constraints on new physics that are potentially different from $N_{\rm eff}$. One is the helium mass fraction Y_p, that we consider in detail in section 3.7. A second quantity is the baryon-to-photon ratio, η. In general, new physics can contribute to a shifts in η^{CMB} relative to η^{BBN} when, for example, there is a period of late energy injection into photons well after the temperature of helium synthesis, $T \sim 0.07$ MeV [110, 356]. In the SM, there is negligible energy injection into photons at this temperature because e^+e^- annihilation is virtually complete, and so $\eta^{CMB} \simeq \eta^{BBN}$. Considering $U(1)_{B-L}$, we also do not have late energy injection directly into photons. We do have energy injection into e^+e^- from $X \to e^+e^-$, but since e^+e^- annihilation did not affect η in the SM, we do not expect these contributions from $X \to e^+e^-$ to shift η from BBN to the CMB era either.

Focusing on $N_{\rm eff}^{\rm CMB}$, we can now turn to the current constraints and future prospects for cosmological measurements of $N_{\rm eff}^{\rm CMB}$. The Planck collaboration (PCP18) have set the best bounds thus far, with various combinations of datasets [15, 16]:

$$N_{\rm eff}^{\rm CMB}|_{1\,\rm pe}^{\rm PCP18} = 2.99\,^{+0.34}_{-0.33} \quad (95\%,\ \text{TT, TE, EE+lowE+ lensing+BAO}) \tag{3.29a}$$

$$N_{\rm eff}^{\rm CMB}|_{+Y_p}^{\rm PCP18} = 2.99\,^{+0.43}_{-0.40} \quad (95\%,\ \text{TT, TE, EE+lowE+ lensing+BAO+Aver [153]}) \tag{3.29b}$$

$$N_{\rm eff}^{\rm CMB}|_{+H_0}^{\rm PCP18} = 3.27\,^{+0.30}_{-0.30} \quad (95\%,\ \text{TT, TE, EE+lowE+ lensing+BAO+R18 [357]}). \tag{3.29c}$$

The first value, $N_{\rm eff}^{\rm CMB}|_{1\,\rm pe}^{\rm PCP18}$, is the on 1-parameter extension to the base-ΛCDM model six parameter fit. However, the primordial helium mass fraction Y_p and $N_{\rm eff}$ are partially degenerate as they both affect the CMB damping tail (i.e. [358]). Allowing Y_p to vary with $N_{\rm eff}$ gives a value of $N_{\rm eff}^{\rm CMB}|_{+Y_p}^{\rm PCP18}$ and $Y_p^{\rm BBN}|_{+Y_p}^{\rm PCP18} = 0.2437 \pm 0.0080$

at 95% C.L.. The combined fit eases the constraint on both $N_{\rm eff}$ and Y_p which has a PDG recommended value of $Y_p|^{\rm PDG} = 0.245 \pm 0.006$ at 95% C.L. [111] based on the analyses in [162–166]. Finally, the $N_{\rm eff}^{\rm CMB}|^{\rm PCP18}_{+H_0}$ partially addresses the $\sim 3\sigma$ tension in the Hubble constant, H_0, between CMB and local observation determinations [357,359,360] by including the analysis in R18 [357]. This fit could potentially increase the tension with weak galaxy lensing and (possibly) cluster count data since it requires an increase in the σ_8 and a decrease in Ω_m values.

After the PCP18 data release and analysis, Yeh2022 [110] presents independent BBN and CMB limits on $N_{\rm eff}$ and η using likelihood analyses and updated evaluations for nuclear rates. The BBN likelihood functions are obtained by varying nuclear reaction rates within their uncertainties via a Monte Carlo, while the CMB likelihoods are derived from PCP18 and marginalized over Y_p. With various combinations of datasets,

$$N_{\rm eff}^{\rm BBN}|^{\rm Yeh2022}_{\rm BBN\ only} = 2.889 \pm 0.229 \quad (68.3\%, Y_p + {\rm D}) \tag{3.30a}$$

$$N_{\rm eff}^{\rm CMB}|^{\rm Yeh2022}_{\rm CMB\ only} = 2.800 \pm 0.294 \quad (68.3\%, {\rm TT,\ TE,\ EE{+}lowE{+}\ lensing}) \tag{3.30b}$$

$$N_{\rm eff}|^{\rm Yeh2022}_{\rm BBN+CMB} = 2.898 \pm 0.141 \quad (68.3\%, {\rm TT,\ TE,\ EE{+}lowE{+}\ lensing} + Y_p + {\rm D}). \tag{3.30c}$$

The first value, $N_{\rm eff}^{\rm BBN}|^{\rm Yeh2022}_{\rm BBN\ only}$, shows limits on $N_{\rm eff}$ at BBN where the BBN likelihood is convolved with the observation determination of Y_p and deuterium abundance D [154–161] likelihoods. The second value, $N_{\rm eff}^{\rm CMB}|^{\rm Yeh2022}_{\rm CMB\ only}$, differs from equation (3.29a) as the Yeh2022 analysis does not assume any relation between the ^{4}He abundance and the baryon density. The third value is the limit set by combining BBN and the CMB assuming no new physics after nucleosynthesis, however this value is not applicable here since X interactions can affect $\Delta N_{\rm eff}$ between BBN and CMB.

Comparing these observations to our results, Figs. 20,21, a conservative analysis suggests $\Delta N_{\rm eff}^{\rm CMB} \lesssim 0.3$-$0.4$ to 95% C.L., and hence the regions labeled dark and light blue are ruled out, with the green region strongly disfavored. The 2018 Planck analysis that incorporated the local Hubble measurement into the fit yielded $N_{\rm eff}^{\rm CMB} \simeq 3.27$, Eq. (3.29c), which would favor the orange region, however this is in tension with more recent analyses of the CMB data. If the ultimate resolution of the Hubble tension involves a slightly larger value of equation (3.29c), then the orange region is favored. Future observatories, including SPT-3G [361], CORE [362], Simons Observatory [363], PICO [364], CMB-S4 [342], CMB-HD [365], are anticipated to reach much smaller values, for example CMB-S4 is anticipated to ultimately obtain $\Delta N_{\rm eff} \simeq 0.06$ at 95% C.L. [342]. Here we see these future experiments are capable of probing a significantly larger fraction of the (m_X, g_X) parameter space in both the Majorana and Dirac neutrino cases. The future CMB observations will be the most sensitive to the presence of a gauged $U(1)_{B-L}$ boson in the regions 1 eV $\lesssim m_X \lesssim$ 20 eV, 0.2 MeV $\lesssim m_X \lesssim$ 20 MeV, and in the Dirac case, $m_X \gtrsim 200$ MeV [148].

3.6 Semi-analytic estimates of $\Delta N_{\rm eff}$

There is an interesting way to cross-check our results in the regime $m_X \ll m_e$, where the only interactions of X are with neutrinos. This semi-analytic approach involves two steps. First, we calculate the energy densities and number densities of X, assuming thermalization occurs at a temperature $T > m_X$. For the purposes of this estimate, we assume that thermalization occurs when X is relativistic and can be treated as massless. The key nontrivial part of this first step is that we are solving for not only the energy densities but also the chemical potentials as X is frozen-in to equilibrium with neutrinos. Next, we use entropy conservation to determine the net effect of X decaying back into neutrinos. Again, this step is nontrivial because

we also must take into account the nonzero chemical potentials of X and the various neutrino species that (were) in equilibrium.

Given these assumptions, we are able to semi-analytically calculate the contribution to $\Delta N_{\rm eff}$. We now present the calculation in two regimes: first, the Majorana case, to get a clear sense of the method and its result. Next, the Dirac case, however we will generalize this to include an arbitrary number of additional species of (right-handed) fermions that carry lepton number. This case will allow us to provide semi-analytic estimates of $\Delta N_{\rm eff}$ in a wider range of models that may be relevant for dark matter and cosmology.

3.6.1 Majorana case. An initial density of left-handed neutrinos with temperature T_{ν_L} is converted to a density of left-handed neutrinos and X,

$$\rho_{\nu_L}(T_{\nu_L}, 0) = \rho_{\nu_L}(T_{\rm eq}, \mu_{\rm eq}) + \rho_X(T_{\rm eq}, 2\mu_{\rm eq}) \tag{3.31a}$$

$$n_{\nu_L}(T_{\nu_L}, 0) = n_{\nu_L}(T_{\rm eq}, \mu_{\rm eq}) + 2n_X(T_{\rm eq}, 2\mu_{\rm eq}), \tag{3.31b}$$

with $T_{\rm eq}, \mu_{\rm eq}$ thermal equilibrium temperature and chemical potential. In the second equation, the factor of 2 arises because one X is produced at the expense of two neutrinos in $\nu_L^i \bar{\nu}_L^i \to X$. These conditions give,

$$T_{\rm eq} = 1.208\, T_{\nu_L}\ , \qquad \mu_{\rm eq} = -1.166\, T_{\nu_L} \tag{3.32}$$

which gives a maximum density ratio $\varrho_X \equiv \rho_X/(\rho_{\nu_L} + \rho_X) = 0.1642$. Had we neglected chemical potential, equation (3.31a) becomes a degree of freedom counting argument which yields $\varrho_X = 3/(6 \times \frac{7}{8} + 3) = \frac{4}{11} = 0.3636$ significantly overestimating the maximum X abundance. Instead, the chemical potential appears as $\varrho_X = 3\,{\rm Li}_4(x)/[6\,{\rm Li}_4(-x) + 3\,{\rm Li}_4(x)]$ with $x \equiv e^{\mu/T}$ and ${\rm Li}_4$ is the $4^{\rm th}$ order polylogarithm.

After thermal equilibrium is reached, we use entropy conservation to write,

$$[s_{\nu_L}(T_{\rm eq},\mu_{\rm eq}) + s_X(T_{\rm eq},2\mu_{\rm eq})]\, a'^3 = s_{\nu_L}(T_\nu,\mu_\nu) a^3 \tag{3.33a}$$

$$[n_{\nu_L}(T_{\rm eq},\mu_{\rm eq}) + 2n_X(T_{\rm eq},2\mu_{\rm eq})]\, a'^3 = n_{\nu_L}(T_\nu,\mu_\nu) a^3. \tag{3.33b}$$

The left-hand side starts at scale factor a' with equilibrium abundance of all relevant particles, while the right-hand side ends at a scale factor a with $T_\nu \ll m_X$, where the entire distribution of X bosons has decayed into neutrinos. We can relate the scale factors through $T'_\gamma a' = T_\gamma a$, since the photon plasma is decoupled from neutrinos. Solving equation (3.33) gives,

$$T_\gamma/T_\nu = 1.278\,, \qquad T_\nu/\mu_\nu = -3.486 \tag{3.34}$$

which can be used to calculate

$$\Delta N_{\rm eff} = N_{\rm eff} - N_{\rm eff}^{\rm SM} = 0.25\,. \tag{3.35}$$

As we discussed in section 3.5.3, the diagonal contours of $\Delta N_{\rm eff}$ in the light regime $m_X \ll 2m_e$ correspond to when the $1 \leftrightarrow 2$ process $X \leftrightarrow \nu\bar{\nu}$ approximately reaches thermal equilibrium. The highest contour shown is 0.3, that is quite close to our semi-analytic estimate in equation (3.35). Of course the semi-analytic method required certain approximations to be taken. Namely, in solving equation (3.33) we used the SM value of T_γ/T_ν in equation (3.10) to relate the scale factors $T'_\gamma a' = T_\gamma a$; and using the numerical value obtaining by solving the Boltzmann equations in equation (3.13) reproduces the correct value of $\Delta N_{\rm eff}$.

3.6.2 Dirac and generalized cases. We now redo the analysis of section 3.6.1 by adding into the thermal bath an arbitrary number N_R of (Weyl) fermion species.[6] As a slight abuse of notation, we will refer to these fermions as

[6]Here N_R refers to the number of $L = \pm 1$ particles, and so not necessarily are they are strictly "right-handed" with $L = 1$. The Dirac case has $N_R = 3$ and $L = 1$ for all species. The sign of the lepton number of any of these species does not enter our discussion below.

"right-handed neutrinos" below, but it should be understood that these fermion fields have $L = \pm 1$ and may or may not pair up with the left-handed neutrinos to gain Dirac masses. All of these right-handed neutrinos will be considered to be either (i) massless, or (ii) having a mass $m_{\nu_R} \lesssim m_X/2$. The Dirac case follows as a special case of this generalization where $N_R = 3$, $m_{\nu_R} = 0$, and two (or three) of these fermion species pair up with left-handed neutrinos.

Following Eqs. (3.31), an initial density of left-handed neutrinos with temperature T_{ν_L} is converted to a energy (number) density of left- and right-handed neutrinos [denote collectively by ρ_ν (n_ν)][7] and X,

$$\rho_{\nu_L}(T_{\nu_L}, 0) = \left(1 + \frac{N_R}{3}\right) \rho_\nu(T_{\rm eq}, \mu_{\rm eq}) + \rho_X(T_{\rm eq}, 2\mu_{\rm eq}) \tag{3.36a}$$

$$n_{\nu_L}(T_{\nu_L}, 0) = \left(1 + \frac{N_R}{3}\right) n_\nu(T_{\rm eq}, \mu_{\rm eq}) + 2n_X(T_{\rm eq}, 2\mu_{\rm eq}) \tag{3.36b}$$

with $T_{\rm eq}, \mu_{\rm eq}$ thermal equilibrium temperature and chemical potential.

After thermal equilibrium is reached, we can again utilize entropy conservation to write,

$$\left[\left(1 + \frac{N_R}{3}\right) s_\nu(T_{\rm eq}, \mu_{\rm eq}) + s_X(T_{\rm eq}, 2\mu_{\rm eq})\right] a'^3 = \left[\left(1 + \frac{N_R}{3}\right) s_\nu(T_\nu, \mu_\nu)\right] a^3 \tag{3.37a}$$

$$\left[\left(1 + \frac{N_R}{3}\right) n_\nu(T_{\rm eq}, \mu_{\rm eq}) + 2n_X(T_{\rm eq}, 2\mu_{\rm eq})\right] a'^3 = \left[\left(1 + \frac{N_R}{3}\right) n_\nu(T_\nu, \mu_\nu)\right] a^3 \tag{3.37b}$$

Again, the left-hand side starts at scale factor a' with equilibrium abundance of all relevant particles and the right-hand side ends at scale factor a with $T_\nu \ll m_X$ where all X distribution has decayed into neutrinos.

3.6.2.1 Dirac case. In the Dirac case ($N_R = 3$; $m_{\nu_R} = 0$), Eqs. (3.36) give

$$T_{\rm eq} = 1.1088\, T_{\nu_L}\,, \qquad \mu_{\rm eq} = -1.3485\, T_{\nu_L} \qquad \text{(Dirac case)} \tag{3.38}$$

[7]Note that both quantities ρ_ν and n_ν include a factor of $g_\star = 6$ corresponding to three fermionic Weyl degrees of freedom in their definition.

which gives a maximum density ratio $\varrho_X \equiv \rho_X/(\rho_{\nu_L} + \rho_X + \rho_{\nu_R}) = 0.07049$. (Again, had we neglected chemical potential, equation (3.36a) becomes $\varrho_X = 3/(12 \times \frac{7}{8} + 3) = \frac{2}{9} = 0.2222$, overestimating the maximum X abundance.) Solving equation (3.37) gives,

$$T_\gamma/T_\nu = 1.322\,, \qquad T_\nu/\mu_\nu = -1.093 \qquad \text{(Dirac case)} \tag{3.39}$$

which can be used to calculate

$$\Delta N_{\rm eff} = N_{\rm eff} - N_{\rm eff}^{\rm SM} = 0.09\,. \tag{3.40}$$

Like our discussion above in the Majorana case, in figure 21 the highest contour consistent with approximate thermalization of $X \leftrightarrow \nu\bar{\nu}$ is 0.1, that agrees with the semi-analytic estimate in equation (3.40).

3.6.2.2 Large number of massless species. Now let's utilize the generalized results in Eqs. (3.36) and (3.37) to apply to the case where there is a large number of massless species $N_R \gg 1$ that X can decay into. Once X and the $1 + N_R/3$ neutrinos have thermalized, it is clear from Eqs. (3.36) that the energy and number density of X is suppressed by the same factor, $1/(1 + N_R/3)$. Most of the energy and number density of left-handed neutrinos is transferred into the larger number of right-handed neutrinos. Then, following Eqs. (3.37), the effect of the small number of X gauge bosons is negligible. That is, in the limit $N_R \gg 1$, there is negligible entropy dumping of X into neutrinos, and so $\Delta N_{\rm eff} \to 0$. For smaller values of N_R, we find, for example $\Delta N_{\rm eff} = 0.12$ ($N_R = 2$), $\Delta N_{\rm eff} = 0.07$ ($N_R = 4$) and $\Delta N_{\rm eff} = 0.03$ ($N_R = 8$). Here we do need to emphasize that while the number of relativistic degrees of freedom nearly matches the SM, the *flavor* of these degrees of freedom is overwhelmingly in the form of the (sterile) neutral fermion species carrying lepton number.

3.6.2.3 Massive species. An alternative scenario occurs if the N_R species are massive, and thus are able to annihilate through X back into (massless) left-handed neutrinos species. Here what happens is that the large entropy of the right-handed neutrinos siphons off virtually all of the entropy in left-handed neutrinos. In the limit $N_R \gg 1$, with $m_{\nu_R} \lesssim m_X/2$, the overwhelming majority of the original energy density of left-handed neutrinos end up as nonrelativistic, massive (sterile) neutral fermion species. This leaves a negligible amount of left-handed neutrinos, and so in this limit, $\Delta N_{\rm eff} \to -3$, i.e., $N_{\rm eff} \to 0$. As a few examples where all N_R species are massive, we find $\Delta N_{\rm eff} = -0.64$ ($N_R = 1$), $\Delta N_{\rm eff} = -1.15$ ($N_R = 2$) and $\Delta N_{\rm eff} = -1.48$ ($N_R = 3$). Notice that $N_R \geq 1$ is already completely excluded by the Planck constraints on the CMB, i.e., equation (3.29).

3.7 BBN Y_p

The primordial abundances of nuclide species are critically sensitive to the expansion history leading up to nucleosynthesis. Precise determinations of these abundances requires solving Boltzmann equations describing the density evolution of each nuclide species (^{2}H, ^{3}He, ^{4}He...) (i.e. [128]). This can be done using publicly available BBN code such as `PArthENoPE` [366,367], `AlterBBN` [368,369], `PRIMAT` [370], or `PRyMordial` [371]; however, this is beyond the scope of this paper.

Instead, we follow an approximation employed in appendix A.4 of [141], that involves modifying the neutron-to-proton conversion rate to include a neutrino chemical potential following the derivation in [115, 117]. The Boltzmann equation

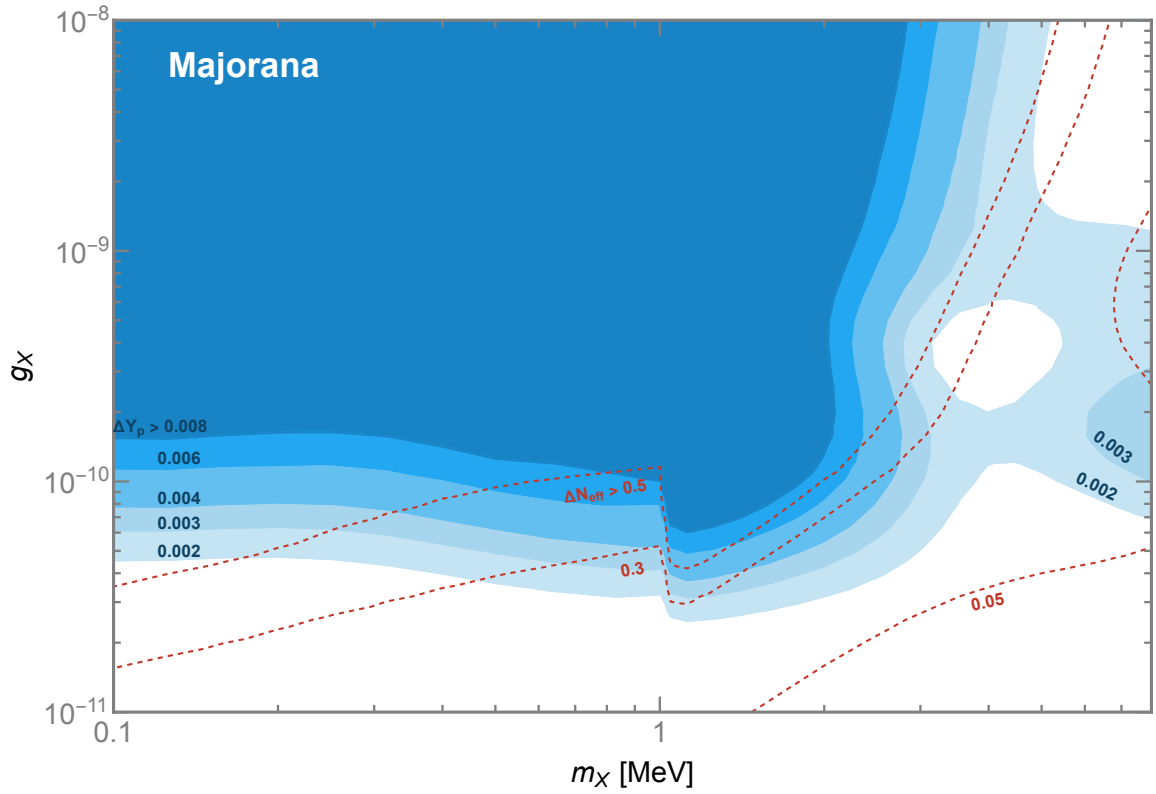


Figure 22. ΔY_p contours for "Majorana" neutrino case. The dashed red lines show the contours from our calculation of $\Delta N_{\rm eff}$ observed by the CMB, from figure 20. A conservative upper bound is $\Delta Y_p = 0.008$ at 95% C.L. [110], see section 3.7 for further discussion.

describing the evolution of neutron fraction $X_n = \frac{n_n}{n_n+n_p}$ is [127]:

$$\frac{dX_n}{dt} = \Gamma_{pn}(1 - X_n) - \Gamma_{np}X_n, \tag{3.41a}$$

$$\Gamma_{np} = K\int_1^\infty d\epsilon \left[\frac{(\epsilon - q)^2(\epsilon^2-1)^{1/2}\epsilon}{(1+e^{-\epsilon z_\gamma})(1+e^{(\epsilon-q-\tilde{\mu}_\nu)z_\nu})} + \frac{(\epsilon + q)^2(\epsilon^2-1)^{1/2}\epsilon}{(1+e^{\epsilon z_\gamma})(1+e^{-(\epsilon-q-\tilde{\mu}_\nu)z_\nu})}\right], \tag{3.41b}$$

$$\Gamma_{pn} = \Gamma_{np}(-q), \tag{3.41c}$$

where $z_i = m_e/T_i$, $\tilde{\mu}_\nu = \mu_\nu/m_e$, $q = (m_n - m_p)/m_e$, and $K \simeq (1.939\tau_n)^{-1}$. We take $m_n - m_p = 1.2933$ MeV and neutron lifetime $\tau_n = 878.4$ s [111]. Here Γ_{np} is the rate for neutron to proton conversion through the weak interactions $n + \nu_e \leftrightarrow p + e^-$, $n + e^+ \leftrightarrow p + \bar{\nu}_e$, and $n \leftrightarrow p + e^- + \bar{\nu}_e$. The evolution of T_γ, T_ν and μ_ν

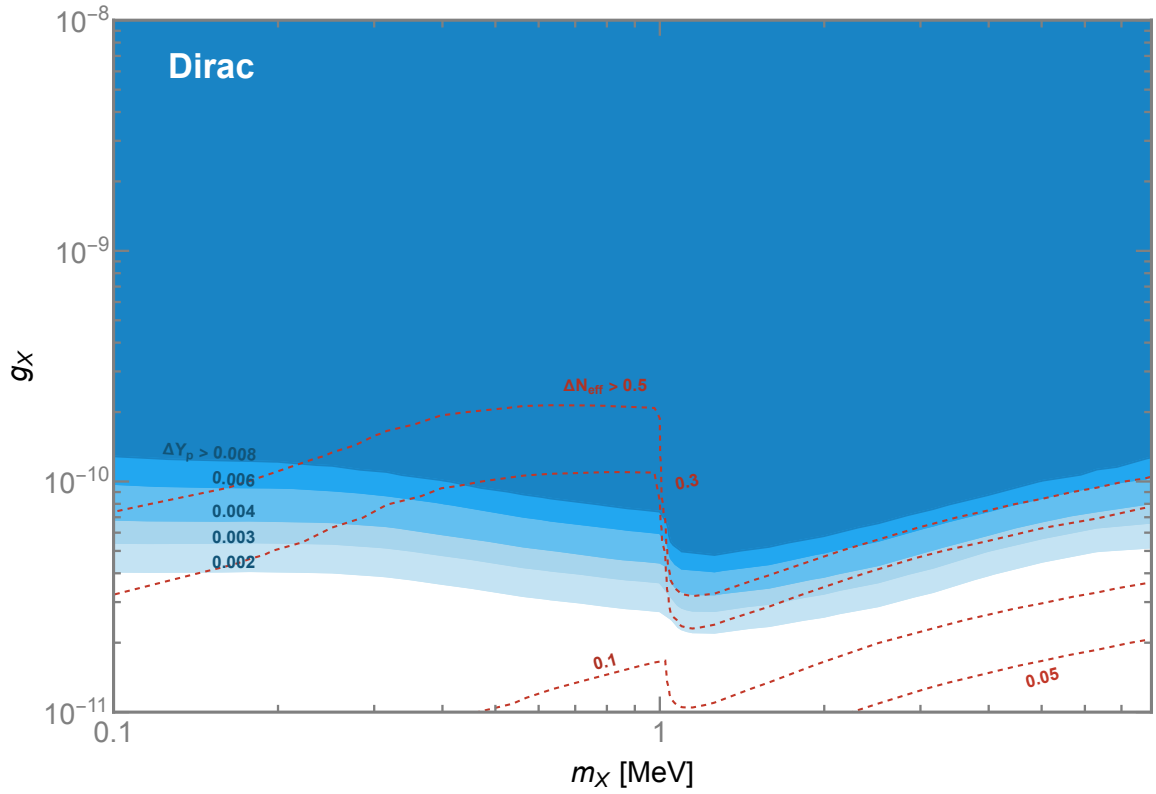


Figure 23. Same as figure 22, but for the "Dirac" neutrino case. The dashed red lines show the contours from our calculation of ΔN_{eff} observed by the CMB, from figure 21.

are obtained separately, by solving equation (3.13) as described in section 3.4.2. To estimate the helium abundance Y_p, we take the limit where all remaining neutrons form helium around the temperature where photons no longer dissociate deuterium $T_D = 0.073$ MeV; in other words,

$$Y_p \simeq 2X_n|_{T=T_D} \,. \tag{3.42}$$

In the SM, applying this procedure yields $Y_p|_{\text{SM}}^{\text{equation 3.42}} = 0.248$ in agreement with $Y_p|^{\text{PDG}} = 0.245 \pm 0.006$ at 95% C.L. [111]. We define the BSM deviation of helium abundance as

$$\Delta Y_p = Y_p|_{\text{BSM}}^{\text{equation 3.42}} - Y_p|_{\text{SM}}^{\text{equation 3.42}}. \tag{3.43}$$

The ΔY_p contours for the Majorana and Dirac case are shown in Figs. 22,23, along with overlays of the respective $\Delta N_{\rm eff}$ contours in red. In accordance with the discussion in section 3.5.5, a conservative upper bound is $\Delta Y_p = 0.008$ at 95% C.L. In both the Majorana and Dirac cases, $\Delta N_{\rm eff}$ constraints are stronger for $m_X > 2m_e$. However, in the Dirac case, we find $\Delta Y_p \gtrsim 0.008$ in the mass region 0.3 MeV $\lesssim m_X \lesssim 2m_e$, where the Planck constraint from the CMB, $\Delta N_{\rm eff} \lesssim 0.3$ is currently weaker. Once the future CMB observatories reach $\Delta N_{\rm eff} \lesssim 0.15$, their constraints will exceed what can be set by this analysis of BBN.

3.8 Discussion

In this paper we calculated the contributions of a light $U(1)_{B-L}$ gauge boson mediator to $\Delta N_{\rm eff}$ as measured by the CMB and Y_p from BBN. Our main result is Figs. 20,21, where we show our predictions for $\Delta N_{\rm eff}$ as a function of of the $U(1)_{B-L}$ gauge boson mass m_X and coupling strength g_X, along with Figs. 22,23 where we show our predictions for the shift in the helium mass fraction ΔY_p, in the same parameter space. While substantial portions of the (m_X, g_X) parameter space have overlapping constraints from other astrophysical or terrestrial experiments, we find there are several regions where future CMB observatories [342, 361–365], have the opportunity to gain sensitivity to a very weakly coupled $U(1)_{B-L}$ gauge boson in certain mass and coupling ranges that is not accessible by any other method.

We have also calculated ΔY_p, the helium abundance, which serves as a proxy for $\Delta N_{\rm eff}$ as observed by BBN. This result utilized an approximation from Ref. [141] to estimate the change in the helium abundance that follows from a nonzero neutrino chemical potential, as occurs with a freeze-in abundance of a $U(1)_{B-L}$ gauge boson. In figure 22, we find that for the Majorana case, the Planck constraints on the CMB are generally stronger than the BBN constraints on Y_p throughout the (m_X, g_X)

plane. For the Dirac case shown in figure 23, however, there is a nontrivial region of parameter space (approximately 0.3 MeV $\lesssim m_X \lesssim$ 1 MeV, $g_X \lesssim 10^{-10}$), where the BBN constraints are stronger than the constraints from ΔN_{eff} from Planck data. However, future CMB observatories [342, 361–365], will be able to fully cover this region, and probe considerably smaller couplings, once they achieve $\Delta N_{\text{eff}} \lesssim 0.1$ sensitivity.

It is interesting to consider whether thermal equilibrium is ever achieved between X and the SM. In general, for large enough couplings, there will be an epoch where we can identify equilibrium. This occurs when the comoving energy densities of X and one or more SM species reach approximately constant values. This epoch cannot last forever, since X subsequently decays back into the SM. For example, in figure 2 where $m_X = 10$ keV, X clearly reaches thermal equilibrium with neutrinos when $g_X = 10^{-10}$, as shown by the plateau of the energy density for a finite range of temperature. The next contour, $g_X = 10^{-11}$, there is hardly any range of temperature where the X density remains constant, and so we see that for this coupling, X approaches thermal equilibrium with neutrinos but never really achieves this before X subsequently decays. Similar results can also be found for the Dirac case, comparing $g = 10^{-10}$ to $g = 10^{-11}$ in figure 4. In the region $m_X \ll 2m_e$, broadly we find that X and neutrinos approximately achieve thermal equilibrium, for a brief point in the temperature evolution of the universe, in the $\Delta N_{\text{eff}} \sim 0.3$ (green) region in figure 5 and the $\Delta N_{\text{eff}} \sim 0.1$ (red) region in figure 6.

We also considered semi-analytic estimates of our ΔN_{eff} results. Our focus for these estimates was the region $m_X \ll 2m_e$, where the only species interacting with X are neutrinos. The semi-analytic estimates, which assume thermal equilibrium is reached between X and neutrinos, allow us to obtain an approximate value for

$\Delta N_{\rm eff} \simeq 0.25$ (0.09) for the Majorana (Dirac) case. The semi-analytic estimates also permit us to determine how our results change if there are additional degrees of freedom, beyond the SM, that the X boson is able to populate. The physical picture is that X slowly freezes in, becomes nonrelativistic, and then decays into SM states plus the additional degrees of freedom beyond the SM. For this analysis, we considered a set N_R of fermions carrying lepton number (right-handed neutrinos with $L = \pm 1$), in two scenarios: the additional fermions stay relativistic (at least until recombination), or the additional fermions have masses and become nonrelativistic matter. If the fermions stay relativistic, $\Delta N_{\rm eff} \to 0$ as N_R becomes large, essentially because they dominate the relativistic degrees of freedom after entropy equilibration. On the other hand, if they become nonrelativistic before recombination, they siphon off most of the relativistic degrees of freedom into matter, and so $N_{\rm eff} \to 0$ ($\Delta N_{\rm eff} \to -3$).

Our results have interesting implications on other scenarios considered in the literature:

Ref. [372] considered light new vectors produced gravitationally during inflation that also couple to neutrinos. The coupling to neutrinos imply the inflationary produced vector can decay into neutrinos, giving additional contributions to $\Delta N_{\rm eff}$, that led to constraints in the (m_X, g_X) plane. These contributions to $\Delta N_{\rm eff}$ rely on a primordial abundance of vector bosons from inflation, and thus constitute a contribution that is *in addition* to the freeze-in abundance of a massive vector that couples to neutrinos. On comparing our bounds to those from [372], we find our constraints would appear to place significant restrictions on the scale of inflation and hence the inflationary production of vector bosons that couple to neutrinos.

One of the additional effects of a light X boson, with a mass well below the neutrino decoupling temperature, $m_X \ll 2$ MeV, is that the interactions with X

can suppress the free streaming of neutrinos, and this has independent constraints from the suppression of small scale structure [373] that results in shifts in the phase and a decrease in the amplitude of the acoustic peaks of the CMB [138, 374–376]. Recently, [150] analyzed the suppression of neutrino free streaming resulting from neutrino interactions within the context of a model with a very light $U(1)_{\mu-\tau}$ gauge boson. By implementing these interactions into the modeling of the CMB, they were able to use Planck data to constrain a broad range of $U(1)_{\mu-\tau}$ gauge boson masses between 10^{-3} eV to 10^{3} eV, with the strongest bound on $g_{\mu-\tau}$ near 1 eV, and rapidly decreasing bounds as the mass moved away from this value. Nevertheless, for masses 1 eV and larger, [150] found that the bounds from $\Delta N_{\rm eff}$ are still stronger than those from the suppression of the free streaming of neutrinos. This is strongly suggestive that the bounds from $\Delta N_{\rm eff}$ are very likely stronger than constraints from the suppression of neutrino free streaming in the model considered in this paper, $U(1)_{B-L}$, though we leave a detailed analysis of this point to future work.

Several other papers have considered a light $U(1)_{B-L}$ gauge boson's effects in various contexts. For example, our work complements and extends the analysis of [51, 142, 147, 148], who considered bounds on a $U(1)_{B-L}$ model in which neutrinos acquire Dirac masses. Our work rules out substantial parts of previously allowed parameter space in [377], who considered constraints on $U(1)_{B-L}$ from neutrino-electron and neutrino-nucleon scattering. As can be seen in figure 20, the remaining region that is more strongly constrained by neutrino-nucleon scattering occurs only when $m_X \gtrsim 10$ MeV in the Majorana case. By contrast, when neutrinos have Dirac masses, the CMB constraints completely dominate the bounds even at larger masses as shown in figure 21 (that includes the results from [148]). Some groups [149,378–380] considered sterile neutrino dark matter arising from interactions with $U(1)_{B-L}$. While

our analysis of the CMB constraints does not rule out the main region favored by [380], essentially all of their parameter space $m_X \lesssim 10$ MeV would be in conflict with the CMB that extends and compliments the existing constraints from beam dump experiments. Ref. [149] calculated CMB constraints in the range $0.001 \text{ MeV} < m_X < 1 \text{ MeV}$, and while the broad trends they find in their paper are similar with our Majorana case results, they did not include a chemical potential for X and neutrinos, making a a quantitative comparison moot.

Beyond $U(1)_{B-L}$, there has also been extensive discussion of equilibration of a dark sector with neutrinos well after BBN [356, 381, 382]. The motivation of this work is to obtain thermal dark matter below an MeV [381, 382]. There are commonalities between this work and ours, specifically the observation that if a light state couples only to neutrinos, equilibration with neutrinos draws heat from the SM, and only after the species decouples, the neutrino bath is heated, contributing to ΔN_{eff}. The distinction between our work and [356, 381, 382] is that we find the Boltzmann equations require the presence of a nonzero chemical potential for X as well as neutrinos, in order to properly track the evolution of the energy densities of the various species, and therefore to accurately calculate ΔN_{eff}. For instance, when our X boson can decay into just one massive species (one massive "sterile" Majorana neutrino), this siphons off a sufficient amount of entropy from the left-handed neutrinos of the SM to already be excluded by Planck data. It would be very interesting to apply our analysis to the specific scenarios of [381,382], to determine if including a chemical potential for the mediators and DM has an effect on the results, but we leave for future work.

Note added: As this work was being completed [152] appeared that also discussed the bounds on a model with a light $U(1)_{B-L}$ (with Majorana neutrino masses) and

$U(1)_{\mu-\tau}$ boson from $\Delta N_{\rm eff}$. Among the differences between their work and ours, we include the coupling of the $U(1)_{B-L}$ mediator to charged leptons (electrons), and the associated $1 \leftrightarrow 2$, $2 \leftrightarrow 2$ processes that are essential to determining the effects on $\Delta N_{\rm eff}$ for temperatures near and above BBN.

APPENDIX A

GENERATING THE DARK MIXING ANGLE

Throughout the paper, we utilized the low energy effective theory of X^μ coupled to a linear combination of the electromagnetic current and $B-L$ current, Eq. 2.2, that can be written as $g_X \left[(\cos\varphi) j_\mu^{\rm EM} + (\sin\varphi) j_\mu^{B-L}\right] X^\mu$. We will not address the strength of the coupling, g_X. In the case of dark photon, generating a small kinetic mixing has been explored [383]; for $B-L$, a small coupling could arise from a gauged (and then spontaneously broken) $U(1)_{B-L}$ group that simply has a small gauge coupling. The question we wish to address is how a dark mixing angle φ could generated by UV physics.

Here we consider extending the SM to include a gauged $U(1)_{B-L}$ at a high scale that is, at lower energies, spontaneously broken to generate a mass for the vector boson that couples to $B-L$. It is well known (e.g., [51,74]) that one-loop corrections arising from matter that transforms under both $U(1)_{B-L}$ and $U(1)_Y$ will lead to these gauge bosons mixing with each other, see Fig. A.24. In the case that is of most interest to us, $g_{B-L} \ll g_Y$, the hypercharge gauge boson remains virtually unchanged due to this mixing. Instead, the gauge boson that (initially) couples to $B-L$, however, will have a sizable one-loop induced coupling to the hypercharge current. The contributions to the loop corrections include "threshold" or "matching" finite corrections from heavy

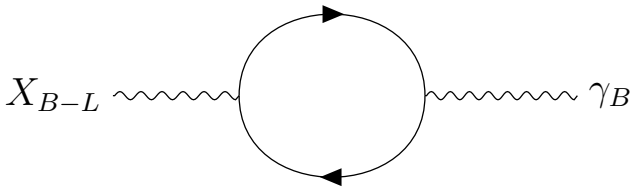


Figure A.24. Contributions to the mixing of $B-L$ with hypercharge.

fields that transform under both $U(1)_{B-L}$ and $U(1)_Y$, as well as renormalization group generated mixing from light fields (including SM fields).

For example, assuming that X^μ couples to just $B-L$ at a high scale $\mu_{\rm high}$, the leading renormalization group induced contribution to hypercharge (and ultimately electric charge) is

$$\epsilon e \;=\; \epsilon g_Y \cos\theta_W \;\simeq\; -\frac{b_{\rm SM}\cos\theta_W}{16\pi^2} g_Y^2 g_{B-L} \ln\frac{\mu_{\rm high}}{\mu_{\rm low}}\,. \tag{A.1}$$

The coefficient $b_{\rm SM} = 32/3$ $(26/3)$ includes (does not include) three right-handed neutrinos. A sizable coupling of X^μ to the electromagnetic current is possible even with just the SM field content and a large amount of renormalization group evolution. Moreover, it is interesting that the SM field content leads to φ evolving *towards* the chargephobic limit ($\varphi > \pi/2$). We caution, however, that Eq. (A.1) is just the leading result; once ϵg_Y is comparable to g_{B-L} there are significant corrections from additional contributions in the RGE. To achieve an arbitrary angle $0 < \varphi < \pi$, additional matter beyond the SM is needed either as threshold corrections or as light(er) fields contributing to the renormalization group evolution.

APPENDIX B

RENORMALIZATION GROUP EQUATIONS

In the chargephobic limit, X^μ couples the linear combination $-j_\mu^{\rm EM} + j_\mu^{B-L}$, corresponding to the mixing angle $\varphi = 3\pi/4$, or equivalently $\epsilon e = -g_{B-L}$. The mixing angle is not stable under renormalization group evolution. We can determine the running of φ by first determining the RGEs of the individual couplings. RGEs have been considered before in similar contexts [384–387]. In our case, the RGEs are given by

$$\mu\frac{de}{d\mu} = \frac{1}{12\pi^2}e^3\sum_i N_c^i Q_i^2 \tag{B.1}$$

$$\mu\frac{dg_{B-L}}{d\mu} = \frac{1}{12\pi^2}g_{B-L}\sum_i N_c^i\left[g_{B-L}^2 q_i^2 + (\varepsilon e)^2 Q_i^2 + 2g_{B-L}(\varepsilon e)Q_i q_i\right] \tag{B.2}$$

$$\mu\frac{d\varepsilon e}{d\mu} = \frac{1}{12\pi^2}\sum_i \left[g_{B-L}^2(\varepsilon e)q_i^2 + (\varepsilon e)^3 Q_i^2 + 2e^2(\varepsilon e)Q_i^2 + 2e^2 g_{B-L}Q_i q_i + 2g_{B-L}(\varepsilon e)^2 Q_i q_i\right] \tag{B.3}$$

where μ is the renormalization scale and the charges of the matter fermions contributing to the RGEs are given by Q_i (EM) and q_i $(B-L)$ in Sec. 2.2.1. Below $\sqrt{s} \sim 2\,\text{GeV}$, QCD is non-perturbative and it is mesons rather than quarks that determine thresholds in RGEs. For a detailed treatment see for example, [388, 389]. The precision obtained from this full treatment is not necessary to derive our constraints. Instead, we employ the following simplification: In the non-perturbative regime, $\sqrt{s} < 2\,\text{GeV}$, quarks are included perturbatively into the RGE at a scale corresponding to lightest meson that "contains" the quarks. Namely, the up and down quark charges are added at the pion mass, the strange quark at the mass of the lightest Kaon, and the charm at the mass of the lightest D meson.

We can solve the RGEs, Eqs. (B.1)-(B.3), to obtain the running of the dark mixing angle as a function of the renormalization scale. This is illustrated in Fig. B.25, where we show the extent of $\varphi(\mu)$ evolution following any given initial value $\varphi_0(\mu =$

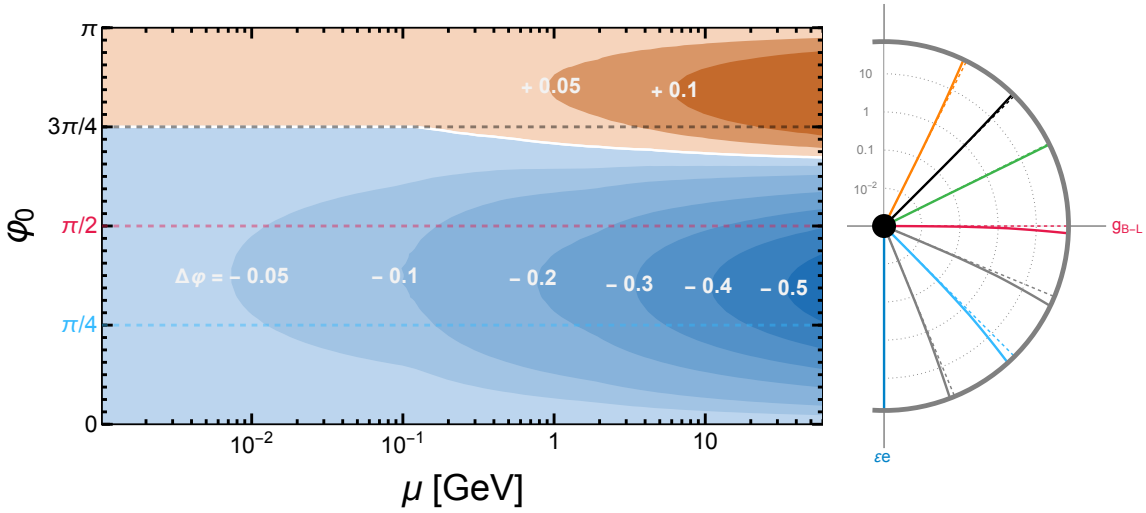


Figure B.25. The running of the dark mixing angle with initial value φ_0 at $\mu = m_e$. The plot on the left contains blue (orange) contours to indicate the negative (positive) deviation from initial dark mixing angle, $\Delta\varphi = \varphi(\mu) - \varphi_0$. The white line represents $\Delta\varphi = 0$ and we note that the chargephobic limit coincides with this line until the pion mass threshold. The plot on the right illustrates the shift using a compass plot as in Fig. 2 for selected dark mixing angles. Here, the radial direction also indicates the renormalization scale μ. Explicitly, the center of the compass corresponds to $\mu = m_e$, the outer thick gray arc to $\mu = 60\,\text{GeV}$, and the dotted arcs to intermediate values of μ.

m_e) up to $\varphi(\mu = 60\text{ GeV})$. Overall, the shifts are relatively modest, which is evident in how the needles on the compass plot are slightly shifted shown in Fig. B.25. Notice that the angle $\varphi(\mu)$ can shift towards positive or negative values depending on the initial value.

In the chargephobic model, we numerically solve Eqs. (B.1)–(B.3) to obtain the running of x_e as shown in Fig. B.26, which also shows the sum of charges at each mass threshold for various configurations of charge assignments. However, one can understand the results more easily by working in the limit $g_X = \sqrt{(\varepsilon e)^2 + g_{B-L}^2} \ll e$,

and then the RGEs simplify to

$$\mu\frac{de}{d\mu} = \frac{1}{12\pi^2}e^3\sum_i N_c^i Q_i^2 \tag{B.4}$$

$$\mu\frac{d\varepsilon e}{d\mu} = \frac{1}{6\pi^2}e^2\sum_i N_c^i\left[(\varepsilon e)Q_i^2 + g_{B-L}Q_i q_i\right] \qquad (g_X \ll e \text{ limit}). \tag{B.5}$$

Here, we have taken g_{B-L} to be constant since the leading contribution to its running is $\mathcal{O}(g_X^3)$ as compared with εe that receives its leading contribution at order $\mathcal{O}(g_X e^2)$. Interestingly, leptons do not contribute to the running of εe. This is clear because the lepton charges satisfy $Q_l^2 = Q_l q_l$ (and neutrinos do not contribute $q_\nu = 0$), and so at the chargephobic mixing angle, $\varepsilon e = -g_{B-L}$, the contribution of leptons to the term in square brackets in Eq. (B.5) vanishes.

The main driver of the εe running is the e running itself. A simple but useful analytic approximation for $\varepsilon e[\mu]$ can be obtained by running e starting at the pion threshold then suppressing the solution by ε. The result is

$$x_e[\mu] = -\frac{1}{\sqrt{2}}\left(1 - \frac{1}{\sqrt{1 - \frac{e^2}{6\pi^2}\left(\frac{11}{3}\right)\log\left(\frac{\mu}{m_\pi}\right)}}\right) \approx \frac{\sqrt{2}}{24\pi^2}\frac{11}{3}e^2\log\left(\frac{\mu}{m_\pi}\right) \qquad \text{(analytic approx.)} \tag{B.6}$$

where the factor of 11/3 is the squared charge sum of the electron, muon, up and down quarks all of which contribute to the running of e above $\mu = m_\pi$. The running of εe can be reformulated into the running of φ. The deviation from φ_0 is

$$\delta\varphi \approx \frac{e^2}{24\pi^2}\left(\frac{11}{3}\right)\log\left(\frac{\mu}{m_\pi}\right). \tag{B.7}$$

Notice that mixing angle receives a positive contribution at larger renormalization scales when starting from the chargephobic limit. This means X^μ slightly shifts from equal couplings $g_X = |\varepsilon e|/\sqrt{2} = g_{B-L}/\sqrt{2}$, to one where X^μ couples *slightly* more to the to the electromagnetic current relative to $B-L$ (φ evolves towards values slightly larger than $3\pi/4$.)

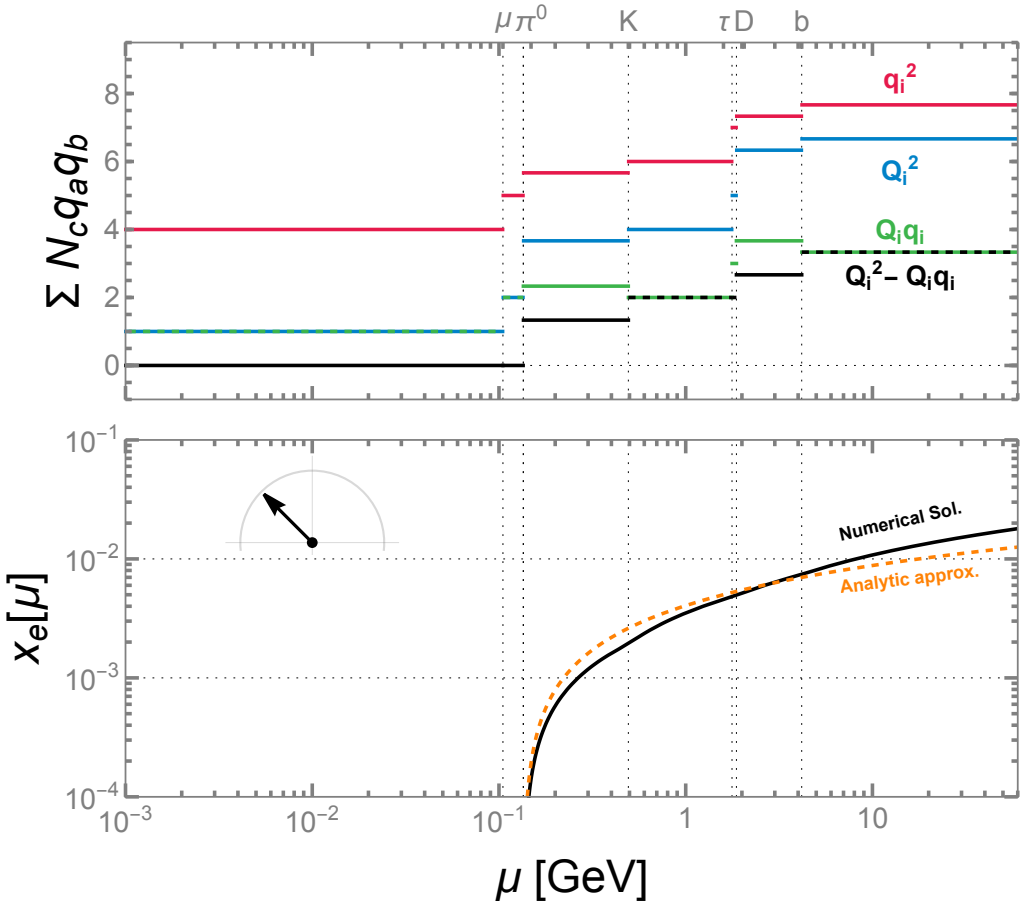


Figure B.26. (Top) the squared charge sum of particles contributing to the RGE at threshold and (bottom) x_e running using the full numerical solution of Eq. B.1-B.3 shown in black for $g_X = 10^{-2}$ or using the simple analytic approximation ($g_X \ll e$) as discussed in the text (orange dashed).

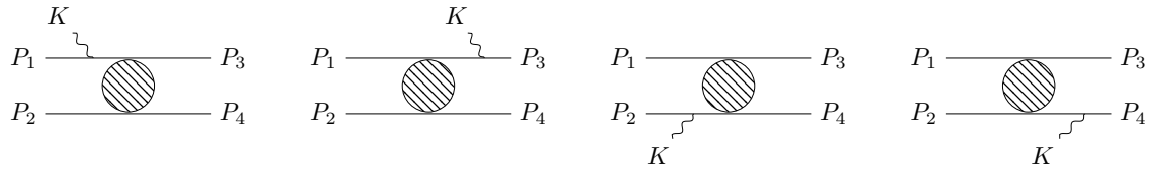
Now let's briefly describe the effect of the renormalization group evolution of φ on various observables. For the purposes of this discussion, we take $\varphi = 3\pi/4$ at low energies, and then consider the effects of the shifts in the couplings of X^μ for observables that are sensitive to energies $\sqrt{s} \gtrsim m_\pi$ where deviations from chargephobic begin to occur, see Fig. B.26. The dominant effect is the appearance of a small coupling of X^μ to charged leptons, since this is a critically important mode for X^μ to be observed. The tail end of current beam dump experiment sensitivity extends into the region $m_\pi < m_X \lesssim 800$ MeV, however we find that the branching fraction $Br(X \to \ell^+\ell^-)$ remains small enough that these experiments remain insensitive in this region. Most of the supernova constraint region is also below the pion mass threshold, and so is not expected to change. The one region that requires a more careful analysis is the low energy supernova constraints (the region labeled LESNe in Fig. 3 [45]). However, it is likely that the hadronic decay of $X \to \pi^+\pi^-$ is the most important mode at larger chargephobic masses $m_X \gtrsim 300$ MeV, and this will require a detailed analysis to determine the sensitivity to a chargephobic vector boson.

The most prominent re-appearance of experiments are LHCb constraints (shown in green in Fig. 4) and the neutrino-electron scattering experiments TEXONO and CHARM (shown in pink and orange in Fig. 4). However, these constraints are subdominant to CEνNS and EWP constraints respectively.

APPENDIX C

BREMSSTRAHLUNG IN PROTO-NEUTRON STAR

The bremsstrahlung channels that contribute to absorption in a general φ model are



(C.1)

where $P_i = \{E_i, \vec{\beta}_i\}$, and $K = \{\omega, \vec{v}\}$ are the momenta of nucleons and X and the shaded circle represents the nucleon-nucleon interaction which takes into account long-distance component arising from pion-exchanges and short-distance components that contribute to nucleon-nucleon scattering [197]. We will designate the charge q_1, q_2 to the upper and lower legs of the diagrams respectively. Following the derivation in [191] with the necessary adjustments, the absorption width

$$\Gamma_{\rm SRA} \simeq \frac{n_i n_j}{256\pi^5 S_{\mathbf{L},\mathbf{T}} \omega T^3 m_N^{7/2}} \int d\cos\theta_{\rm CM} d^3\vec{p}_+ d^3\vec{p}_- \overline{(\tilde{\varepsilon}\cdot J)}^2 e^{-\frac{|\vec{p}_+|^2+|\vec{p}_-|^2}{4m_N T}} \sqrt{T_{\rm CM}} \frac{d\sigma_{ij}}{d\cos\theta_{\rm CM}}, \tag{C.2}$$

where $S_{\mathbf{L}}(S_{\mathbf{T}}) = 1(2)$ is the spin degeneracy of the polarization states, n_i is the number density of nucleons, m_N is the nucleon mass, $T_{\rm CM} = (\vec{p}_1 - \vec{p}_2)^2/4m_N$ is the center of mass kinetic energy, $\vec{p}_\pm = \vec{p}_1 \pm \vec{p}_2$, $\theta_{\rm CM}$ is the scattering angle. Furthermore, $\tilde{\varepsilon}_\mu$ is the X polarization,

$$J^\mu = \left[q_1 \left(\frac{P_1}{P_1\cdot K} - \frac{P_3}{P_3\cdot K} \right) + q_2 \left(\frac{P_2}{P_2\cdot K} - \frac{P_4}{P_4\cdot K} \right) \right]^\mu, \tag{C.3}$$

is the quadrupole current, and $\overline{(\tilde{\varepsilon}\cdot J)}^2 \equiv \int d\Omega' \, \Sigma_{\rm pols.} (\tilde{\varepsilon}_\mu J^\mu)^2$ integrated over the X scattering angle. To leading order, this integral projected onto the transverse and

longitudinal polarizations is

$$\overline{(\tilde{\varepsilon}\cdot J)}^2_{\mathbf{L},\mathbf{T}} = \frac{8\pi}{15}\frac{T_{\rm CM}}{m_N\omega^2}\begin{cases}\left[10q_-^2(1-\cos\theta)+3v^2\frac{T_{\rm CM}}{m_N}q_+^2(1-\cos^2\theta)\right] & (\mathbf{T})\\ \left[5q_-^2(1-\cos\theta)+2v^2\frac{T_{\rm CM}}{m_N}q_+^2(1-\cos^2\theta)\right](1-v^2) & (\mathbf{L})\end{cases} \tag{C.4}$$

where $q_\pm = q_1 \pm q_2$. The width in Eq. C.2 for the transverse mode becomes

$$\Gamma_{\rm SRA|\mathbf{T}} = \frac{n_i n_j}{30\pi^{1/2}\omega^3 m_N^3 T^{3/2}}\int |\vec{p}_-|^2 d|\vec{p}_-| e^{-|\vec{p}_-|^2/4m_N T} T_{\rm CM}^{3/2}\left[10q_-^2\sigma_{ij}^{(2)} + 3v^2\frac{T_{\rm CM}}{m_N}q_+^2\sigma_{ij}^{(4)}\right], \tag{C.5}$$

where the p_+ integral was evaluated to $\int |\vec{p}_+|^2 e^{-|\vec{p}_+|^2/4m_N T} d|\vec{p}_+| = 2\sqrt{\pi(m_N T)^3}$ and we defined

$$\sigma_{ij}^{(2)}(T_{\rm CM}) \equiv \int d\cos\theta_{\rm CM}(1-\cos\theta_{\rm CM})\frac{d\sigma_{ij}}{d\cos\theta_{\rm CM}} \tag{C.6}$$

$$\sigma_{ij}^{(4)}(T_{\rm CM}) \equiv \int d\cos\theta_{\rm CM}(1-\cos^2\theta_{\rm CM})\frac{d\sigma_{ij}}{d\cos\theta_{\rm CM}}. \tag{C.7}$$

Finally, we change to a dimensionless variable $x = T_{\rm CM}/T$ and do the $|p_-|$ integral and go through a similar process for the longitudinal mode to get inverse bremsstrahlung rate

$$\Gamma_{\rm ibr|\mathbf{L},\mathbf{T}} = \frac{8n_i n_j}{15\pi^2\omega^3 S_{\mathbf{L},\mathbf{T}}}\left(\frac{\pi T}{m_N}\right)^{3/2}\begin{cases}\left[10q_-^2\langle\sigma_{ij}^{(2)}\rangle + 9q_+^2\frac{Tv^2}{m_N}\langle\sigma_{ij}^{(4)}\rangle\right] & (\mathbf{T})\\ \left[5q_-^2\langle\sigma_{ij}^{(2)}\rangle + 6q_+^2\frac{Tv^2}{m_N}\langle\sigma_{ij}^{(4)}\rangle\right](1-v^2) & (\mathbf{L})\end{cases} \tag{C.8}$$

where

$$\langle\sigma_{ij}^{(2)}(T)\rangle = \frac{1}{2}\int_0^\infty dx e^{-x}x^2\sigma_{ij}^{(2)}(xT) \tag{C.9}$$

$$\langle\sigma_{ij}^{(4)}(T)\rangle = \frac{1}{6}\int_0^\infty dx e^{-x}x^3\sigma_{ij}^{(4)}(xT) \tag{C.10}$$

are the energy and angle-averaged nucleon nucleon scattering cross section found in [197]. The calculation for production rate is identical with the restriction that the X^μ energy must not exceed the energy of the collision. This takes $\int_0^\infty \to \int_{\omega/T}^\infty$; for example $\langle\sigma_{ij}^{(2)}(T)\rangle \to \langle\sigma_{ij}^{(2)}(T,\omega)\rangle = \frac{1}{2}\int_{\omega/T}^\infty dx e^{-x}x^2\sigma_{ij}^{(2)}(xT)$.

APPENDIX D

RIGHT-HANDED NEUTRINO DECAY IN MAJORANA CASE

In the regime $M_R > m_h + m_\nu$, the 2-body decay is rapid, and the right-handed neutrinos will have completely decayed well prior to BBN. When $M_R < m_h$, the decay is 3-body, with an off-shell Higgs that will also be suppressed by the small Yukawa coupling $y_{\rm SM}$ of the Higgs to lighter SM fermions. An estimate of this 3-body width to one SM fermion pair is sufficient for our purposes,

$$\Gamma(\nu_R \to \nu_L f \bar{f}) \;\sim\; \frac{y_D^2 y_{\rm SM}^2 M_R^5}{128\pi^3 m_h^4}\,, \tag{D.1}$$

where we have neglected the final state phase space. If a SM neutrino species has a mass $m_\nu \sim (y_D v)^2/M_R$, the width becomes

$$\Gamma(\nu_R \to \nu_L f \bar{f}) \;\sim\; \frac{m_\nu y_{\rm SM}^2 M_R^6}{128\pi^3 v^2 m_h^4} \tag{D.2}$$

leading to a lifetime

$$\tau(\nu_R \to \nu_L f \bar{f}) \;\sim\; (1\text{ s}) \times \left(\frac{10\text{ GeV}}{M_R}\right)^6 \times \left(\frac{0.1\text{ eV}}{m_\nu}\right) \times \left(\frac{y_b}{y_{\rm SM}}\right)^2\,, \tag{D.3}$$

where we have normalized the Yukawa coupling $y_{\rm SM}$ to the b-quark Yukawa coupling. If $M_R \gtrsim 2m_b$, we expect ν_R to decay predominantly a $b\bar{b}$ pair since this is the heaviest SM fermions that are kinematically available for the 2-body decay. If M_R is slightly less than the $2m_b$ threshold, decays to $c\bar{c}$ and $\tau^+\tau^-$ would be present, with $y_{\rm SM}$ slightly smaller than y_b.

In any case, the above estimate demonstrates that for $M_R \lesssim 10$ GeV, ν_R are comparatively long-lived and can disrupt BBN light element abundance predictions due to the electromagnetic energy deposition [390]. Given that the width, equation (D.2), depends on the 6th power of M_R, one only needs slightly larger masses, $M_R \gtrsim 20$ GeV, to cause ν_R to decay sufficiently fast to completely avoid BBN constraints.

This leads to two possibilities in the Majorana scenario:

If ν_R was in thermal equilibrium in the early Universe, $M_R \gtrsim 20$ GeV is required to avoid BBN constraints, and thus $v_X \gtrsim (20 \text{ GeV})/y_M$. If X^μ acquires *all* of its mass from just the ϕ_X vev, then m_X is determined once g_X is specified, specifically, $m_X = 2g_X v_X$. The scalar Higgs sector of $U(1)_{B-L}$ need not be minimal. There could be other scalars with $B-L$ charge that differ ϕ_X, i.e., $\phi_{X'}$ with $q_{X'} \neq \pm 2$. These do not lead to contributions to the Majorana masses, but will lead to an additional contribution to the X^μ gauge boson mass, $m_X^2 = g_X^2\,(4v_X^2 + q_{X'}^2 v_{X'}^2)$. Hence, we see that the minimal case $m_X = 2g_X v_X$ is a *lower* bound on m_X for a generic $U(1)_{B-L}$ breaking sector. Said directly, the bound $M_R \gtrsim 20$ GeV implies

$$\begin{aligned} g_X &< \frac{m_X}{2v_X} \\ &\lesssim 2.5 \times 10^{-5} \frac{m_X}{1 \text{ MeV}} \qquad \text{(if } \nu_R \text{ in early thermal equilibrium).} \end{aligned} \tag{D.4}$$

On the other hand, it could be that ν_R was never in thermal equilibrium in the early universe. In this case, no population of ν_R's were generated, and there is no bound on g_X from ν_R decay.

APPENDIX E

FINITE TEMPERATURE EFFECTS

In the SM, finite temperature effects [120,141,349] result in an $\mathcal{O}(0.01)$ correction to $N_{\rm eff}$. One example is the finite shift in the photon's propagator due its self-energy $\Pi_{\mu\nu}$ in presence of an e^+e^- background. This shift generates a complex effective mass for the photon and modifies the dispersion relation of the longitudinal and transverse spin polarizations of the photon. To $\mathcal{O}(\alpha)$, a simplified version of the effective masses is

$$m_\gamma^2 = \begin{cases} 4\pi\alpha(n_e/m_e) & (T \ll m_e) \\ \frac{2}{3}\pi\alpha T^2 & (T \gg m_e). \end{cases} \tag{E.1}$$

A similar story generates an effective mass for electrons

$$m_{e,\rm eff}^2(T) \approx m_{e,0}^2 + \pi\alpha T^2. \tag{E.2}$$

Note that $m_\gamma(T) < 2m_{e,\rm eff}(T)$ and hence photon decay to e^+e^- pair is always kinematically forbidden.

Finite temperature correction to early universe dynamics with an additional hidden photon (which we label X for convenience) has also been explored in [391–397] and most relevant to our discussion here are [135, 350, 353, 398]. We will summarize this discussion and use the results to calculate the contribution of finite temperature effects in our model. In what follows, we only take the transverse part of photon polarization tensor, since it was shown in [135] that the longitudinal part of the photon polarization tensor does not significantly contribute to the finite temperature effects.

Following [353], for a given interaction $a\bar{a} \to X$, one can write the additional interaction $a\bar{a} \to \gamma \to X$, where $\gamma \to X$ is the contribution of all allowed fermion loops in medium. In vacuum, such interactions are loop-suppressed and are

negligible. However, in a medium with finite temperature/density, these interactions are important and can, in some cases, dominate the rate [191, 192, 210, 353, 399, 400]. The $a\bar{a} \to \gamma \to X$ diagram is proportional to

$$e\frac{-i}{k^2 - \Pi_{\gamma-(f)-\gamma}} i\Pi_{\gamma-(f)-X}, \tag{E.3}$$

where e is the electromagnetic coupling, the second piece is the in-medium photon propagator, and the third is the induced $\gamma - X$ mixing in medium. Assuming the two polarization tensors have the same fermion loops, then $\Pi_{\gamma-(f)-X} = (g_X/e)\Pi_{\gamma-(f)-\gamma}$. The sum of the two diagrams is now given by

$$(a\bar{a} \to X) + (a\bar{a} \to \gamma \to X) \propto g_X \left(1 + \frac{\Pi_{\gamma\gamma}}{k^2 - \Pi_{\gamma\gamma}}\right) \tag{E.4}$$

$$= g_X \frac{m_X^2}{m_X^2 - \Pi_{\gamma\gamma}}, \tag{E.5}$$

and the modification to the coupling in medium can be written as,

$$g_{X,m}^2 = \frac{g_X^2 m_X^4}{|m_X^2 - \Pi|^2} = \frac{g_X^2 m_X^4}{(m_X^2 - m_\gamma^2)^2 + (\mathrm{Im}\,\Pi)^2}, \tag{E.6}$$

where $\mathrm{Re}\,\Pi = m_\gamma^2$ in Eq. E.1. The imaginary part $\mathrm{Im}\,\Pi$ [211] encodes the rate at which the photon's distribution approaches a thermal equilibrium,

$$\mathrm{Im}\,\Pi = -\omega\Gamma \equiv -\omega[\Gamma_{\mathrm{decay}}(\omega) + \Gamma_{\mathrm{inverse}}(\omega)]. \tag{E.7}$$

The imaginary part of the self-energy arises at two-loops and we generically have $\mathrm{Im}\,\Pi \ll \mathrm{Re}\,\Pi$. The effective coupling in Eq. E.6 can be discussed in three regimes; $m_\gamma(T) \gg m_X$, $m_X = m_\gamma(T_r)$, and $m_\gamma(T) \ll m_X$. The middle regime, $m_X = m_\gamma(T_r)$, is resonant. If the resonance occurs when the electrons are relativistic, $T \gg m_e$, the resonance temperature is

$$T_r = \sqrt{\frac{3}{2\pi\alpha}} m_X \approx 8 m_X \qquad (T \gg m_e). \tag{E.8}$$

If the electrons are non-relativistic when the resonance occurs then $m_\gamma(T_r) \propto T_r^{3/2} e^{-m_e/T_r}$ as per Eq. E.1. The photon plasma mass is extremely sensitive to T and

the resonance occurs around $T_r \sim 0.2 m_e$ for a wide range of masses $m_X \sim (1 - 10^5\,\mathrm{eV})$. We now discuss the regimes.

E.1 $m_\gamma(T) \ll m_X$

In this regime, the in-medium coupling $g_{X,m}$ reduces to its vacuum value g_X. We start by examining the entropy scaled number density $Y_X = n_X/s$ produced from forward interactions to X using only the vacuum coupling. We write the simplest Boltzmann equation

$$s\dot{Y}_X = \dot{n}_X + 3Hn_X = \sum_a \frac{3}{2\pi^2}\Gamma_{X\to a\bar{a}} m_X^2 T K_1(m_X/T). \tag{E.9}$$

Here, we have assumed massless particles a with zero chemical potential and took the Maxwell-Boltzmann approximation for distributions in the collision term. Explicitly, the collision term includes $e^+e^- \to X$ and $\nu_i\bar{\nu}_i \to X$. The final Y_X^f from the following two forward interactions can be calculated

$$Y_X = \int_0^\infty dT \frac{\dot{Y}_X}{H(T)T} = \frac{3}{16\pi^2}\frac{g_X^2 m_X^4}{[Hs]_{T=m_X}} \times \begin{cases} (1) & (e^+e^- \to X) \\ (\frac{3}{2}) & (\nu\bar{\nu} \to X)\,. \end{cases} \tag{E.10}$$

In the next sections, we show that the finite temperature effects contributions to Y_X are negligible compared to Eq. E.10.

E.2 $m_\gamma(T) \gg m_X$

Here, the coupling $g_{X,m}$ is suppressed by a factor of m_X^2/m_γ^2 compared to its vacuum counterpart. However, this suppression occurs above resonance, $T_r > 8m_X$, where the X production rates are inefficient even in the vacuum case. In our Boltzmann evolution of X population and for small values of g_X, a negligible amount of X is produced in this temperature range. This makes this regime unimportant for our analysis, since this suppression would only decrease the amount of X produced. We ignore this regime in all subsequent discussion.

E.3 $m_\gamma(T) = m_X$ resonance

We now discuss the interactions that are allowed during the resonance and thus contribute to the resonant X production. *Importantly, the second diagram in Eq. E.4 does not exist for $\nu_i\bar{\nu}_i \to X$. The neutrino coalescence rate is not changed by finite temperature effects* [1]. Thus, Our treatment of neutrinos rates is complete and neutrinos do *not* contribute to the resonance. Furthermore, $e^+e^- \to X$ is kinematically allowed only for $m_X > 2m_{e,\text{eff}}$ or when

$$T \leq T_c = \sqrt{\frac{m_X^2 - 4m_{e,0}^2}{4\pi\alpha}} < T_r. \tag{E.11}$$

Hence, e^+e^- coalescence also does *not* contribute to the resonance since the interaction is only allowed for temperatures strictly below T_{res}. This point is emphasized in [350], but missed in more recent literature [135,398]. The contribution to the resonance in both our and the hidden photon case, comes from pair annihilation $e^+e^- \leftrightarrow \gamma X$ and semi-Compton $e\gamma \leftrightarrow eX$. The resonant production increases the initial value of ρ_X at the expense of energy density of the $e-\gamma$ plasma. The decay of X back into SM particles is unchanged. Explicitly, a larger initial ρ_X or a smaller initial $\rho_{\gamma-e}$ causes an increase the value of ΔN_{eff}.

In this case, the entropy scaled number density $Y_{X,\,\text{res}}$ produced from the resonance through the interaction $a + b \to X + c$ is [350],

$$s\dot{Y}_X = \int dn_a dn_b \tilde{\sigma}_{2\to2}(s) v_{\text{Möl}} \frac{g_X^2 m_X^4}{(m_X^2 - m_\gamma^2)^2 + (\text{Im}\Pi)^2}, \tag{E.12}$$

where $\int dn_i = \int g_i dp_i^3 f_i/(2\pi)^3$, the $\tilde{\sigma} = \sigma/g_{X,m}^2$, and $v_{\text{Möl}}$ is the Moeller velocity. At resonance, expanding $m_\gamma^2 = m_X + (m_\gamma^2)'(T - T_r) + \ldots$ and using the narrow width

[1] The transfer rate $\delta\rho_{X\to\nu_i\bar{\nu}_i}/\delta t$ is proportional to the distribution f_X. The only modification to this rate at a given temperature stems from modifications to f_X from other enhanced electron interactions. Nonetheless, The coupling g_X in the neutrino coalescence rate is unchanged.

approximation,

$$\frac{g_X^2 m_X^4}{(m_X^2 - m_\gamma^2)^2 + (\mathrm{Im}\Pi)^2} = g_X^2 m_X^4 \frac{\pi}{(m_\gamma^2)' \mathrm{Im}\Pi} \delta(T - T_r)$$
$$= g_X^2 m_X^2 \frac{T}{j(T)} \frac{\pi}{\mathrm{Im}\Pi} \delta(T - T_r), \tag{E.13}$$

where $j(T) \equiv \frac{T}{m_\gamma^2}(m_\gamma^2)'$ is a function defined in [350]. The integrals can be performed to obtain

$$Y_{X,\,\mathrm{res}} = \frac{2}{3\pi} g_X^2 m_X^2 \int_{m_X}^{\infty} d\omega \frac{1}{j(T_r)[Hs]_{T=T_r}} \frac{\sqrt{\omega^2 - m_X^2}}{e^{\omega/T_r} - 1}$$
$$\approx \left(\frac{\pi}{9 j(T_r)} \frac{m_X^3}{T_r^3} \right) \left(\frac{[\sqrt{g_*} g_{*S}]_{T=m_X}}{[\sqrt{g_*} g_{*S}]_{T=T_r}} \right) \frac{g_X^2 m_X^4}{[Hs]_{T=m_X}} \equiv \mathcal{A}\mathcal{B} \frac{g_X^2 m_X^4}{[Hs]_{T=m_X}}, \tag{E.14}$$

where g_*, g_{*S} are the standard relativistic degrees of freedom in energy and entropy density. The factors $\mathcal{A}$ and $\mathcal{B}$ are defined as the terms in first and second set of parentheses respectively. In all cases, $T_r > m_X$ and $\mathcal{B} \leq 1$ and $\mathcal{B}$ thus can only decrease the prefactor in Eq. E.14 in comparison to Eq. E.10. We will conservatively ignore $\mathcal{B}$ in our argument as it depends on value of m_X. Furthermore, In a more detailed treatment of this derivation, m_γ^2, and subsequently T_r and $j(T)$, have ω dependence. However, a numerical evaluation of the integral in Eq. E.14 taking this dependence into accounts does not significantly change the values of $Y_{X,\mathrm{res}}$ discussed here.

E.4 Implications of the resonance on our results

For $m_X \gtrsim 2m_e$, the resonance occurs at $T_r \sim 8m_X$ where $j(T_r) = 2$. With these substitutions, the factor $\mathcal{A}$ in Eq. E.14 is suppressed by $1/8^3$ and is $\mathcal{A} \sim \mathcal{O}(10^{-4})$. Since $e^+e^- \to X$ is active, comparing these values to $\mathcal{O}(10^{-2})$ prefactor in Eq. E.10 one finds that finite temperature effects contribute at most a few percent to Y_X.

For $m_X \ll m_e$, the resonance occurs around $30 - 200\,\mathrm{keV}$ for a wide range of masses $m_X \sim 1 - 10^4\,\mathrm{eV}$. Importantly, the resonance is the only active mechanism that permits energy from the $e^+e^-\gamma$ plasma to be transferred into X bosons. For

example, for $m_X = 10\,\mathrm{keV}$, the resonance temperature is $T_r \approx 200\,\mathrm{keV}$ and $j(T_r) \approx 4$ giving $\mathcal{A} \sim \mathcal{O}(10^{-5})$. For $m_X = 10\,\mathrm{eV}$, then $T_r \approx 40\,\mathrm{keV}$ and $j(T_r) \approx 10$ giving $\mathcal{A} \sim \mathcal{O}(10^{-13})$. Consequently, when the resonance process dominates the contribution to ΔN_{eff}, the constraints on g_X become increasingly weaker at lower m_X mass, illustrated by the $\Delta N_{\mathrm{eff}} = 0.4, 0.5$ contours in figure 20 and $\Delta N_{\mathrm{eff}} = 0.2$ and larger contours in figure 21.

REFERENCES CITED

[1] G. Bertone, D. Hooper, and J. Silk, "Particle dark matter: Evidence, candidates and constraints," *Phys. Rept.* **405** (2005) 279–390, arXiv:hep-ph/0404175.

[2] V. C. Rubin and W. K. Ford, Jr., "Rotation of the Andromeda Nebula from a Spectroscopic Survey of Emission Regions," *Astrophys. J.* **159** (1970) 379–403.

[3] V. C. Rubin, N. Thonnard, and W. K. Ford, Jr., "Rotational properties of 21 SC galaxies with a large range of luminosities and radii, from NGC 4605 /R = 4kpc/ to UGC 2885 /R = 122 kpc/," *Astrophys. J.* **238** (1980) 471.

[4] A. Bosma, "21-cm line studies of spiral galaxies. 2. The distribution and kinematics of neutral hydrogen in spiral galaxies of various morphological types.," *Astron. J.* **86** (1981) 1825.

[5] Y. Sofue and V. Rubin, "Rotation curves of spiral galaxies," *Ann. Rev. Astron. Astrophys.* **39** (2001) 137–174, arXiv:astro-ph/0010594.

[6] W. J. G. de Blok, F. Walter, E. Brinks, C. Trachternach, S.-H. Oh, and R. C. Kennicutt, Jr., "High-Resolution Rotation Curves and Galaxy Mass Models from THINGS," *Astron. J.* **136** (2008) 2648–2719, arXiv:0810.2100 [astro-ph].

[7] F. Iocco, M. Pato, and G. Bertone, "Evidence for dark matter in the inner Milky Way," *Nature Phys.* **11** (2015) 245–248, arXiv:1502.03821 [astro-ph.GA].

[8] D. Clowe, M. Bradac, A. H. Gonzalez, M. Markevitch, S. W. Randall, C. Jones, and D. Zaritsky, "A direct empirical proof of the existence of dark matter," *Astrophys. J. Lett.* **648** (2006) L109–L113, arXiv:astro-ph/0608407.

[9] R. Massey *et al.*, "Dark matter maps reveal cosmic scaffolding," *Nature* **445** (2007) 286, arXiv:astro-ph/0701594.

[10] H. Hoekstra and B. Jain, "Weak Gravitational Lensing and its Cosmological Applications," *Ann. Rev. Nucl. Part. Sci.* **58** (2008) 99–123, arXiv:0805.0139 [astro-ph].

[11] **2dFGRS** Collaboration, S. Cole *et al.*, "The 2dF Galaxy Redshift Survey: Power-spectrum analysis of the final dataset and cosmological implications," *Mon. Not. Roy. Astron. Soc.* **362** (2005) 505–534, arXiv:astro-ph/0501174.

[12] **SDSS** Collaboration, D. J. Eisenstein *et al.*, "Detection of the Baryon Acoustic Peak in the Large-Scale Correlation Function of SDSS Luminous Red Galaxies," *Astrophys. J.* **633** (2005) 560–574, arXiv:astro-ph/0501171.

[13] M. Davis, G. Efstathiou, C. S. Frenk, and S. D. M. White, "The Evolution of Large Scale Structure in a Universe Dominated by Cold Dark Matter," *Astrophys. J.* **292** (1985) 371–394.

[14] V. Springel, C. S. Frenk, and S. D. M. White, "The large-scale structure of the Universe," *Nature* **440** (2006) 1137, arXiv:astro-ph/0604561.

[15] **Planck** Collaboration, N. Aghanim *et al.*, "Planck 2018 results. I. Overview and the cosmological legacy of Planck," *Astron. Astrophys.* **641** (2020) A1, arXiv:1807.06205 [astro-ph.CO].

[16] **Planck** Collaboration, N. Aghanim *et al.*, "Planck 2018 results. VI. Cosmological parameters," *Astron. Astrophys.* **641** (2020) A6, arXiv:1807.06209 [astro-ph.CO]. [Erratum: Astron.Astrophys. 652, C4 (2021)].

[17] **Atacama Cosmology Telescope** Collaboration, E. Calabrese *et al.*, "The Atacama Cosmology Telescope: DR6 constraints on extended cosmological models," *JCAP* **11** (2025) 063, arXiv:2503.14454 [astro-ph.CO].

[18] B. Patt and F. Wilczek, "Higgs-field portal into hidden sectors," arXiv:hep-ph/0605188.

[19] J. Alexander *et al.*, "Dark Sectors 2016 Workshop: Community Report," 8, 2016. arXiv:1608.08632 [hep-ph].

[20] M. Battaglieri *et al.*, "US Cosmic Visions: New Ideas in Dark Matter 2017: Community Report," in *U.S. Cosmic Visions: New Ideas in Dark Matter*. 7, 2017. arXiv:1707.04591 [hep-ph].

[21] C. D. Carone and H. Murayama, "Possible light U(1) gauge boson coupled to baryon number," *Phys. Rev. Lett.* **74** (1995) 3122–3125, arXiv:hep-ph/9411256.

[22] C. D. Carone and H. Murayama, "Realistic models with a light U(1) gauge boson coupled to baryon number," *Phys. Rev. D* **52** (1995) 484–493, arXiv:hep-ph/9501220.

[23] S. Tulin, "New weakly-coupled forces hidden in low-energy QCD," *Phys. Rev. D* **89** no. 11, (2014) 114008, arXiv:1404.4370 [hep-ph].

[24] B. A. Dobrescu and C. Frugiuele, "Hidden GeV-Scale Interactions of Quarks," *Phys. Rev. Lett.* **113** (2014) 061801, arXiv:1404.3947 [hep-ph].

[25] R. Foot, G. C. Joshi, and H. Lew, "Gauged Baryon and Lepton Numbers," *Phys. Rev. D* **40** (1989) 2487–2489.

[26] P. Fileviez Perez and M. B. Wise, "Baryon and lepton number as local gauge symmetries," *Phys. Rev. D* **82** (2010) 011901, arXiv:1002.1754 [hep-ph]. [Erratum: Phys.Rev.D 82, 079901 (2010)].

[27] P. Schwaller, T. M. P. Tait, and R. Vega-Morales, "Dark Matter and Vectorlike Leptons from Gauged Lepton Number," *Phys. Rev. D* **88** no. 3, (2013) 035001, arXiv:1305.1108 [hep-ph].

[28] L. Di Luzio, M. Nardecchia, S. Scacco, and C. Toni, "A framework for missing-energy searches with anomalous light vectors," arXiv:2603.04394 [hep-ph].

[29] J. A. Dror, R. Lasenby, and M. Pospelov, "Dark forces coupled to nonconserved currents," *Phys. Rev. D* **96** no. 7, (2017) 075036, arXiv:1707.01503 [hep-ph].

[30] L. Michaels and F. Yu, "Probing new $U(1)$ gauge symmetries via exotic $Z \to Z'\gamma$ decays," *JHEP* **03** (2021) 120, arXiv:2010.00021 [hep-ph].

[31] J. A. Dror, R. Lasenby, and M. Pospelov, "New constraints on light vectors coupled to anomalous currents," *Phys. Rev. Lett.* **119** no. 14, (2017) 141803, arXiv:1705.06726 [hep-ph].

[32] B. C. Allanach, J. Davighi, and S. Melville, "An Anomaly-free Atlas: charting the space of flavour-dependent gauged $U(1)$ extensions of the Standard Model," *JHEP* **02** (2019) 082, arXiv:1812.04602 [hep-ph]. [Erratum: JHEP 08, 064 (2019)].

[33] J. Heeck and W. Rodejohann, "Gauged $L_\mu - L_\tau$ Symmetry at the Electroweak Scale," *Phys. Rev. D* **84** (2011) 075007, arXiv:1107.5238 [hep-ph].

[34] W. Altmannshofer, S. Gori, M. Pospelov, and I. Yavin, "Quark flavor transitions in $L_\mu - L_\tau$ models," *Phys. Rev. D* **89** (2014) 095033, arXiv:1403.1269 [hep-ph].

[35] W. Altmannshofer and I. Yavin, "Predictions for lepton flavor universality violation in rare B decays in models with gauged $L_\mu - L_\tau$," *Phys. Rev. D* **92** no. 7, (2015) 075022, arXiv:1508.07009 [hep-ph].

[36] R. Alonso, P. Cox, C. Han, and T. T. Yanagida, "Flavoured $B - L$ local symmetry and anomalous rare B decays," *Phys. Lett. B* **774** (2017) 643–648, arXiv:1705.03858 [hep-ph].

[37] C. Bonilla, T. Modak, R. Srivastava, and J. W. F. Valle, "$U(1)_{B_3-3L_\mu}$ gauge symmetry as a simple description of $b \to s$ anomalies," *Phys. Rev. D* **98** no. 9, (2018) 095002, arXiv:1705.00915 [hep-ph].

[38] B. C. Allanach and J. Davighi, "Third family hypercharge model for $R_{K^{(*)}}$ and aspects of the fermion mass problem," *JHEP* **12** (2018) 075, arXiv:1809.01158 [hep-ph].

[39] M. Bauer, P. Foldenauer, and J. Jaeckel, "Hunting All the Hidden Photons," *JHEP* **07** (2018) 094, arXiv:1803.05466 [hep-ph].

[40] M. Bauer, P. Foldenauer, and M. Mosny, "Flavor structure of anomaly-free hidden photon models," *Phys. Rev. D* **103** no. 7, (2021) 075024, arXiv:2011.12973 [hep-ph].

[41] B. Holdom, "Two U(1)'s and Epsilon Charge Shifts," *Phys. Lett. B* **166** (1986) 196–198.

[42] P. Ilten, Y. Soreq, M. Williams, and W. Xue, "Serendipity in dark photon searches," *JHEP* **06** (2018) 004, arXiv:1801.04847 [hep-ph].

[43] M. Fabbrichesi, E. Gabrielli, and G. Lanfranchi, "The Dark Photon," arXiv:2005.01515 [hep-ph].

[44] A. Caputo, A. J. Millar, C. A. J. O'Hare, and E. Vitagliano, "Dark photon limits: A handbook," *Phys. Rev. D* **104** no. 9, (2021) 095029, arXiv:2105.04565 [hep-ph].

[45] A. Caputo, J. Park, and S. Yun, "The Heavy Dark Photon Handbook: Cosmological and Astrophysical Bounds," arXiv:2511.15785 [hep-ph].

[46] A. Davidson, "$B - L$ as the fourth color within an $\mathrm{SU}(2)_L \times \mathrm{U}(1)_R \times \mathrm{U}(1)$ model," *Phys. Rev. D* **20** (1979) 776.

[47] R. E. Marshak and R. N. Mohapatra, "Quark - Lepton Symmetry and B-L as the U(1) Generator of the Electroweak Symmetry Group," *Phys. Lett. B* **91** (1980) 222–224.

[48] R. N. Mohapatra and R. E. Marshak, "Local B-L Symmetry of Electroweak Interactions, Majorana Neutrinos and Neutron Oscillations," *Phys. Rev. Lett.* **44** (1980) 1316–1319. [Erratum: Phys.Rev.Lett. 44, 1643 (1980)].

[49] C. Wetterich, "Neutrino Masses and the Scale of B-L Violation," *Nucl. Phys. B* **187** (1981) 343–375.

[50] R. Harnik, J. Kopp, and P. A. N. Machado, "Exploring ν Signals in Dark Matter Detectors," *JCAP* **1207** (2012) 026, arXiv:1202.6073 [hep-ph].

[51] J. Heeck, "Unbroken B – L symmetry," *Phys. Lett. B* **739** (2014) 256–262, arXiv:1408.6845 [hep-ph].

[52] H. Esseili and G. D. Kribs, "Hiding a Light Vector Boson from Terrestrial Experiments: A Chargephobic Dark Photon," arXiv:2512.10916 [hep-ph].

[53] T. Fujiwara, T. Kugo, H. Terao, S. Uehara, and K. Yamawaki, "Nonabelian Anomaly and Vector Mesons as Dynamical Gauge Bosons of Hidden Local Symmetries," *Prog. Theor. Phys.* **73** (1985) 926.

[54] H. Esseili and G. D. Kribs, "Cosmological implications of gauged $U(1)_{B-L}$ on ΔN_{eff} in the CMB and BBN," *JCAP* **05** (2024) 110, arXiv:2308.07955 [hep-ph].

[55] D. Croon, G. Elor, R. K. Leane, and S. D. McDermott, "Supernova Muons: New Constraints on Z' Bosons, Axions and ALPs," *JHEP* **01** (2021) 107, arXiv:2006.13942 [hep-ph].

[56] C. S. Shin and S. Yun, "Dark gauge boson production from neutron stars via nucleon-nucleon bremsstrahlung," *JHEP* **02** (2022) 133, arXiv:2110.03362 [hep-ph].

[57] S. Knapen, T. Lin, and K. M. Zurek, "Light Dark Matter: Models and Constraints," *Phys. Rev. D* **96** no. 11, (2017) 115021, arXiv:1709.07882 [hep-ph].

[58] P. Fayet, "Effects of the Spin 1 Partner of the Goldstino (Gravitino) on Neutral Current Phenomenology," *Phys. Lett. B* **95** (1980) 285–289.

[59] P. Fayet, "On the Search for a New Spin 1 Boson," *Nucl. Phys. B* **187** (1981) 184–204.

[60] P. Fayet, "The Fifth Interaction in Grand Unified Theories: A New Force Acting Mostly on Neutrons and Particle Spins," *Phys. Lett. B* **172** (1986) 363–368.

[61] P. Fayet, "The Fifth Force Charge as a Linear Combination of Baryonic, Leptonic (Or B^-l) and Electric Charges," *Phys. Lett. B* **227** (1989) 127–132.

[62] P. Fayet, "Extra U(1)'s and New Forces," *Nucl. Phys. B* **347** (1990) 743–768.

[63] P. Langacker, "The Physics of Heavy Z' Gauge Bosons," *Rev. Mod. Phys.* **81** (2009) 1199–1228, arXiv:0801.1345 [hep-ph].

[64] R. Foot, "New Physics From Electric Charge Quantization?," *Mod. Phys. Lett. A* **6** (1991) 527–530.

[65] X.-G. He, G. C. Joshi, H. Lew, and R. R. Volkas, "Simplest Z-prime model," *Phys. Rev. D* **44** (1991) 2118–2132.

[66] R. Foot, X. G. He, H. Lew, and R. R. Volkas, "Model for a light Z-prime boson," *Phys. Rev. D* **50** (1994) 4571–4580, arXiv:hep-ph/9401250.

[67] E. Ma, "Gauged B - 3L(tau) and radiative neutrino masses," *Phys. Lett. B* **433** (1998) 74–81, arXiv:hep-ph/9709474.

[68] E. Ma and D. P. Roy, "Phenomenology of the B - 3L(τ) gauge boson," *Phys. Rev. D* **58** (1998) 095005, arXiv:hep-ph/9806210.

[69] T. Appelquist, B. A. Dobrescu, and A. R. Hopper, "Nonexotic Neutral Gauge Bosons," *Phys. Rev. D* **68** (2003) 035012, arXiv:hep-ph/0212073.

[70] C. Boehm and P. Fayet, "Scalar dark matter candidates," *Nucl. Phys. B* **683** (2004) 219–263, arXiv:hep-ph/0305261.

[71] P. Fayet, "Light spin 1/2 or spin 0 dark matter particles," *Phys. Rev. D* **70** (2004) 023514, arXiv:hep-ph/0403226.

[72] P. Fayet, "Constraints on Light Dark Matter and U bosons, from psi, Upsilon, K+, pi0, eta and eta-prime decays," *Phys. Rev. D* **74** (2006) 054034, arXiv:hep-ph/0607318.

[73] P. Fayet, "U-boson production in e+ e- annihilations, psi and Upsilon decays, and Light Dark Matter," *Phys. Rev. D* **75** (2007) 115017, arXiv:hep-ph/0702176.

[74] E. Salvioni, A. Strumia, G. Villadoro, and F. Zwirner, "Non-universal minimal Z' models: present bounds and early LHC reach," *JHEP* **03** (2010) 010, arXiv:0911.1450 [hep-ph].

[75] P. Fayet, "The light U boson as the mediator of a new force, coupled to a combination of Q, B, L and dark matter," *Eur. Phys. J. C* **77** no. 1, (2017) 53, arXiv:1611.05357 [hep-ph].

[76] P. Fayet, "U boson interpolating between a generalized dark photon or dark Z , an axial boson, and an axionlike particle," *Phys. Rev. D* **103** no. 3, (2021) 035034, arXiv:2010.04673 [hep-ph].

[77] A. Celis, J. Fuentes-Martin, M. Jung, and H. Serodio, "Family nonuniversal Z' models with protected flavor-changing interactions," *Phys. Rev. D* **92** no. 1, (2015) 015007, arXiv:1505.03079 [hep-ph].

[78] M. Bauer, S. Diefenbacher, T. Plehn, M. Russell, and D. A. Camargo, "Dark Matter in Anomaly-Free Gauge Extensions," *SciPost Phys.* **5** no. 4, (2018) 036, arXiv:1805.01904 [hep-ph].

[79] W. Altmannshofer, M. Tammaro, and J. Zupan, "Non-standard neutrino interactions and low energy experiments," *JHEP* **09** (2019) 083, arXiv:1812.02778 [hep-ph]. [Erratum: JHEP 11, 113 (2021)].

[80] J. Heeck, M. Lindner, W. Rodejohann, and S. Vogl, "Non-Standard Neutrino Interactions and Neutral Gauge Bosons," *SciPost Phys.* **6** no. 3, (2019) 038, arXiv:1812.04067 [hep-ph].

[81] M. Escudero, D. Hooper, G. Krnjaic, and M. Pierre, "Cosmology with A Very Light $L_\mu - L_\tau$ Gauge Boson," *JHEP* **03** (2019) 071, arXiv:1901.02010 [hep-ph].

[82] T. Han, J. Liao, H. Liu, and D. Marfatia, "Nonstandard neutrino interactions at COHERENT, DUNE, T2HK and LHC," *JHEP* **11** (2019) 028, arXiv:1910.03272 [hep-ph].

[83] P. Coloma, M. C. Gonzalez-Garcia, and M. Maltoni, "Neutrino oscillation constraints on U(1)' models: from non-standard interactions to long-range forces," *JHEP* **01** (2021) 114, arXiv:2009.14220 [hep-ph]. [Erratum: JHEP 11, 115 (2022)].

[84] D. K. Ghosh, P. Ghosh, S. Jeesun, and R. Srivastava, "Neff at CMB challenges U(1)X light gauge boson scenarios," *Phys. Rev. D* **110** no. 7, (2024) 075032, arXiv:2404.10077 [hep-ph].

[85] E. Salvioni, G. Villadoro, and F. Zwirner, "Minimal Z-prime models: Present bounds and early LHC reach," *JHEP* **11** (2009) 068, arXiv:0909.1320 [hep-ph].

[86] G. D. Kribs, G. Lee, and A. Martin, "Effective field theory of Stückelberg vector bosons," *Phys. Rev. D* **106** no. 5, (2022) 055020, arXiv:2204.01755 [hep-ph].

[87] "Garching Core Collapse Supernova Archive." https://wwwmpa.mpa-garching.mpg.de/ccsnarchive/archive.html.

[88] J. A. Dror, R. Lasenby, and M. Pospelov, "Light vectors coupled to bosonic currents," *Phys. Rev. D* **99** no. 5, (2019) 055016, arXiv:1811.00595 [hep-ph].

[89] J. A. Dror, "Discovering leptonic forces using nonconserved currents," *Phys. Rev. D* **101** no. 9, (2020) 095013, arXiv:2004.04750 [hep-ph].

[90] J. L. Feng, J. Kumar, and D. Sanford, "Xenophobic Dark Matter," *Phys. Rev. D* **88** no. 1, (2013) 015021, arXiv:1306.2315 [hep-ph].

[91] **FASER** Collaboration, H. Abreu *et al.*, "Search for dark photons with the FASER detector at the LHC," *Phys. Lett. B* **848** (2024) 138378, arXiv:2308.05587 [hep-ex].

[92] **FASER** Collaboration, A. Ariga *et al.*, "FASER's physics reach for long-lived particles," *Phys. Rev. D* **99** no. 9, (2019) 095011, arXiv:1811.12522 [hep-ph].

[93] **KLOE-2** Collaboration, F. Archilli *et al.*, "Search for a vector gauge boson in ϕ meson decays with the KLOE detector," *Phys. Lett. B* **706** (2012) 251–255, arXiv:1110.0411 [hep-ex].

[94] S. Bilmis, I. Turan, T. M. Aliev, M. Deniz, L. Singh, and H. T. Wong, "Constraints on Dark Photon from Neutrino-Electron Scattering Experiments," *Phys. Rev. D* **92** no. 3, (2015) 033009, arXiv:1502.07763 [hep-ph].

[95] M. Lindner, F. S. Queiroz, W. Rodejohann, and X.-J. Xu, "Neutrino-electron scattering: general constraints on Z' and dark photon models," *JHEP* **05** (2018) 098, arXiv:1803.00060 [hep-ph].

[96] V. De Romeri, O. G. Miranda, D. K. Papoulias, G. Sanchez Garcia, M. Tórtola, and J. W. F. Valle, "Physics implications of a combined analysis of COHERENT CsI and LAr data," *JHEP* **04** (2023) 035, arXiv:2211.11905 [hep-ph].

[97] P. Z. et al. (Particle Data Group), "Review of Particle Physics," *Progress of Theoretical and Experimental Physics* **2020** no. 8, (08, 2020) , https://academic.oup.com/ptep/article-pdf/2020/8/083C01/34673722/ptaa104.pdf. https://doi.org/10.1093/ptep/ptaa104. 083C01.

[98] V. V. Ezhela, S. B. Lugovsky, and O. V. Zenin, "Hadronic part of the muon g-2 estimated on the σ**2003(tot)($e^+e^- \to$ hadrons) evaluated data compilation," arXiv:hep-ph/0312114.

[99] **BaBar** Collaboration, J. P. Lees *et al.*, "Precise Measurement of the $e^+e^- \to \pi^+\pi^-(\gamma)$ Cross Section with the Initial-State Radiation Method at BABAR," *Phys. Rev. D* **86** (2012) 032013, arXiv:1205.2228 [hep-ex].

[100] **BaBar** Collaboration, B. Aubert *et al.*, "Study of $e^+e^- \to \pi^+\pi^-\pi^0$ process using initial state radiation with BaBar," *Phys. Rev. D* **70** (2004) 072004, arXiv:hep-ex/0408078.

[101] **BaBar** Collaboration, J. P. Lees *et al.*, "Precision measurement of the $e^+e^-ßK^+K^-(\gamma)$ cross section with the initial-state radiation method at BABAR," *Phys. Rev. D* **88** no. 3, (2013) 032013, arXiv:1306.3600 [hep-ex].

[102] **BaBar** Collaboration, B. Aubert *et al.*, "Measurements of $e^+e^- \to K^+K^-\eta$, $K^+K^-\pi^0$ and $K^0_sK^\pm\pi^\mp$ cross- sections using initial state radiation events," *Phys. Rev. D* **77** (2008) 092002, arXiv:0710.4451 [hep-ex].

[103] **BaBar** Collaboration, J. P. Lees *et al.*, "Initial-State Radiation Measurement of the $e^+e^- - > \pi^+\pi^-\pi^+\pi^-$ Cross Section," *Phys. Rev. D* **85** (2012) 112009, arXiv:1201.5677 [hep-ex].

[104] **BaBar** Collaboration, J. P. Lees *et al.*, "Measurement of the $e^+e^-\to\pi^+\pi^-\pi^0\pi^0$ cross section using initial-state radiation at BABAR," *Phys. Rev. D* **96** no. 9, (2017) 092009, arXiv:1709.01171 [hep-ex].

[105] M. N. Achasov *et al.*, "Study of the process e+ e- —> pi+ pi- pi0 in the energy region s**(1/2) below 0.98-GeV," *Phys. Rev. D* **68** (2003) 052006, arXiv:hep-ex/0305049.

[106] M. N. Achasov *et al.*, "Study of the process e+ e- —> pi+ pi- pi0 in the energy region s**(1/2) from 0.98-GeV to 1.38-GeV," *Phys. Rev. D* **66** (2002) 032001, arXiv:hep-ex/0201040.

[107] **CMS** Collaboration, A. M. Sirunyan *et al.*, "Search for a Narrow Resonance Lighter than 200 GeV Decaying to a Pair of Muons in Proton-Proton Collisions at $\sqrt{s} = 13$ TeV," *Phys. Rev. Lett.* **124** no. 13, (2020) 131802, arXiv:1912.04776 [hep-ex].

[108] R. H. Cyburt, B. D. Fields, K. A. Olive, and T.-H. Yeh, "Big Bang Nucleosynthesis: 2015," *Rev. Mod. Phys.* **88** (2016) 015004, arXiv:1505.01076 [astro-ph.CO].

[109] T.-H. Yeh, K. A. Olive, and B. D. Fields, "The impact of new $d(p, \gamma)3$ rates on Big Bang Nucleosynthesis," *JCAP* **03** (2021) 046, arXiv:2011.13874 [astro-ph.CO].

[110] T.-H. Yeh, J. Shelton, K. A. Olive, and B. D. Fields, "Probing physics beyond the standard model: limits from BBN and the CMB independently and combined," *JCAP* **10** (2022) 046, arXiv:2207.13133 [astro-ph.CO].

[111] **Particle Data Group** Collaboration, R. L. Workman *et al.*, "Review of Particle Physics," *PTEP* **2022** (2022) 083C01.

[112] P. F. de Salas and S. Pastor, "Relic neutrino decoupling with flavour oscillations revisited," *JCAP* **07** (2016) 051, arXiv:1606.06986 [hep-ph].

[113] G. Mangano, G. Miele, S. Pastor, T. Pinto, O. Pisanti, and P. D. Serpico, "Relic neutrino decoupling including flavor oscillations," *Nucl. Phys. B* **729** (2005) 221–234, arXiv:hep-ph/0506164.

[114] A. D. Dolgov, "Neutrinos in cosmology," *Phys. Rept.* **370** (2002) 333–535, arXiv:hep-ph/0202122.

[115] D. A. Dicus, E. W. Kolb, A. M. Gleeson, E. C. G. Sudarshan, V. L. Teplitz, and M. S. Turner, "Primordial Nucleosynthesis Including Radiative, Coulomb, and Finite Temperature Corrections to Weak Rates," *Phys. Rev. D* **26** (1982) 2694.

[116] S. Hannestad and J. Madsen, "Neutrino decoupling in the early universe," *Phys. Rev. D* **52** (1995) 1764–1769, arXiv:astro-ph/9506015.

[117] S. Dodelson and M. S. Turner, "Nonequilibrium neutrino statistical mechanics in the expanding universe," *Phys. Rev. D* **46** (1992) 3372–3387.

[118] A. D. Dolgov, S. H. Hansen, and D. V. Semikoz, "Nonequilibrium corrections to the spectra of massless neutrinos in the early universe," *Nucl. Phys. B* **503** (1997) 426–444, arXiv:hep-ph/9703315.

[119] S. Esposito, G. Miele, S. Pastor, M. Peloso, and O. Pisanti, "Nonequilibrium spectra of degenerate relic neutrinos," *Nucl. Phys. B* **590** (2000) 539–561, arXiv:astro-ph/0005573.

[120] G. Mangano, G. Miele, S. Pastor, and M. Peloso, "A Precision calculation of the effective number of cosmological neutrinos," *Phys. Lett. B* **534** (2002) 8–16, arXiv:astro-ph/0111408.

[121] J. Birrell, C.-T. Yang, and J. Rafelski, "Relic Neutrino Freeze-out: Dependence on Natural Constants," *Nucl. Phys. B* **890** (2014) 481–517, arXiv:1406.1759 [nucl-th].

[122] E. Grohs, G. M. Fuller, C. T. Kishimoto, M. W. Paris, and A. Vlasenko, "Neutrino energy transport in weak decoupling and big bang nucleosynthesis," *Phys. Rev. D* **93** no. 8, (2016) 083522, arXiv:1512.02205 [astro-ph.CO].

[123] M. Cielo, M. Escudero, G. Mangano, and O. Pisanti, "Neff in the Standard Model at NLO is 3.043," arXiv:2306.05460 [hep-ph].

[124] K. Akita and M. Yamaguchi, "A precision calculation of relic neutrino decoupling," *JCAP* **08** (2020) 012, arXiv:2005.07047 [hep-ph].

[125] J. Froustey, C. Pitrou, and M. C. Volpe, "Neutrino decoupling including flavour oscillations and primordial nucleosynthesis," *JCAP* **12** (2020) 015, arXiv:2008.01074 [hep-ph].

[126] J. J. Bennett, G. Buldgen, P. F. De Salas, M. Drewes, S. Gariazzo, S. Pastor, and Y. Y. Y. Wong, "Towards a precision calculation of $N_{\rm eff}$ in the Standard Model II: Neutrino decoupling in the presence of flavour oscillations and finite-temperature QED," *JCAP* **04** (2021) 073, arXiv:2012.02726 [hep-ph].

[127] S. Sarkar, "Big bang nucleosynthesis and physics beyond the standard model," *Rept. Prog. Phys.* **59** (1996) 1493–1610, arXiv:hep-ph/9602260.

[128] F. Iocco, G. Mangano, G. Miele, O. Pisanti, and P. D. Serpico, "Primordial Nucleosynthesis: from precision cosmology to fundamental physics," *Phys. Rept.* **472** (2009) 1–76, arXiv:0809.0631 [astro-ph].

[129] M. Pospelov and J. Pradler, "Big Bang Nucleosynthesis as a Probe of New Physics," *Ann. Rev. Nucl. Part. Sci.* **60** (2010) 539–568, arXiv:1011.1054 [hep-ph].

[130] M. Blennow, E. Fernandez-Martinez, O. Mena, J. Redondo, and P. Serra, "Asymmetric Dark Matter and Dark Radiation," *JCAP* **07** (2012) 022, arXiv:1203.5803 [hep-ph].

[131] C. Boehm, M. J. Dolan, and C. McCabe, "Increasing Neff with particles in thermal equilibrium with neutrinos," *JCAP* **12** (2012) 027, arXiv:1207.0497 [astro-ph.CO].

[132] C. Boehm, M. J. Dolan, and C. McCabe, "A Lower Bound on the Mass of Cold Thermal Dark Matter from Planck," *JCAP* **08** (2013) 041, arXiv:1303.6270 [hep-ph].

[133] C. Brust, D. E. Kaplan, and M. T. Walters, "New Light Species and the CMB," *JHEP* **12** (2013) 058, arXiv:1303.5379 [hep-ph].

[134] H. Vogel and J. Redondo, "Dark Radiation constraints on minicharged particles in models with a hidden photon," *JCAP* **02** (2014) 029, arXiv:1311.2600 [hep-ph].

[135] A. Fradette, M. Pospelov, J. Pradler, and A. Ritz, "Cosmological Constraints on Very Dark Photons," *Phys. Rev. D* **90** no. 3, (2014) 035022, arXiv:1407.0993 [hep-ph].

[136] K. M. Nollett and G. Steigman, "BBN And The CMB Constrain Neutrino Coupled Light WIMPs," *Phys. Rev. D* **91** no. 8, (2015) 083505, arXiv:1411.6005 [astro-ph.CO].

[137] M. A. Buen-Abad, G. Marques-Tavares, and M. Schmaltz, "Non-Abelian dark matter and dark radiation," *Phys. Rev. D* **92** no. 2, (2015) 023531, arXiv:1505.03542 [hep-ph].

[138] Z. Chacko, Y. Cui, S. Hong, and T. Okui, "Hidden dark matter sector, dark radiation, and the CMB," *Phys. Rev. D* **92** (2015) 055033, arXiv:1505.04192 [hep-ph].

[139] R. J. Wilkinson, A. C. Vincent, C. Bœhm, and C. McCabe, "Ruling out the light weakly interacting massive particle explanation of the Galactic 511 keV line," *Phys. Rev. D* **94** no. 10, (2016) 103525, arXiv:1602.01114 [astro-ph.CO].

[140] G.-y. Huang, T. Ohlsson, and S. Zhou, "Observational Constraints on Secret Neutrino Interactions from Big Bang Nucleosynthesis," *Phys. Rev. D* **97** no. 7, (2018) 075009, arXiv:1712.04792 [hep-ph].

[141] M. Escudero, "Neutrino decoupling beyond the Standard Model: CMB constraints on the Dark Matter mass with a fast and precise $N_{\rm eff}$ evaluation," *JCAP* **02** (2019) 007, arXiv:1812.05605 [hep-ph].

[142] K. N. Abazajian and J. Heeck, "Observing Dirac neutrinos in the cosmic microwave background," *Phys. Rev. D* **100** (2019) 075027, arXiv:1908.03286 [hep-ph].

[143] M. Ibe, S. Kobayashi, Y. Nakayama, and S. Shirai, "Cosmological constraint on dark photon from N_{eff}," *JHEP* **04** (2020) 009, arXiv:1912.12152 [hep-ph].

[144] M. Escudero Abenza, " Precision Early Universe Thermodynamics Made Simple: $N_{\rm eff}$ and Neutrino Decoupling in the Standard Model and Beyond," *JCAP* **05** (2020) 048, arXiv:2001.04466 [hep-ph].

[145] J. Coffey, L. Forestell, D. E. Morrissey, and G. White, "Cosmological Bounds on sub-GeV Dark Vector Bosons from Electromagnetic Energy Injection," *JHEP* **07** (2020) 179, arXiv:2003.02273 [hep-ph].

[146] X. Luo, W. Rodejohann, and X.-J. Xu, "Dirac neutrinos and $N_{\rm eff}$," *JCAP* **06** (2020) 058, arXiv:2005.01629 [hep-ph].

[147] X. Luo, W. Rodejohann, and X.-J. Xu, "Dirac neutrinos and N_{eff}. Part II. The freeze-in case," *JCAP* **03** (2021) 082, arXiv:2011.13059 [hep-ph].

[148] P. Adshead, P. Ralegankar, and J. Shelton, "Dark radiation constraints on portal interactions with hidden sectors," *JCAP* **09** (2022) 056, arXiv:2206.13530 [hep-ph].

[149] S. Eijima, O. Seto, and T. Shimomura, "Revisiting sterile neutrino dark matter in gauged U(1)B-L model," *Phys. Rev. D* **106** no. 10, (2022) 103513, arXiv:2207.01775 [hep-ph].

[150] S. Sandner, M. Escudero, and S. J. Witte, "Precision CMB constraints on eV-scale bosons coupled to neutrinos," arXiv:2305.01692 [hep-ph].

[151] L. J. Hall, K. Jedamzik, J. March-Russell, and S. M. West, "Freeze-In Production of FIMP Dark Matter," *JHEP* **03** (2010) 080, arXiv:0911.1120 [hep-ph].

[152] S.-P. Li and X.-J. Xu, "N_{eff} constraints on light mediators coupled to neutrinos: the dilution-resistant effect," *JHEP* **10** (2023) 012, arXiv:2307.13967 [hep-ph].

[153] E. Aver, K. A. Olive, and E. D. Skillman, "The effects of He I λ10830 on helium abundance determinations," *JCAP* **07** (2015) 011, arXiv:1503.08146 [astro-ph.CO].

[154] M. Pettini and R. Cooke, "A new, precise measurement of the primordial abundance of Deuterium," *Mon. Not. Roy. Astron. Soc.* **425** (2012) 2477–2486, arXiv:1205.3785 [astro-ph.CO].

[155] R. Cooke, M. Pettini, R. A. Jorgenson, M. T. Murphy, and C. C. Steidel, "Precision measures of the primordial abundance of deuterium," *Astrophys. J.* **781** no. 1, (2014) 31, arXiv:1308.3240 [astro-ph.CO].

[156] S. Riemer-Sørensen, J. K. Webb, N. Crighton, V. Dumont, K. Ali, S. Kotuš, M. Bainbridge, M. T. Murphy, and R. Carswell, "A robust deuterium abundance; Re-measurement of the z=3.256 absorption system towards the quasar PKS1937-1009," *Mon. Not. Roy. Astron. Soc.* **447** (2015) 2925, arXiv:1412.4043 [astro-ph.CO].

[157] R. J. Cooke, M. Pettini, K. M. Nollett, and R. Jorgenson, "The primordial deuterium abundance of the most metal-poor damped Lyα system," *Astrophys. J.* **830** no. 2, (2016) 148, arXiv:1607.03900 [astro-ph.CO].

[158] S. A. Balashev, E. O. Zavarygin, A. V. Ivanchik, K. N. Telikova, and D. A. Varshalovich, "The primordial deuterium abundance: subDLA system at $z_{\rm abs} = 2.437$ towards the QSO J 1444+2919," *Mon. Not. Roy. Astron. Soc.* **458** no. 2, (2016) 2188–2198, arXiv:1511.01797 [astro-ph.GA].

[159] S. Riemer-Sørensen, S. Kotuš, J. K. Webb, K. Ali, V. Dumont, M. T. Murphy, and R. F. Carswell, "A precise deuterium abundance: remeasurement of the z = 3.572 absorption system towards the quasar PKS1937–101," *Mon. Not. Roy. Astron. Soc.* **468** no. 3, (2017) 3239–3250, arXiv:1703.06656 [astro-ph.CO].

[160] E. O. Zavarygin, J. K. Webb, S. Riemer-Sørensen, and V. Dumont, "Primordial deuterium abundance at $z_{abs} = 2{:}504$ towards Q1009+2956," *J. Phys. Conf. Ser.* **1038** no. 1, (2018) 012012, arXiv:1801.04704 [astro-ph.CO].

[161] R. J. Cooke, M. Pettini, and C. C. Steidel, "One Percent Determination of the Primordial Deuterium Abundance," *Astrophys. J.* **855** no. 2, (2018) 102, arXiv:1710.11129 [astro-ph.CO].

[162] E. Aver, D. A. Berg, K. A. Olive, R. W. Pogge, J. J. Salzer, and E. D. Skillman, "Improving helium abundance determinations with Leo P as a case study," *JCAP* **03** (2021) 027, arXiv:2010.04180 [astro-ph.CO].

[163] M. Valerdi, A. Peimbert, M. Peimbert, and A. Sixtos, "Determination of the Primordial Helium Abundance Based on NGC 346, an H ii Region of the Small Magellanic Cloud," *Astrophys. J.* **876** no. 2, (2019) 98, arXiv:1904.01594 [astro-ph.GA].

[164] V. Fernández, E. Terlevich, A. I. Díaz, and R. Terlevich, "A Bayesian direct method implementation to fit emission line spectra: Application to the primordial He abundance determination," *Mon. Not. Roy. Astron. Soc.* **487** no. 3, (2019) 3221–3238, arXiv:1905.09215 [astro-ph.GA].

[165] O. A. Kurichin, P. A. Kislitsyn, V. V. Klimenko, S. A. Balashev, and A. V. Ivanchik, "A new determination of the primordial helium abundance using the analyses of H II region spectra from SDSS," *Mon. Not. Roy. Astron. Soc.* **502** no. 2, (2021) 3045–3056, arXiv:2101.09127 [astro-ph.CO].

[166] T. Hsyu, R. J. Cooke, J. X. Prochaska, and M. Bolte, "The PHLEK Survey: A New Determination of the Primordial Helium Abundance," *Astrophys. J.* **896** no. 1, (2020) 77, arXiv:2005.12290 [astro-ph.GA].

[167] **Kamiokande-II** Collaboration, K. Hirata *et al.*, "Observation of a Neutrino Burst from the Supernova SN 1987a," *Phys. Rev. Lett.* **58** (1987) 1490–1493.

[168] R. M. Bionta *et al.*, "Observation of a Neutrino Burst in Coincidence with Supernova SN 1987a in the Large Magellanic Cloud," *Phys. Rev. Lett.* **58** (1987) 1494.

[169] A. Burrows and J. M. Lattimer, "The birth of neutron stars," *Astrophys. J.* **307** (1986) 178–196.

[170] A. Burrows and J. M. Lattimer, "Neutrinos from SN 1987A," *Astrophys. J. Lett.* **318** (1987) L63–L68.

[171] D. F. G. Fiorillo, M. Heinlein, H.-T. Janka, G. Raffelt, E. Vitagliano, and R. Bollig, "Supernova simulations confront SN 1987A neutrinos," *Phys. Rev. D* **108** no. 8, (2023) 083040, arXiv:2308.01403 [astro-ph.HE].

[172] G. G. Raffelt, "Astrophysical methods to constrain axions and other novel particle phenomena," *Phys. Rept.* **198** (1990) 1–113.

[173] G. G. Raffelt, *Stars as laboratories for fundamental physics: The astrophysics of neutrinos, axions, and other weakly interacting particles*. 5, 1996.

[174] A. Burrows, "A Brief History of the Co-evolution of Supernova Theory with Neutrino Physics," 12, 2018. arXiv:1812.05612 [astro-ph.SR].

[175] H.-T. Janka, K. Langanke, A. Marek, G. Martinez-Pinedo, and B. Mueller, "Theory of Core-Collapse Supernovae," *Phys. Rept.* **442** (2007) 38–74, arXiv:astro-ph/0612072.

[176] D. F. G. Fiorillo, G. G. Raffelt, and E. Vitagliano, "Strong Supernova 1987A Constraints on Bosons Decaying to Neutrinos," *Phys. Rev. Lett.* **131** no. 2, (2023) 021001, arXiv:2209.11773 [hep-ph].

[177] K. Akita, S. H. Im, and M. Masud, "Probing non-standard neutrino interactions with a light boson from next galactic and diffuse supernova neutrinos," *JHEP* **12** (2022) 050, arXiv:2206.06852 [hep-ph].

[178] V. Syvolap, "Testing heavy neutral leptons produced in the supernovae explosions with future neutrino detectors," arXiv:2301.07052 [hep-ph].

[179] K. Akita, S. H. Im, M. Masud, and S. Yun, "Limits on heavy neutral leptons, Z' bosons and majorons from high-energy supernova neutrinos," *JHEP* **07** (2024) 057, arXiv:2312.13627 [hep-ph].

[180] V. Syvolap and O. Ruchayskiy, "High-energy neutrino signals from supernova explosions: A new window into dark photon parameter space," *Phys. Rev. D* **110** no. 11, (2024) 115043, arXiv:2404.19191 [hep-ph].

[181] B. Telalovic, D. F. G. Fiorillo, P. Martínez-Miravé, E. Vitagliano, and M. Bustamante, "The next galactic supernova can uncover mass and couplings of particles decaying to neutrinos," *JCAP* **11** (2024) 011, arXiv:2406.15506 [hep-ph].

[182] N. Blinov, P. J. Fox, K. J. Kelly, R. Plestid, and T. Zhou, "$L_\mu - L_\tau$ gauge bosons in beam dumps and supernovae," arXiv:2511.09619 [hep-ph].

[183] A. Pastorello *et al.*, "Low luminosity type II supernovae: spectroscopic and photometric evolution," *Mon. Not. Roy. Astron. Soc.* **347** (2004) 74, arXiv:astro-ph/0309264.

[184] N. Prantzos *et al.*, "The 511 keV emission from positron annihilation in the Galaxy," *Rev. Mod. Phys.* **83** (2011) 1001–1056, arXiv:1009.4620 [astro-ph.HE].

[185] S. Spiro *et al.*, "Low luminosity type ii supernovae – ii. pointing towards moderate mass precursors," *Monthly Notices of the Royal Astronomical Society* **439** no. 3, (Feb., 2014) 2873–2892. http://dx.doi.org/10.1093/mnras/stu156.

[186] A. Sung, H. Tu, and M.-R. Wu, "New constraint from supernova explosions on light particles beyond the Standard Model," *Phys. Rev. D* **99** no. 12, (2019) 121305, arXiv:1903.07923 [hep-ph].

[187] A. Caputo, H.-T. Janka, G. Raffelt, and E. Vitagliano, "Low-Energy Supernovae Severely Constrain Radiative Particle Decays," *Phys. Rev. Lett.* **128** no. 22, (2022) 221103, arXiv:2201.09890 [astro-ph.HE].

[188] M. Diamond, D. F. G. Fiorillo, G. Marques-Tavares, I. Tamborra, and E. Vitagliano, "Multimessenger Constraints on Radiatively Decaying Axions from GW170817," *Phys. Rev. Lett.* **132** no. 10, (2024) 101004, arXiv:2305.10327 [hep-ph].

[189] D. F. G. Fiorillo, T. Pitik, and E. Vitagliano, "Energy Transfer by Feebly Interacting Particles in Supernovae: The Trapping Regime," *Phys. Rev. Lett.* **135** no. 7, (2025) 071005, arXiv:2503.13653 [hep-ph].

[190] F. R. Candón, D. F. G. Fiorillo, H.-T. Janka, B. F. A. van Baal, and E. Vitagliano, "Small Progenitors, Large Couplings: Type Ic Supernova Constraints on Radiatively Decaying Particles," arXiv:2509.18253 [hep-ph].

[191] J. H. Chang, R. Essig, and S. D. McDermott, "Revisiting Supernova 1987A Constraints on Dark Photons," *JHEP* **01** (2017) 107, arXiv:1611.03864 [hep-ph].

[192] E. Hardy and R. Lasenby, "Stellar cooling bounds on new light particles: plasma mixing effects," *JHEP* **02** (2017) 033, arXiv:1611.05852 [hep-ph].

[193] K. Mori, T. Takiwaki, and K. Kohri, "Verifying the failing supernova constraint on dark photons with two-dimensional hydrodynamic simulations," *Phys. Rev. D* **113** no. 4, (2026) L041303, arXiv:2511.18122 [astro-ph.HE].

[194] J. D. Bjorken, R. Essig, P. Schuster, and N. Toro, "New Fixed-Target Experiments to Search for Dark Gauge Forces," *Phys. Rev. D* **80** (2009) 075018, arXiv:0906.0580 [hep-ph].

[195] J. B. Dent, F. Ferrer, and L. M. Krauss, "Constraints on Light Hidden Sector Gauge Bosons from Supernova Cooling," arXiv:1201.2683 [astro-ph.CO].

[196] D. Kazanas, R. N. Mohapatra, S. Nussinov, V. L. Teplitz, and Y. Zhang, "Supernova Bounds on the Dark Photon Using its Electromagnetic Decay," *Nucl. Phys. B* **890** (2014) 17–29, arXiv:1410.0221 [hep-ph].

[197] E. Rrapaj and S. Reddy, "Nucleon-nucleon bremsstrahlung of dark gauge bosons and revised supernova constraints," *Phys. Rev. C* **94** no. 4, (2016) 045805, arXiv:1511.09136 [nucl-th].

[198] A. Caputo, G. Raffelt, and E. Vitagliano, "Muonic boson limits: Supernova redux," *Phys. Rev. D* **105** no. 3, (2022) 035022, arXiv:2109.03244 [hep-ph].

[199] A. Caputo, G. Raffelt, and E. Vitagliano, "Radiative transfer in stars by feebly interacting bosons," *JCAP* **08** no. 08, (2022) 045, arXiv:2204.11862 [astro-ph.SR].

[200] D. F. G. Fiorillo, G. G. Raffelt, and E. Vitagliano, "Supernova emission of secretly interacting neutrino fluid: Theoretical foundations," *Phys. Rev. D* **109** no. 2, (2024) 023017, arXiv:2307.15122 [hep-ph].

[201] D. F. G. Fiorillo, G. G. Raffelt, and E. Vitagliano, "Large Neutrino Secret Interactions Have a Small Impact on Supernovae," *Phys. Rev. Lett.* **132** no. 2, (2024) 021002, arXiv:2307.15115 [hep-ph].

[202] K.-C. Lai, C. S. J. Leung, and G.-L. Lin, "SN1987A constraints to BSM models with extra neutral bosons near the trapping regime: U(1)Lμ-Lτ model as an illustrative example," *Phys. Rev. D* **110** no. 10, (2024) 103023, arXiv:2401.16023 [hep-ph].

[203] A. W. Steiner, M. Hempel, and T. Fischer, "Core-collapse supernova equations of state based on neutron star observations," *Astrophys. J.* **774** (2013) 17, arXiv:1207.2184 [astro-ph.SR].

[204] J. M. Lattimer and F. D. Swesty, "A Generalized equation of state for hot, dense matter," *Nucl. Phys. A* **535** (1991) 331–376.

[205] S. E. Woosley, A. Heger, and T. A. Weaver, "The evolution and explosion of massive stars," *Rev. Mod. Phys.* **74** (2002) 1015–1071.

[206] T. Sukhbold, S. Woosley, and A. Heger, "A High-resolution Study of Presupernova Core Structure," *Astrophys. J.* **860** no. 2, (2018) 93, arXiv:1710.03243 [astro-ph.HE].

[207] S. E. Woosley and A. Heger, "Nucleosynthesis and Remnants in Massive Stars of Solar Metallicity," *Phys. Rept.* **442** (2007) 269–283, arXiv:astro-ph/0702176.

[208] R. Bollig, W. DeRocco, P. W. Graham, and H.-T. Janka, "Muons in Supernovae: Implications for the Axion-Muon Coupling," *Phys. Rev. Lett.* **125** no. 5, (2020) 051104, arXiv:2005.07141 [hep-ph]. [Erratum: Phys.Rev.Lett. 126, 189901 (2021)].

[209] E. Braaten and D. Segel, "Neutrino energy loss from the plasma process at all temperatures and densities," *Phys. Rev. D* **48** (1993) 1478–1491, arXiv:hep-ph/9302213.

[210] H. An, M. Pospelov, and J. Pradler, "New stellar constraints on dark photons," *Phys. Lett. B* **725** (2013) 190–195, arXiv:1302.3884 [hep-ph].

[211] H. A. Weldon, "Simple Rules for Discontinuities in Finite Temperature Field Theory," *Phys. Rev. D* **28** (1983) 2007.

[212] E. Braaten, "Neutrino emissivity of an ultrarelativistic plasma from positron and plasmino annihilation,".

[213] E. Hardy, A. Sokolov, and H. Stubbs, "Supernova bounds on new scalars from resonant and soft emission," arXiv:2410.17347 [hep-ph].

[214] J. Marteau, J. Delorme, and M. Ericson, "Neutrino oxygen interactions: Role of nuclear physics in the atmospheric neutrino anomaly," in *34th Rencontres de Moriond: Electroweak Interactions and Unified Theories*, pp. 121–126. 1999. arXiv:hep-ph/9906449.

[215] E. Kolbe, K. Langanke, and P. Vogel, "Estimates of weak and electromagnetic nuclear decay signatures for neutrino reactions in Super-Kamiokande," *Phys. Rev. D* **66** (2002) 013007.

[216] A. Strumia and F. Vissani, "Precise quasielastic neutrino/nucleon cross-section," *Phys. Lett. B* **564** (2003) 42–54, arXiv:astro-ph/0302055.

[217] J. A. Formaggio and G. P. Zeller, "From eV to EeV: Neutrino Cross Sections Across Energy Scales," *Rev. Mod. Phys.* **84** (2012) 1307–1341, arXiv:1305.7513 [hep-ex].

[218] **IMB** Collaboration, C. B. Bratton *et al.*, "Angular Distribution of Events From Sn1987a," *Phys. Rev. D* **37** (1988) 3361.

[219] L. Oberauer, C. Hagner, G. Raffelt, and E. Rieger, "Supernova bounds on neutrino radiative decays," *Astropart. Phys.* **1** (1993) 377–386.

[220] T. Piran, "Gamma-ray bursts and the fireball model," *Phys. Rept.* **314** (1999) 575–667, arXiv:astro-ph/9810256.

[221] M. Diamond, D. F. G. Fiorillo, G. Marques-Tavares, and E. Vitagliano, "Axion-sourced fireballs from supernovae," *Phys. Rev. D* **107** no. 10, (2023) 103029, arXiv:2303.11395 [hep-ph]. [Erratum: Phys.Rev.D 108, 049902 (2023)].

[222] W. DeRocco, P. W. Graham, D. Kasen, G. Marques-Tavares, and S. Rajendran, "Observable signatures of dark photons from supernovae," *JHEP* **02** (2019) 171, arXiv:1901.08596 [hep-ph].

[223] **LIGO Scientific, Virgo** Collaboration, B. P. Abbott *et al.*, "GW170817: Observation of Gravitational Waves from a Binary Neutron Star Inspiral," *Phys. Rev. Lett.* **119** no. 16, (2017) 161101, arXiv:1710.05832 [gr-qc].

[224] A. Murguia-Berthier, E. Ramirez-Ruiz, F. De Colle, A. Janiuk, S. Rosswog, and W. H. Lee, "The Fate of the Merger Remnant in GW170817 and its Imprint on the Jet Structure," *Astrophys. J.* **908** no. 2, (2021) 152, arXiv:2007.12245 [astro-ph.HE].

[225] J. Liao and D. Marfatia, "Coherent constraints on nonstandard neutrino interactions," *Physics Letters B* **775** (12, 2017) 54–57. http://dx.doi.org/10.1016/j.physletb.2017.10.046.

[226] **COHERENT** Collaboration, D. Akimov *et al.*, "Observation of Coherent Elastic Neutrino-Nucleus Scattering," *Science* **357** no. 6356, (2017) 1123–1126, arXiv:1708.01294 [nucl-ex].

[227] M. Abdullah *et al.*, "Coherent elastic neutrino-nucleus scattering: Terrestrial and astrophysical applications," arXiv:2203.07361 [hep-ph].

[228] J. B. Dent, B. Dutta, S. Liao, J. L. Newstead, L. E. Strigari, and J. W. Walker, "Probing light mediators at ultralow threshold energies with coherent elastic neutrino-nucleus scattering," *Phys. Rev. D* **96** no. 9, (2017) 095007, arXiv:1612.06350 [hep-ph].

[229] I. M. Shoemaker, "COHERENT search strategy for beyond standard model neutrino interactions," *Phys. Rev. D* **95** no. 11, (2017) 115028, arXiv:1703.05774 [hep-ph].

[230] D. K. Papoulias and T. S. Kosmas, "COHERENT constraints to conventional and exotic neutrino physics," *Phys. Rev. D* **97** no. 3, (2018) 033003, arXiv:1711.09773 [hep-ph].

[231] M. Abdullah, J. B. Dent, B. Dutta, G. L. Kane, S. Liao, and L. E. Strigari, "Coherent elastic neutrino nucleus scattering as a probe of a Z' through kinetic and mass mixing effects," *Phys. Rev. D* **98** no. 1, (2018) 015005, arXiv:1803.01224 [hep-ph].

[232] P. B. Denton, Y. Farzan, and I. M. Shoemaker, "Testing large non-standard neutrino interactions with arbitrary mediator mass after COHERENT data," *JHEP* **07** (2018) 037, arXiv:1804.03660 [hep-ph].

[233] **CONNIE** Collaboration, A. Aguilar-Arevalo *et al.*, "Search for light mediators in the low-energy data of the CONNIE reactor neutrino experiment," *JHEP* **04** (2020) 054, arXiv:1910.04951 [hep-ex].

[234] M. Cadeddu, N. Cargioli, F. Dordei, C. Giunti, Y. F. Li, E. Picciau, and Y. Y. Zhang, "Constraints on light vector mediators through coherent elastic neutrino nucleus scattering data from COHERENT," *JHEP* **01** (2021) 116, arXiv:2008.05022 [hep-ph].

[235] O. G. Miranda, D. K. Papoulias, G. Sanchez Garcia, O. Sanders, M. Tórtola, and J. W. F. Valle, "Implications of the first detection of coherent elastic neutrino-nucleus scattering (CEvNS) with Liquid Argon," *JHEP* **05** (2020) 130, arXiv:2003.12050 [hep-ph]. [Erratum: JHEP 01, 067 (2021)].

[236] **CONUS** Collaboration, H. Bonet *et al.*, "Novel constraints on neutrino physics beyond the standard model from the CONUS experiment," *JHEP* **05** (2022) 085, arXiv:2110.02174 [hep-ph].

[237] L. M. G. de la Vega, L. J. Flores, N. Nath, and E. Peinado, "Complementarity between dark matter direct searches and CEνNS experiments in U(1)' models," *JHEP* **09** (2021) 146, arXiv:2107.04037 [hep-ph].

[238] P. Coloma, I. Esteban, M. C. Gonzalez-Garcia, L. Larizgoitia, F. Monrabal, and S. Palomares-Ruiz, "Bounds on new physics with data of the Dresden-II reactor experiment and COHERENT," *JHEP* **05** (2022) 037, arXiv:2202.10829 [hep-ph].

[239] M. Atzori Corona, M. Cadeddu, N. Cargioli, F. Dordei, C. Giunti, Y. F. Li, E. Picciau, C. A. Ternes, and Y. Y. Zhang, "Probing light mediators and $(g-2)_\mu$ through detection of coherent elastic neutrino nucleus scattering at COHERENT," *JHEP* **05** (2022) 109, arXiv:2202.11002 [hep-ph].

[240] V. De Romeri, D. K. Papoulias, and G. Sanchez Garcia, "Implications of the first CONUS+ measurement of coherent elastic neutrino-nucleus scattering," *Phys. Rev. D* **111** no. 7, (2025) 075025, arXiv:2501.17843 [hep-ph].

[241] A. Chattaraj, A. Majumdar, and R. Srivastava, "Probing standard model and beyond with reactor CEνNS data of CONUS+ experiment," *Phys. Lett. B* **864** (2025) 139438, arXiv:2501.12441 [hep-ph].

[242] **TEXONO** Collaboration, S. Karadağ *et al.*, "Constraints on new physics with light mediators and generalized neutrino interactions via coherent elastic neutrino nucleus scattering," *Phys. Rev. D* **112** no. 3, (2025) 035038, arXiv:2502.20007 [hep-ex].

[243] **COHERENT** Collaboration, D. Akimov *et al.*, "Measurement of the Coherent Elastic Neutrino-Nucleus Scattering Cross Section on CsI by COHERENT," *Phys. Rev. Lett.* **129** no. 8, (2022) 081801, arXiv:2110.07730 [hep-ex].

[244] **COHERENT** Collaboration, D. Akimov *et al.*, "First Measurement of Coherent Elastic Neutrino-Nucleus Scattering on Argon," *Phys. Rev. Lett.* **126** no. 1, (2021) 012002, arXiv:2003.10630 [nucl-ex].

[245] N. Ackermann *et al.*, "Direct observation of coherent elastic antineutrino–nucleus scattering," *Nature* **643** no. 8074, (2025) 1229–1233, arXiv:2501.05206 [hep-ex].

[246] A. M. Konovalov, "Status of the COHERENT Experiment and New Physics Opportunities at the SNS Facility," *Moscow Univ. Phys. Bull.* **79** no. Suppl 1, (2024) 220–226.

[247] E. Picciau, *Low-energy signatures in DarkSide-50experiment and neutrino scattering processes*. PhD thesis, Università degli Studi di Cagliari, Italy, Cagliari U., 2022.

[248] J. Colaresi, J. I. Collar, T. W. Hossbach, C. M. Lewis, and K. M. Yocum, "Measurement of Coherent Elastic Neutrino-Nucleus Scattering from Reactor Antineutrinos," *Phys. Rev. Lett.* **129** no. 21, (2022) 211802, arXiv:2202.09672 [hep-ex].

[249] **TEXONO** Collaboration, S. Karmakar *et al.*, "New Limits on the Coherent Neutrino-Nucleus Elastic Scattering Cross Section at the Kuo-Sheng Reactor-Neutrino Laboratory," *Phys. Rev. Lett.* **134** no. 12, (2025) 121802, arXiv:2411.18812 [nucl-ex].

[250] **NUCLEUS** Collaboration, C. Goupy *et al.*, "Exploring coherent elastic neutrino-nucleus scattering of reactor neutrinos with the NUCLEUS experiment," *SciPost Phys. Proc.* **12** (2023) 053, arXiv:2211.04189 [physics.ins-det].

[251] **Ricochet** Collaboration, C. Augier *et al.*, "Fast neutron background characterization of the future Ricochet experiment at the ILL research nuclear reactor," *Eur. Phys. J. C* **83** no. 1, (2023) 20, arXiv:2208.01760 [astro-ph.IM].

[252] **CONNIE** Collaboration, A. A. Aguilar-Arevalo *et al.*, "Searches for CEνNS and Physics beyond the Standard Model using Skipper-CCDs at CONNIE," arXiv:2403.15976 [hep-ex].

[253] M. Atzori Corona, M. Cadeddu, N. Cargioli, F. Dordei, and C. Giunti, "Reactor antineutrinos CEνNS on germanium: CONUS+ and TEXONO as a new gateway to SM and BSM physics," *Phys. Rev. D* **112** no. 1, (2025) 015007, arXiv:2501.18550 [hep-ph].

[254] M. Atzori Corona, M. Cadeddu, N. Cargioli, F. Dordei, C. Giunti, and R. Pavarani, "Toward precision physics tests with future COHERENT detectors," arXiv:2509.04205 [physics.ins-det].

[255] G. Bellini *et al.*, "Precision measurement of the 7Be solar neutrino interaction rate in Borexino," *Phys. Rev. Lett.* **107** (2011) 141302, arXiv:1104.1816 [hep-ex].

[256] **Borexino** Collaboration, G. Bellini *et al.*, "Final results of Borexino Phase-I on low energy solar neutrino spectroscopy," *Phys. Rev. D* **89** no. 11, (2014) 112007, arXiv:1308.0443 [hep-ex].

[257] **BOREXINO** Collaboration, G. Bellini *et al.*, "Neutrinos from the primary proton–proton fusion process in the Sun," *Nature* **512** no. 7515, (2014) 383–386.

[258] **Borexino** Collaboration, M. Agostini *et al.*, "First Simultaneous Precision Spectroscopy of *pp*, ^{7}Be, and *pep* Solar Neutrinos with Borexino Phase-II," *Phys. Rev. D* **100** no. 8, (2019) 082004, arXiv:1707.09279 [hep-ex].

[259] **BOREXINO** Collaboration, M. Agostini *et al.*, "Comprehensive measurement of *pp*-chain solar neutrinos," *Nature* **562** no. 7728, (2018) 505–510.

[260] **BOREXINO** Collaboration, M. Agostini *et al.*, "Experimental evidence of neutrinos produced in the CNO fusion cycle in the Sun," *Nature* **587** (2020) 577–582, arXiv:2006.15115 [hep-ex].

[261] **TEXONO** Collaboration, M. Deniz *et al.*, "Measurement of Nu(e)-bar -Electron Scattering Cross-Section with a CsI(Tl) Scintillating Crystal Array at the Kuo-Sheng Nuclear Power Reactor," *Phys. Rev. D* **81** (2010) 072001, arXiv:0911.1597 [hep-ex].

[262] P. V. et al., "Precision measurement of electroweak parameters from the scattering of muon-neutrinos on electrons," *Physics Letters B* **335** no. 2, (1994) 246–252. https://www.sciencedirect.com/science/article/pii/0370269394914214.

[263] **CHARM-II** Collaboration, P. Vilain *et al.*, "Measurement of differential cross-sections for muon-neutrino electron scattering," *Phys. Lett. B* **302** (1993) 351–355.

[264] P. Vogel and J. Engel, "Neutrino Electromagnetic Form-Factors," *Phys. Rev. D* **39** (1989) 3378.

[265] P. Coloma, M. C. Gonzalez-Garcia, M. Maltoni, J. a. P. Pinheiro, and S. Urrea, "Constraining new physics with Borexino Phase-II spectral data," *JHEP* **07** (2022) 138, arXiv:2204.03011 [hep-ph]. [Erratum: JHEP 11, 138 (2022)].

[266] P. J. Fox, R. Harnik, J. Kopp, and Y. Tsai, "LEP Shines Light on Dark Matter," *Phys. Rev. D* **84** (2011) 014028, arXiv:1103.0240 [hep-ph].

[267] **NA64** Collaboration, D. Banerjee *et al.*, "Search for vector mediator of Dark Matter production in invisible decay mode," *Phys. Rev. D* **97** no. 7, (2018) 072002, arXiv:1710.00971 [hep-ex].

[268] **BaBar** Collaboration, J. P. Lees *et al.*, "Search for Invisible Decays of a Dark Photon Produced in e^+e^- Collisions at BaBar," *Phys. Rev. Lett.* **119** no. 13, (2017) 131804, arXiv:1702.03327 [hep-ex].

[269] **Belle-II** Collaboration, I. Adachi *et al.*, "Search for an Invisibly Decaying Z' Boson at Belle II in $e^+e^- \to \mu^+\mu^-(e^\pm\mu^\mp)$ Plus Missing Energy Final States," *Phys. Rev. Lett.* **124** no. 14, (2020) 141801, arXiv:1912.11276 [hep-ex].

[270] **NA62** Collaboration, E. Cortina Gil *et al.*, "Search for production of an invisible dark photon in π^0 decays," *JHEP* **05** (2019) 182, arXiv:1903.08767 [hep-ex].

[271] **NA64** Collaboration, Y. M. Andreev *et al.*, "Constraints on New Physics in Electron $g-2$ from a Search for Invisible Decays of a Scalar, Pseudoscalar, Vector, and Axial Vector," *Phys. Rev. Lett.* **126** no. 21, (2021) 211802, arXiv:2102.01885 [hep-ex].

[272] **NA64** Collaboration, Y. M. Andreev *et al.*, "Search for a New B-L Z' Gauge Boson with the NA64 Experiment at CERN," *Phys. Rev. Lett.* **129** no. 16, (2022) 161801, arXiv:2207.09979 [hep-ex].

[273] **NA64** Collaboration, Y. M. Andreev *et al.*, "Search for Light Dark Matter with NA64 at CERN," *Phys. Rev. Lett.* **131** no. 16, (2023) 161801, arXiv:2307.02404 [hep-ex].

[274] **DONuT** Collaboration, K. Kodama *et al.*, "Final tau-neutrino results from the DONuT experiment," *Phys. Rev. D* **78** (2008) 052002, arXiv:0711.0728 [hep-ex].

[275] **SHiP** Collaboration, M. Anelli *et al.*, "A facility to Search for Hidden Particles (SHiP) at the CERN SPS," arXiv:1504.04956 [physics.ins-det].

[276] **FASER** Collaboration, H. Abreu *et al.*, "Detecting and Studying High-Energy Collider Neutrinos with FASER at the LHC," *Eur. Phys. J. C* **80** no. 1, (2020) 61, arXiv:1908.02310 [hep-ex].

[277] **SHiP** Collaboration, C. Ahdida *et al.*, "SND@LHC," arXiv:2002.08722 [physics.ins-det].

[278] F. Kling, "Probing light gauge bosons in tau neutrino experiments," *Phys. Rev. D* **102** no. 1, (2020) 015007, arXiv:2005.03594 [hep-ph].

[279] F. Kling, P. Reimitz, and A. Ritz, "Dark Vector Boson Bremsstrahlung: New Form Factors for a Broader Class of Models," arXiv:2509.09437 [hep-ph].

[280] S. Alekhin *et al.*, "A facility to Search for Hidden Particles at the CERN SPS: the SHiP physics case," *Rept. Prog. Phys.* **79** no. 12, (2016) 124201, arXiv:1504.04855 [hep-ph].

[281] **SHiP** Collaboration, C. Ahdida *et al.*, "Sensitivity of the SHiP experiment to dark photons decaying to a pair of charged particles," *Eur. Phys. J. C* **81** no. 5, (2021) 451, arXiv:2011.05115 [hep-ex].

[282] T. Zhou, R. Plestid, K. J. Kelly, N. Blinov, and P. J. Fox, "Long-lived vectors from electromagnetic cascades at SHiP," *JHEP* **02** (2025) 107, arXiv:2412.01880 [hep-ph].

[283] J. D. Bjorken, S. Ecklund, W. R. Nelson, A. Abashian, C. Church, B. Lu, L. W. Mo, T. A. Nunamaker, and P. Rassmann, "Search for Neutral Metastable Penetrating Particles Produced in the SLAC Beam Dump," *Phys. Rev. D* **38** (1988) 3375.

[284] Y.-S. Tsai, "AXION BREMSSTRAHLUNG BY AN ELECTRON BEAM," *Phys. Rev. D* **34** (1986) 1326.

[285] S. Andreas, *Light Weakly Interacting Particles: Constraints and Connection to Dark Matter*. PhD thesis, Hamburg U., 2013.

[286] M. Davier and H. Nguyen Ngoc, "An Unambiguous Search for a Light Higgs Boson," *Phys. Lett. B* **229** (1989) 150–155.

[287] A. Konaka *et al.*, "Search for Neutral Particles in Electron Beam Dump Experiment," *Phys. Rev. Lett.* **57** (1986) 659.

[288] **NA64** Collaboration, D. Banerjee *et al.*, "Search for a Hypothetical 16.7 MeV Gauge Boson and Dark Photons in the NA64 Experiment at CERN," *Phys. Rev. Lett.* **120** no. 23, (2018) 231802, arXiv:1803.07748 [hep-ex].

[289] **NA64** Collaboration, D. Banerjee *et al.*, "Improved limits on a hypothetical X(16.7) boson and a dark photon decaying into e^+e^- pairs," *Phys. Rev. D* **101** no. 7, (2020) 071101, arXiv:1912.11389 [hep-ex].

[290] E. M. Riordan *et al.*, "A Search for Short Lived Axions in an Electron Beam Dump Experiment," *Phys. Rev. Lett.* **59** (1987) 755.

[291] A. Bross, M. Crisler, S. H. Pordes, J. Volk, S. Errede, and J. Wrbanek, "A Search for Shortlived Particles Produced in an Electron Beam Dump," *Phys. Rev. Lett.* **67** (1991) 2942–2945.

[292] J. R. Cudell, V. Ezhela, P. Gauron, K. Kang, Y. V. Kuyanov, S. Lugovsky, B. Nicolescu, and N. Tkachenko, "Hadronic scattering amplitudes: Medium-energy constraints on asymptotic behavior," *Phys. Rev. D* **65** (2002) 074024, arXiv:hep-ph/0107219.

[293] J. Blumlein and J. Brunner, "New Exclusion Limits for Dark Gauge Forces from Beam-Dump Data," *Phys. Lett. B* **701** (2011) 155–159, arXiv:1104.2747 [hep-ex].

[294] S. N. Gninenko, "Stringent limits on the $\pi^0 \to \gamma X, X \to e^+e^-$ decay from neutrino experiments and constraints on new light gauge bosons," *Phys. Rev. D* **85** (2012) 055027, arXiv:1112.5438 [hep-ph].

[295] S. N. Gninenko, "Constraints on sub-GeV hidden sector gauge bosons from a search for heavy neutrino decays," *Phys. Lett. B* **713** (2012) 244–248, arXiv:1204.3583 [hep-ph].

[296] J. Blümlein and J. Brunner, "New Exclusion Limits on Dark Gauge Forces from Proton Bremsstrahlung in Beam-Dump Data," *Phys. Lett. B* **731** (2014) 320–326, arXiv:1311.3870 [hep-ph].

[297] **NOMAD** Collaboration, P. Astier *et al.*, "Search for heavy neutrinos mixing with tau neutrinos," *Phys. Lett. B* **506** (2001) 27–38, arXiv:hep-ex/0101041.

[298] G. Bernardi *et al.*, "Search for Neutrino Decay," *Phys. Lett. B* **166** (1986) 479–483.

[299] Y.-D. Tsai, P. deNiverville, and M. X. Liu, "Dark Photon and Muon $g-2$ Inspired Inelastic Dark Matter Models at the High-Energy Intensity Frontier," *Phys. Rev. Lett.* **126** no. 18, (2021) 181801, arXiv:1908.07525 [hep-ph].

[300] **APEX** Collaboration, S. Abrahamyan *et al.*, "Search for a New Gauge Boson in Electron-Nucleus Fixed-Target Scattering by the APEX Experiment," *Phys. Rev. Lett.* **107** (2011) 191804, arXiv:1108.2750 [hep-ex].

[301] **A1** Collaboration, H. Merkel *et al.*, "Search for Light Gauge Bosons of the Dark Sector at the Mainz Microtron," *Phys. Rev. Lett.* **106** (2011) 251802, arXiv:1101.4091 [nucl-ex].

[302] H. Merkel *et al.*, "Search at the Mainz Microtron for Light Massive Gauge Bosons Relevant for the Muon g-2 Anomaly," *Phys. Rev. Lett.* **112** no. 22, (2014) 221802, arXiv:1404.5502 [hep-ex].

[303] M. Battaglieri *et al.*, "The Heavy Photon Search Test Detector," *Nucl. Instrum. Meth. A* **777** (2015) 91–101, arXiv:1406.6115 [physics.ins-det].

[304] P. H. Adrian *et al.*, "Searching for prompt and long-lived dark photons in electroproduced e+e- pairs with the heavy photon search experiment at JLab," *Phys. Rev. D* **108** no. 1, (2023) 012015, arXiv:2212.10629 [hep-ex].

[305] **NA48/2** Collaboration, J. R. Batley *et al.*, "Search for the dark photon in π^0 decays," *Phys. Lett. B* **746** (2015) 178–185, arXiv:1504.00607 [hep-ex].

[306] P. S. B. Dev, B. Dutta, T. Han, A. Karthikeyan, D. Kim, and H. Kim, "New physics at a neutron beam dump," *Phys. Rev. D* **110** no. 5, (2024) L051703, arXiv:2311.10078 [hep-ph].

[307] **LHCb** Collaboration, R. Aaij *et al.*, "Search for Dark Photons Produced in 13 TeV *pp* Collisions," *Phys. Rev. Lett.* **120** no. 6, (2018) 061801, arXiv:1710.02867 [hep-ex].

[308] **KLOE-2** Collaboration, D. Babusci *et al.*, "Limit on the production of a light vector gauge boson in phi meson decays with the KLOE detector," *Phys. Lett. B* **720** (2013) 111–115, arXiv:1210.3927 [hep-ex].

[309] A. Anastasi *et al.*, "Limit on the production of a low-mass vector boson in $e^+e^- \to U\gamma$, $U \to e^+e^-$ with the KLOE experiment," *Phys. Lett. B* **750** (2015) 633–637, arXiv:1509.00740 [hep-ex].

[310] **KLOE-2** Collaboration, A. Anastasi *et al.*, "Combined limit on the production of a light gauge boson decaying into $\mu^+\mu^-$ and $\pi^+\pi^-$," *Phys. Lett. B* **784** (2018) 336–341, arXiv:1807.02691 [hep-ex].

[311] **BESIII** Collaboration, M. Ablikim *et al.*, "Dark Photon Search in the Mass Range Between 1.5 and 3.4 GeV/c^2," *Phys. Lett. B* **774** (2017) 252–257, arXiv:1705.04265 [hep-ex].

[312] **BaBar** Collaboration, J. P. Lees *et al.*, "Search for a Dark Photon in e^+e^- Collisions at BaBar," *Phys. Rev. Lett.* **113** no. 20, (2014) 201801, arXiv:1406.2980 [hep-ex].

[313] M. Graham, C. Hearty, and M. Williams, "Searches for Dark Photons at Accelerators," *Ann. Rev. Nucl. Part. Sci.* **71** (2021) 37–58, arXiv:2104.10280 [hep-ph].

[314] D. Craik, P. Ilten, D. Johnson, and M. Williams, "LHCb future dark-sector sensitivity projections for Snowmass 2021," in *Snowmass 2021*. 3, 2022. arXiv:2203.07048 [hep-ph].

[315] O. Seto, T. Shimomura, and S. Yoshida, "New rare meson decay constraints on a light vector in $U(1)_{B-L}$, $U(1)_R$ and the dark photon," *JHEP* **09** (2025) 211, arXiv:2504.15896 [hep-ph].

[316] **REDTOP** Collaboration, J. Elam *et al.*, "The REDTOP experiment: Rare η/η' Decays To Probe New Physics," arXiv:2203.07651 [hep-ex].

[317] M. Pospelov, "Secluded U(1) below the weak scale," *Phys. Rev. D* **80** (2009) 095002, arXiv:0811.1030 [hep-ph].

[318] R. H. Parker, C. Yu, W. Zhong, B. Estey, and H. Müller, "Measurement of the fine-structure constant as a test of the Standard Model," *Science* **360** (2018) 191, arXiv:1812.04130 [physics.atom-ph].

[319] L. Morel, Z. Yao, P. Cladé, and S. Guellati-Khélifa, "Determination of the fine-structure constant with an accuracy of 81 parts per trillion," *Nature* **588** no. 7836, (2020) 61–65.

[320] X. Fan, T. G. Myers, B. A. D. Sukra, and G. Gabrielse, "Measurement of the Electron Magnetic Moment," *Phys. Rev. Lett.* **130** no. 7, (2023) 071801, arXiv:2209.13084 [physics.atom-ph].

[321] P. Clade, E. de Mirandes, M. Cadoret, S. Guellati-Khelifa, C. Schwob, F. Nez, L. Julien, and F. Biraben, "Determination of the Fine Structure Constant Based on Bloch Oscillations of Ultracold Atoms in a Vertical Optical Lattice," *Phys. Rev. Lett.* **96** (2006) 033001, arXiv:physics/0510101.

[322] R. Aliberti *et al.*, "The anomalous magnetic moment of the muon in the Standard Model: an update," *Phys. Rept.* **1143** (2025) 1–158, arXiv:2505.21476 [hep-ph].

[323] A. Hook, E. Izaguirre, and J. G. Wacker, "Model Independent Bounds on Kinetic Mixing," *Adv. High Energy Phys.* **2011** (2011) 859762, arXiv:1006.0973 [hep-ph].

[324] D. Curtin, R. Essig, S. Gori, and J. Shelton, "Illuminating Dark Photons with High-Energy Colliders," *JHEP* **02** (2015) 157, arXiv:1412.0018 [hep-ph].

[325] B. M. Loizos, X. G. Wang, A. W. Thomas, M. J. White, and A. G. Williams, "Constraints on the dark sector from electroweak precision observables," *J. Phys. G* **51** no. 7, (2024) 075002, arXiv:2306.13408 [hep-ph].

[326] M. Zieliński and C. Gatto, "The REDTOP Experiment: an η/η' Factory to Explore Dark Matter and Physics Beyond the Standard Model," *Acta Phys. Polon. Supp.* **18** no. 4, (2025) 4–A5, arXiv:2509.26552 [hep-ex].

[327] L. Gan, B. Kubis, E. Passemar, and S. Tulin, "Precision tests of fundamental physics with η and η' mesons," *Phys. Rept.* **945** (2022) 1–105, arXiv:2007.00664 [hep-ph].

[328] N. Arkani-Hamed, D. P. Finkbeiner, T. R. Slatyer, and N. Weiner, "A Theory of Dark Matter," *Phys. Rev. D* **79** (2009) 015014, arXiv:0810.0713 [hep-ph].

[329] M. Pospelov and A. Ritz, "Astrophysical Signatures of Secluded Dark Matter," *Phys. Lett. B* **671** (2009) 391–397, arXiv:0810.1502 [hep-ph].

[330] A. E. Nelson and N. Tetradis, "CONSTRAINTS ON A NEW VECTOR BOSON COUPLED TO BARYONS," *Phys. Lett. B* **221** (1989) 80–84.

[331] X. G. He, G. C. Joshi, H. Lew, and R. R. Volkas, "NEW Z-prime PHENOMENOLOGY," *Phys. Rev. D* **43** (1991) 22–24.

[332] N. Okada, S. Okada, and Q. Shafi, "Light Z' and dark matter from $\mathrm{U}(1)_X$ gauge symmetry," *Phys. Lett. B* **810** (2020) 135845, arXiv:2003.02667 [hep-ph].

[333] M. Bordag, U. Mohideen, and V. M. Mostepanenko, "New developments in the Casimir effect," *Phys. Rept.* **353** (2001) 1–205, arXiv:quant-ph/0106045.

[334] M. Bordag, G. L. Klimchitskaya, U. Mohideen, and V. M. Mostepanenko, *Advances in the Casimir effect*, vol. 145. Oxford University Press, 2009.

[335] E. G. Adelberger, B. R. Heckel, S. A. Hoedl, C. D. Hoyle, D. J. Kapner, and A. Upadhye, "Particle Physics Implications of a Recent Test of the Gravitational Inverse Sqaure Law," *Phys. Rev. Lett.* **98** (2007) 131104, arXiv:hep-ph/0611223.

[336] E. G. Adelberger, J. H. Gundlach, B. R. Heckel, S. Hoedl, and S. Schlamminger, "Torsion balance experiments: A low-energy frontier of particle physics," *Prog. Part. Nucl. Phys.* **62** (2009) 102–134.

[337] M. Kawasaki, K. Kohri, and T. Moroi, "Big-Bang nucleosynthesis and hadronic decay of long-lived massive particles," *Phys. Rev. D* **71** (2005) 083502, arXiv:astro-ph/0408426.

[338] T. Kanzaki, M. Kawasaki, K. Kohri, and T. Moroi, "Cosmological Constraints on Neutrino Injection," *Phys. Rev. D* **76** (2007) 105017, arXiv:0705.1200 [hep-ph].

[339] M. Kawasaki, K. Kohri, T. Moroi, K. Murai, and H. Murayama, "Big-bang nucleosynthesis with sub-GeV massive decaying particles," *JCAP* **12** (2020) 048, arXiv:2006.14803 [hep-ph].

[340] J. Berger, K. Jedamzik, and D. G. E. Walker, "Cosmological Constraints on Decoupled Dark Photons and Dark Higgs," *JCAP* **11** (2016) 032, arXiv:1605.07195 [hep-ph].

[341] M. E. Peskin and D. V. Schroeder, *An Introduction to quantum field theory*. Addison-Wesley, Reading, USA, 1995.

[342] K. Abazajian *et al.*, "CMB-S4 Science Case, Reference Design, and Project Plan," arXiv:1907.04473 [astro-ph.IM].

[343] J. Preskill, "Gauge anomalies in an effective field theory," *Annals Phys.* **210** (1991) 323–379.

[344] N. Craig, I. Garcia Garcia, and G. D. Kribs, "The UV fate of anomalous U(1)s and the Swampland," *JHEP* **11** (2020) 063, arXiv:1912.10054 [hep-ph].

[345] S. Weinberg, *Cosmology*. 2008.

[346] L. C. Thomas, T. Dezen, E. B. Grohs, and C. T. Kishimoto, "Electron-Positron Annihilation Freeze-Out in the Early Universe," *Phys. Rev. D* **101** no. 6, (2020) 063507, arXiv:1910.14050 [hep-ph].

[347] S. Hannestad, "Oscillation effects on neutrino decoupling in the early universe," *Phys. Rev. D* **65** (2002) 083006, arXiv:astro-ph/0111423.

[348] A. D. Dolgov, S. H. Hansen, S. Pastor, S. T. Petcov, G. G. Raffelt, and D. V. Semikoz, "Cosmological bounds on neutrino degeneracy improved by flavor oscillations," *Nucl. Phys. B* **632** (2002) 363–382, arXiv:hep-ph/0201287.

[349] N. Fornengo, C. W. Kim, and J. Song, "Finite temperature effects on the neutrino decoupling in the early universe," *Phys. Rev. D* **56** (1997) 5123–5134, arXiv:hep-ph/9702324.

[350] J. Redondo and M. Postma, "Massive hidden photons as lukewarm dark matter," *JCAP* **02** (2009) 005, arXiv:0811.0326 [hep-ph].

[351] G. Raffelt and D. Seckel, "Bounds on Exotic Particle Interactions from SN 1987a," *Phys. Rev. Lett.* **60** (1988) 1793.

[352] H. An, M. Pospelov, J. Pradler, and A. Ritz, "Direct Detection Constraints on Dark Photon Dark Matter," *Phys. Lett. B* **747** (2015) 331–338, arXiv:1412.8378 [hep-ph].

[353] S.-P. Li and X.-J. Xu, "Production rates of dark photons and Z' in the Sun and stellar cooling bounds," arXiv:2304.12907 [hep-ph].

[354] S. K. A., A. Majumdar, D. K. Papoulias, H. Prajapati, and R. Srivastava, "Implications of first LZ and XENONnT results: A comparative study of neutrino properties and light mediators," *Phys. Lett. B* **839** (2023) 137742, arXiv:2208.06415 [hep-ph].

[355] **CHARM** Collaboration, F. Bergsma *et al.*, "Search for Axion Like Particle Production in 400-GeV Proton - Copper Interactions," *Phys. Lett. B* **157** (1985) 458–462.

[356] A. Berlin, N. Blinov, and S. W. Li, "Dark Sector Equilibration During Nucleosynthesis," *Phys. Rev. D* **100** no. 1, (2019) 015038, arXiv:1904.04256 [hep-ph].

[357] A. G. Riess *et al.*, "New Parallaxes of Galactic Cepheids from Spatially Scanning the Hubble Space Telescope: Implications for the Hubble Constant," *Astrophys. J.* **855** no. 2, (2018) 136, arXiv:1801.01120 [astro-ph.SR].

[358] Z. Hou, R. Keisler, L. Knox, M. Millea, and C. Reichardt, "How Massless Neutrinos Affect the Cosmic Microwave Background Damping Tail," *Phys. Rev. D* **87** (2013) 083008, arXiv:1104.2333 [astro-ph.CO].

[359] A. G. Riess *et al.*, "A 2.4% Determination of the Local Value of the Hubble Constant," *Astrophys. J.* **826** no. 1, (2016) 56, arXiv:1604.01424 [astro-ph.CO].

[360] A. G. Riess *et al.*, "Milky Way Cepheid Standards for Measuring Cosmic Distances and Application to Gaia DR2: Implications for the Hubble Constant," *Astrophys. J.* **861** no. 2, (2018) 126, arXiv:1804.10655 [astro-ph.CO].

[361] **SPT-3G** Collaboration, B. A. Benson *et al.*, "SPT-3G: A Next-Generation Cosmic Microwave Background Polarization Experiment on the South Pole Telescope," *Proc. SPIE Int. Soc. Opt. Eng.* **9153** (2014) 91531P, arXiv:1407.2973 [astro-ph.IM].

[362] **CORE** Collaboration, E. Di Valentino *et al.*, "Exploring cosmic origins with CORE: Cosmological parameters," *JCAP* **04** (2018) 017, arXiv:1612.00021 [astro-ph.CO].

[363] **Simons Observatory** Collaboration, P. Ade *et al.*, "The Simons Observatory: Science goals and forecasts," *JCAP* **02** (2019) 056, arXiv:1808.07445 [astro-ph.CO].

[364] **NASA PICO** Collaboration, S. Hanany *et al.*, "PICO: Probe of Inflation and Cosmic Origins," arXiv:1902.10541 [astro-ph.IM].

[365] N. Sehgal *et al.*, "CMB-HD: An Ultra-Deep, High-Resolution Millimeter-Wave Survey Over Half the Sky," arXiv:1906.10134 [astro-ph.CO].

[366] R. Consiglio, P. F. de Salas, G. Mangano, G. Miele, S. Pastor, and O. Pisanti, "PArthENoPE reloaded," *Comput. Phys. Commun.* **233** (2018) 237–242, arXiv:1712.04378 [astro-ph.CO].

[367] S. Gariazzo, P. F. de Salas, O. Pisanti, and R. Consiglio, "PArthENoPE revolutions," *Comput. Phys. Commun.* **271** (2022) 108205, arXiv:2103.05027 [astro-ph.IM].

[368] A. Arbey, "AlterBBN: A program for calculating the BBN abundances of the elements in alternative cosmologies," *Comput. Phys. Commun.* **183** (2012) 1822–1831, arXiv:1106.1363 [astro-ph.CO].

[369] A. Arbey, J. Auffinger, K. P. Hickerson, and E. S. Jenssen, "AlterBBN v2: A public code for calculating Big-Bang nucleosynthesis constraints in alternative cosmologies," *Comput. Phys. Commun.* **248** (2020) 106982, arXiv:1806.11095 [astro-ph.CO].

[370] C. Pitrou, A. Coc, J.-P. Uzan, and E. Vangioni, "Precision big bang nucleosynthesis with improved Helium-4 predictions," *Phys. Rept.* **754** (2018) 1–66, arXiv:1801.08023 [astro-ph.CO].

[371] A.-K. Burns, T. M. P. Tait, and M. Valli, "PRyMordial: The First Three Minutes, Within and Beyond the Standard Model," arXiv:2307.07061 [hep-ph].

[372] G. Krnjaic, "Dark Radiation from Inflationary Fluctuations," *Phys. Rev. D* **103** no. 12, (2021) 123507, arXiv:2006.13224 [hep-ph].

[373] F.-Y. Cyr-Racine and K. Sigurdson, "Limits on Neutrino-Neutrino Scattering in the Early Universe," *Phys. Rev. D* **90** no. 12, (2014) 123533, arXiv:1306.1536 [astro-ph.CO].

[374] S. Bashinsky and U. Seljak, "Neutrino perturbations in CMB anisotropy and matter clustering," *Phys. Rev. D* **69** (2004) 083002, arXiv:astro-ph/0310198.

[375] D. Baumann, D. Green, J. Meyers, and B. Wallisch, "Phases of New Physics in the CMB," *JCAP* **01** (2016) 007, arXiv:1508.06342 [astro-ph.CO].

[376] G. Choi, C.-T. Chiang, and M. LoVerde, "Probing Decoupling in Dark Sectors with the Cosmic Microwave Background," *JCAP* **06** (2018) 044, arXiv:1804.10180 [astro-ph.CO].

[377] T. Schwemberger and T.-T. Yu, "Detecting beyond the standard model interactions of solar neutrinos in low-threshold dark matter detectors," *Phys. Rev. D* **106** no. 1, (2022) 015002, arXiv:2202.01254 [hep-ph].

[378] K. Kaneta, Z. Kang, and H.-S. Lee, "Right-handed neutrino dark matter under the $B - L$ gauge interaction," *JHEP* **02** (2017) 031, arXiv:1606.09317 [hep-ph].

[379] A. Biswas and A. Gupta, "Freeze-in Production of Sterile Neutrino Dark Matter in $U(1)_{B-L}$ Model," *JCAP* **09** (2016) 044, arXiv:1607.01469 [hep-ph]. [Addendum: JCAP 05, A01 (2017)].

[380] K. J. Kelly, M. Sen, W. Tangarife, and Y. Zhang, "Origin of sterile neutrino dark matter via secret neutrino interactions with vector bosons," *Phys. Rev. D* **101** no. 11, (2020) 115031, arXiv:2005.03681 [hep-ph].

[381] A. Berlin and N. Blinov, "Thermal Dark Matter Below an MeV," *Phys. Rev. Lett.* **120** no. 2, (2018) 021801, arXiv:1706.07046 [hep-ph].

[382] A. Berlin and N. Blinov, "Thermal neutrino portal to sub-MeV dark matter," *Phys. Rev. D* **99** no. 9, (2019) 095030, arXiv:1807.04282 [hep-ph].

[383] T. Gherghetta, J. Kersten, K. Olive, and M. Pospelov, "Evaluating the price of tiny kinetic mixing," *Phys. Rev. D* **100** no. 9, (2019) 095001, arXiv:1909.00696 [hep-ph].

[384] F. del Aguila, G. D. Coughlan, and M. Quiros, "Gauge Coupling Renormalization With Several U(1) Factors," *Nucl. Phys. B* **307** (1988) 633. [Erratum: Nucl.Phys.B 312, 751 (1989)].

[385] F. del Aguila, M. Masip, and M. Perez-Victoria, "Physical parameters and renormalization of $U(1)_a \times U(1)_b$ models," *Nucl. Phys. B* **456** (1995) 531–549, arXiv:hep-ph/9507455.

[386] K. S. Babu, C. F. Kolda, and J. March-Russell, "Leptophobic U(1) s and the R(b) - R(c) crisis," *Phys. Rev. D* **54** (1996) 4635–4647, arXiv:hep-ph/9603212.

[387] K. R. Dienes, C. F. Kolda, and J. March-Russell, "Kinetic mixing and the supersymmetric gauge hierarchy," *Nucl. Phys. B* **492** (1997) 104–118, arXiv:hep-ph/9610479.

[388] S. Eidelman and F. Jegerlehner, "Hadronic contributions to $g - 2$ of the leptons and to the effective fine structure constant $\alpha(M_Z^2)$," *Z. Phys. C* **67** (1995) 585–602, arXiv:hep-ph/9502298.

[389] F. Jegerlehner, "Precision measurements of sigma(hadronic) for alpha(eff)(E) at ILC energies and (g-2)(mu)," *Nucl. Phys. B Proc. Suppl.* **162** (2006) 22–32, arXiv:hep-ph/0608329.

[390] K. Jedamzik, "Big bang nucleosynthesis constraints on hadronically and electromagnetically decaying relic neutral particles," *Phys. Rev. D* **74** (2006) 103509, arXiv:hep-ph/0604251.

[391] J. Jaeckel, J. Redondo, and A. Ringwald, "Signatures of a hidden cosmic microwave background," *Phys. Rev. Lett.* **101** (2008) 131801, arXiv:0804.4157 [astro-ph].

[392] A. Mirizzi, J. Redondo, and G. Sigl, "Microwave Background Constraints on Mixing of Photons with Hidden Photons," *JCAP* **03** (2009) 026, arXiv:0901.0014 [hep-ph].

[393] P. Arias, D. Cadamuro, M. Goodsell, J. Jaeckel, J. Redondo, and A. Ringwald, "WISPy Cold Dark Matter," *JCAP* **06** (2012) 013, arXiv:1201.5902 [hep-ph].

[394] S. D. McDermott and S. J. Witte, "Cosmological evolution of light dark photon dark matter," *Phys. Rev. D* **101** no. 6, (2020) 063030, arXiv:1911.05086 [hep-ph].

[395] S. J. Witte, S. Rosauro-Alcaraz, S. D. McDermott, and V. Poulin, "Dark photon dark matter in the presence of inhomogeneous structure," *JHEP* **06** (2020) 132, arXiv:2003.13698 [astro-ph.CO].

[396] A. Caputo, H. Liu, S. Mishra-Sharma, and J. T. Ruderman, "Modeling Dark Photon Oscillations in Our Inhomogeneous Universe," *Phys. Rev. D* **102** no. 10, (2020) 103533, arXiv:2004.06733 [astro-ph.CO].

[397] A. Caputo, H. Liu, S. Mishra-Sharma, and J. T. Ruderman, "Dark Photon Oscillations in Our Inhomogeneous Universe," *Phys. Rev. Lett.* **125** no. 22, (2020) 221303, arXiv:2002.05165 [astro-ph.CO].

[398] J.-T. Li, G. M. Fuller, and E. Grohs, "Probing dark photons in the early universe with big bang nucleosynthesis," *JCAP* **12** (2020) 049, arXiv:2009.14325 [astro-ph.CO].

[399] J. Redondo, "Helioscope Bounds on Hidden Sector Photons," *JCAP* **07** (2008) 008, arXiv:0801.1527 [hep-ph].

[400] J. Redondo and G. Raffelt, "Solar constraints on hidden photons re-visited," *JCAP* **08** (2013) 034, arXiv:1305.2920 [hep-ph].